University of California
Santa Barbara

Dynamics of Ultracold Lithium in Modulated Optical Lattices

A dissertation submitted in partial satisfaction
of the requirements for the degree

Doctor of Philosophy
in
Physics

by

Coraline Junko Fujiwara

Committee in charge:

Professor David Weld, Chair
Professor Mark Sherwin
Professor Mark Srednicki

December 2019

The Dissertation of Coraline Junko Fujiwara is approved.

Professor Mark Sherwin

Professor Mark Srednicki

Professor David Weld, Committee Chair

July 2019

Dynamics of Ultracold Lithium in Modulated Optical Lattices

by

Coraline Junko Fujiwara

To those who come before and those who will follow.
To those who could not and those who cannot.

Acknowledgements

My path through graduate school has been winding with a diverse set of experiences and influences with both triumphs and trials. And while the following paragraphs can neither hope to fully capture my gratitude for those whose support I benefited nor depict a faithful retelling of the past seven years, I hope they convey the profundity of my experiences in graduate school – academically, professionally, and personally.

First, I thank my advisor David Weld who has provided mentorship over all these years. His patience and willingness to listen helped flourish my academic growth, and his desire to acknowledge and confront challenges of all kinds head-on has molded my own judgement. I also greatly appreciate our frank discussions on both physics and life and respect his ability to make me feel like an equal in our discussions. He also taught me to not only think with my head but also with my nose[1].

Next, I acknowledge the other four that made up the OG5 graduate students — Zach, Ruwan, Shankari, and Kevin[2]. As I look around the lab, I am reminded of their presence in every corner of the room where we spent the better part of a decade working, laughing, sweating, and sometimes bleeding together[3]. The dried epoxy on the ground; the beer stains on the wall; the poorly documented lab notebooks; the fiber glass encrusted bakers hat on the shelf; the fire charred lab coat; the boxed Blue Springsteen; the randomly distributed ball magnets; the disassembled magnet winding rigs; the boxes of shame and sacrifice; the lost archives of lab snaps; and the GR8T PICS: they are all the quirky remnants of the lab we helped build (and sometimes destroy).

As the first set of graduate students, we were all incredibly self-motivated to learn and experiment, and I cannot count the number of lessons I have learned from them all. However, I will name a few of the strongest personal associations I have (none mutually exclusive). From Zach, I learned the utility of playful experimentation and the importance of persistent determination. From Ruwan, I learned the beauty of theory, cricket, and the music of Ke$ha. From Shankari, I learned to not fear calling vendors or colleagues and the value of urgency. And from Kevin, I learned to not be intimidated by others and to approach problems with unbridled enthusiasm. Graduate school would have been for the worse without any one of them. I will always fondly remember science slumber parties while baking the machines, running around the lab after our first MOT, the dual BEC party and the "Evening of Quantum Degeneracy", playing beer pong on optical tables, and countless other hijinks. From our first MOT, to our first BECs, and each one afterwards, I am proud to have had the honor and privilege of working with each of them and sharing our names on our papers.

I am incredibly proud to be handing off the experiments to the next generation of students – Peter Dotti, Quinn Simmons, Roshan Sajjad, Jeremy Tanlimco, Enrique

[1] *sniff sniff*

[2] Also known as Zags, Ruwizzle, Shanqueray, and Decrease; Anger, Sadness, Disgust, and Joy; or Fire, Heart, Wind, and Earth.

[3] As well as drinking.

Morell, Alec Cao, and Max Prichard. In particular, Peter Dotti and Quinn Simmons have shown incredible growth as the new senior students and leaders of the lab. It is challenging to enter a space with so much existing technical knowledge as well as cultural quirks, but I think they have all flourished. As I have transitioned out of the lab at the twilight of my graduate school tenure, I am excited to have witnessed them transform the lab into their own space. I have no doubt that some of my reluctance to endorse some proposed changes in the lab is a consequence of my own inability to let go and fully pass the lab over. More importantly, it is also likely indicative of their own academic growth and readiness to succeed without me[4]. I thank them all for their patience in receiving my advice and mentorship, and I hope I have been a positive influence in their graduate school experience.

I have also had the privilege of working with two post-docs during graduate school. Vyacheslav Lebedev first taught me how to fiber couple and that post-docs could have a life outside of work. Toshihiko Shimasaki has been a constant positive steady force in the lab since he first joined the group. He not only has shown great ability to adapt and bring fresh ideas, but also has taught me how to be a better mentor. From him, I learned that good mentoring sometimes necessitates letting go and allowing others to learn in their own time and way[5].

During my time at Santa Barbara, I have also had the opportunity to work with a variety of researchers at diverse stages in their academic careers. They all contributed greatly to the success of the lab, and I wish them nothing but the best in their futures. Thanks to Erik Anciaux, Andrew Ballin, Morgan Brubaker, Cècile Carcy, James Chow, Sean Frazier, Delia Gratta, Ian Harley, Anne Hèbert, Jacob Hines, Dylan Kennedy, Shura Kotlerman, Alan Long, Shuo Ma, Erica Mason, Krutik Patel, Ted Robinson, Eli Wolf, Xiaofei Zhou, and Yi Zeng. In particular, Sean Frazier made considerable contributions to development of the DDS modulation technology of our optical lattices which is foundational for the data taken in this thesis.

Various staff at the university have also been instrumental in helping me succeed. I cannot fathom how they can manage successive generations of naive and bright-eyed graduate students. Eternal thanks to Jennifer Farrar, Dave Prine, Lynne Leininger, Dan Daniels, Erin Ferguson, Glenn Schiferl, Rick Barber, Guy Patterson, Dan Stack, and the legendary Mike Deal. They and the other employees of the university are vital components to successful research at this institution. I cannot stress enough that nothing would ever get done without any of them.

I have also benefited from incredible physical and mental health support from a variety of institutions and individuals. I do not believe I could have survived graduate school without their support. A heartfelt thanks to Mario Barfield, Shereen Barr, John Kowalczyk, Jessica Lieberman, Erin Moore, Janet Osimo, and Tina Panteleakos.

Finally, thank you to all my friends, family, and loved ones. Thank you. Thank you. Thank you.

[4]SCIENCE MONSTERS. PERFECT STRAIGHT LINE.

[5]Fast food is a great motivator for hungry students. “nyyyaa!”

Curriculum Vitæ

Coraline Junko Fujiwara

Education

2019	Ph.D. Physics (Expected), University of California, Santa Barbara.
2016	M.A. Physics, University of California, Santa Barbara.
2012	B.A. Physics, University of California, Berkeley.

Publications

Quantifying and controlling Prethermal Nonergodicity in Interacting Floquet Matter. K. Singh*, **C.J. Fujiwara***, Z.A. Geiger, E.Q. Simmons, M. Lipatov, A. Cao, P. Dotti, S.V. Rajagopal, R. Senaratne, T. Shimasaki, M. Heyl, A. Eckardt, and D.M. Weld. *Phys. Rev. X* **9**, 041021 (2019)

Transport in Floquet Bloch Bands. **C.J. Fujiwara***, K. Singh*, Z.A. Geiger, R. Senaratne, S.V. Rajagopal, M. Lipatov, and D.M. Weld. *Phys. Rev. Lett.* **122**, 010402 (2019).

Quantum Simulation of ultrafast dynamics using trapped ultracold atoms. R. Senaratne, S.V.Rajagopal, T. Shimasaki, P.E. Dotti, **K.M. Fujiwara**, K. Singh, Z.A. Geiger, and D.M. Weld. *Nature Communications* **9**, 2065 (2018).

Observation and uses of position-space Bloch Oscillations in an Ultracold Gas. Z.A. Geiger*, **K.M. Fujiwara***, K. Singh, R. Senaratne, S.V. Rajagopal, M. Lipatov, T. Shimasaki, R. Driben, V.V. Konotop, T. Meier, and D.M. Weld. *Phys. Rev. Lett.* **120**, 213201 (2018).

Experimental Realization of a Relativistic Harmonic Oscillator. **K.M. Fujiwara***, Z.A. Geiger*, K. Singh, R. Senaratne, S.V. Rajagopal, M. Lipatov, T. Shimasaki, and D.M. Weld. *New J. Phys.* **20**, 063027 (2018).

Quantum Emulation of Extreme Non-equilibrium Phenomena with Trapped Atoms. S.V. Rajagopal, **K.M. Fujiwara**, R. Senaratne, K. Singh, Z.A. Geiger,and D.M. Weld. *Ann. Phys.* **529**, 1700008 (2017).

Effusive Atomic Oven Nozzle Design Using an Aligned Microcapillary Array .R. Senaratne, S.V. Rajagopal, Z. Geiger, **K.M. Fujiwara**, V. Lebedev, and D.M. Weld. *Rev. Sci. Instrum.* 86, 023105 (2015)

Abstract

Dynamics of Ultracold Lithium in Modulated Optical Lattices

by

Coraline Junko Fujiwara

The extreme tunability and control that atomic physics provides makes quantum gases ideal platforms for experimentally realizing novel synthetic materials beyond what is traditionally realizable in condensed matter experiments. In particular, the ability to control interparticle interactions allows for the realization of long lived nonequilibrium states, and strong periodic modulation of lattice potentials realizes novel Floquet matter. In this thesis I shall present a series of experiments studying the dynamics of ultracold lithium in modulated and static one-dimensional optical lattices. First, I present an overview of the experimental apparatus which includes a description of the generation of our Bose-Einstein condensate and optical lattices. Then I step through four experiments which we conducted. The first two involve studying spatial dynamics in static optical lattices in the ground and the excited bands which realize position-space Bloch oscillations and a relativistic harmonic oscillator respectively. The third experiment studies transport in Floquet hybridized optical lattice Bloch bands, and the fourth experiment investigates prethermalization in strongly modulated lattices with tunable interactions.

Contents

Chapter 1

Introduction

Atoms are one of the fundamental building blocks of our universe, and the field of atomic physics has made tremendous contributions not only to our fundamental understanding of the universe but also to the explosive development of modern technologies. Such a tradition stems from such philosophers as Democritus in the 5th century BCE and extends to this very day. In some sense, the success of the field is owed to the simplicity of atoms and their identical nature throughout the universe.

Of particular relevance to me is the realization of novel states of quantum matter using ultracold gases of neutral atoms in optical lattices. The extreme precision and control that laser physics affords over atomic systems has enabled the generation and manipulation of quantum matter inaccessible in traditional laboratory settings. Such advances have enabled near ideal experimental realization of theoretical models of exotic materials, offering a complementary window on the fields of materials science and condensed matter physics. This concept has been dubbed "quantum simulation" or "quantum emulation".

Ultracold atoms in optical lattices can also create states of matter beyond traditional definitions of materials, and the contents of this thesis represent advances in this vein. In particular, the ability to control particle interactions allows creation and study of highly

excited states of matter that would typically lead to decay and destruction in normal materials. Periodic modulation of lattice potentials can generate excitations to higher bands or hybridize bands into novel excited states. Such modulation can even be many times stronger than typical binding energies and still create long lived states that only exist in the presence of strong driving.

In our lab, I have had the privilege to participate in the design, construction, and implementation of two cold atom machines using lithium and strontium, and I have focused on experiments conducted using ultracold lithium in driven optical lattices. It is difficult to express the feeling of starting with an empty laboratory space and ending with a machine studying quantum matter on the edge of scientific understanding. Moreover, I have had the opportunity to guide the direction of scientific exploration of our group and realize a satisfyingly complete scientific narrative.

The four experiments detailed in this thesis are organized to demonstrate such a narrative. The first involves studying position space Bloch oscillations in the ground band of an optical lattice when a force is applied. The second studies transport properties in the second excited band and realizes for the first time a relativistic harmonic oscillator. The third experiment connects these two experiments via continuous periodic modulation of the lattice amplitude which hybridizes the ground and excited bands. And the fourth experiment studies the stability of interacting samples in the presence of such periodic modulation. Conducted in the strongly driven regime, this experiment probes the question of thermalization and stability of driven many-body quantum systems.

1.1 Dissertation Overview

This dissertation discusses some of the work I performed in the process of designing, constructing, and operating the lithium BEC machine in conjunction with many others in the group. And it is intentionally written to complement the other theses published by this group on this BEC machine. As such, many specifics of the design and construction of the machine are omitted for the sake of brevity. This particular dissertation focuses on providing a holistic perspective on the most relevant physics in our experiments. **Chapter 1** contains a brief discussion on the atomic physics required to understand the rest of the thesis. **Chapter 2** contains an overview of the experimental sequence to generate a Bose-Einstein condensate and load it into optical lattices. **Chapter 3** describes the theory underpinning our one-dimensional optical lattice experiment with a focus on providing a theoretical framework for understanding Floquet optical lattices. **Chapters 5, 6, 7, and 8** are reproductions of the papers I coauthored studying lithium condensates in optical lattices. The appendices contain a collection of notes on some important technical details which is mostly relevant to graduate students in our group.

1.2 Permissions and Attributions

1. Most of the theory in this dissertation is adapted from *Atomic Physics* by Christopher Foot [1], *Bose-Einstein Condensation in Dilute Gases* by C.J. Pethick and H. Smith [2], and *Floquet engineering with quasienergy bands of periodically driven optical lattices* by Martin Holthaus [3].

2. Many experimental details came from the theses of Zachary Geiger [4], Ruwan Senaratne [5], Kevin Singh [6], and Shankari Rajagopal [7].

3. The thesis of Florian Schreck [8] served as a guide for designing the machine. It

also provided a helpful roadmap towards condensation.

4. The content of Chapter 5 is the result of collaboration with Zachary Geiger, Kevin Singh, Ruwan Senaratne, Shankari Rajagopal, Mikhail Lipatov, Toshihiko Shimasaki, Rodislav Driben, Vladimir Konotop, Torsten Meier, and David Weld, and has previously appeared in *Physical Review Letters*.
   It is reproduced here with the permission of the American Physical Society : https://journals.aps.org/copyrightFAQ.html

5. The content of Chapter 6 is the result of collaboration with Zachary Geiger, Kevin Singh, Ruwan Senaratne, Shankari Rajagopal, Mikhail Lipatov, Toshihiko Shimasaki, and David Weld, and has previously appeared in *New Journal of Physics*.
   It is reproduced here with the permission of the IOP Publishing : https://iopscience.iop.org/journal/1367-2630/page/Copyright%20and%20permissions

6. The content of Chapter 7 is the result of collaboration with Kevin Singh, Zachary Geiger, Ruwan Senaratne, Shankari Rajagopal, Mikhail Lipatov, and David Weld, and has previously appeared in *Physical Review Letters*.
   It is reproduced here with the permission of the American Physical Society : https://journals.aps.org/copyrightFAQ.html

7. The content of Chapter 8 is the result of collaboration with Kevin Singh, Zachary Geiger, Ethan Simmons, Mikhail Lipatov, Alec Cao, Peter Dotti, Shankari Rajagopal, Ruwan Senaratne, Toshihiko Shimasaki, Markus Heyl, Andre Eckhardt, and David Weld.

8. The content of Appendix A is the result of collaboration with David Weld.

Chapter 2

Background

This chapter briefly introduces some important concepts that are critical to understanding many of the phenomena covered in this thesis. The goal is to provide a qualitative understanding of the most relevant physics concerning cold atomic gases. Detailed theoretical derivations and calculations are intentionally omitted in exchange for brevity and emphasis on understanding how measurements are conducted in the laboratory.

2.1 Lithium

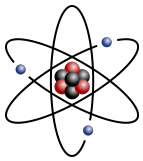

Figure 2.1: Lithium is the canonical atom.

All the experiments in this thesis are conducted with cold samples of gaseous atomic lithium, specifically ^{7}Li whose nucleus is composed of three protons and four neutrons as shown in Fig. 2.1. As an alkali metal, lithium lies in group I of the periodic table and has a single valence electron. While the history of lithium in context of quantum emulation is rich, we shall focus on a few key aspects of ^{7}Li which tailor it specifically for the experiments detailed in this thesis. This is summarized below and in Figure 2.2.

- **Simple energy structure** - The atomic structure of lithium is well understood and its principal atomic transitions are easily accessible with commercial lasers.
- **Low mass** - Being more massive only than hydrogen and helium, lithium is one of the lightest neutral atoms brought to quantum degeneracy. This causes the dynamics of lithium to be quicker than those of other neutral atoms.
- **Magnetic** - The ground state of lithium is magnetic and can be controlled with radiation and fields.
- **Tunable interactions** - Both isotopes of lithium exhibit a magnetic Feshbach resonance which allow the two body interaction energy to be controlled via an applied magnetic field.

With a single valence electron, the energy structure of lithium is well described by the so called L-S scheme and can be labeled using the Russell-Saunders notation $n^{2S+1}L_J$.

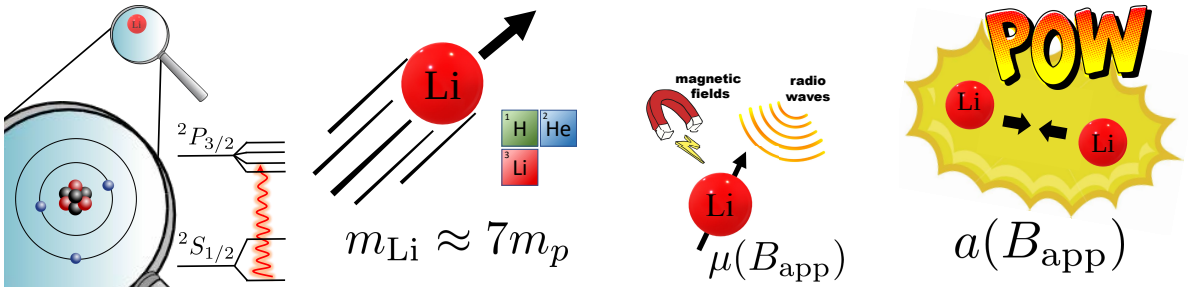

Figure 2.2: A few key properties of ^{7}Li - simple energy structure, low mass, magnetic ground state, and tunable interactions.

The number n is the principal quantum number and describes the radial energy shell of the valence electron; L is the electron orbital angular momentum number; S is the electron spin angular momentum number, which is 1/2; J is the total electron angular momentum number. With a nuclear spin of $I = 3/2$, the interaction of the nuclear and electron angular momentum induces a hyperfine splitting in ^{7}Li. This is diagonalized using the total composite internal angular momentum of the atom $\mathbf{F} = \mathbf{I} + \mathbf{J}$ such that the set of good quantum numbers describing the internal atomic state are n, S, L, J, I, F, and m_F. The resultant energy structure at zero magnetic field is shown in Figure 2.3. In this thesis, we adopt the notation[1].

$$n^{2S+1}L_J \ \ |F, m_F\rangle \,. \tag{2.1}$$

The level structure provided in Figure 2.3 is complete for the purposes of this thesis. The electric dipole transitions from the $2S_{1/2}$ to $2P_{1/2}$ or $2P_{3/2}$ states, referred as the D1 and D2 transitions, are accessible through commercial lasers, and some important properties of these transitions are provided in Table 2.1. The energy structure is probed via saturated absorption spectroscopy as shown in Figure 2.4, and we use this signal to lock our resonant laser system. A complete treatment of how we generate our laser light

[1]The nuclear spin I is always $\frac{3}{2}$.

	Symbol	D1 line	D2 line
Frequency	f	446.8002 THz	446.8102 THz
Wavelength (vacuum)	λ	670.9766 nm	670.9615 nm
Lifetime	τ	27.102 ns	27.102 ns
Natural Linewidth	Γ	$2\pi\times$ 5.8724 MHz	$2\pi\times$ 5.8724 MHz
Recoil velocity	v_{rec}	0.08477 m/s	0.08477 m/s
Recoil temperature	T_{rec}	3.033 μK	3.033 μK
Saturation intensity	I_{sat}		2.54 mW/cm^2
Doppler temperature limit	T_{Dopp}	140.98 μK	140.98 μK
Doppler velocity limit	v_{Dopp}	0.4009 m/s	0.4009 m/s

Table 2.1: Lithium-7 D line optical properties.

may be found in other theses published by this group [4, 6].

As alluded to earlier, the energy of these states change with external magnetic field. This energy is a combination of the electron-nucleus interaction that gives rise to the $|F, m_F\rangle$ labeling and their individual interaction with the external magnetic field. To lowest order this is expressed by the Zeeman Hamiltonian of equation 2.2.

$$\hat{H} = A\hat{\mathbf{I}} \cdot \hat{\mathbf{J}} - \hat{\mu_e} \cdot \mathbf{B} - \hat{\mu_n} \cdot \mathbf{B} \tag{2.2}$$

As the magnetic field increases, the $|J, I, F, m_F\rangle$ quantum numbers no longer accurately describe the energy eigenstates and are better described by the individual spin components using the state labeling $|I, m_I, J, m_J\rangle$. Numerical calculations of the internal state energy as a function of applied magnetic field are provided in Figure 2.5 [2]. This Zeeman energy can be used to mediate a radiation pressure force such as in the magneto-optical trap or can be used alone to trap atoms such as in the magnetic trap. Furthermore, an applied magnetic field can induce a magnetic Feshbach resonance which tunes the interatomic interactions and is discussed in the next chapter.

With or without a magnetic field, transitions between these energy states can be

[2] More precise calculations require including higher order terms

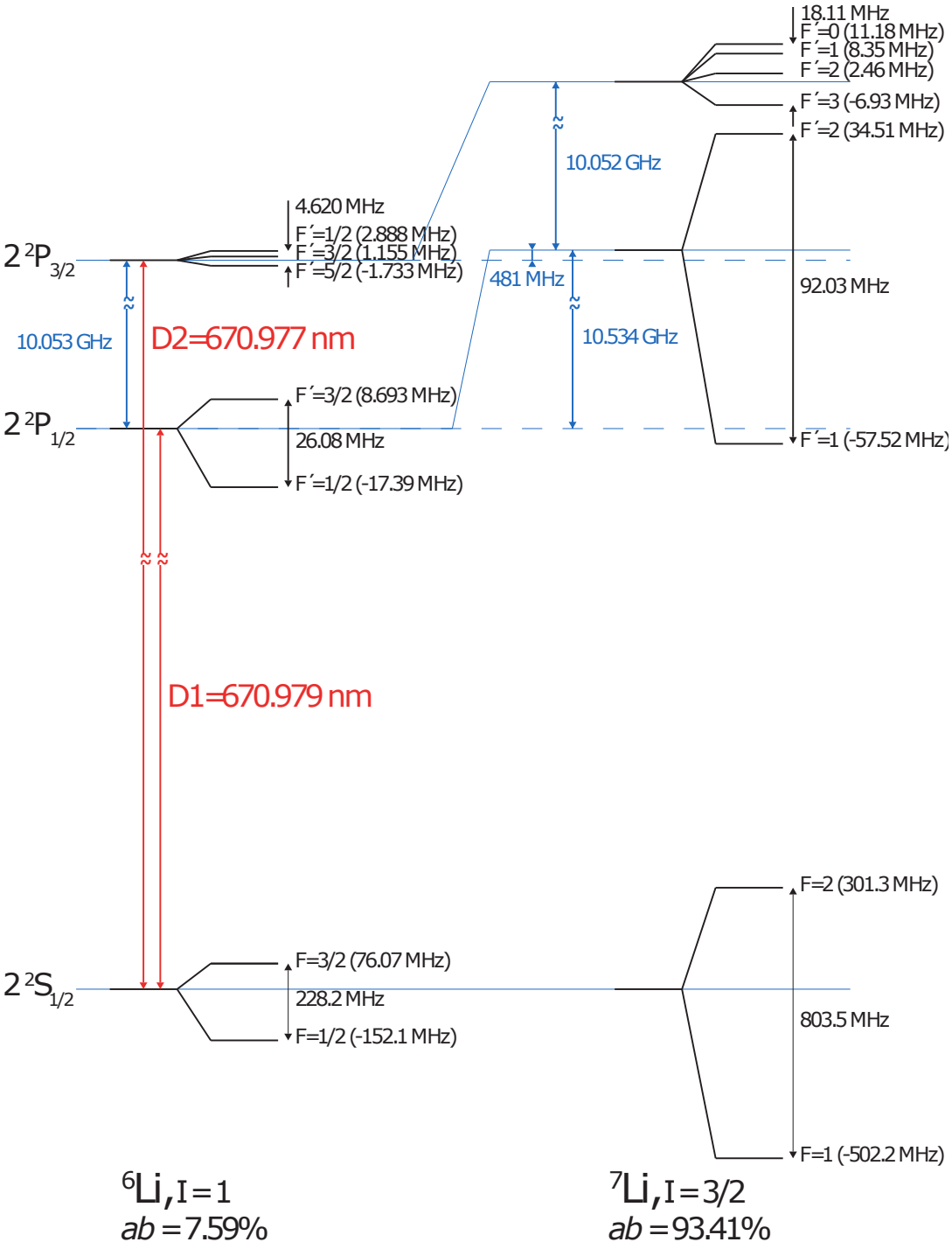

Figure 2.3: Energy level structure for both ^{6}Li and ^{7}Li; the natural abundance of each isotope is *ab* [9].

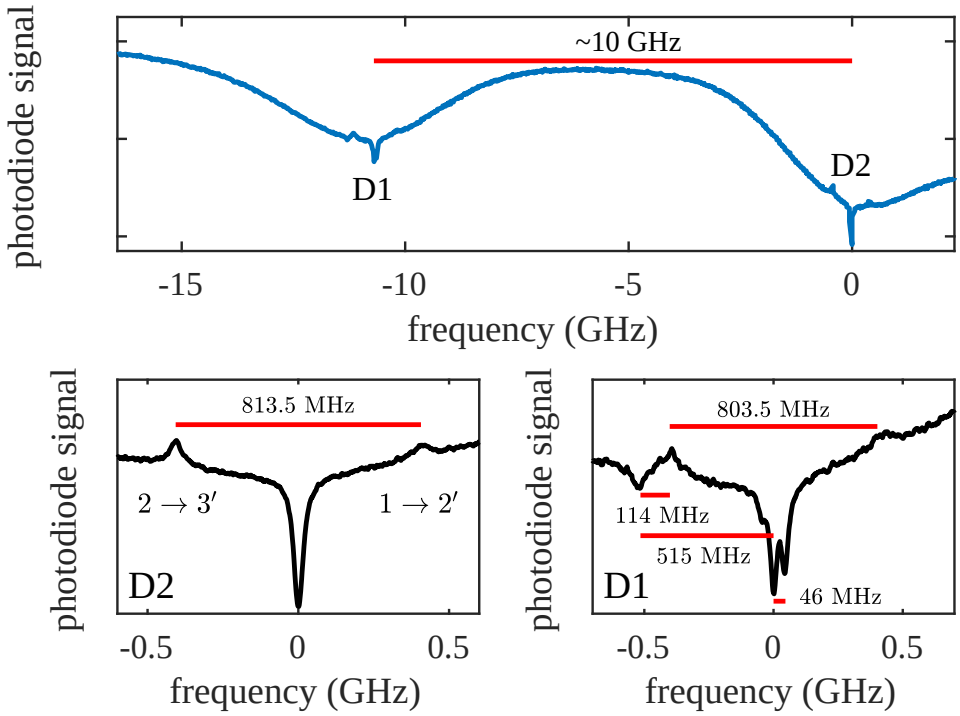

Figure 2.4: Lithium energy structure as measured via saturated absorption spectroscopy. The measured signal is the transmission of a probe beam through a vapor cell of lithium heated to 350°C, and the frequency features are consistent with Figure 2.3. **(top)** A wide frequency scan of many GHz probes both the D1 and D2 transitions which are evident by an increase in absorption. The separation between the transitions is around 10 GHz. The broad absorption is caused from the large thermal velocity distribution. **(bottom left)** Fine frequency scan about the D2 transition. The absorption feature is that of a lambda crossover with the $2S_{1/2}$ ground manifold. The unresolved splitting of the $2P_{3/2}$ manifold increases the effective splitting by 10 MHz to 813.5 MHz. Our laser system is locked to the absorption crossover. **(bottom right)** Fine frequency scan about the D1 transition. The primary features can be intepreted as two lambda energy structures between the $2S_{1/2}$ and $2P_{1/2}$ manifolds. This is evidenced by the 46 MHz splitting between the two crossover features which is half the $2P_{1/2}$ splitting. A smaller crossover absorption from the D2 transition of ^{6}Li is seen at 515 MHz with a splitting of 114 MHz. This is consistent with the relative isotope shifts and hyperfine splitting of ^{6}Li. The relative amplitude of the absorption features are consistent with the relative natural abundance of the two isotopes.

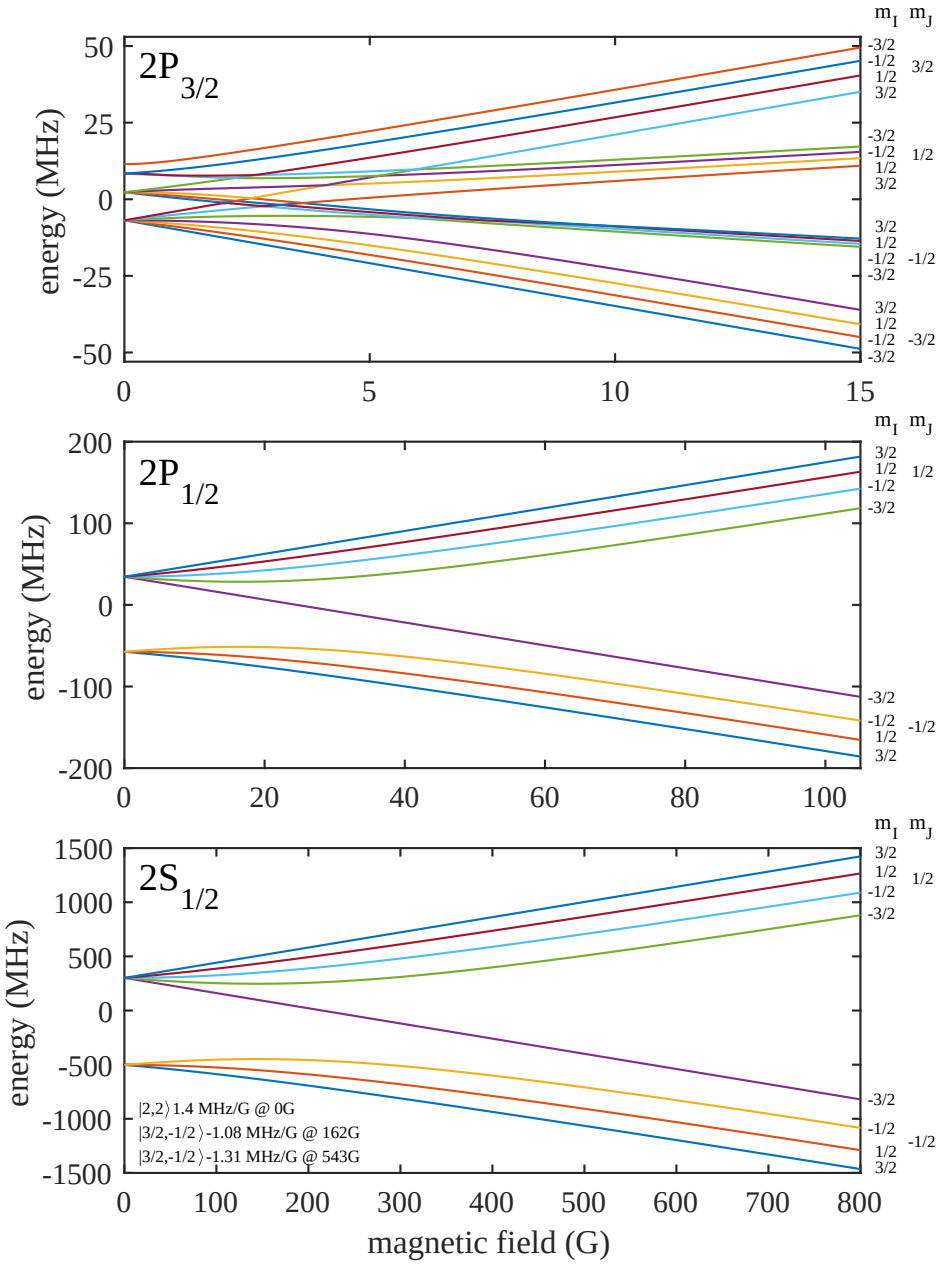

Figure 2.5: Numerically calculated Zeeman splitting of ^{7}Li using equation 2.2. As the magnetic field strength increases, a description of the states using the quantum numbers m_I and m_J becomes appropriate.

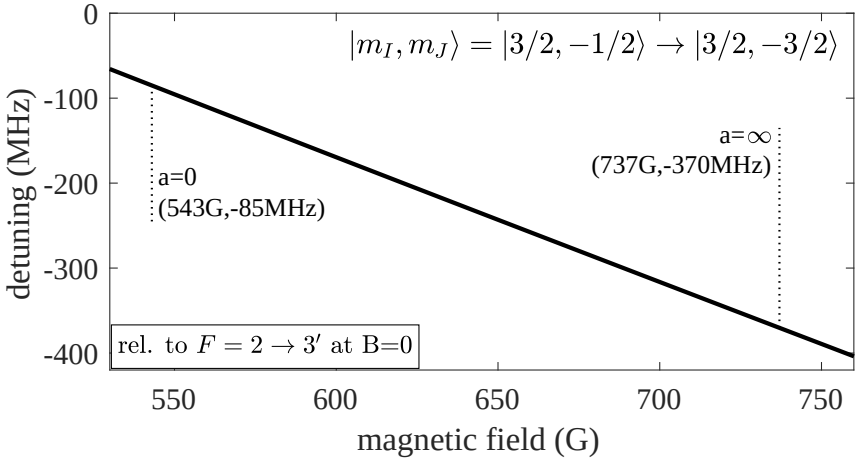

Figure 2.6: Tracking the imaging transition for varying magnetic field strength. The detuning is empirically optimized for each operating magnetic field.

excited with laser light. With a $\Delta L = 1$, the $2S_{1/2}$ energy states are resonantly excited to either the $2P_{1/2}$ or $2P_{3/2}$ energy manifolds via an electric dipole transition with wavelength $\lambda = 671$ nm. The amount of stimulated absorption depends on the frequency dependent absorption cross section $\sigma(\omega)$ as expressed in equation 2.3 [1].

$$\sigma(\omega) = \sigma_0 \frac{\Gamma^2/4}{(\omega - \omega_0)^2 + \Gamma^2/4} \tag{2.3}$$

$$\sigma_0 = C^2 \frac{\lambda^2}{2\pi} \tag{2.4}$$

Here Γ is the transition linewidth of Table 2.1, and the detuning $(\omega - \omega_0) = 2\pi(f - f_0)$ is the difference in frequency of the applied laser light f relative to the resonant transition frequency f_0. The relative detuning can change with the laser frequency itself, the internal energy changing from the Zeeman shift, or from the Doppler effect which induces a frequency shift of v/λ where v is the velocity of the atom. At resonance, $\sigma(\omega)$ reduces to the resonant absorption cross section σ_0, where $0 < C < 1$ is a phenomenological parameter which approximately accounts for non cycling transitions.

While imaging shall be discussed in more detail in the following section, the absorption

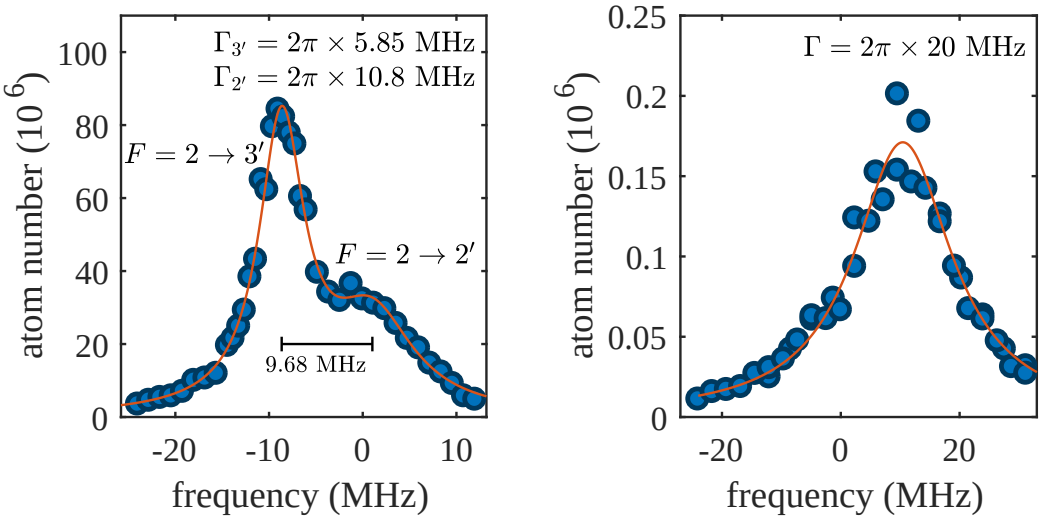

Figure 2.7: Lineshape measurements taken via absorption imaging. **(left)** Taken at 0 G from the spin polarized $|2, 2\rangle$ state to the $2P_{3/2}$ manifold in the magnetic trap. The unresolved splitting of the excited state is seen as a double feature lineshape. The fitted separation of 9.68 MHz is consistent with the excited state splitting in Figure 2.3 of 9.39 MHz. The fitted linewidths to the two features are different which we attribute to noncycling behavior. **(right)** Taken at 720 G from the initial $|m_I, m_J\rangle = |3/2, -1/2\rangle$ state to the $|3/2, -3/2\rangle$ state using a Bose-Einstein condensate.

of resonant light is how we conduct all of our measurements. Of importance then, is the observation that the resonant frequency f_0 changes with applied magnetic field which must be compensated for by our imaging lasers. The calculated relative frequency shift is shown in Figure 2.6, and example measurements of the lineshape $\sigma(\omega)$ at some relevant magnetic field strengths are shown in Figure 2.7.

The absorption of photons also induces momentum transfer due to the discrete photon momentum $p_\gamma = h/\lambda$. For a simple two level atom, this radiation pressure force takes the following form

$$F_{\text{scatt}} = \frac{h}{\lambda}\frac{\Gamma}{2}\frac{I/I_{\text{sat}}}{1 + I/I_{\text{sat}} + (\omega - \omega_0)^2/\Gamma^2} \tag{2.5}$$

which has a maximum value of the photon momentum multiplied by the maximum scattering rate $\Gamma/2$ [1]. Importantly, for a constant laser frequency then, the radiation pressure force is mediated by the Doppler and Zeeman effect. This is of particular

importance for the physics of the optical molasses, the Zeeman slower, and the magneto-optical trap. While not discussed here, application of far detuned light or multi frequency light induces AC Stark effects and Raman transitions. These effects are of particular importance for the optical dipole trap and gray molasses.

2.2 Absorption Imaging

Since the atomic gases of our experiments are confined within a vacuum chamber, we only conduct measurements by the atoms' interaction with light. As discussed in the previous section, atoms will absorb light that is resonant with an atomic transition. **Absorption imaging** is performed by imaging the absorption shadow cast by a resonant probe beam impinging upon the atomic cloud to reconstruct the spatial density of the absorbing atomic gas. For a resonant probe beam with sufficiently small intensity I_{i}, the transmitted intensity I_{f} through the diffuse atomic gas is given by **Beer's law**,

$$I_{\mathrm{f}} = I_{\mathrm{i}} e^{-\mathrm{OD}} \tag{2.6}$$

$$\mathrm{OD} = n\sigma_0 \tag{2.7}$$

where the dimensionless quantity optical density (OD) describes the amount of light absorbed. From equation 2.7, it is evident that optical density is linearly related to the resonant cross section σ_0 and the number area density of the atomic cloud n. Therefore, imaging of the transmitted probe beam I_{f} and subsequent calculation of the optical density allows determination of the spatial distribution of the atomic cloud n transverse to the probe beam propagation.

To elucidate the physical origin of equation 2.7 and demonstrate its veracity we shall quickly consider a more general situation. As the probe beam travels through the atomic cloud, the intensity I is both attenuated by stimulated absorption and aided by stimulated emission. Including the possibility that the probe beam is not resonant this is described in equation 2.8.

$$\frac{dI}{dz} = -\left(n_1 - n_2\right)\sigma\left(\omega\right) I\left(\omega\right) \tag{2.8}$$

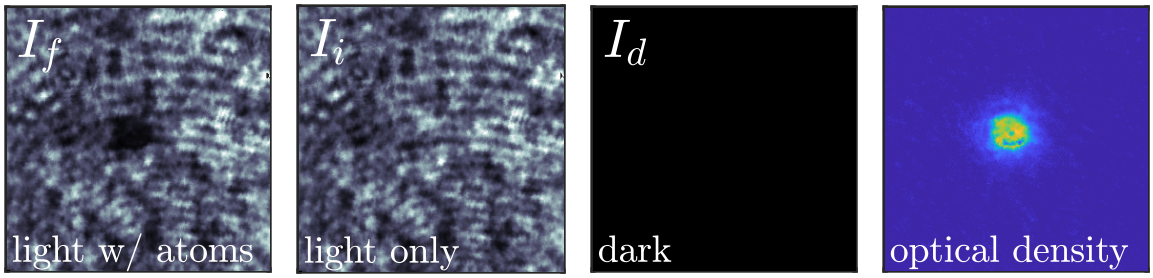

Figure 2.8: Extracting optical density from the raw images. The atoms cast a shadow on the camera sensor when impinged with resonant light. This is seen as a depression in the image count in the "light w/ atoms" image. When normalized against the "light only" and "dark" images, the optical density profile is extracted using equation 2.12.

Here n_1 is the number density of atoms in the absorbing ground state, n_2 is the number density in the excited state, and $\sigma(\omega)$ is the frequency dependent cross section. The presence of stimulated emission from the excited state in Eq. 2.8 complicates the relationship between attenuation and number density but can be neatly accounted for below [1],

$$\frac{dI}{dz} = \kappa(\omega, I)I(\omega) \tag{2.9}$$

$$\kappa\left(\omega, I\right) = n\sigma_0 \frac{\Gamma^2/4}{\left(\omega - \omega_0\right)^2 + \frac{1}{4}\Gamma^2\left(1 + \frac{I}{I_{sat}}\right)}, \tag{2.10}$$

where σ_0 is the resonant cross section from the previous section, I_{sat} is the saturation intensity, and Γ the linewidth. Important features of Eq. 2.10 are (1) more atoms absorb more light, (2) large linewidths and hence large spontaneous emission allow for more absorption, (3) attenuation is maximized at resonance, and (4) large intensity broadens the absorption width and makes for a non-linear response. To maximize the signal for a given atom number, the attenuation $\kappa(\omega, I)$ must be maximized while maintaining a linear response by enforcing the probe beam be resonant ($\omega = \omega_0$) and having a low intensity ($I \ll I_{\text{sat}}$). When this is satisfied $\kappa = n\sigma_0$, and equation 2.7 is recovered.

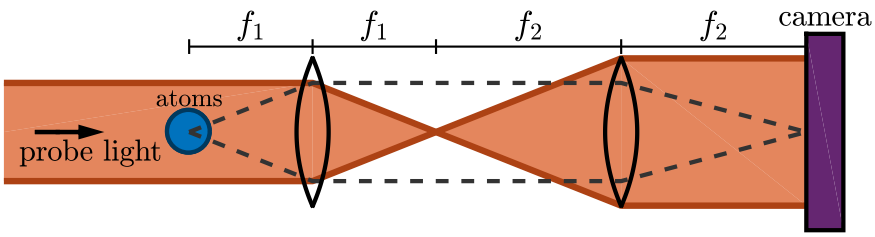

Figure 2.9: The 4F imaging system. The atomic cloud is at the focal plane of an objective lens with focal length f_1 with a refocusing lens of focal length f_2. The separation between the atoms and the camera sensor is four focal lengths (hence the name). When a collimated probe beams (red) impinges upon the atomic cloud (blue) the shadow cast (dashed) is imaged onto the camera sensor.

In practice, the optical density is measured from images of the absorption with pixels corresponding to some physical area A_{px} at the location of the atoms. We also introduce $I_{\text{d,px}}$, the measured background intensity per pixel which manifests as common mode noise. Discretization of equation 2.7 yields the number of atoms for a given pixel N_{px} to be

$$N_{\text{px}} = \frac{A_{\text{px}}}{\sigma_0}\text{OD} \tag{2.11}$$

$$N_{\text{px}} = \frac{A_{\text{px}}}{\sigma_0}\ln\left(\frac{I_{\text{i,px}} - I_{\text{d,px}}}{I_{\text{f,px}} - I_{\text{d,px}}}\right), \tag{2.12}$$

While the mapping of camera pixels to real space pixels is in general quite complicated, we shall complete this discussion of absorption imaging by introducing a simple imaging system which is commonly used in our laboratory. As previously alluded, the atomic spatial distribution is extracted from the absorption profile of the probe beam at the location of the atoms. This requires that the location of the atoms be an image plane of the camera, which is equivalent to mapping the camera sensor onto the location of the atoms. One of the simplest such optical systems is the 4F imaging system which is realized utilizing two lenses with focal length f_1 and f_2 in the configuration outlined in Figure 2.9. In this setup, the image of the shadow at the atoms is mapped onto the

camera sensor with a magnification M given by the ratio of the focal lengths $M = -f_2/f_1$.

2.3 Ballistic Time of Flight

In addition to imaging the spatial distribution of the atomic cloud, we also measure the momentum distribution in a technique called **time of flight** (TOF). The technique relies on suddenly turning off the forces trapping the atomic cloud and measuring the atomic motion in free expansion. Since the gases are so dilute, inter-atomic interactions are minimal during free expansion such that the position of an atom x_f depends mainly on its initial position x_i, initial velocity v_i, and flight time t.

$$\vec{x}_\mathrm{f} = \vec{x}_\mathrm{i} + \vec{v}_\mathrm{i} t \tag{2.13}$$

In the long time of flight limit, the spatial distribution is just the velocity distribution (and therefore momentum) scaled by the time of flight. In practice, multiple images are taken to fully reconstruct the initial velocity and spatial distribution. This rather simple technique is a powerful tool afforded to experiments with cold atomic gases and is enabled by the fine control over confining potentials with lasers.

To elucidate the utility of this technique, we shall now demonstrate how the temperature T of an atomic cloud is measured using time of flight. The starting point is a Gaussian probability distribution P of the atomic position $\vec{r}_0$ and momentum $\vec{p}_0$ as given by equation 2.14. Such a distribution is well motivated by a harmonically trapped

atomic cloud in thermal equilibrium obeying the equipartition theorem.

$$P\left(\vec{r}_0, \vec{p}_0\right) = \prod_{i=x,y,z} g\left(\vec{r}_{0i}, \sigma_i\right) g\left(\vec{p}_{0i}, \sigma_{p_i}\right) \tag{2.14}$$

$$g\left(x, \sigma\right) = \frac{1}{\sqrt{2\pi\sigma^2}} \exp\left(-\frac{x^2}{2\sigma^2}\right) \tag{2.15}$$

Here, each σ describes the Gaussian radius of the probability distribution for position and momentum. Since each spatial dimension is uncorrelated, the problem reduces to an equivalent one dimensional case without loss of generality.

$$P\left(x_0, p_0\right) = \left[\frac{1}{\sqrt{2\pi\sigma_x}} \exp\left(-x^2/2\sigma_x^2\right)\right] \left[\frac{1}{\sqrt{2\pi\sigma_p}} \exp\left(-p^2/2\sigma_p^2\right)\right] \tag{2.16}$$

Once the atoms are released, the position of a particular atom after some time of flight is given by equation 2.13, and the ensemble spatial probability distribution is given by the convolution of the initial position and momentum distributions shown in equation 2.17. This can be intuited as the sum over all starting possible x_0 and p_0 that would lead to final position x at time t.

$$P\left(x, t\right) = \int \mathrm{d}x_0 \ \mathrm{d}p_0 \ g\left(x_0, \sigma_x\right) g\left(p_0, \sigma_p\right) \delta\left(p_0 - m(x - x_0)/t\right) \tag{2.17}$$

$$= \int \mathrm{d}p_0 \ g\left(x - p_0 t/m, \sigma_x\right) g\left(p_0, \sigma_p\right) \tag{2.18}$$

$$= \frac{1}{\sqrt{2\pi\Sigma(t)^2}} \exp\left(-\frac{x^2}{2\Sigma(t)^2}\right) \tag{2.19}$$

$$\Sigma(t)^2 = \sigma_v^2 t^2 + \sigma_x^2 \tag{2.20}$$

Therefore, the imaged spatial distribution after the time of flight is a Gaussian whose radius $\Sigma(t)$ is a combination of the initial momentum and position radii[3]. If $\sigma_v t \gg \sigma_x$,

[3] "A convolution of Gaussian with a Gaussian is another Gaussian."

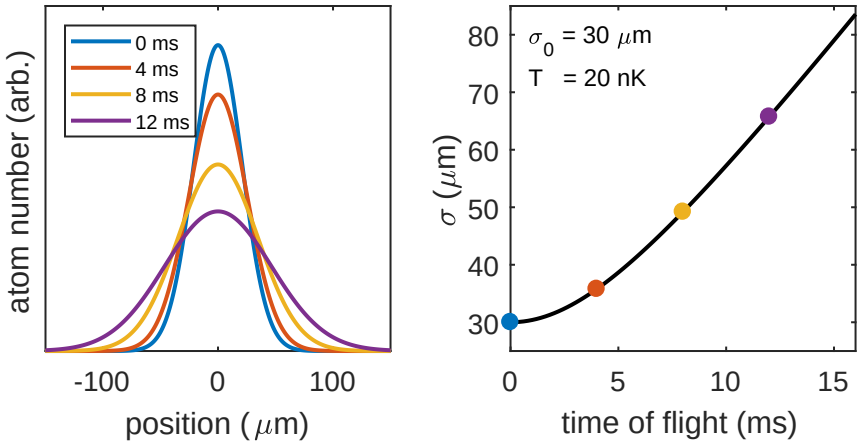

Figure 2.10: Thermometry using time of flight. **(left)** After being released from the trap, the atomic cloud spreads in spatial extent shown here in only one dimension. **(right)** Fitting the increase of the spatial Gaussian radius σ as a function of flight time reveals the temperature of the atomic gas using equation 2.21. In this example, the initial cloud size is 30 μm and the temperature 20 nK.

the resultant spatial distribution is equal to the initial momentum distribution scaled by the time of flight. In practice, because absorption imaging is destructive, the Gaussian radii σ_x and σ_p are extracted by varying the time of flight over identical realizations of the atomic cloud. The Gaussian radius of the momentum distribution is directly related to the temperature via the equipartition theorem $\sigma_p = \sqrt{mk_BT}$ such that $\Sigma(t)$ is given by equation 2.21. An example of this calculation is summarized in Figure 2.10.

$$\Sigma(t) = \sqrt{\left(\frac{k_BT}{m}\right)t^2 + \sigma_x^2} \tag{2.21}$$

In this way, time of flight imaging allows for almost complete reconstruction of the *insitu* position and momentum distributions. Not only is this critical in accessing cooling towards quantum degeneracy, but also is useful for characterization of the quantum state during experiments. As such, the majority of the data presented in this thesis will be taken using time of flight.

2.4 Bose Einstein Condensation

All of the experiments conducted in this thesis utilize condensed atomic ^{7}Li. Creation of this coherent object enables the study of quantum correlated behavior and enhances specificity of the initial experimental state. Qualitatively, a Bose-Einstein condensate is created when the interparticle spacing is approximately equal to the particles' thermal de Broglie wavelength λ_{dB}.

$$\lambda_{\mathrm{dB}}(T) = \frac{h}{\sqrt{\langle p^2 \rangle}} \tag{2.22}$$

$$= \frac{h}{\sqrt{2mk_BT}} \tag{2.23}$$

Intuitively, this means that the particle spatial wavefunctions are highly overlapped which results in correlated quantum behavior. This is also understood as the regime where the ensemble position and momentum uncertainty reach the Heisenberg limit $\sigma_x \sigma_p \approx \frac{\hbar}{2}$. This criterion is expressed by the dimensionless quantity ρ, the phase space density.

$$\rho = n_0 \Lambda^3(T) \tag{2.24}$$

It follows that quantum degeneracy is achieved when $\rho \sim 1$. In practice, the phase space density is measured using time of flight to extract the atom number, temperature, and spatial size. Note that this quantum correlated regime can be achieved by both increasing the density or reducing the temperature. A cartoon of this process is described in Figure 2.11. Solid formation tends to limit atomic gas densities to around $10^{14}/\mathrm{cm}^3$ ($\sim$ 200 nm separation, compare to a typical solid separation of 1 nm) which results in the requirement of temperatures on the scale of 10^{-9} K. Therefore, a considerable amount of

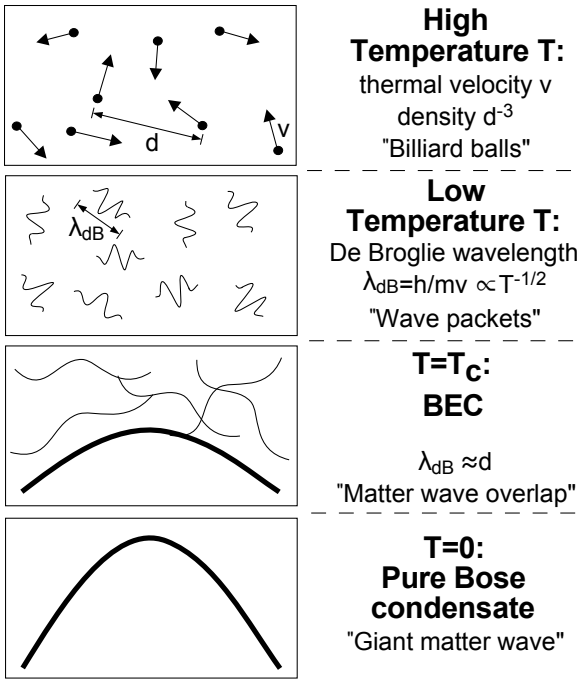

Figure 2.11: The formation of a Bose-Einstein by lowering the temperature. At high temperatures the short thermal de Broglie wavelength causes the particles to act like balls. As the temperature lowers, the de Broglie wavelengths increases causing matter wave overlap. At sufficiently low temperatures, the wavefunctions overlap and a many body coherent quantum matter wave is created [10].

effort is expended on bringing our atomic gases to sufficiently cold temperatures. Indeed, almost the entirety of the following chapter is devoted to describing the precise steps required to cool to such low temperatures. While interactions and trap geometries play a significant role in the physics of condensation, the perspective presented in Figure 2.11 remains qualitatively correct. And this perspective is the only requirement for understanding the qualitative cooling steps outlined in this thesis.

Chapter 3

Experiment Overview

This chapter discusses the experimental sequence for generating our Bose-Einstein condensates and loading them into optical lattice potentials. The goal of this chapter is to provide a qualitative understanding of the various cooling and trapping steps in the sequence. An analysis of typical operating conditions and operating tips is emphasized. While the author laments not including many experimental infrastructure details that she constructed, the author directs the interested reader to other theses published by this group for infrastructure and design considerations [4, 5, 7, 6] . A few highlights of this apparatus are given below and a summary of our experimental sequence is provided in Figure 3.3.

- Generates a BEC of approximately 10^5 lithium atoms every 30 s.
- Creates magnetic fields exceeding 1000 G for Feshbach tunable interactions and magnetic field gradients up to 450 G/cm.
- Realizes 1D optical lattices which features two phase shifted lattices which allows for fast lattice depth modulation exceeding 100% at MHz speeds.

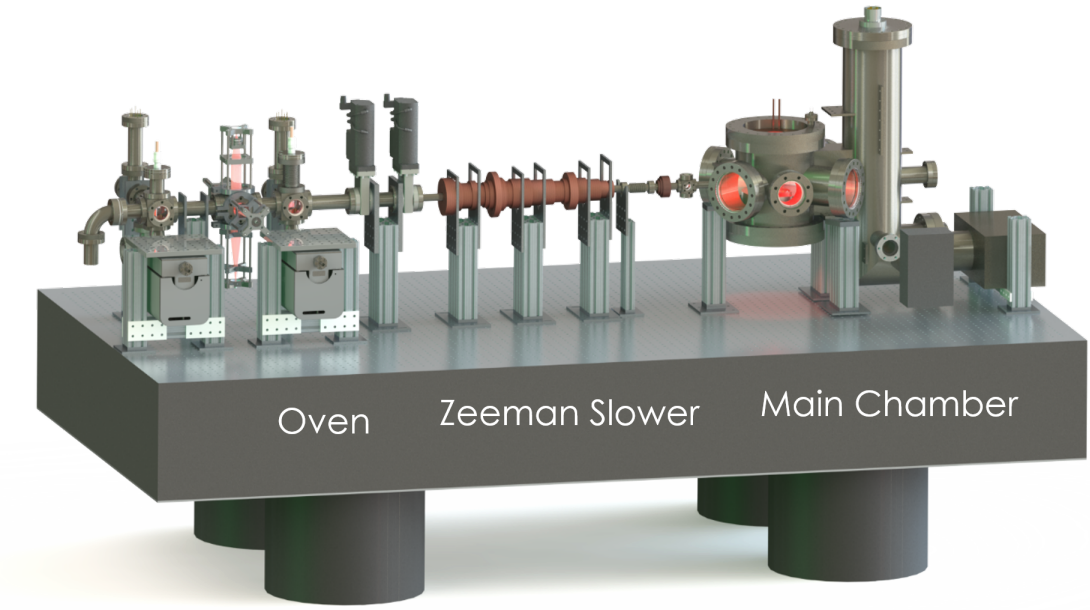

Figure 3.1: Rendering of the lithium experimental apparatus. The atoms begin at the oven on the left and eventually are trapped and cooled in the main chamber on the right. There are a variety of ion pumps, differential pumping tubes, gate valves, and gauges. There is also a redisual gas analyzer and Titanium sublimation pump on the main chamber. The multitude of breadboards, optics, and electromagnets are not shown for visual clarity.

- Maintains UHV pressures around 2×10^{-12} Torr which allows for BEC lifetimes exceeding 10 s.
- Utilizes a plugged quadrupolar magnetic trap for quick RF evaporation.
- Uses low inductance coils for fast manipulation of magnetic fields.
- Implements a hexagonally packed microcapillary array nozzle which is expected to extend the oven lifetime to several decades.

The experimental apparatus consists of a stainless steel ultra high vacuum (UHV) chamber. It is roughly separated into three components as shown in Figure 3.1 - the oven, the Zeeman slower, and the main chamber. The atoms are trapped, cooled, and

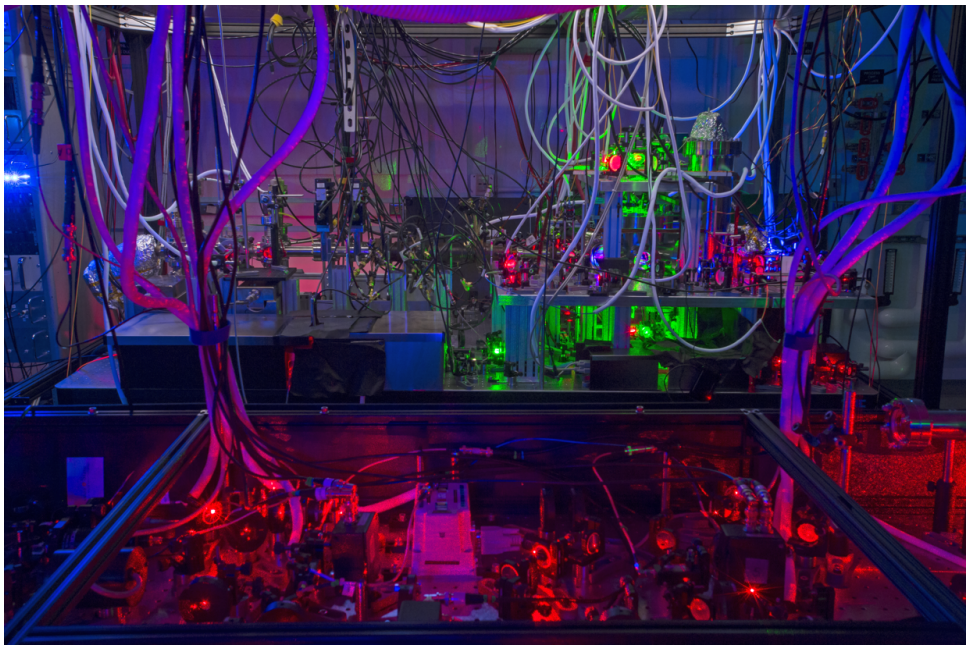

Figure 3.2: The machine table (background) and the resonant laser table (foreground).

brought to quantum degeneracy inside the main chamber. The optical lattices that form the basis for the experiments conducted in this thesis are also inside the main chamber. A schematic of most of the laser beams entering the main chamber is provided in Figure 3.4. An image of the machine is provided in Figure 3.2

The main chamber was designed to be flexible and allow for a variety of experiments. Therefore large windows with wide optical access were emphasized; a schematic is provided in Figure 3.5[1]. The main chamber features large viewports of 4.5" and 6" in diameter to optimize optical access and allow for lasers beams at 45°, 60°, and 120°. This arrangement was chosen to allow for the generation of a variety of two-dimensional lattice configurations. The chamber also features three reentrant windows - two along the vertical axis and one along the transverse axis for high NA imaging. The vertical reentrant windows also enable placement of the primary electromagnets close to the atoms to optimize the produced magnetic field and field gradients along the vertical axis.

[1]See technical drawings for precise specifications.

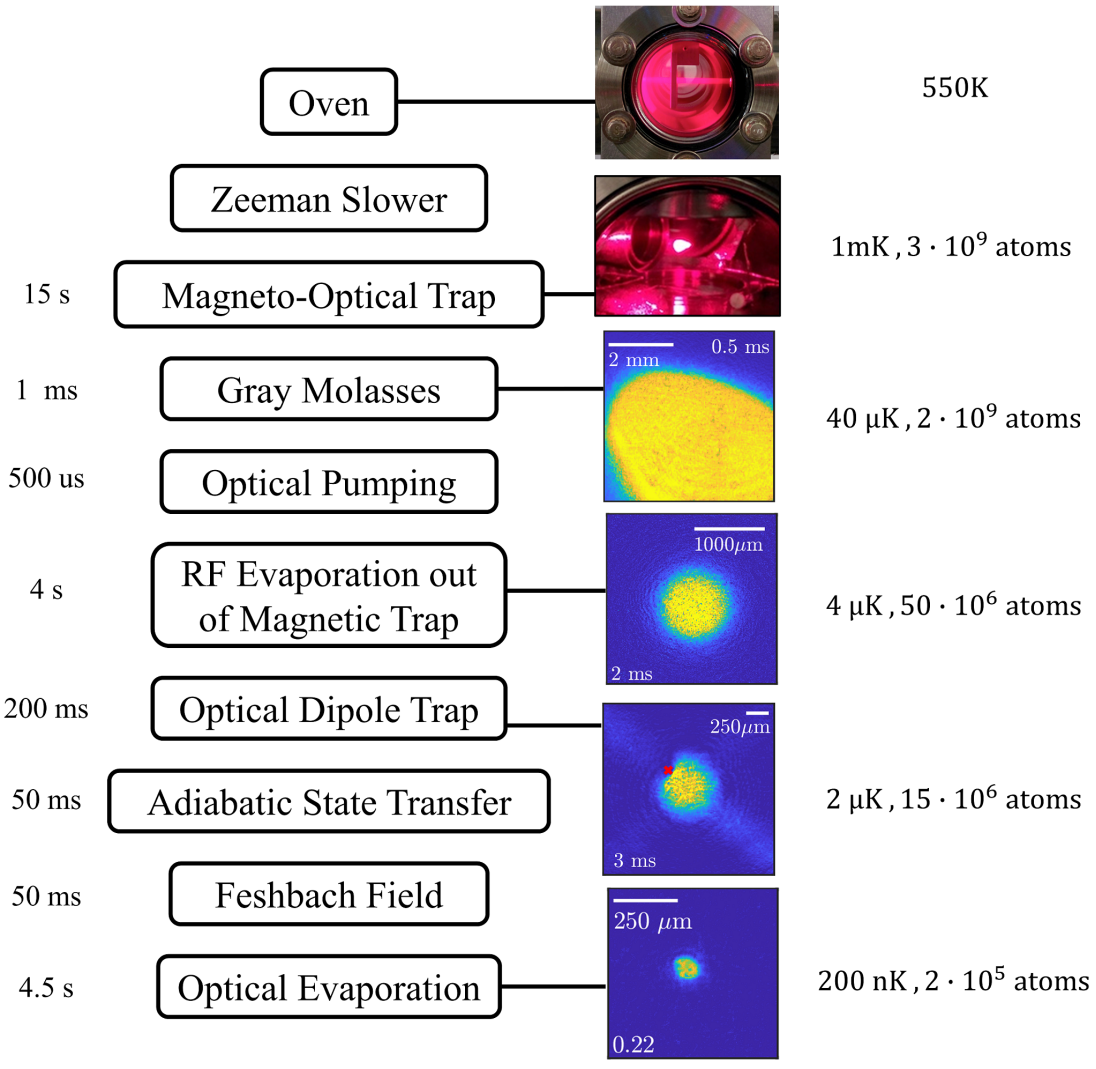

Figure 3.3: Summary of the cooling steps to cool the atomic gas to quantum degeneracy. The left side indicates the approximate duration of the step while the right side gives approximate temperatures and atom number.

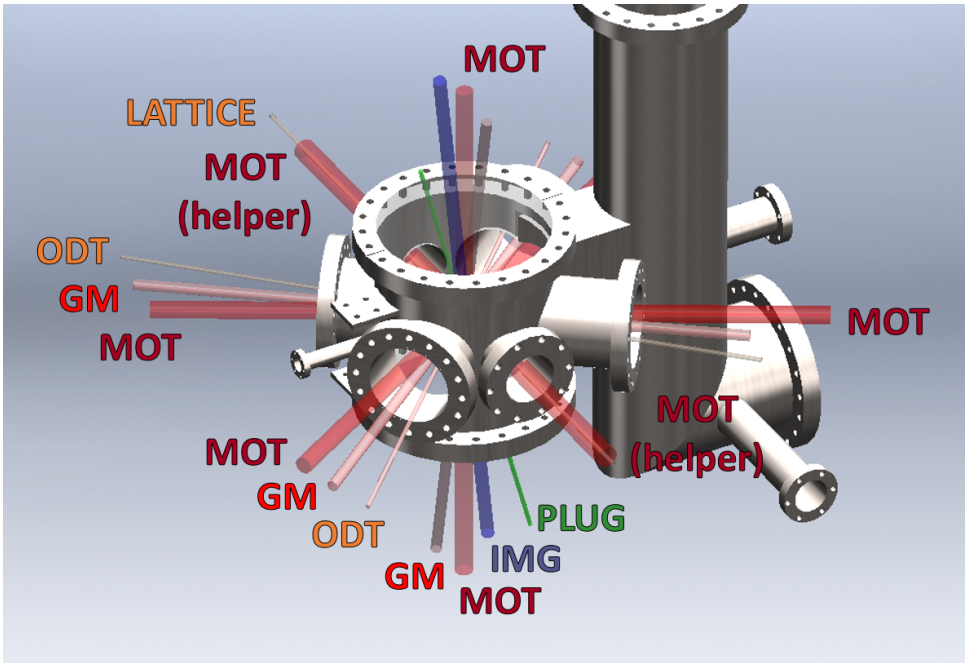

Figure 3.4: Schematic of the laser beams in the main chamber. All beams except for the Zeeman slower and additional imaging beams along the transverse and ODT axes are shown.

These design considerations came at the cost of placing the large windows away from the orthogonal condition at 52.5° away from the transverse axis. Due to the presence of the side reentrant window, we are unable to position our large MOT beams at 90°.

As of writing of this thesis, we do not use the reentrant windows for high NA imaging, and our existing and planned experiments utilize measurables that occur on fairly large length scales. Therefore, we have considered removing the side reentrant window, but have no immediate plans to do so. Additionally, our current experiments utilize one dimensional optical lattices along the transverse axis, and the author wishes she had the opportunity to realize 2D physics using the windows for their designed purpose.

The main chamber also has a large chimney with a titanium sublimation pump (TSP) and ion pump. The presence of the chimney results in the asymmetry of the window placement shown in Figure 3.5. Good UHV and baking practices that we developed over the years results in our low pressures, and we only need to fire the TSP once a year at

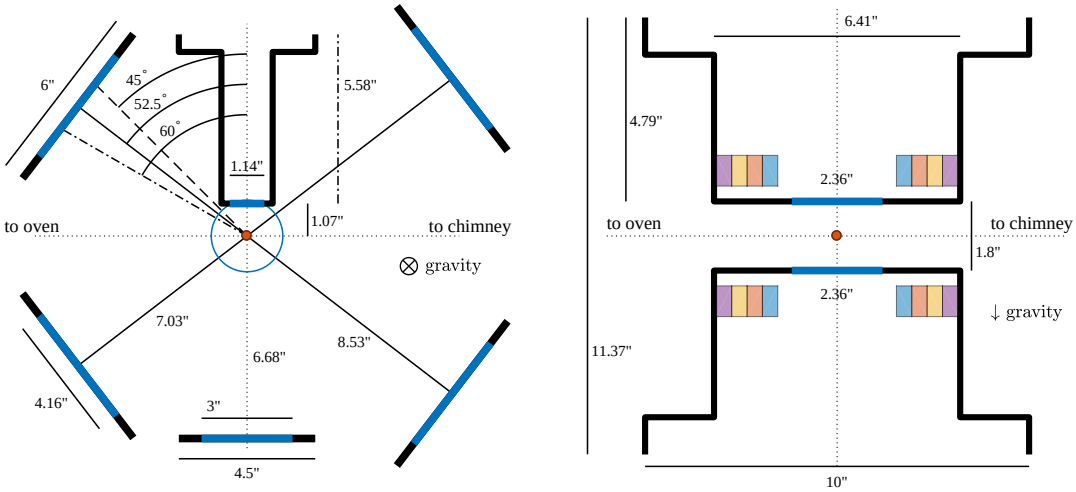

Figure 3.5: Schematic of the main chamber optical access. **(left)** The optical acess from the top perspective. Note that the four 6" windows are at 52.5° away from the transverse axis (vertical on the page). The side reentrant window is 1.07" away from the location of the atoms (red circle). The blue circle indicates the edge of the vertical reentrant window. **(right)** The optical access as viewed from the side. The vertical reentrant windows of 2.36" diameter are separated by approximately 1.8". The primary magnets are drawn in cross section as colored rectangular boxes (blue, red, yellow, purple) which indicate the separately addressable electrical components of the electromagnets.

most. The author is satisfied with the condensate lifetime.

The close proximity of the low inductance primary electromagnets inside the vertical reentrant windows has been a boon. Relatively fast control over the currents and the ability to realize large field gradients has proven to be quite helpful. The author is also particularly fond of the idea of fast modulation of the interaction strength but did not get an opportunity to investigate thoroughly. Good control over the magnetic field gradients and strengths has been a continual effort over the years and has enabled the experiments in this thesis. While we have developed good infrastructure to control magnetic forces, it is the opinion of the author that additional foresight in design of the main chamber with regards to magnetic field would have been helpful. In particular, all the primary

electromagnets have the same sign of magnetic field curvature at the location of the atoms.

The resonant laser light stems from a Toptica TA-Pro with a LD-0670-35-AR-2 671 nm diode and is locked to a spectroscopy cell via saturated absorption spectroscopy. We have three additional tapered amplifiers (TA), one BoosTA from Toptica and two homebuilt ones. While the homebuilt TAs are affordable, the poor output transverse mode has made beam shaping challenging at times. The performance of all our tapered amplifiers have decreased from their specified output powers of 500 mW to their current values at around 300 mW. However, the author's opinion is that we have ample optical power. The laser system also features two injection locked slave diodes, and we are generally pleased with their performance. We have needed to replace the diodes only once during my graduate student tenure and have found the injection locks to be robust.

The magnetic nature of lithium has made imaging at different interaction strengths somewhat challenging. Our current system utilizes a chain of AOMs to image at a variety of fields strengths, and construction of an offset locked imaging ECDL has been in discussion for a number of years. The author has also been very much interested in implementing a phase contrast imaging system.

The off resonant laser light consists of a 1064 nm 50 W fiber amplifier from Nufern[2] and an 532 nm 10 W Sprout-G from Lighthouse Photonics. We are reasonably pleased with the performance of both these lasers, and have not found power or pointing noise to inhibit any of the experiments conducted in this thesis. The seed for the fiber amplifier is from NKT Photonics and is shared with the Strontium machine. We have an additional seed from Orbits Lightwave and another Nufern fiber amplifier, and we are currently keeping them as backups (although using them would be fun!).

[2]We lament that Nufern is discontinuuing support for our fiber amplifier.

3.1 Oven and Atomic Beam

The atom source for our experiment comes from a heated stainless steel cup of lithium, which we refer to as the oven. Its purpose is to provide gaseous lithium of sufficient number density to be trapped by the rest of the experimental sequence. We are required to heat the oven to around 500°C to achieve high enough vapor pressures (Figure 3.6). These large temperatures result in a large thermal velocity distribution that mandate the necessity of a Zeeman slower, which constrains the geometry of the gaseous lithium produced by the oven to be a linear beam. Such large vapor pressures are also incompatible with quantum-degenerate gases, and therefore the oven must be physically separated from the main chamber. The interconnected nature of the oven with the rest of experimental apparatus makes it difficult to discuss holistically without considering the entire machine. The discussion in this thesis is limited to a general description of the oven and characterization of typical operating conditions. Experimental details and design considerations may be found in other documentation published by this group [5, 7, 11].

The primary components of the oven consist of a stainless steel cup of lithium and a small exit aperture called the nozzle as diagrammed in Figures 3.7 and 3.8. The cup is oriented vertically with respect to gravity to prevent liquid lithium from entering the rest of the chamber and is loaded with approximately 20 g of lithium under argon flow. A 90° elbow connects the cup to the nozzle. The nozzle consists of an array of microcapillary tubes which reduces the transverse velocity profile of the atomic beam exiting the oven. Band heaters are strategically placed to locally heat the cup, cup flange, and nozzle, and the entire manifold is wrapped in insulation. Typical operating temperatures are listed in Table 3.1. We maintain the nozzle as the hottest component to prevent lithium buildup in the small aperture. After the nozzle there is another aperture which we call the cold plate to capture excess lithium produced by the nozzle.

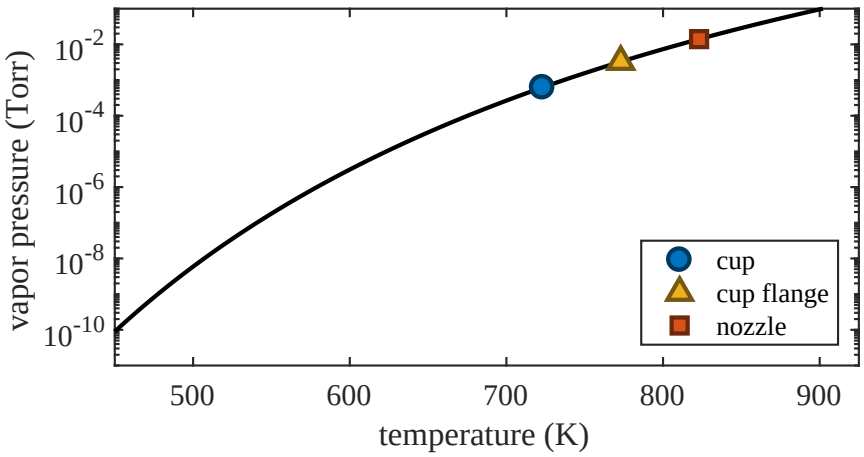

Figure 3.6: Vapor pressure for liquid lithium as a function of temperature [5]. The points indicate temperatures of the oven components. The nozzle is the hottest component to prevent build up in the tubes of the nozzle. The melting point of lithium at 450 K is located at the left axis.

State	**Oven**	**Elbow**	**Nozzle**
Operational	450 °C	500 °C	550 °C
Idle	300 °C	350 °C	400 °C

Table 3.1: Summary of the temperature of the oven components at both operating conditions and idle conditions. At the end of the day we turn the temperatures down to the idle ones.

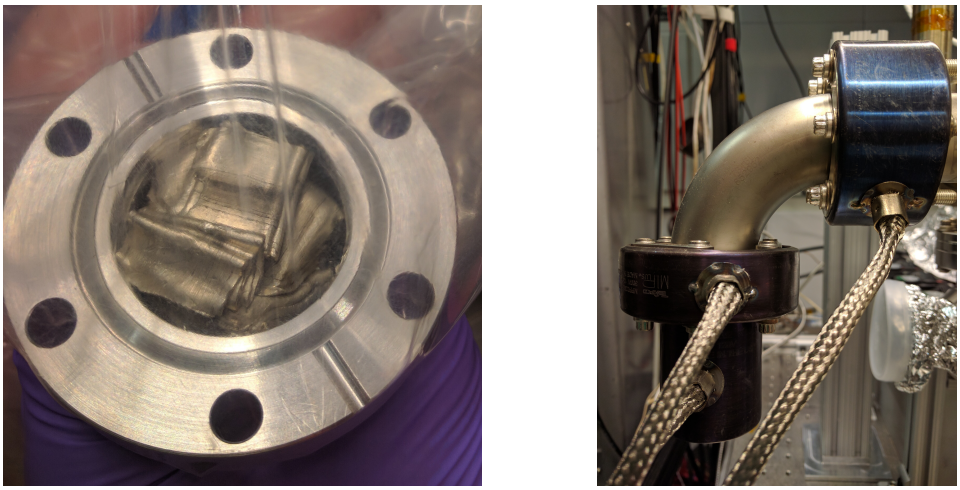

Figure 3.7: Pictures of the lithium oven during assembly. **(left)** Lithium is placed inside the stainless steel cup inside a glove bag under argon flow. The lithium comes in tape form and needs to folded and compacted into the cup. **(right)** The assembled oven. The three band heaters are visible over the cup, cup flange, and nozzle. The entire assembly is wrapped in insulation afterwards.

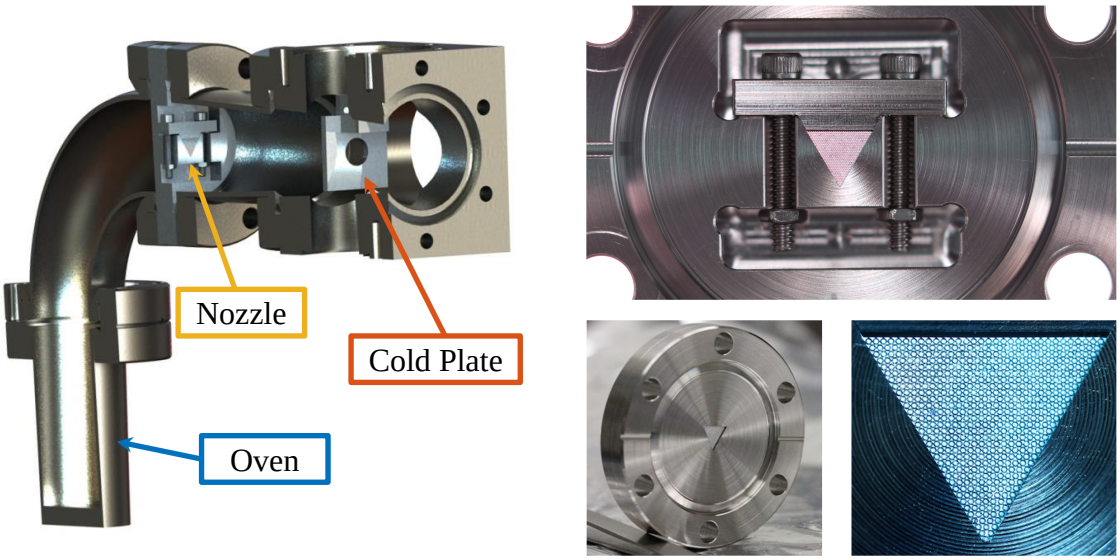

Figure 3.8: The lithium oven. **(left)** Rendering of the oven in cross-section. The cup holding the lithium (blue), the nozzle (yellow), and cold plate (red) are indicated. **(right)** Images of the nozzle after assembly. The bottom left shows a close up of the tube array in its close packed arrangement.

Figure 3.9: The fluorescing atomic beam. The Zeeman slower beam causes the atomic beam to fluoresce as it passes through the cold plate. The oven and nozzle are towards the left. The atomic beam is traveling from left to right, and the Zeeman slower beam travels from right to left.

While these kinds of ovens are typical in many atomic physics labs, the unique feature of our machine is the design of the nozzle [11]. The nozzle consists of a hexagonally packed array of microcapillary tubes as shown in Figure 3.8. With diameter 100 μm and length 5 mm, each tube only permits atoms with small transverse velocities to successfully pass through. This design has a two fold effect: (1) it collimates the atomic gas into a one dimensional velocity distribution which improves the capture efficiency (2) it increases the lifetime of oven by restricting the flow of atoms to those that we can reasonably laser cool. While groups have used microcapillary tubes to collimate atomic beams, the hexagonal close packing enforced by the triangular aperture prevents relative angular deviations of the tubes as the nozzle is thermally and mechanically stressed. The resultant atomic beam can be easily seen by eye in Figure 3.9 as it passes through the cold plate while it fluoresces from the Zeeman slower cooling beam.

Quantitative analysis of the atomic beam is performed by measuring the absorption of a weak probe beam passing transversely to the atomic beam propagation axis. This

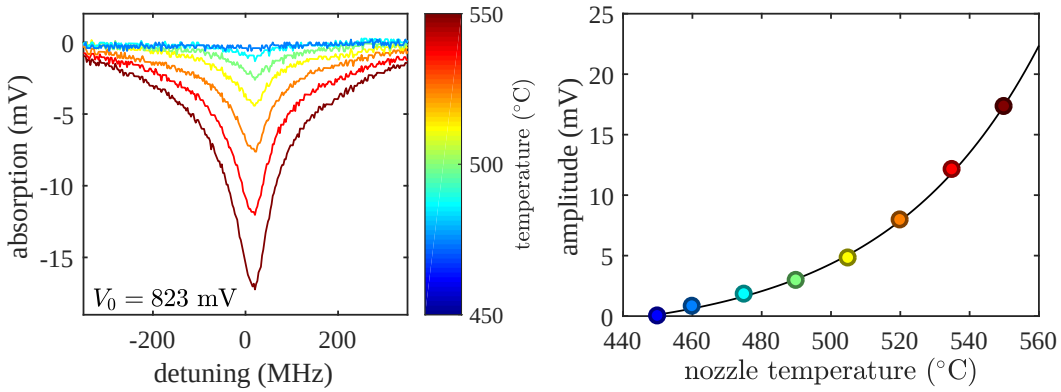

Figure 3.10: Quantitative analysis of the atomic beam taken via a probe beam transverse to the atomic beam at the cold plate. Beam diameter 1 mm, 50:50 cyler to repumper power balance, and total power far below saturation. **(left)** The measured transverse doppler shift for varying nozzle temperatures. The cup and cup flange temperatures are increased commensurately. With a characteristic linewidth of around 100 MHz, the lineshape is consistent with theoretical predictions [11]. **(right)** Peak absorption for varying nozzle temperatures. The black line is an exponential fit meant to demonstrate the increase in beam flux for increasing temperatures.

directly measures the transverse velocity profile via the doppler shift $\delta f = v/\lambda$. The result of such measurements is summarized in Figure 3.10 for varying nozzle temperatures. The measured profile is fitted with a sum of a Gaussian and and Lorentzian distribution. The measured linewidth of around 100 MHz is consistent with theoretical modeling of the microcapillary tubes and verifies the efficacy of our design.

3.2 Zeeman Slower

The **Zeeman slower** prepares the atomic beam from the oven for trapping in the magneto-optical trap. Its necessity arises from the fact that while the transverse velocity profile of the atomic beam is relatively narrow, the axial velocity is in thermal equilibrium with the oven temperature and therefore is quite fast - much too fast to be reasonably captured by the magneto-optical trap. As it's name suggests, the primary purpose of the Zeeman slower is to reduce the axial velocity distribution of the atomic beam low enough to be captured by the magneto-optical trap. The fundamental cooling mechanism relies on an optical molasses radiation pressure force that is kept in resonance by a spatially varying Zeeman shift as is diagrammed in Figure 3.11. This compensates for the changing Doppler shift as the atomic beam slows down while traveling along the slower. Specific details about the design and implementation of our slower may be found in other theses produced by this group [4, 7, 5].

We implement a spin flip electromagnetic axial Zeeman slower whose magnetic field profile is generated by four separately addressable tapered solenoids. The entrance and exit axial magnetic field are approximately 780 G and -232 G. The slowing laser beam consists of light 407 MHz (65Γ) red detuned of the zero field transitions for both the $F = 1$ and $F = 2$ ground states as indicated in Figure 3.13. From the detuning and peak field, we estimate the capture velocity to be 1 km/s and the exit velocity to be 50 m/s. This is outlined in Figure 3.12. The light originates from an injection locked slave diode and the $F = 1$ light is generated via a resonant 813.5 MHz EOM with an approximate 13% sideband amplitude. The total power in the beam is 45 mW with an initial beam diameter of 1" at the vacuum chamber entrance which is focused to around 5 mm at the approximate location of the nozzle a few meters away. Such focusing is intended to compensate for the increase in the transverse spatial extent of the atomic

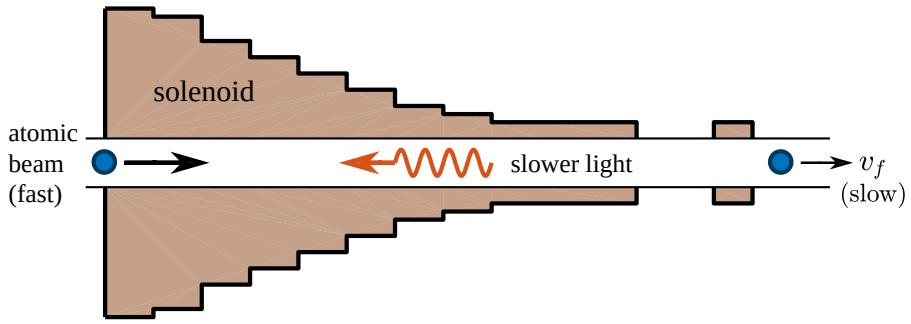

Figure 3.11: Cartoon of the Zeeman slower. A tapered solenoid (brown) generates a spatially dependent magnetic field which induces a varying Zeeman shift along the slower. This causes the slower light to be resonant and provide a optical molasses force as the atoms travel. The exit velocity v_f is slow compared to the entrance velocities.

beam a it travels down the length of the slower. To prevent undesirebable buildup of Lithium on the beam entrance window, we heat it to 140 °C and also shine 401 nm light on it. We also implemented two transverse cooling stages before and after the Zeeman slower. At nominal operating conditions, the Zeeman slower loads the MOT with a rate of approximately $160 \times 10^6/s$. A summary of the performance of the Zeeman slower is provided in Figure 3.14.

Quantitative assessment of the Zeeman slower is challenging beyond simple bulk load rate measurements. This is because its performance couples to that of the oven, transverse cooling, and the MOT. Experimentally, we only require that the Zeeman slower performs well enough to not inhibit trapping sufficient atoms in the magneto-optical trap. Furthermore, detailed analysis is inhibited by uncertainty in the magnetic field profile. Failed electrical connections resulted in the unusability of a few windings of the electromagnets of the tapered solenoid, and rewinding the solenoid would require breaking vacuum. As such, the Zeeman slower remains a component of the machine that falls under the category "if it's not broken, don't fix it".

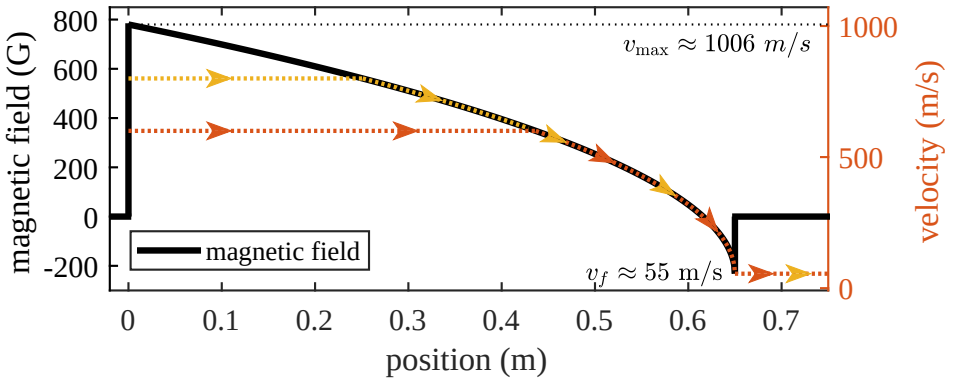

Figure 3.12: Schematic of the magnetic field profile and velocity distribution. The magnetic field of the of slower starts at approximately 780 G and ends at -232 G. Atoms with a given entrance velocity (yellow and red) become resonant with the slowing beam at some point along the slower and cooled to the exit velocity v_f.

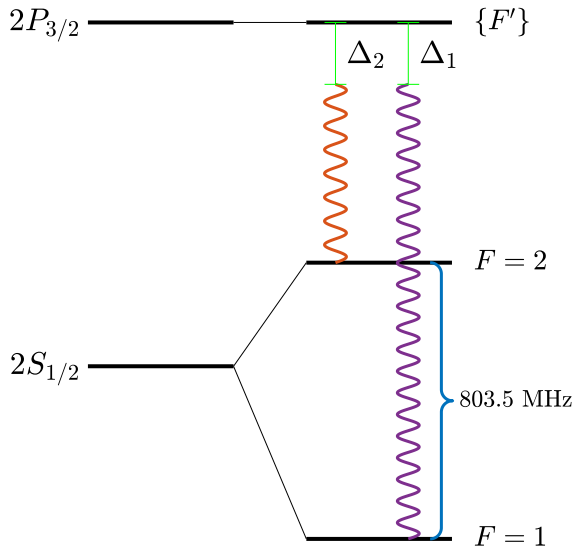

Figure 3.13: Schematic of the detunings Δ_1 and Δ_2 of the light for the Zeeman slower drawn with respect to the zero field splittings. As specified in the text, $\Delta_1 \approx \Delta_2 \approx 407$ MHz $= 65\Gamma$.

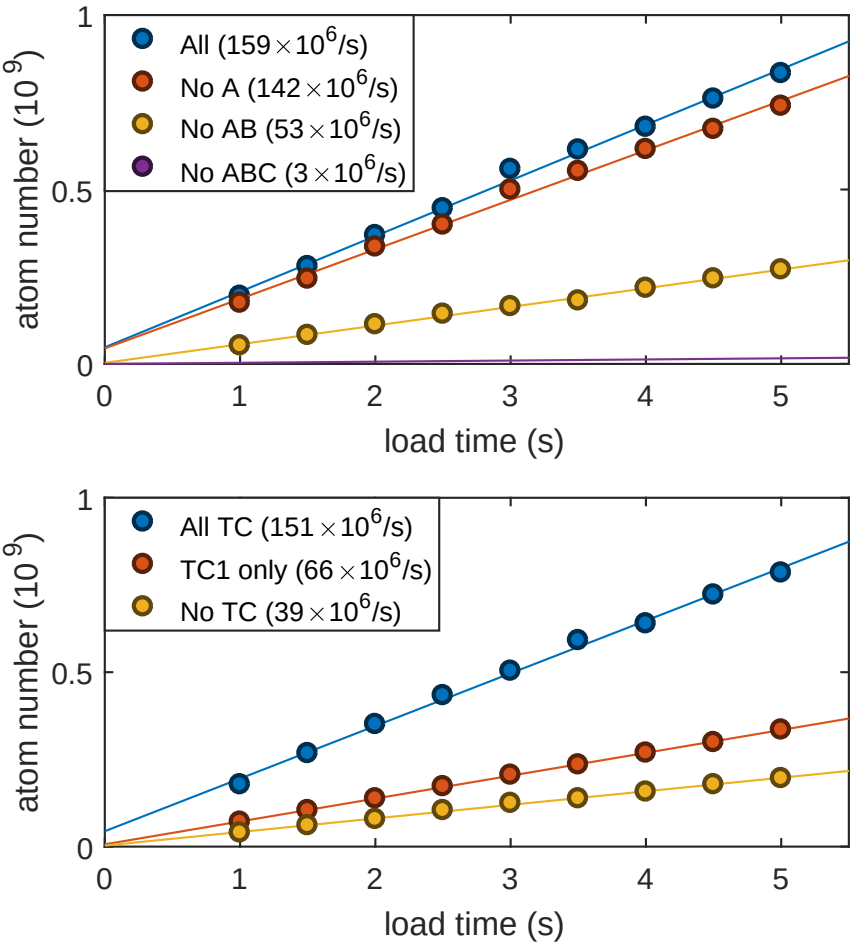

Figure 3.14: Performance of the Zeeman slower as measured via the MOT load rate. **(top)** Measured MOT load rate utilizing different sections of the Zeeman slower. The data for No ABC was measured at 30 s. **(bottom)** The effect of transverse cooling on the MOT load rate. The relative increase of the load rate with transverse cooling (blue) is 387% compared to no transverse cooling (yellow). The second tranverse cooling stage is more important as is evidenecd by the more modest increase of the load rate with only the first transverse cooling stage (red).

3.3 Magneto-Optical Trap

The magneto-optical trap (MOT) is the first trapping stage that the atoms encounter, and it collects atoms delivered from the Zeeman slower. For this reason, it functionally serves as an atomic reservoir upon which all steps in the experiment rely, and therfore, its reliable performance is paramount for the success of any experiment. The trapping mechanism relies on a spatially dependent radiation pressure force that is mediated by the Zeeman shift of a quadrupolar magnetic field as diagrammed in Figure 3.3. The history of MOTs is extensive, and this thesis limits the discussion to a few key experimental details and measurements. More complete descriptions of the design and infrastructure of our MOT may be found in other theses [4, 6, 7, 5].

The expression for the radiation pressure force is given by equation 3.1 [1].

$$\mathbf{F}_{\mathrm{MOT}} = -\alpha \mathbf{v} - \frac{\alpha}{k}\frac{g\mu_B}{\hbar}\mathbf{r}\ \nabla|\mathbf{B}|, \tag{3.1}$$

The first term which depends on the atom velocity v represents a frictional force, and the second term, which depends on the atom position relative to the magnetic trap center is the trapping force. In this way, a MOT provides both cooling and trapping.

Our MOT operates on the D2 transition which couples the ground $2S_{1/2}$ and excited $2P_{3/2}$ manifolds as outlined in Figure 3.3. While nominally a cycling transition from the $F = 2$ to $F' = 3$ states, the unresolved nature of the excited manifold makes it non-cycling and mandates usage of a repumper of equivalent intensity to that of the cycler. Therefore, out MOT consists of two colors of light addressing the transitions from both the $F = 2$ and $F = 1$ hyperfine states in the $2S_{1/2}$ manifold to the excited $2P_{3/2}$ manifold. The unresolved nature of the excited state also precludes polarization gradient cooling which limits our MOT temperatures to the Doppler cooling limit. Consistent

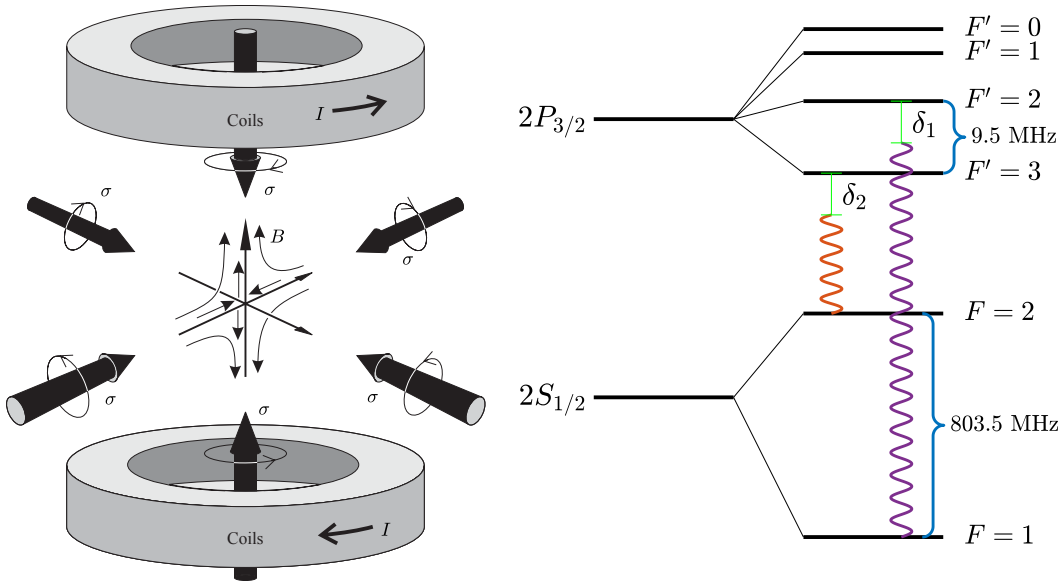

Figure 3.15: Schematic of the MOT. **(left)** A traditional six beam MOT is created with a quadrupolar magnetic field profile generated from a pair of electromagnets in an anti-Helmholtz configuration. Diagram from Foot [1]. **(right)** Frequency schematic of the MOT transitions. The nominally cycling transition from the $F = 2$ to $F' = 3$ transition is in red while the repumper transition from the $F = 1$ to $F' = 2$ transition is in purple. Note that the energy separation between the $F' = 2$ and $F' = 3$ of 9.5 MHz is comparable to the linewidth 5.92 MHz.

with other groups using ^{7}Li, we operate our MOT at approximate detunings $\delta_1 \approx 4.5\Gamma$ and $\delta_2 \approx 6.5\Gamma$ and an axial field gradient of 20 G/cm. Each of the beams are collimated to an approximate $1/e^2$ diameter of 1" and are aligned in a co-linear configuration with their counter-propagating partner. An analysis of the dependence of the MOT size on the optical power in the MOT beams is shown in Figure 3.16.

Our MOT utilizes a unique eight beam configuration with six horizontal beams and two vertical beams as shown in Figure 3.17. The necessity of eight beams in contrast to the traditional six is a consequence of the design of our vacuum chamber which restricts the angular access away from typical orthogonal orientations. Calculations during the design of the main chamber indicated that angling the MOT beams away from the orthogonal condition would not affect the MOT capture size [7]. However, we found that

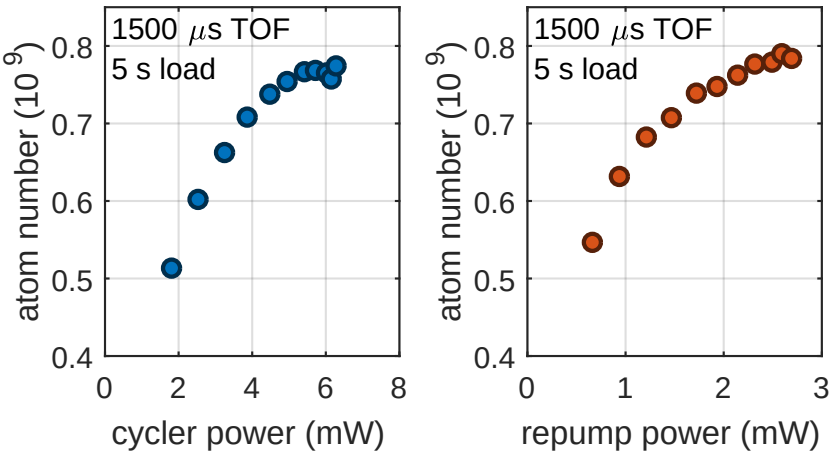

Figure 3.16: Dependence of MOT size on the optical power in the repumper and cycler. The size and detuning of the beams are as specified in the text. The power measured is in the south-west beam.

this limited our MOT capacity to a few hundred million and prevented RF evaporation out of the magnetic trap. Adding additional beams along the transverse axis increased our MOT capacity sufficiently to achieve quantum degeneracy. We estimate our MOT capacity be around a few 10^9 with an approximate temperature of 1 mK which we load in about 15 s. The physical extent of the MOT is difficult to accurately measure due to its opacity, but is estimated to be around 1 cm in diameter.

As atoms are trapped in the MOT they scatter photons as described by equation 3.1, and the spontaneously emitted photons as the atoms de-excite from the $2P_{3/2}$ state can be seen by eye which is shown in Figure 3.18. For a MOT of this size, visual inspection by humans not only is a pleasure, but also serves as a useful diagnostic of the quality of the MOT on a day to day basis. A more practical diagnostic however, is to record the fluorescence on a photodiode shown also in Figure 3.18.

While the photodiode signal serves as a useful diagnostic tool, it is difficult to extract an accurate measure of the capture number. While estimations of the atom number from fluorescence are consistent with that performed via absorption imaging, the non-linear

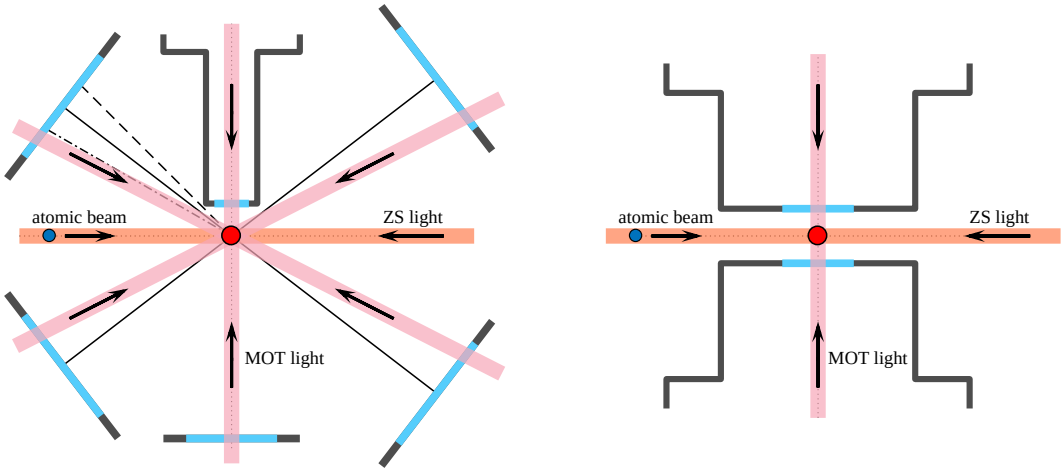

Figure 3.17: Geometry of the MOT beams. **(left)** Perspective from the top. The horizontal MOT beams (pink) are not at the traditional 90°, and we find the usage of additional beams to be required to make a large enough MOT (red). The windows are 52.5° (black) away from the transverse axis (dotted). Lines for 45° (dashed) and 60° (dot-dashed) away from the transverse axis are also drawn. The presence of the side bucket window prohibits the large MOT beam of 1" diameter from coming in at 45°. **(right)** Perspective from the side. The MOT beams (pink) come in vertically through the bucket windows.

relationship between atom number and photodiode fluorescence makes it generally inappropriate beyond diagnostic purposes. A comparison of the absorption and fluorescence signal is shown in Figure 3.19 and represents how we estimate our atom number in the MOT. For short load times, the fluorescence and atom number increase linearly with each other until the absorption imaging count rapidly saturates. This coincides with the saturation of the measured optical density of around four which represents a limitation in the dynamic range of our imaging system. As of writing of this thesis, we do not have a quantitative understanding of this effect. The ease of measuring the fluorescence in comparison to absorption imaging make it a more practical diagnostic tool for the MOT.

After the MOT has been loaded we engage a compressed MOT (CMOT) phase. The fundamental idea is that the MOT parameters are chosen for maximizing the MOT

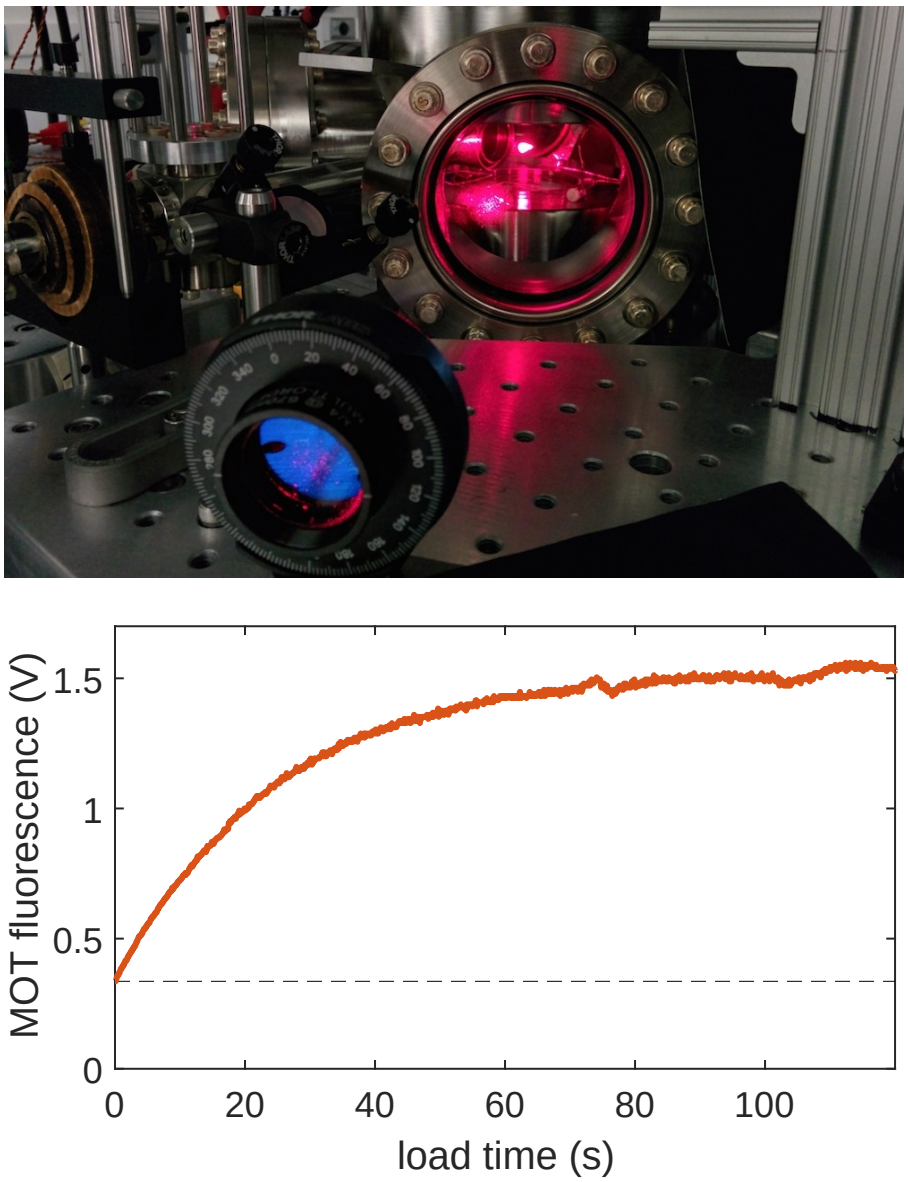

Figure 3.18: Atoms in the magneto-optical trap. As atoms are captured in the MOT, the amount of scattered photons from the trapping beam is indicative of the atom number trapped. **(top)** An image of the MOT taken with a cellphone camera. The fluorescence can easily be seen by the human eye. **(bottom)** The measured fluorescence as captured by a photodiode monotonically increases with the number of atoms captured by the MOT from the Zeeman slower. The MOT loads to its maximum capacity in around one minute with an estimated capacity of $5 \cdot 10^9$.

capture size and not for mode matching into the next experimental step. In general this optimum condition may not coincide with optimizing the phase space density. Since the next part of the experimental sequence is gray molasses which cools the atomic cloud, the primary purpose of the CMOT then is to reduce the spatial extent of the cloud. To achieve this, we first quickly increase the field gradient from 20 G/cm to 100 G/cm. We then bring the cycling beam closer to resonance while turning down the repumper power. The net effect is to reduce the size of the atomic cloud.

As of writing of this thesis, the benefit of the CMOT is debatable and currently represents a portion of the experimental sequence that falls under the category "if it's not broken, don't fix it". In fact, the CMOT can be quite detrimental to the performance of the machine if the MOT beams are not intensity balanced appropriately about the magnetic field zero. This can be directly observed by asymmetric deformation or translation of the *in situ* atomic cloud during the CMOT phase. Moreover, the tuning range of the CMOT is limited by the finite tuning range of the double pass AOM used to tune the cycler beam. While certain members of this group are convinced at the usefulness of the CMOT, this author's personal opinion is to agree with empirically supported conclusions[3].

[3]All hail the dark ritual.

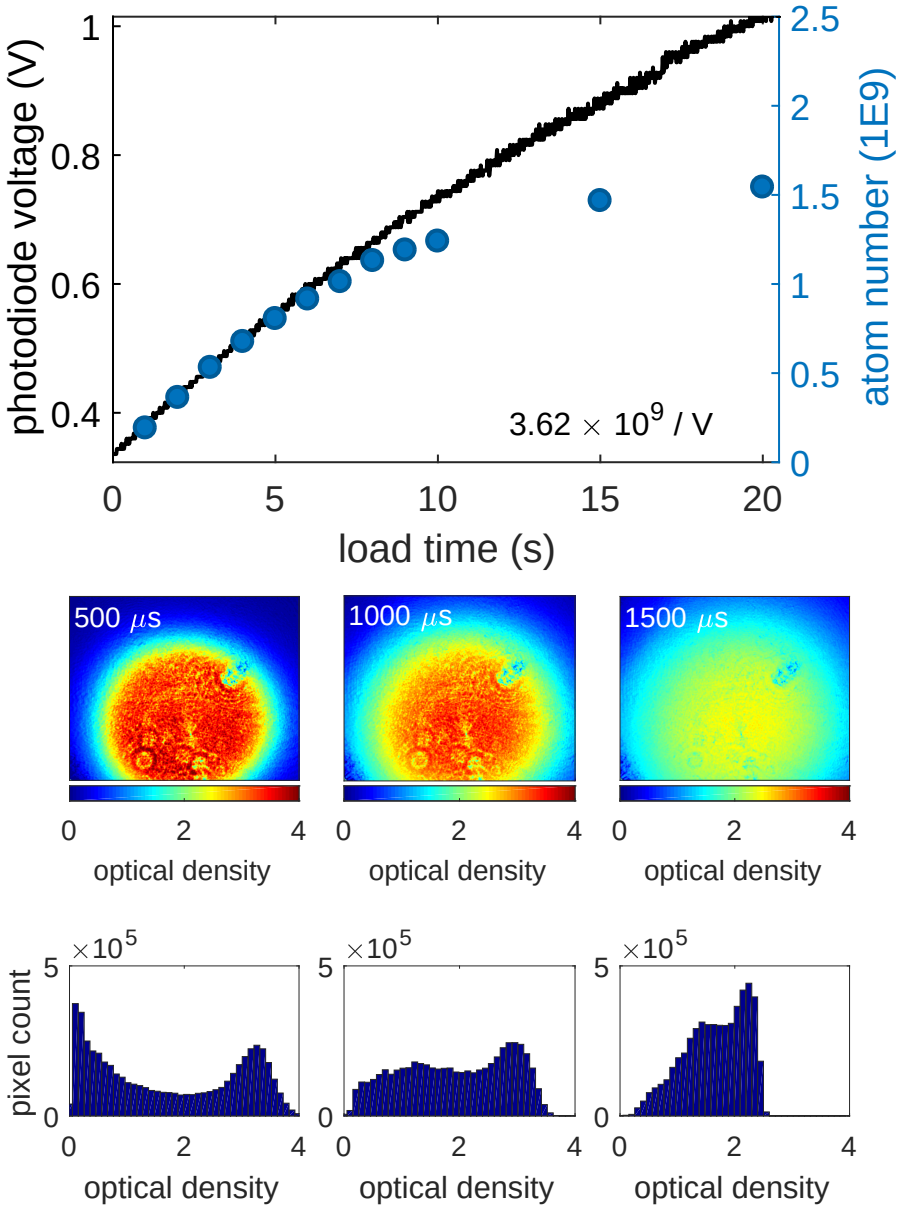

Figure 3.19: Analysis of quantitative diagnostics for the MOT. **(top)** Comparison of the measured fluorescence and absorption of the MOT for varying load times. For short times the two signals are linear with each other, but the absorption number increase falls off quickly for atom number larger than 10^9. Fitting of the short time relationship yields an estimated 3.62×10^9/V scaling between fluorescence and atom number. The non-linear relationship of fluorescence and atom number make this scaling a lower bound on the atom number. **(bottom)** Saturation of the measured optical density. Shown here are the measured optical densities for varying time of flights which should have the same atom number. Saturation of the atomic density limits our ability to accurately measure atom number for very dense clouds.

3.4 Gray Molasses

As discussed in the previous section, the temperature of the MOT is limited to around a millikelvin. This is because polarization gradient cooling is unviable in ^{7}Li due to its unresolved excited state hyperfine stucture. This is compounded with the fact that the scattering length of ^{7}Li exhibits a zero crossing at moderate kinetic energies which inhibits evaporative cooling at millikelvin temperatures. To circumvent this limitation, we implement a sub-Doppler cooling technique known as **Gray Molasses** (GM) after the CMOT phase. The fundamental cooling mechanism of GM relies on a two-photon lambda coupling and a spatially modulated AC stark shift. Diagonalizing in the position basis generates coupling and non-coupling states whose energies are modulated spatially. The combination of motional and two photon momentum Raman coupling results in a sisyphus like cooling mechanism. A more detailed description of our optical setup may be found in [6, 4]. We follow the scheme outlined in [12].

The GM scheme is realized by applying light near the two photon resonance condition on the D1 transition as outlined in Figure 3.20; the relevant parameters in this scheme are the single photon detuning δ, the two photon detuning Δ, and the intensities I_1 and I_2. The detunings for the individual single photon transitions from the ground state manifolds are $\delta_1 = \delta - \Delta$ and $\delta_2 = \delta$, and we operate with $\Delta \approx 0$ and $\delta \approx 5\Gamma$. The relative intensity of the beams is $I_1/I_2 \approx 2\%$, where I_1 is generated via an 803.5 MHz EOM. Cooling in the horizontal plane is done in a retro-reflected bow-tie configuration with total power 38 mW and waist 0.25" and cooling with the vertical direction is done with a single retro-reflected beam with total power 34 mW and waist 0.25". The estimated saturation parameter is 20, but is somewhat uncertain due to the poor beam mode coming from our home built TA. The GM beams are pulsed for 1 ms after the CMOT and a magnetic field ring down time of 500 μs. We find that our gray molasses cools the atomic

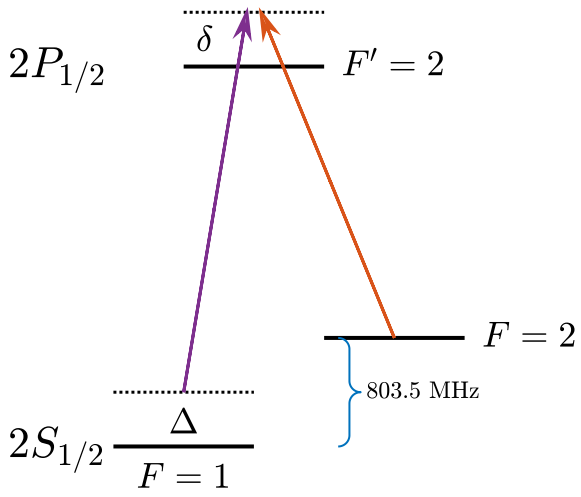

Figure 3.20: Energy level schematic of the gray molasses cooling scheme.

cloud to around 30 μK - 50 μK with near unity capture efficiency.

Bridging the relatively large frequency shift of 10.053 GHz between the D1 transition and the D2 transition where our resonant laser system is locked is a technical challenge. While other groups utilize a beat locked ECDL, we injection lock a slave laser diode on a sideband of a 9.2 GHz resonant EOM. We find this large frequency shift allows locking with sufficient discrimination against undesired frequency components [4]. Alignment of the horizontal GM beams is done by visualizing aligning them with the MOT with at an increased field gradient to create a small target. By injection locking to the wrong sideband, the GM light does not affect the MOT and can be easily aligned by the human eye with appropriate irising. The vertical beam is aligned by locking to the correct EOM sideband and maximizing the displacement of the MOT subjected to the vertical GM beam.

An investigation of the performance of GM with respect to the two photon detuning and optical power is explored in Figures 3.23 and 3.22. We find that performance of

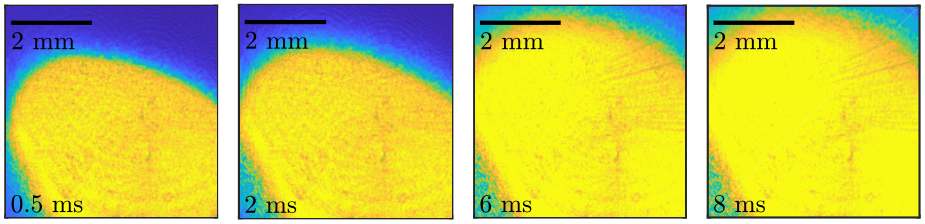

Figure 3.21: Gray molasses in time of flight. The optical density remains high for tens of milliseconds which is a consequence of the high atom number capture and low temperature. Accurate atom counting and thermometry is challenging for this zoomed in imaging axis, but previous imaging indicated near unity capture efficiency.

GM monotonically increases with the total intensity. While the measured temperature is higher for larger optical powers, this coincides with a larger capture efficiency. This behavior suggest that decreasing the optical power during the GM pulse may provide lower temperatures while still retaining a high capture efficiency. We also find that the optimum two photon detuning Δ be zero, which is evidenced by a sharp decrease in temperature and increase in phase space density at the two photon resonance. These observations are consistent with those found by other groups [12]. The capture efficiency is asymmetric across the resonant condition as measured by the atom number. Since evaporative cooling is non-linear in atom number, the operating two photon detuning is empirically set by optimizing the atom number after RF evaporation in the magnetic trap.

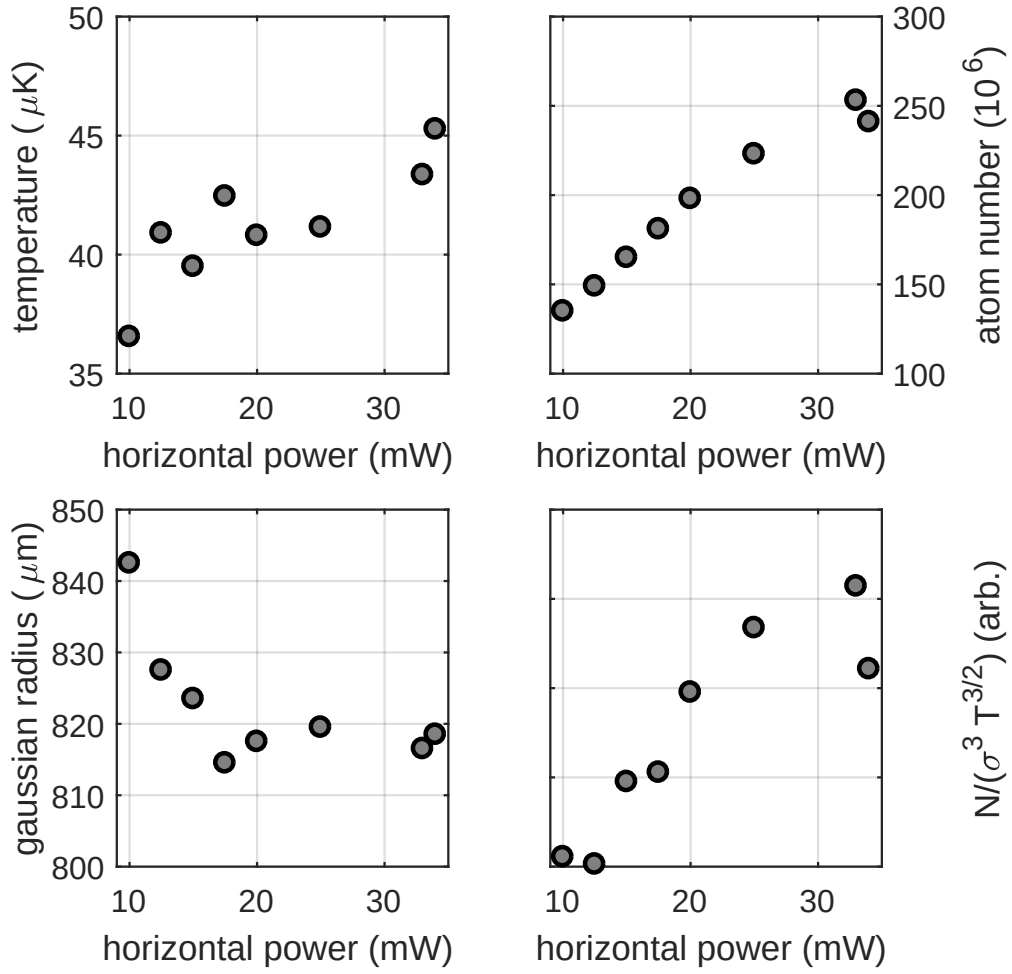

Figure 3.22: Exploring the performance of gray molasses for varying total optical power under the experimental parameters outlined in the text. Gray molasses is pulsed for 1 ms following a 1 s MOT load. The measure temperatures, atom number, and sizes are extracted from a time of flight measurement. As the total power in the horizontal beam is varied, the vertical total power is varied by the same ratio. **(top left)** The measured temperature increases with total optical power. **(top right)** The capture efficiency monotonically increases with optical power. **(bottom left)** The minimum cloud size decreases with increasing optical power. **(bottom right)** The measured phase space density monotonically increases with optical power.

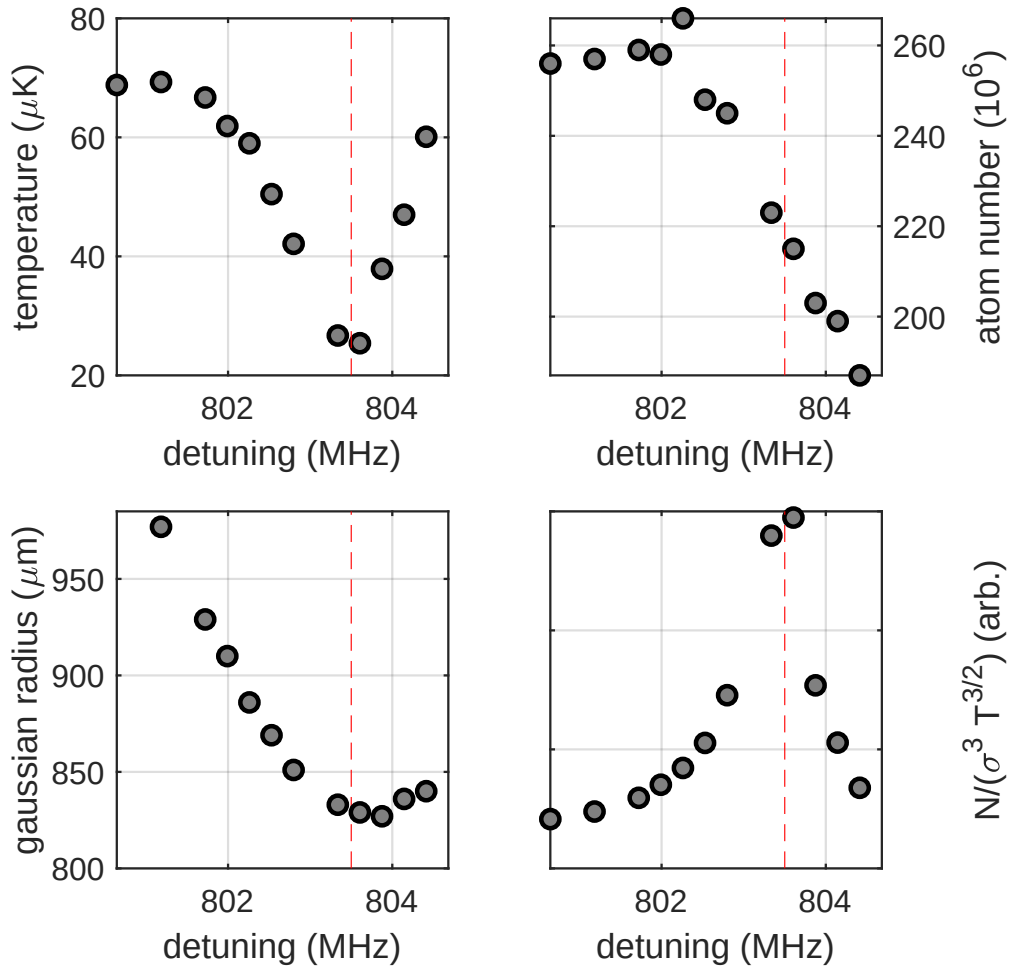

Figure 3.23: Exploring the performance of gray molasses for varying two photon detuning Δ. This is plotted as the EOM sideband frequency generating the light resonant with the $F = 1$ ground state manifold; here $\Delta = 0$ is achieved when the sideband frequency is equal to the ground state splitting of 803.5 MHz which is indicated by the red dashed line. The remaining experimental parameters are as outlined in the text. Gray molasses is pulsed for 1 ms following a 1 s MOT load. The measure temperatures, atom number, and sizes are extracted from a time of flight measurement. The relative intensities between remains fixed as the EOM response is constant over this range. **(top left)** The measured temperature sharply decreases at the two photon resonance. **(top right)** The capture efficiency monotonically decreases across the two photon resonance. **(bottom left)** The minimum cloud size is minimized at the two photon resonance. **(bottom right)** The measured phase space density peaks at the resonance condition which is primarly govered by the sharp response in temperature.

3.5 Optical Pumping

After gray molasses, the atomic cloud is prepared for trapping and cooling in the magnetic trap. The spin state after gray molasses is a random spin mixture among the $2S_{1/2}$ manifold because gray molasses couples the F states in the absence of a quantizing magnetic field. As discussed in the next section, the magnetic trap requires the internal state of the atomic cloud be spin polarized to the $|2,2\rangle$ state, which we achieve via **optical pumping**. Due to the unresolved energy structure of the excited $2P_{3/2}$ manifold of the D2 transition, we elect to optically pump via the $2P_{1/2}$ manifold of the D1 transition as outlined in Figure 3.24. Absorption of σ^+ polarized radiation coupled with randomly polarized spontaneous emission from the excited state tends to increase the magnetic quantum number m_F. Importantly, this optical pumping is self terminating because the $|2,2\rangle$ state lacks an $m_F = 3$ state to excite to in the $F' = 2$ manifold. This self termination is critical because it minimizes the stimulated absorption from optical pumping which heats the cloud to the Doppler cooling limit. After optical pumping, the resultant spin state of the atomic cloud is polarized into the desired $|2,2\rangle$ state.

The light for D1 optical pumping is generated from the same pathway as the GM light with a few modifications to the AOMs and utilization of only the vertical beam path [4]. The single photon detunings are brought closer to resonance with $\delta_2 \approx 0$ and $\delta_1 \approx 3\Gamma$, and the beam has total optical power of 55 mW and waist 0.4". The RF power in the 803.5 MHz EOM is increased to increase the relative intensity resonant with the $F = 1$ ground state. The pumping beam is pulsed for 500 μs after applying a vertical magnetic bias field of approximately 3 G.

While the effect of optical pumping can be directly observed by imaging the cloud after D1 pumping, it more useful to empirically optimize the atom number in the magnetic trap. This is because imaging the optically pumped cloud resolves the relative populations

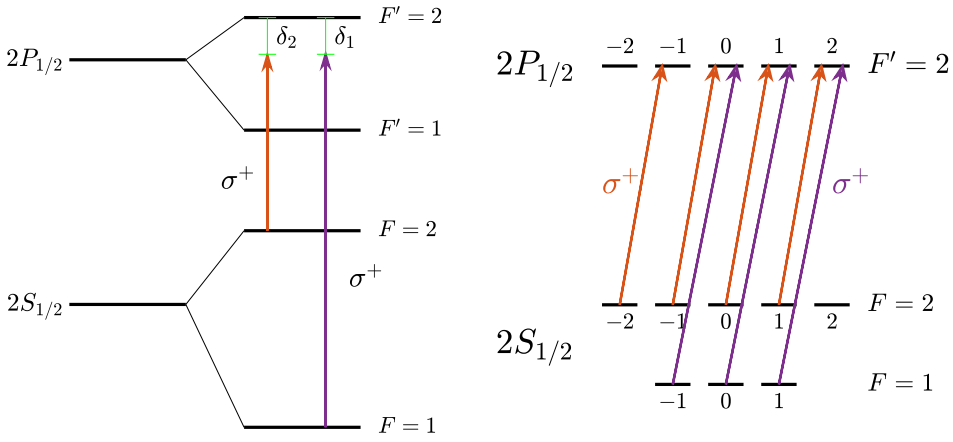

Figure 3.24: Schematic of D1 optical pumping. **(left)** Optical pumping consistents of apply circularly polarized light from the $2S_{1/2}$ state to the $2P_{1/2}$ state. **(right)** By using circularly polarized light the $F = 2$, $m_F = 2$ state is dark because there is no $m_F = 3$ state in the excited state manifold. Spontaneous emission which randomly populates the ground manifold from the excited manifold is not depicted.

in the F manifolds but does not adequately distinguish the m_F states. In contrast, the magnetic trap is extremely sensitive to the specific $|F, m_F\rangle$ state and is optimum only for a spin polarized atomic gas in the magnetically trappable stretched states $|1, -1\rangle$ and $|2, 2\rangle$. Since we conduct RF evaporation in the magnetic trap on the $|2, 2\rangle$ state it is therefore experimentally desirable to optimize D1 pumping in this way. This results of this optimization with respect to pumping time and detuning is described in Figure 3.25.

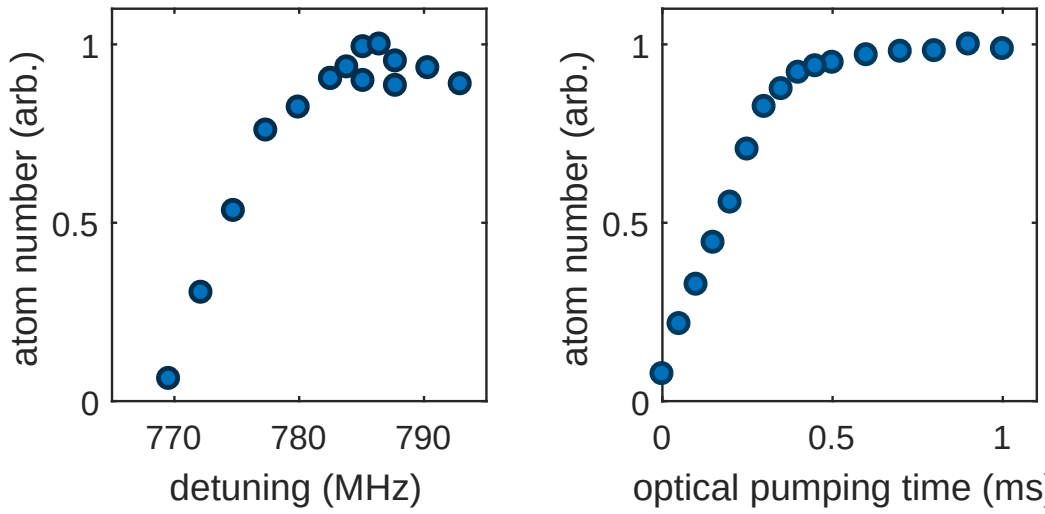

Figure 3.25: Optimization of D1 optical pumping via the magnetic trap. **(left)** Atom number as a function of the relative detuning between the two optical pumping beams. The two photon resonance condition occurs at a detuning of approximately 803.5 MHz. Operating away from the resonance suppresses spin changing two photon dynamics which maximizes the single pumping efficiency. **(right)** Atom number as a function of optical pumping time. The atom number saturates for a pumping times longer that about 500 μs. A relative increase in the atom number with and without optical pumping larger than the multiplicity of the magnetically capturable states is a consequence of spin exchange loss during the hold in the magnetic trap.

3.6 Magnetic Trap

The **magnetic trap** (MT) is the next trapping stage for the cold atomic gas. In contrast to the magneto-optical trap, the magnetic trap consists only of a spatially dependent Zeeman shift from a quadrupolar magnetic field profile. The resultant potential energy landscape localizes the atomic gas about the magnetic field zero. Cooling is performed via radio frequency (RF) evaporation which induces transitions to magnetically untrappable states. As the highest energy atoms are ejected from the trap, the temperature of the remaining ensemble decreases after thermalization. Importantly, the magnetic trap marks a division in the experimental sequence where resonant light is no longer utilized because the cloud is significantly colder than the Doppler cooling limit. As such, any resonant light represents a source of heating in the magnetic trap and for all future steps in the experimental sequence. Historically speaking, the technical challenges of the magnetic trap proved to be a large roadblock for the group towards achieving condensation, and on a day-to-day basis, the magnetic trap is one of the more unreliable steps in the experimental sequence. From a hollistic perspective, the stringent technical requirements stem from the fact that evaporative cooling intrinsically relies on inter-atomic interactions. This causes the hold time in the magnetic trap to be relatively "long", and therefore trap losses must be mitigated.

The discussion of the magnetic trap found in this section is divided into a few parts. Such a division is motivated by the desire to provide first an overview of the key components of the magnetic trap, and then discuss in detail a few important technical aspects. A detailed discussion of the experimental infrastructure of the magnetic trap is omitted, and the author directs the reader to other theses [4, 5, 7].

The trapping potential is provided by the weak field Zeeman shift of equation 3.2 which depends on the local magnetic field magnitude. Here, a good basis is given by

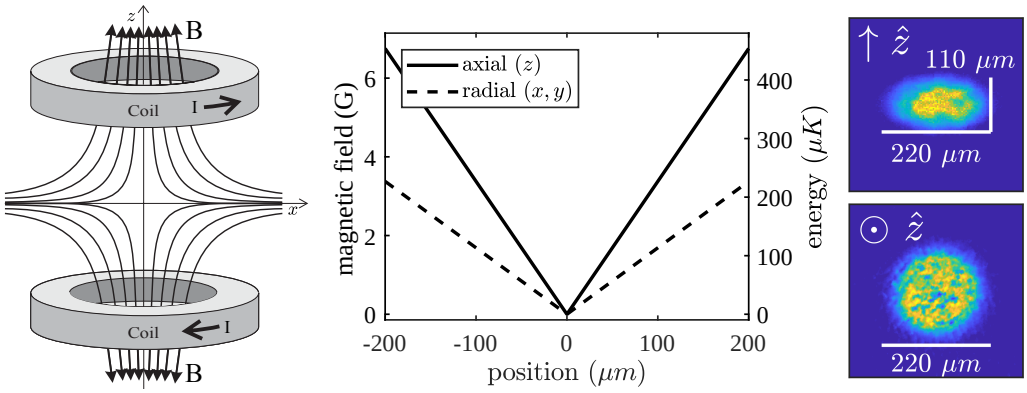

Figure 3.26: Basic trapping mechanism of the magnetic trap. **(left)** A quadrupolar magnetic field profile is created from electromagnets in an anti-Helmholtz configuration. The magnitude of the magnetic field increases away from the center of the coils [1]. **(center)** The magnetic field and trap depth increase linearly away from the center of the magnetic trap, shown here for the magnetically trappable $F = 2$, $m_F = 2$ state. The field gradient is 338 G/cm. The trap strength in the radial directions (x, y) are twice as weak as the axial one (z). **(right)** Demonstration of the aspect ratio of the magnetic trap. Images taken along the axial dimension (bottom) show an equal size between the two radial dimensions while images taken from the side (top) reveal the 1:2 aspect ratio. These images are taken after RF evaporation with a field gradient of 338 G/cm.

the magnetic labeling $|F, m_F\rangle$ restricted to the $2S_{1/2}$ ground manifold. The magnetic field profile produced by the primary magnets in an anti-Helmholtz configuration is well approximated by equation 3.3, where the field gradient along the axial dimension is G[4].

$$U(\vec{r}) = m_F g_F \mu_B B(\vec{r}) \tag{3.2}$$

$$B(\vec{r}) = G\sqrt{\frac{\left(x^2 + y^2 + 4z^2\right)^2}{2}} \tag{3.3}$$

For any trappable state ($m_F g_F > 0$), the resultant potential energy landscape is a linear trap with a 1:2 aspect ratio between the vertical and the horizontal directions. For the $F = 1$ manifold $g_F = -\frac{1}{2}$, and for the $F = 2$ manifold $g_F = \frac{1}{2}$. Therefore only the $|2, 2\rangle$, $|2, 1\rangle$, and $|1, -1\rangle$ states are magnetically trappable of which we use

[4]Unless specified, all field gradients shall be reported along the z direction

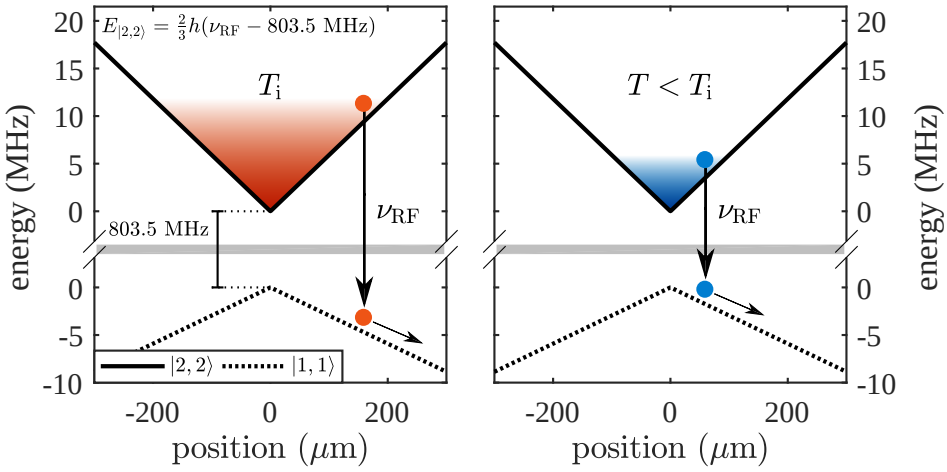

Figure 3.27: Schematic of radio frequency (RF) evaporation out of the magnetic trap. Atoms with the highest energy and entropy travel the furthest away from the trap center where the spatially dependent Zeeman shift can bring them into resonance with the applied RF radiation. The RF induces magnetic dipole transitions from the trappable $F = 2$, $m_F = 2$ state (black) to the magnetically untrappable $F = 1$, $m_F = 1$ state (dotted) which then leaves the trap. The temperature of the remaining sample decreases after thermalization. In practice the RF frequency $\nu_{\rm RF}$ begins far above the ground state splitting of 803.5 MHz and is slowly brought closer towards it.

only the $|2,2\rangle$ state. A schematic of the magnetic trap and a brief discussion of the potential is shown in Figure 3.26. Once the atomic cloud is trapped inside the magnetic trap, evaporation proceeds via application of RF magnetic radiation polarized along the axial dimension from a loop antenna. As diagrammed in Figure 3.27, this radiation induces magnetic dipole transitions from the original magnetically trappable $|2,2\rangle$ state to the untrappable $|1,1\rangle$ state dependent on the resonance condition of equation 3.4. By setting the RF frequency $\nu_{\rm RF}$ sufficiently above the zero field splitting of 803.5 MHz, this selectively ejects the highest energy atoms out of the trap. By decreasing $\nu_{\rm RF}$ slowly enough to allow for thermalization, the temperature of the remaining sample decreases.

$$E_{|2,2\rangle} = \frac{2}{3}h\left(\nu_{\rm RF} - 803.5\ {\rm MHz}\right) \tag{3.4}$$

In principle, it is desirable to operate the sweep as fast as possible to reduce the

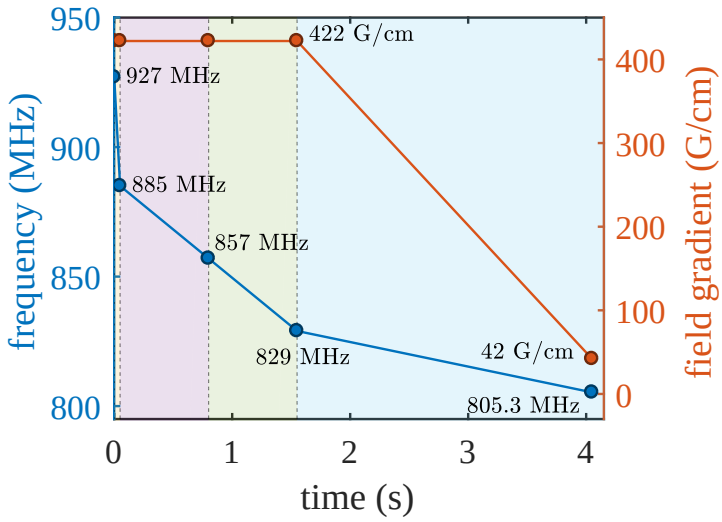

Figure 3.28: Piecewise linear sweep of the RF radiation and field gradient during RF evaporation.

overall time in the magnetic trap and to minimize trap losses. However, this is limited by both the elastic scattering rate which sets the thermalization timescale and the Rabi frequency of the radio frequency which governs how efficiently atoms are ejected from the trap. Experimentally, the elastic scattering rate is optimized by operating at a high field gradient, and the Rabi frequency is optimized via usage of a high power 200 W RF amplifier. A more detailed discussion of the balancing between these parameters and the relevant loss mechanisms is found later in this section.

An overview of experimental sequence during RF evaporation is now provided which is similar to the discussion found in the Geiger thesis [4]. After optical pumping, a high voltage capacitor bank is used to rapidly snap the field gradient to 80 G/cm. The field gradient is then increased to 422 G/cm in 150 ms which is the maximum value possible of our power supplies. The radio frequency sweep begins at 920 MHz which corresponds to ejection of atoms at 3.7 mK. The RF frequency ν_{RF} is then piecewise linearly swept to 805.3 MHz in tandem with the field gradient decreasing to 42 G/cm over approximately 4 s. While theoretical models of evaporation suggest exponential-like curves, we find

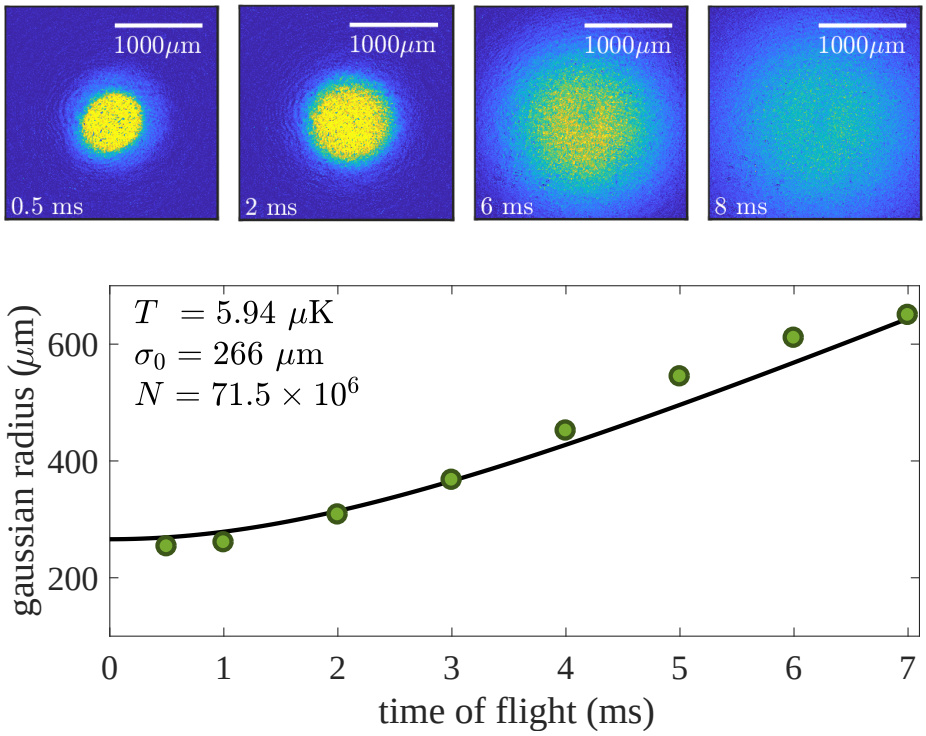

Figure 3.29: Time of flight out of the evaporated magnetic trap. **(top)** Optical densities of the images in time of flight. The effect of the plug beam can be observed in time of flight as a decrease in local atom number density. **(bottom)** Measurement of the increase of the cloud size as function of time of flight yields a temperature of 5.94 μK. The atom number is around 71.5×10^6 with a minimal gaussian radius of 266 μm.

the simplicity of the piecewise optimization to be beneficial. A summary of the sweep is presented in Figure 3.28. At the end of RF evaporation the atom number ranges between 40-70$\times 10^6$ at an approximate temperature of 7 μK, which is shown in time of flight in Figure 3.29

3.6.1 Thermodynamics

The technical discussion of the magnetic trap begins with the single particle partition function expressed in equation 3.5. In the classical non-interacting limit, all relevant

experimental observables are obtained through the single particle partition function

$$Z_1 = \left(\frac{32\pi}{P^3\beta^3}\right)\left(\frac{8\pi m}{\beta h^2}\right)^{\frac{3}{2}} \tag{3.5}$$

where $\beta = 1/(k_B T)$ and $P := m_F g_F \mu_B G$. This is obtained via integration over the kinetic and spatial degrees of freedom.

$$Z_1 = Z_U Z_{\mathrm{KE}} \tag{3.6}$$

$$Z_U = \int \mathrm{d}^3\vec{x} e^{-\beta U(\vec{r})} \tag{3.7}$$

$$Z_{\mathrm{KE}} = \frac{1}{h^3}\int \mathrm{d}^3\vec{p} e^{-\beta p^2/2m} \tag{3.8}$$

The *in situ* peak number density is found from the spatial probability density:

$$n_0 = N\frac{e^{-\beta U(0)}}{Z_U} \tag{3.9}$$

$$= N\frac{P^3\beta^3}{32\pi} \tag{3.10}$$

And the peak phase space density ρ can be calculated

$$\rho(N, G, T) = n_0 \Lambda(T)^3 \tag{3.11}$$

$$= \left(N\frac{P^3\beta^3}{32\pi}\right)\left(\frac{\hbar^2\beta}{2m}\right)^{\frac{3}{2}} \tag{3.12}$$

Inspection of equation 3.12 shows that the quantity $G^3/T^{9/2}$ remains a constant under adiabatic manipulation of the trap. Importantly, this also shows that $T \propto G^{2/3}$ and $n_0 \propto G$.

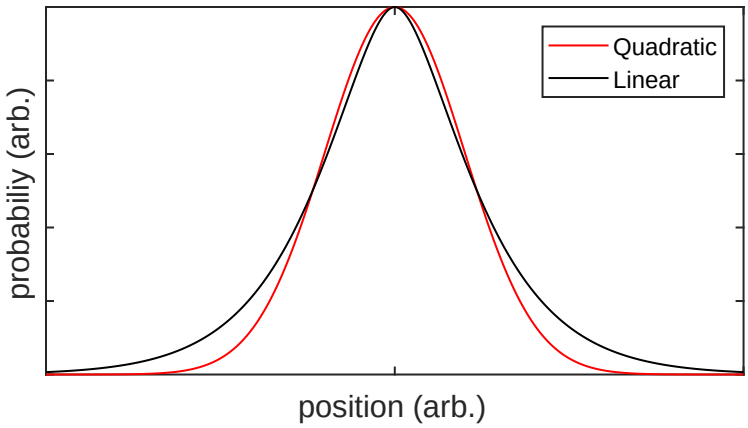

Figure 3.30: Comparison of the a gaussian position distribution for a harmonic trap and the solution for the linear trap for equivalent full width half maximums. The solution to the linear trap has a slower fall off which is to be expected from the constant confining force.

Additionally, the projected spatial distribution[5] is given by

$$P(z) = \frac{1}{Z_U} \int \mathrm{d}x\mathrm{d}y \; e^{-\beta U(\vec{r})} \tag{3.13}$$

$$= \frac{8\pi}{P^2\beta^2} \left(1 + P\beta|z|\right) e^{-P\beta|z|} \tag{3.14}$$

which as shown in Figure 3.30 is not all too different from a Gaussian distribution. Therefore, on an every day basis we do not alter our analysis techniques for the magnetic trap. Practically, the saturation of the measured optical density makes it challenging to accurately discern small differences in the functional form of the *in situ* number density. Analytic calculations of the cloud in time of flight are also well approximated by the Gaussian approximation.

[5]Colloquially known as the Fujiwara function.

3.6.2 Diabatic Projection

We use equation 3.12 to set the ideal turn on procedure for the magnetic trap to mode match the gray molasses cloud. Such calculations are directly related to the necessity of our high voltage capacitor bank [4]. If the confining potential is turned on too slowly, the atomic cloud will diffuse, reducing the number density. However, if the confining potential is turned on quickly to too high a level, the atoms will experience a strong force which will heat them up. In general, the ideal turn on procedure balances these two considerations to maximize the phase space density in the magnetic trap. For simplicity, we restrict ourselves to the parameter space of diabatic turn on of the magnets. In this case, it is relevant to calculate the amount of energy given to the atomic cloud from the potential energy of the magnetic trap. Making use of the virial theorem $2\langle T\rangle = \langle U\rangle$, the final and initial energies relate by equation 3.16.

$$E_f = E_i + U_i \tag{3.15}$$

$$\frac{9}{2}Nk_BT_f = \frac{3}{2}Nk_BT_i + U_i \tag{3.16}$$

The initial potential energy U_i is found by projecting the spatial distribution of the atomic cloud onto the magnetic trap. For simplicity, we model the gray molasses atomic cloud as a three dimensional spherical Gaussian with Gaussian radius σ.

$$n_i(\vec{r}) = N\frac{1}{(2\pi\sigma^2)^{\frac{3}{2}}}e^{-\frac{r^2}{2\sigma^2}} \tag{3.17}$$

$$U_i = \int \mathrm{d}^3\vec{r}\; n_i(\vec{r})U(\vec{r}) \tag{3.18}$$

$$U_i(\sigma) = NP\sigma\frac{2\sqrt{3} + \cosh^{-1}(2)}{\sqrt{6\pi}} \tag{3.19}$$

Combining this result with equation 3.16 yields a final temperature of:

$$T_f = \frac{T_i}{3} + \kappa \frac{m_F \mu_B G \sigma_i}{k_B} \tag{3.20}$$

$$\kappa = 0.122358 \tag{3.21}$$

The resultant phase space density is computed using this final temperature and the peak spatial density profile.

$$\rho = n_0 \Lambda^3(T_f) \tag{3.22}$$

$$= \frac{N}{64\pi\sqrt{2}} \frac{h^3 P^3}{(k_B T_f)^3 (k_B T_f m)^{\frac{3}{2}}} \tag{3.23}$$

$$= \frac{N}{512\pi\sqrt{2}} \frac{h^3 m_F^3 \mu_B^3 G^3}{(k_B m)^{\frac{3}{2}} \left(\frac{T_i}{3} + \kappa \frac{G m_F \mu_B \sigma_i}{k_B}\right)^{\frac{9}{2}}} \tag{3.24}$$

The optimum field gradient G_0 in equation 3.25 is found by maximizing $\rho(G)$. This is shown for experimentally relevant parameters in Figure 3.31.

$$G_0 = \frac{2k_B}{3\kappa m_F \mu_B} \left(\frac{T_i}{\sigma_i}\right) \tag{3.25}$$

While the predictions of equations 3.12 and 3.25 are useful in designing the high voltage capacitor bank, the snap on field gradient is empirically set by varying the charge time of the capacitor bank and optimizing the atom number after RF evaporation.

Next we discuss the trap frequency which roughly sets the timescale of dynamics and determines the criterion for adiabatic and diabatic processes. The anharmonic nature of the linear trap manifests as an energy dependent trap frequency $f(E)$ given by equation 3.26 [13]. An ensemble expectation value $\langle f \rangle$ is found using the virial theorem and is plotted in Figure 3.33.

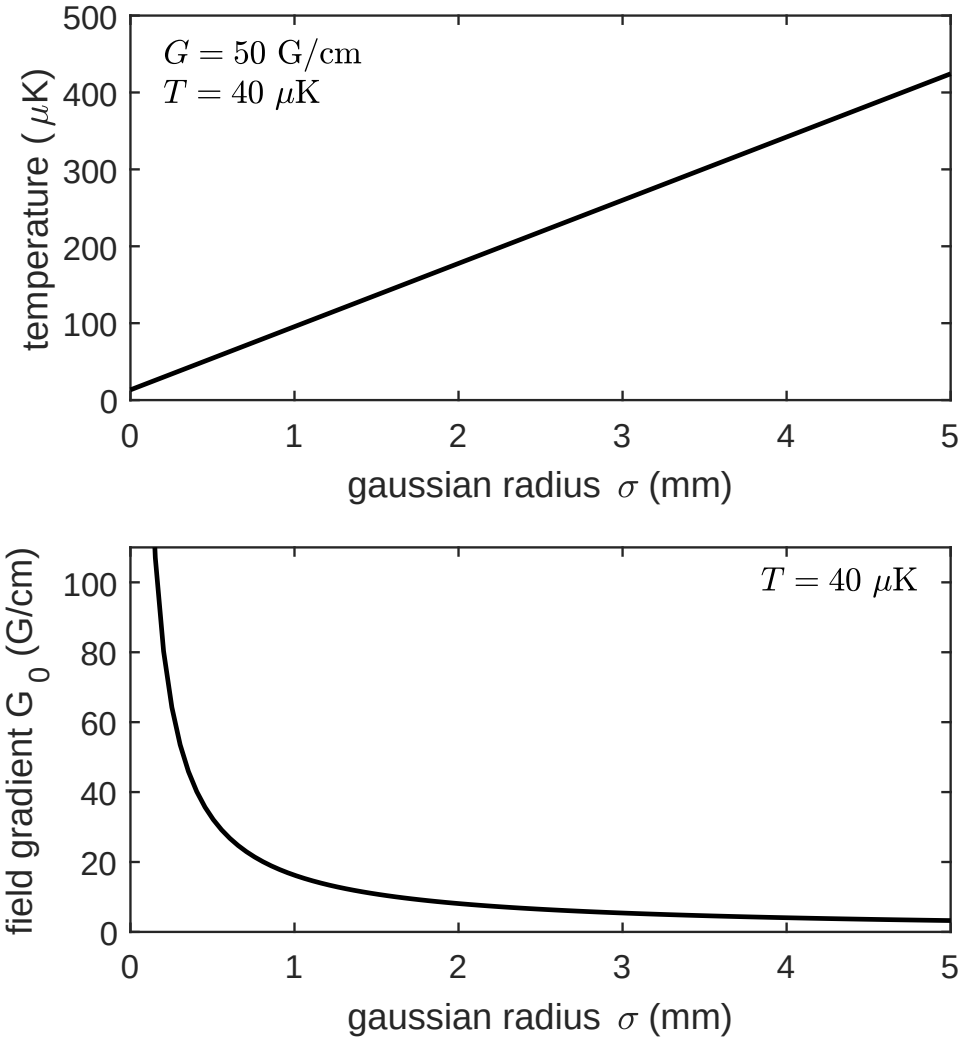

Figure 3.31: Theoretical prediction for ideal diabatic snap-on field gradient. **(top)** The calculated final temperature of an atomic cloud with initial temperature 40 μK and for a snap on field gradient of 50 G/cm. The final temperature increases monotonically with initial cloud size as the force from the snap on potential linearly increases away from the origin. **(bottom)** The ideal calculated snap on field gradient G_0 as a function of cloud size σ with initial temperature 40 μK. The actual snap on value is empirically found by optimizing the magnetic trap.

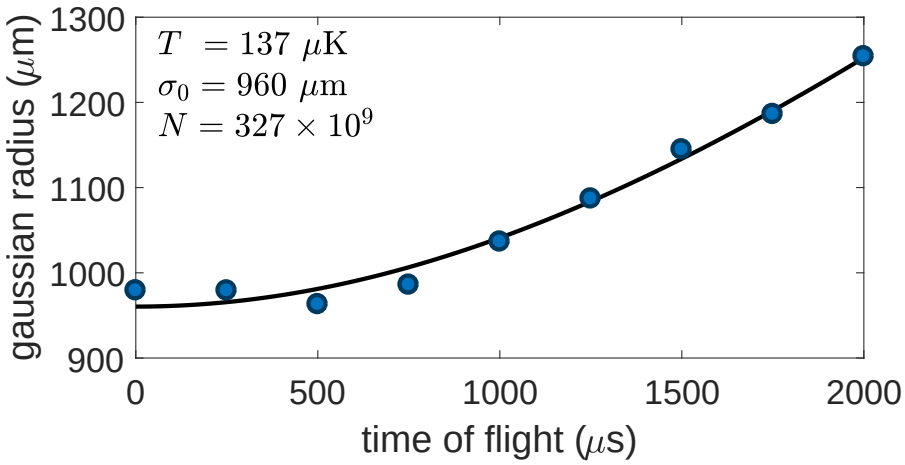

Figure 3.32: Thermometry via time of flight after the diabatic turn on of the magnetic trap after gray molasses and optical pumping. Here for a MOT load time of 1 s and initial field gradient of 77 G/cm. The measured temperature is 137 μK and initial size is fitted to be 960 μm. The increase in temperature and hence reduction in phase space density ρ relative to the gray molasses cloud is consequence of the energy imparted from the diabatic projection as given by 3.16.

$$f(E) = \frac{P}{\sqrt{32Em}} \tag{3.26}$$

$$\langle f \rangle = \frac{P}{12\sqrt{mk_BT}} \tag{3.27}$$

3.6.3 Beyond the non-interacting approximation

As alluded to previously, there are a multitude of loss mechanisms inside the magnetic trap which must be controlled or mitigated. From a phenomenological perspective, these loss mechanisms are as loss rates $\dot{N} \propto -\Gamma(n)$ on the total atom number N. We further categorize the mechanisms based upon their functional dependence on atom number density n (one-body), n^2 (two-body), n^3 (three-body), etc. Of particular interest is the balancing of these losses against the elastic scattering rate which is a key requirement for

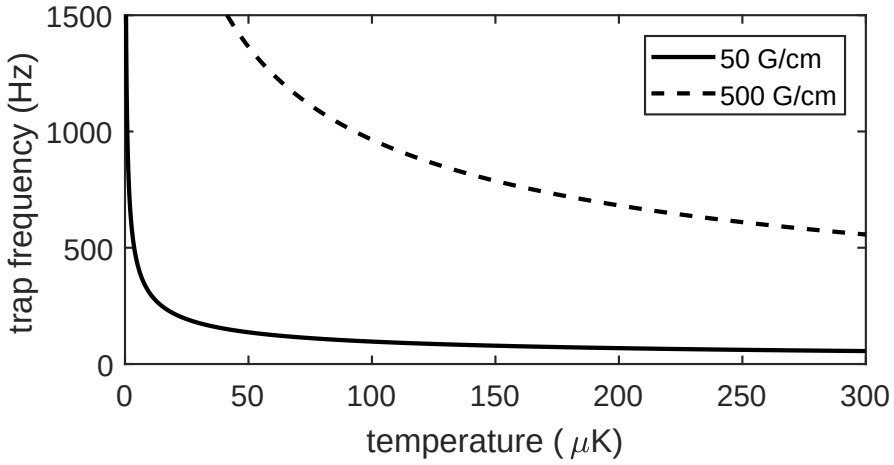

Figure 3.33: Expectation value of the trap frequency in a magnetic trap. The calculated ensemble trap frequency given by equation 3.27 is shown for field gradients of 50 G/cm and 500 G/cm which represent the approximate ranges of field gradients that our magnetic trap implements.

thermalization during evaporation. While a complete treatment of these mechanisms in the magnetic trap is challenging, it is the goal of this section to provide some intuition and to document some relevant calculations.

In general, a two-body interaction couples the non-interacting atomic states which can be labeled by their internal and external degrees of freedom $|\mathbf{p}, F, m_F\rangle$. Assuming a central field coupling, the scattering event is best expressed by a partial wave expansion in angular momentum as shown in equation 3.28.

$$\langle l_f, F_{1f}, F_{2f}, m_{1f}, m_{2f}|\hat{\mathbf{V}}_{\text{int}}|l_i, F_{1i}, F_{2i}, m_{1i}, m_{2i}\rangle \tag{3.28}$$

While such a general expansion is not of practical use, the theoretical form of the total interaction Hamiltonian motivates analysis by quantum number selection rules. Of these, the elastic collisions are the "good" kind since they couple motional degrees of freedom while maintaining spin polarization. Including those up to third order, a qualitative summary of the relevant mechanisms inside the magnetic trap are listed below:

- **Elastic Collisions** (n^2) - only orbital momentum interact; no interactions of spins. $(\Delta l = \{\Delta m_i\} = \{\Delta F_i\} = 0)$.
- **Spin Exchange** (n^2) - external momentum and spin couple independently. Total spin is conserved.$(\Delta l = \Delta F_{\text{tot}} = \Delta m_{\text{tot}} = 0)$
- **Dipolar Relaxation** (n^2) - momentum and spin couple together.
- **Three Body Recombination** - (n^3) two atoms bind together to form a molecule while the third one carries away the binding energy in the form of kinetic energy
- **Majorana Losses** (n) - In the magnetic quadrupole trap, atoms can make transitions to magnetically untrappable states at the field zero where no quantization axis is defined.
- **Background Gas** (n) - atoms make collisions with background gases

And the net effect of the "bad" mechanisms are summarized as density dependent loss rates Γ_i with coefficients γ_i as shown in equation 3.30

$$\dot{N} = -\int \mathrm{d}^3 r \Gamma(\vec{\mathbf{r}}) n(\vec{\mathbf{r}}) \tag{3.29}$$

$$\Gamma(\vec{\mathbf{r}}) = \gamma_1 + 2\gamma_2 n(\vec{\mathbf{r}}) + 3\gamma_3 n^2(\vec{\mathbf{r}}) \tag{3.30}$$

Of these mechansims, this section focuses on the elastic scattering rate and majorana losses. Spin exchange collisions are eliminated by using a spin polarized stretched state; three body recombination is limited by operating at not too high a field gradient; and background gas collisions are reduced by maintaining UHV. Majorana losses are prevented by a plug laser while dipolar relaxation is always present. The elastic scattering

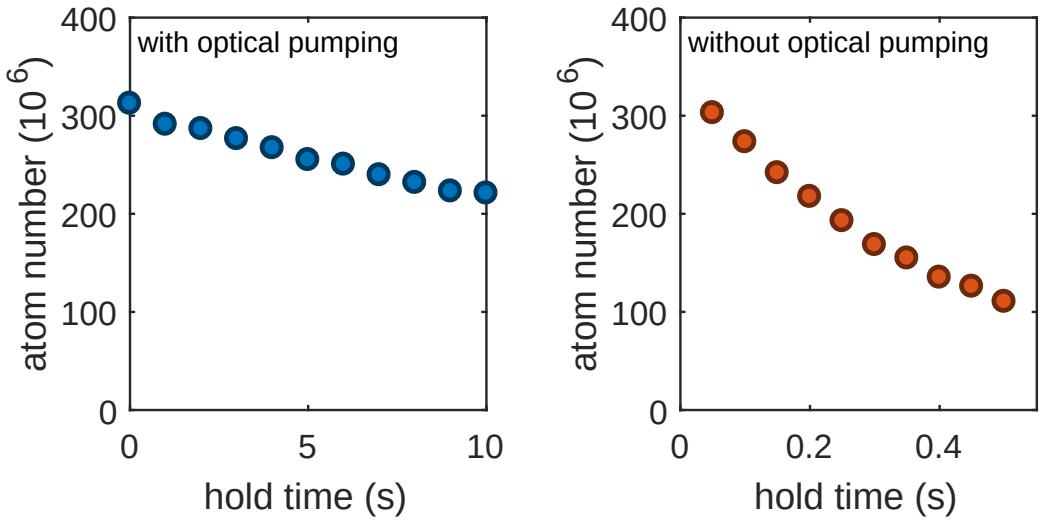

Figure 3.34: Lifetime of magnetically trappable $F = 2$ atoms in the magnetic trap and suppression of spin-exchange collisions from spin polarization. Majorana losses and three-body recombination are not relevant at these temperature and density regimes. **(left)** The atom number in the magnetic trap as a function of hold time for a MOT load time of 1 s and field gradient 77 G/cm. The measured $1/e$ lifetime is greater than 10 s and is sufficiently larger than the total RF evaporation timescale of about 4 s. In general, the actual lifetime depends non-linearly on the atomic number, temperature, and field gradient. **(right)** The atom number in the magnetic trap as a function of hold time without spin polarization. Here for a MOT load time of 5 s and field gradient 77 G/cm. In the absence of optical pumping the atom number is evenly distributed throughout the magnetically trappable states. This allows for spin exchange collisions which is observed through the sharp decrease in lifetime. Initially magnetically untrappable states are ejected on shorter timescales than measured here.

rate is optimized by working at high field gradients. A more detailed discussion of these mechanisms can be found in [14, 15]. Experimentally, our magnetic trap lifetimes are sufficiently larger than the timescale of RF evaporation, and a measurement of the lifetime is shown in Figure 3.34.

3.6.4 Elastic Scattering

For a single particle traveling with velocity v through scatterers with density n and collision cross section σ, the rate of scattering events is given by equation 3.31, and in the

low energy s-wave scattering limit, the cross section σ is set only by the s-wave scattering length a as shown in equation 3.32

$$\gamma = n\sigma v \tag{3.31}$$

$$\sigma = 8\pi a^2 \tag{3.32}$$

We estimate the ensemble elastic scattering rate using the peak density n_0 from equation 3.10 and the RMS velocity $v_{\mathrm{RMS}}(T)$.

$$\gamma \approx n_0(8\pi a^2)\sqrt{\frac{3k_BT}{m}} \tag{3.33}$$

Note that maximizing the density n_0 and the scattering length a is paramount to maximizing the elastic scattering rate. For this reason we utilize the $|2,2\rangle$ state which has an s-wave scattering length of $-27.6a_0$, which is the largest in magnitude among the spin polarized magnetic ground states for low magnetic fields. Increasing the field gradient increases the rate of elastic collisions since $n_0 \propto G$ and $T \propto G^{2/3}$ under adiabatic compression. Experimentally, this is the motivation for working at large field gradients G. However, as discussed in Appendix D, the negative scattering length of the $|2,2\rangle$ state causes the expression for σ in equation 3.32 to break down for sufficiently large energies which is set by the effect range r_e, and results in a zero crossing of the collision cross section at an approximate temperature $T = 5.15$ mK as demonstrated in Figure 3.35. This reduction in the cross section creates an upper bound for which atoms can participate in evaporation and has historically made ^{7}Li

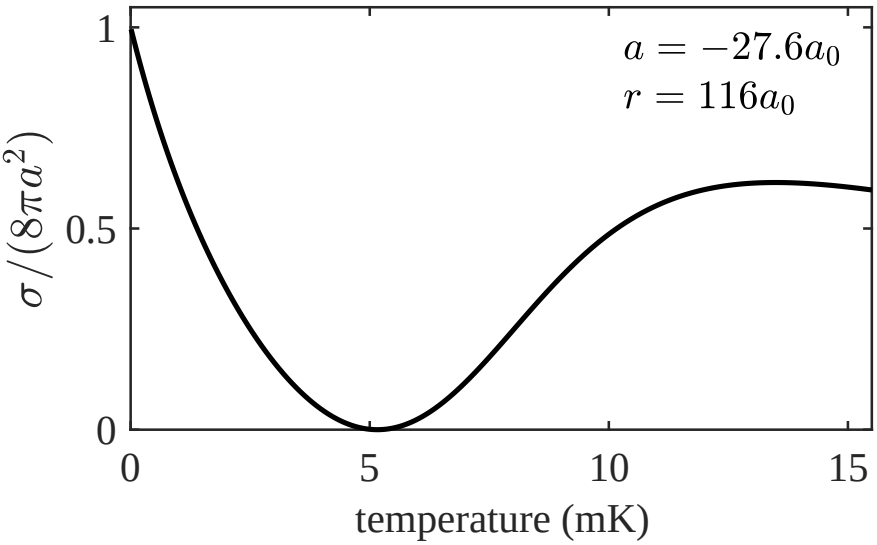

Figure 3.35: Calculated temperature dependent collision cross section σ normalized to the zero energy collision cross section $8\pi a^2$. The negative sign of the scattering length a causes the energy dependent cross section to go to zero at approximately 5.15 mK.

3.6.5 Majorana losses, plug laser, and magnetic field shimming

In the absence of a local magnetic field, the m_F states in the hyperfine manifolds become degenerate, and the atomic cloud can lose its m_F spin polarization. While technically the magnetic field zero only occurs at a single point in space for our quadrupolar field, so called Majorana spin flips to other magnetic states can still proceed. This occurs when the Larmor frequency ν_L is close to the rate of change in the local magnetic field direction. These are defined in equations 3.34 and 3.35 where the rate of change in the local magnetic field has been recast in terms of an impact parameter b and an approach speed v. Classically, the spin flips can be visualized as the inability of the spin of the atom to precess coherently about the local magnetic field. Such spin transitions are undesriable for a myriad of reasons. They reduce the elastic scattering rate via a reduction in the s-wave scattering length a, allow transitions to magnetically untrappable states,

and enable spin exchange collisions.

$$h\nu_L = m_F g_F \mu_B B \tag{3.34}$$

$$\frac{1}{B}\frac{dB}{dt} = \frac{v}{b} \tag{3.35}$$

The critical impact parameter b_0 as a function of approach speed v is defined by equating the two rates where $B = m_F g_F \mu_B G b_0 = P b_0$. Utilization of the equipartition theorem yields at a temperature dependent critical impact parameter in equation 3.37 below which atoms will undergo Majorana losses.

$$b_0 = \sqrt{\frac{hv}{P}} \tag{3.36}$$

$$b_0 = \sqrt{\frac{h}{P}} \left(\frac{k_B T}{m}\right)^{\frac{1}{4}} \tag{3.37}$$

This corresponds to a loss rate $\dot{N}$ by calculating the flux of atoms passing through the cross sectional area given by the critical impact parameter b_0.

$$-\dot{N} := \gamma N \tag{3.38}$$

$$\approx n_0 v \left(\pi b_0^2\right) \tag{3.39}$$

$$= \left(N \frac{P^3 \beta^3}{32\pi}\right) \left(\sqrt{\frac{k_B T}{m}}\right) \left(\pi \frac{h}{P} \sqrt{\frac{k_B T}{m}}\right) \tag{3.40}$$

Which after simplification leads to the loss coefficient γ in equation 3.41 with a characteristic $1/e$ lifetime of $\tau = 1/\gamma$.

$$\gamma = \frac{\hbar}{m}\frac{\pi}{16}\left(\frac{g_F m_F \mu_B G}{k_B T}\right)^2 \tag{3.41}$$

The critical impact parameter b_0 and the Majorana lifetime τ are plotted in Figure

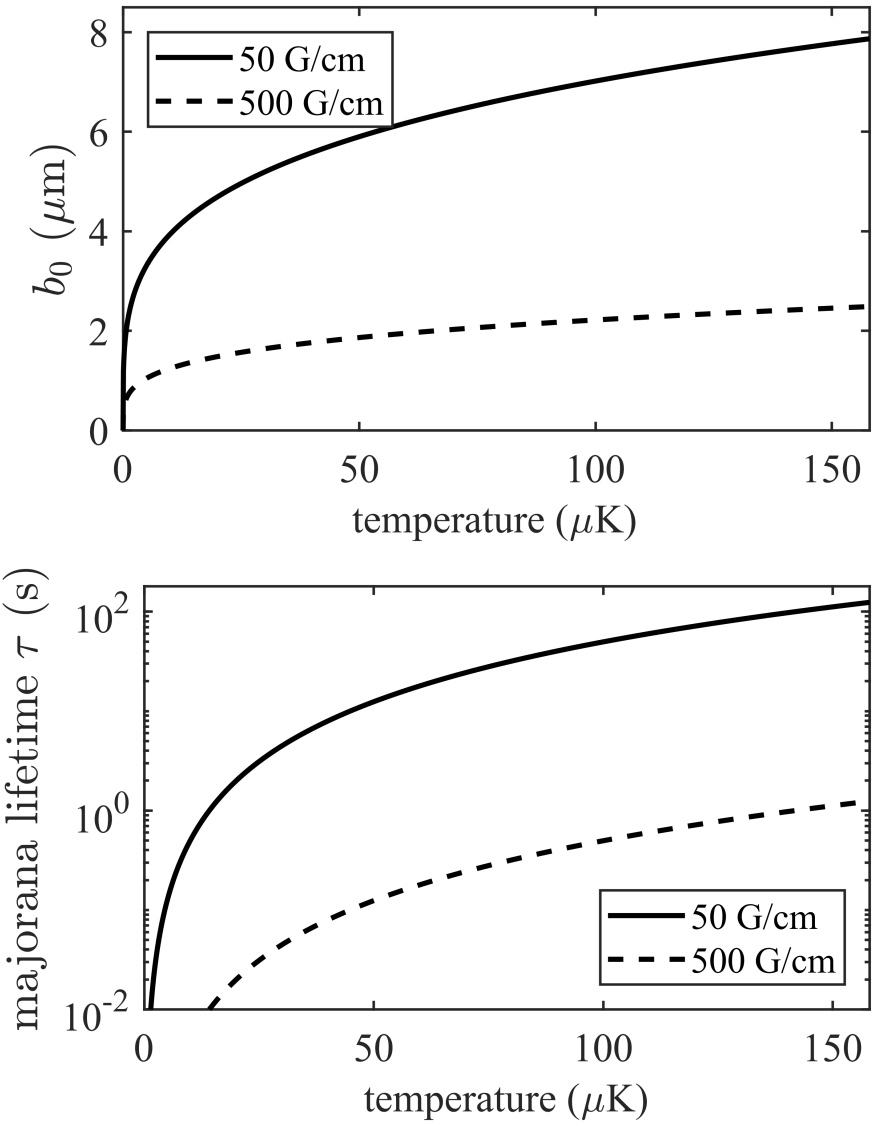

Figure 3.36: The temperature dependence of Majorana spin flip loses from a quadrupolar magnetic trap. Shown here for the approximate range of field gradients we experimentally operate at 50 G/cm (solid) and 500 G/cm (dashed). **(top)** The critical impact parameter b_0 below which Majorana spin flip losses take place as given by equation 3.37. For all relevant experimental parameters the impact parameter remains a few microns in size. **(bottom)** The calculated $1/e$ Majorana lifetime as calculated by equation 3.41 plotted on a semilog axis. The relevant timescale here is order seconds which is how long RF evaporation takes.

3.36 as a function of temperature for realistic experimental parameters. With a characteristic lifetime below 1 s and an RF evaporation of a few seconds, Majorana losses must be prevented to successfully enable evaporation from the quadrupolar magnetic trap.

Experimentally, Majorana losses are prevented through use of a so called plug laser which is a 10 W 532 nm laser beam focused to an approximate $1/e^2$ diameter of 30 μm. This generates a repulsive AC stark shift that prevents atoms from entering the loss region set by b_0. Other solutions to prevent Majorana losses include use of an Ioffe-Prichard magnetic trap which does not have a magnetic field zero at the trap center, or a TOP trap which periodically translates the magnetic field zero to limit the loss rate. The Majorana loss rate is directly probed in Figure 3.38 by measuring the lifetime in the magnetic trap after RF evaporation with and without the plug laser. In the presence of the plug, the lifetime is around 10 s while without the plug, Majorana losses decrease the lifetime to 1.3 s, which is consistent with predictions from equation 3.41. We find that we operate well above the threshold power required to sufficiently prevent Majorana losses as summarized in Figure 3.37. This opens up the possibility of slightly defocusing the plug beam to increase the tolerance in alignment, but the current stability of the plug is acceptable to not dominate our current experimental uncertainty.

An important experimental consideration which dictates the performance of the plug is the presence of residual magnetic fields in the vacuum chamber. Such fields can arise from the Earth's local magnetic field and any nearby magnetic objects. Any background magnetic field B_0 causes the trap center to translate with the quadrupolar field gradient G. If this translation distance is on the scale of the critical impact parameter b_0 or the spatial extent of the plug beam, the plug becomes misaligned and no longer prevents Majorana losses. This translation is a consequence of the fact that "a line plus another

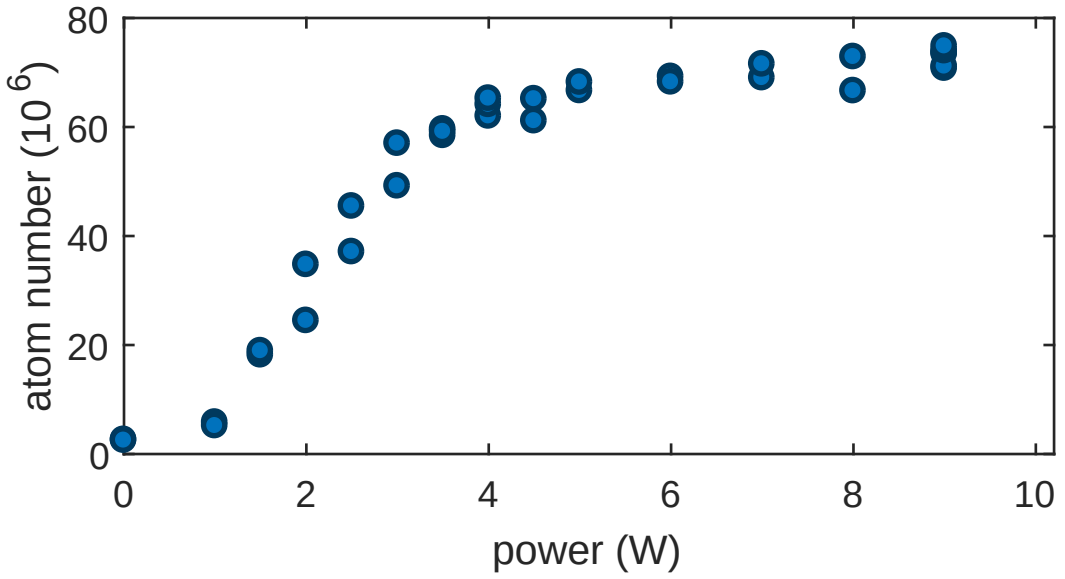

Figure 3.37: Efficacy of the plug beam to prevent Majorana losses from the RF evaporated magnetic trap. The measured atom number after RF evaporation is plotted as a function of the power in the 532 nm plug laser. Above optical powers of approximately 5 W the benefits of the plug are reduced.

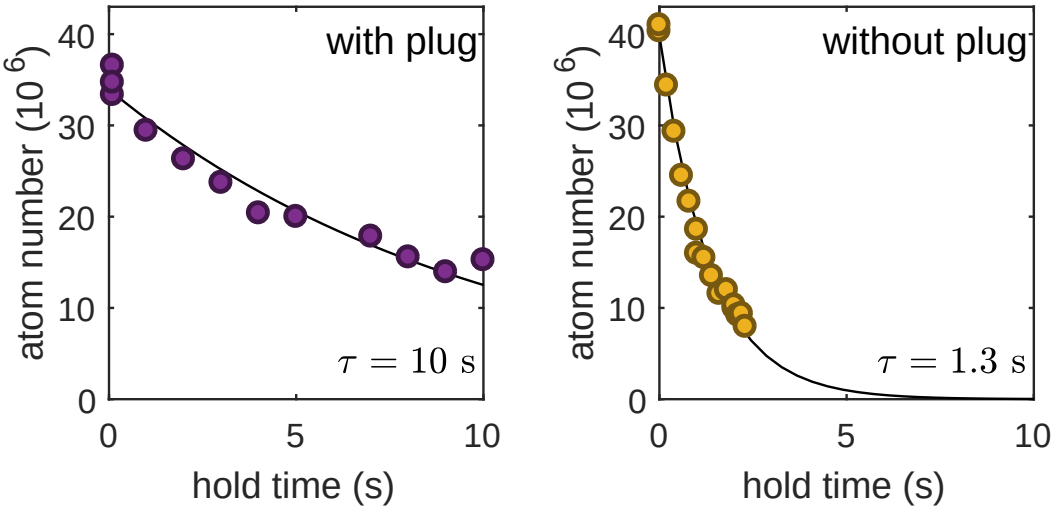

Figure 3.38: Lifetime in the magnetic trap after RF evaporation with and without the plug. The vertical field gradient is 42 G/cm with an initial temperature of approximately 8 μK. Under normal operating procedures the magnetic trap is immediately loaded into the crossed optical dipole trap after RF evaporation. **(left)** In the presence of the plug, the $1/e$ lifetime of the magnetic trap after RF evaporation is about 10 s. **(right)** The atom number in the magnetic trap after RF evaporation where the plug beam power is turned off in around 200 ms at the beginning of the hold allowing Majorana spin flips to occur. The fitted $1/e$ lifetime is 1.3 s which is consistent with predictions from equation 3.41.

line is a line with a different x-intercept" as outlined in equation 3.43.

$$B(x) = Gx + B_0 \tag{3.42}$$

$$x(B = 0) = -B_0/G \tag{3.43}$$

To eliminate this motion, we run current through our shim coils to offset any background magnetic field. The shim currents are calibrated directly imaging the *in situ* atomic cloud density, fitting the cloud center position, and minimizing the motion with respect to the applied gradient. Example theory and experimental data are shown in Figure 3.39 and indicate that we cancel the residual field B_0 to less than 10 mG. We find that any time we add any moderately sized metallic objects near the UHV chamber we need to redo the measurement and calibration of the shim currents, but once the shim currents are set, we typically only need to reshim once every few months.

The validity of equation 3.43 assumes that the physical center of the magnetic trap not change. However, the thermal dissipation of running up to 500 A through the primary magnets historically made the reliability of the magnetic trap center challenging to maintain. We found that the reliability of the plug alignment was greatly improved through the implementation of robust electrical connections and parallelization of water cooling through each addressable magnet layer [4].

The other requirement for a well aligned plug is the green beam itself. We minimize pointing noise by implementing a relatively simple and short beam path [6], and also find it helpful useful to put "roofs" over the beam path to reduce wind current induced pointing noise. We utilize a picomotor (Newport 8821) with 0.7 μrad resolution to align the plug beam. At an approximate distance of 10" from the location of the atoms, this corresponds to an approximate alignment sensitivity of 2 μm/10 steps at the location of the atoms, and we empirically find that the alignment is sensitive to within a 60×60

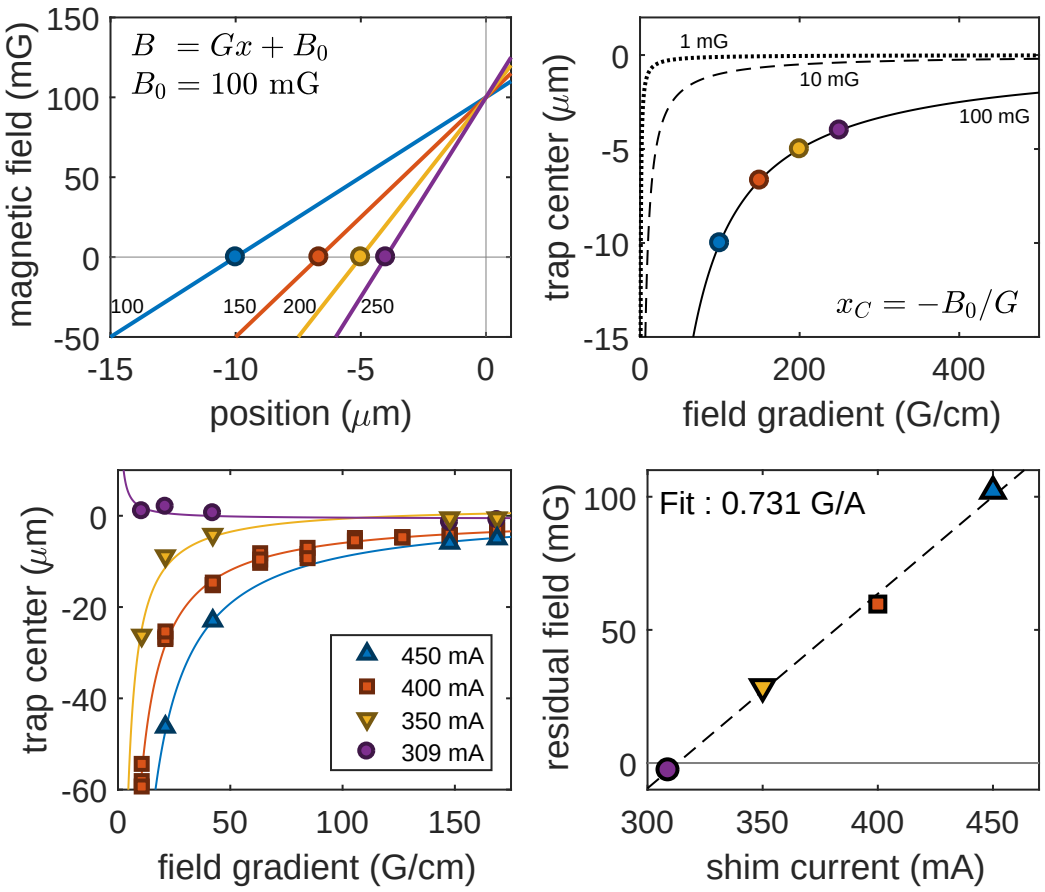

Figure 3.39: The importance of the shim currents in the magnetic trap to minimize the cloud motion. **(top left)** Any residual magnetic field B_0 will cause the magnetic trap center to translate as the field gradient is altered. Shown here is the magnetic field profile for field gradients between 100 G/cm to 250 G/cm with a residual constant field $B_0 = 100$ mG. **(top right)** The calculated effective trap center motion versus field gradients for experimentally relevant parameters. Minimization of the motion below a few microns requires the elimination of the residual field to around 10 mG or less. **(bottom left)** Experimentally measured magnetic trap center as a function of field gradient for varying shim currents. Measured via the atomic cloud center in the magnetic trap after RF evaporation and a final ramp of the field gradient. The change in sign of the motion for 309 mA is a consequence of the sign change in the residual field B_0. **(bottom right)** The fitted residual field B_0 as a function of the applied shim current. The linear response yields a calibration of the shim field to be 0.731 G/A.

step size area.

The initial alignment and focusing of the plug beam was performed by directly imaging the atomic cloud density along the plug beam axis and focusing it at the image plane; this is also how we estimate the plug size. However, at the time of measurement, we neglected to account for the chromaticity of our imaging lenses, and so the exact size is slightly ambiguous. Furthermore, it is unclear to the author whether the beam parameters are different at low power, where the beam was imaged, compared to the high power operating state. Experimentally however, all that matters is that the plug indeed helps the magnetic trap, and we empirically optimize the focus [6].

After this initial alignment, we image the direct effect of the plug on the atomic cloud density. The precision required of aligning the plug with size a few tens of microns to the magnetic trap center makes it unlikely to observe any benefit of the plug after RF evaporation (there will just be no signal to optimize). Instead, we image the depression in local number density caused by the plug partially through evaporation as outlined in Figure 3.40. This requires some finesse as the plug must be aligned enough to hit the remaining atomic cloud, but misaligned enough to hit a region of space with low enough number density to have a resolvable effect. Tracking the depression as a function of picomotor step indicates an approximate alignment sensitivity of 2.4 μm/10 step. This process is then iterated by evaporating further to walk the plug beam closer to the magnetic trap center until a positive effect on the total atom number is observed which is shown in Figure 3.41. Once this occurs, the final plug beam position is empirically optimized by maximizing the total atom number after the RF evaporation. We find that plug beam needs to realigned as often as twice a day to once every few weeks. We also find that large instability in the BEC atom number can commonly be attributed to a slightly misaligned plug which results in an increased sensitivity to fluctuations in the alignment.

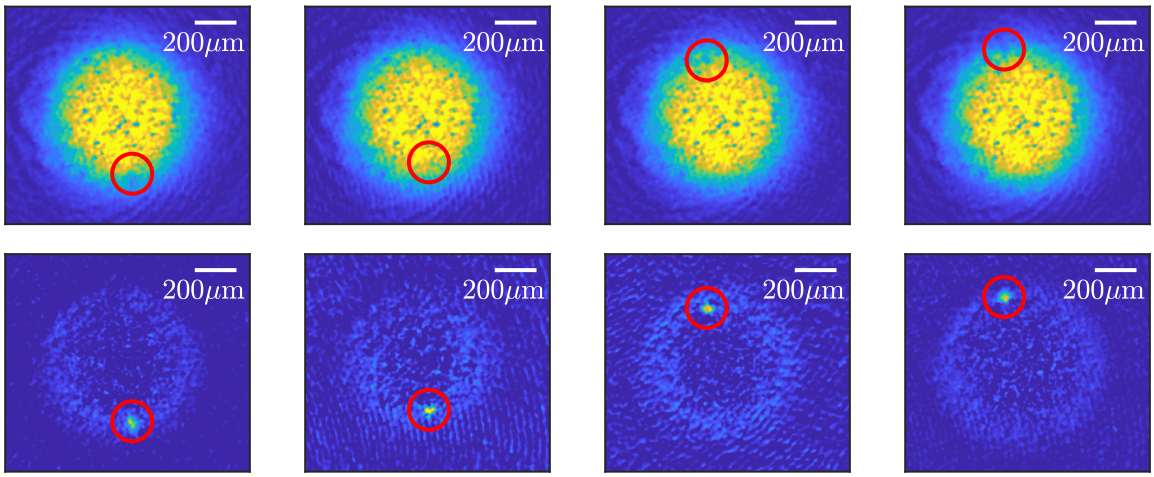

Figure 3.40: Coarse alignment of the plug beam as directly observed via the *in situ* atomic cloud optical density partially through RF evaporation as the plug beam is translated across the atomic cloud. **(top)** A decrease in the local number density can be seen as the plug beam traverses across the atomic cloud. The human eye can more easily see this during an animation. **(bottom)** The difference in the optical density between the image in the top row and the average image as the plug is translated. The effect of the plug is seen as a clear depression of the local number density. Tracking the depression feature as a function of picomotor step size yields an approximate sensitivity of 2.4 μm/10 step

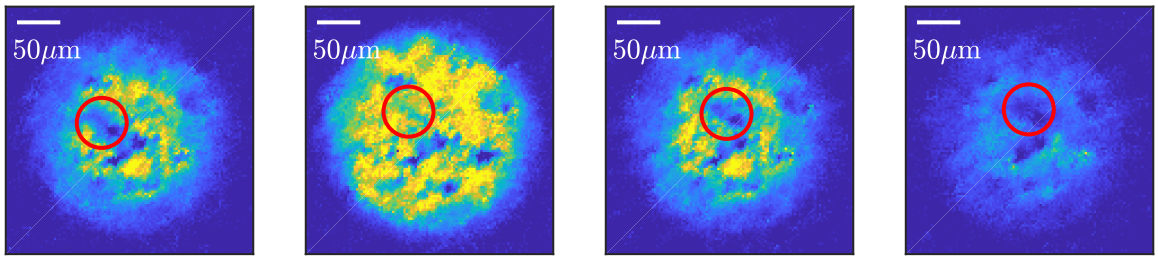

Figure 3.41: Finer alignment of the plug beam as directly observed via the *in situ* atomic cloud density further into RF evaporation than Figure 3.40. The depression in atomic density is more easily seen due to the lower overall atom number and spatial extent along the imaging axis. As the plug laser is brought closer to the magnetic trap center Majorana losses begin to be prevented as seen by an increase in the total atom number as evidence in the picture by a larger optical density.

3.7 Crossed Optical Dipole Trap

After RF evaporation in the magnetic trap, the next trapping and cooling stage of the experimental sequence is optical evaporation out of a **crossed optical dipole trap** using a large scattering length induced by a Feshbach resonance. The crossed optical dipole trap is the trap in which Bose condensation occurs, and is governed by the same physics as the optical lattice potentials. The trap is formed at the region of maximum laser intensity located at the intersection of two focused laser beams (ie. "crossed") as shown in Figure 3.42. The fundamental trapping mechanism relies on an induced dipole moment caused from the electric field of a far off resonant laser beam. This section shall focus primarily on the trapping mechanism of the optical dipole trap and transfer into it from the magnetic trap.

This beam arrangement generates a spatially dependent AC stark shift which provides a trapping potential proportional to the local laser intensity as shown below.

$$U_{\text{dip}} = \frac{3\pi c^2}{2\omega_0^3}\frac{\Gamma}{\Delta}I(\mathbf{r}) \tag{3.44}$$

Here, $\omega_0 = 2\pi c/\lambda$, c is the speed of light, Γ is the linewidth, Δ is the detuning, and I is the local laser intensity. This can generally be expressed in terms of the atomic polarizability α, where $U_{\text{dip}} = -1/2\langle\vec{p}_{\text{dip}}\cdot\vec{E}\rangle$ and $\vec{p}_{\text{dip}} = \alpha\vec{E}$. While extensive theoretical and experimental literature exists on the trapping mechanism and applications of this dipole potential [16], we shall instead discuss a few key considerations and calculations specifically relevant to our experiment. Inspection of equation 3.44 shows that maximizing the intensity I or minimizing the detuning Δ generates a stronger potential energy, and changing the sign of the detuning makes the effect repulsive ($\Delta > 0$) or attractive ($\Delta < 0$). While selecting a laser with small detuning from an atomic transition seems

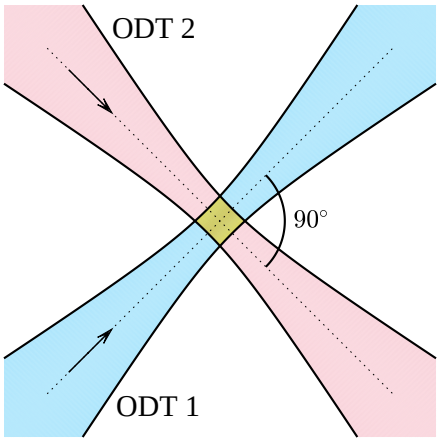

Figure 3.42: Visualization of the crossed optical dipole trap. Two focused laser beams (pink and blue) intersect to form a trap at their intersection (yellow). The potential energy is proportional to the local electric field intensity.

initially attractive, doing so comes at the cost of an increased scattering rate

$$\Gamma_{\text{sc}} = \frac{3\pi c^2}{2\hbar\omega_0^3}\left(\frac{\Gamma}{\Delta}\right)^2 I(\mathbf{r}). \tag{3.45}$$

For these reasons, we utilize the commonly commercially available high power single mode 1064 nm fiber amplifiers for our trapping beams. To realize a trap of sufficient depth and volume required to both capture a large number of atoms from the magnetic trap and obtain the high densities required to evaporate to quantum degeneracy, we focus these beams to a few hundred microns in size. The intensity pattern of a single focused laser beam is

$$I(r,z) = I_0\left(\frac{w_0}{w(z)}\right)^2 \exp\left(-\frac{2r^2}{w(z)^2}\right) \tag{3.46}$$

$$w(z) = w_0\sqrt{1+\left(\frac{z}{z_R}\right)^2} \tag{3.47}$$

$$z_R = \frac{\pi w_0^2}{\lambda}. \tag{3.48}$$

The parameter w_0 is the waist and corresponds to the radius at which the intensity drops to $1/e^2$ of its peak value and 95% of the total beam power is contained in the disc $r < w_0$. The parameter z_R is the Rayleigh range which corresponds to the axial distance at which the peak intensity drops by a factor of two and roughly correlates with the distance over which a beam is collimated. Given the linearity between I and U_{dip} in equation 3.44, we can think of the intensity pattern as being a direct proxy for the potential energy. It also useful to approximate this as an anisotropic harmonic potential $\frac{1}{2}m\omega^2x^2$ with trap frequencies given below.

$$f_r = \frac{1}{2\pi}\sqrt{\frac{4U_0}{mw_0^2}} \tag{3.49}$$

$$f_z = \frac{1}{2\pi}\sqrt{\frac{2U_0}{mz_R^2}} \tag{3.50}$$

where U_0 is the peak trap depth located at the focus of the beam at $r = z = 0$. Since the waist is much smaller than the Rayleigh range, this creates a rather large anistropy which necessitates the need for a crossed trap in order to provide tight enough trapping in all spatial dimensions.

Experimentally, our two ODT beams have a $w_0 = 80$ μm, $\lambda = 1064$ nm, $z_R = 18.9$ mm, and a maximum total power of about 6 W each. This corresponds to a single beam trap depth of $U_0 = 29.6$ μK (24.7 E_R) and trap frequencies $f_r = 746$ Hz and $f_z = 2.2$ Hz. These calculations are shown over experimentally realizable optical powers in Figure 3.43. The angle between the two beams is approximately 90° which results in the frequencies adding in quadrature. Defining the intersection of the beams to be in the $x - y$ plane, this results in trapping frequencies $f_x = f_y \approx 746$ Hz and $f_z \approx \sqrt{2} \times 746$ Hz $= 1055$ Hz. The light is generated from a 50 W fiber amplifier from Nufern (NUA-1064-PD-0050-D0) and a series of accouto-optic modulators [4, 6, 7]. From the

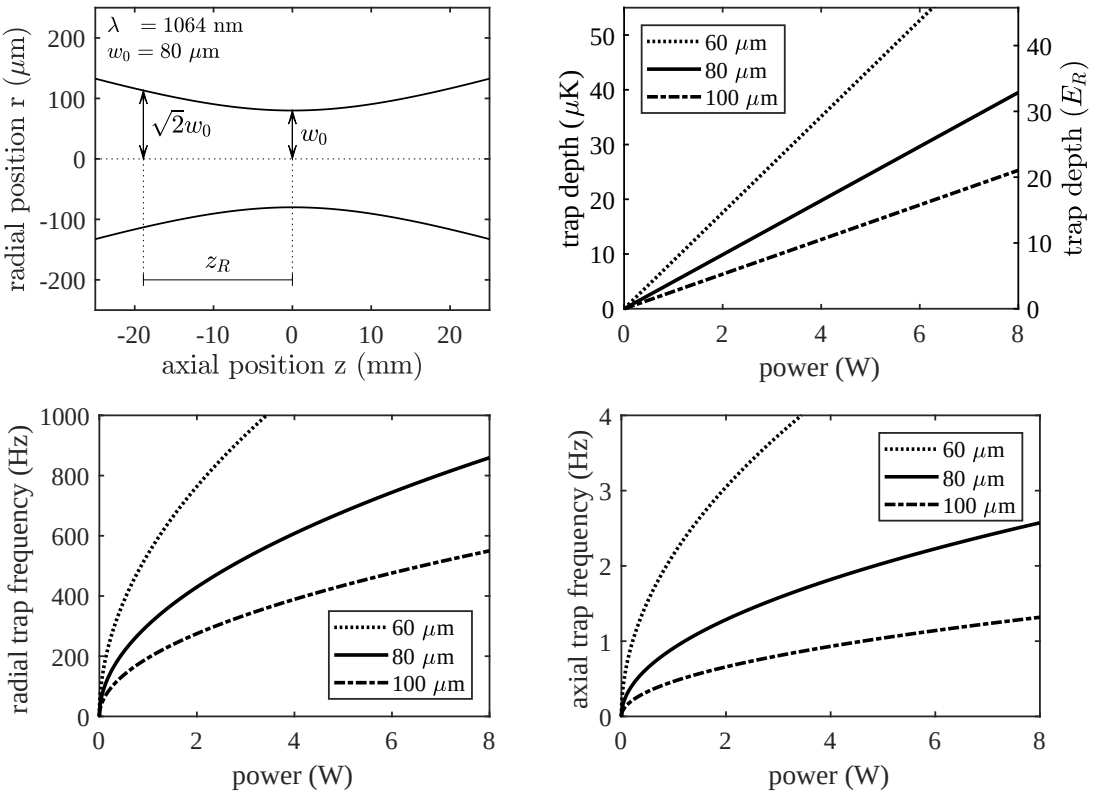

Figure 3.43: Characterizing the optical dipole trap. All atomic parameters are assumed to be for Lithium-7 and $\lambda = 1064$ nm. **(top left)** Plotting $w(z)$ as a function along the axial position. At an axial distance equal to a Rayleigh range, the beam radius has increased by a factor of $\sqrt{2}$. **(top right)** The peak trap depth U_0 as a function of optical power for a variety of beam waists. **(bottom left)** The radial trap frequency f_r as a function of optical power for a variety of beam waists. **(bottom right)** The axial trap frequncy f_z as a function of optical power for a variety of beam waists.

magnetic trap, we trap approximately 10×10^6 atoms at a temperature of 2 μK as shown in Figure 3.44.

Coarse alignment of the ODT beams is performed by imaging the *in situ* magnetic trap profile along the propagation axis of the respective ODT and aligning the beam to the position of the magnetic trap. Coarse focusing is done by minimizing the beam size at the image plane using a translation stage on the final focusing lens with $f = 300$ mm. As of writing of this thesis, the focusing procedure is inaccurate due to the chromaticity

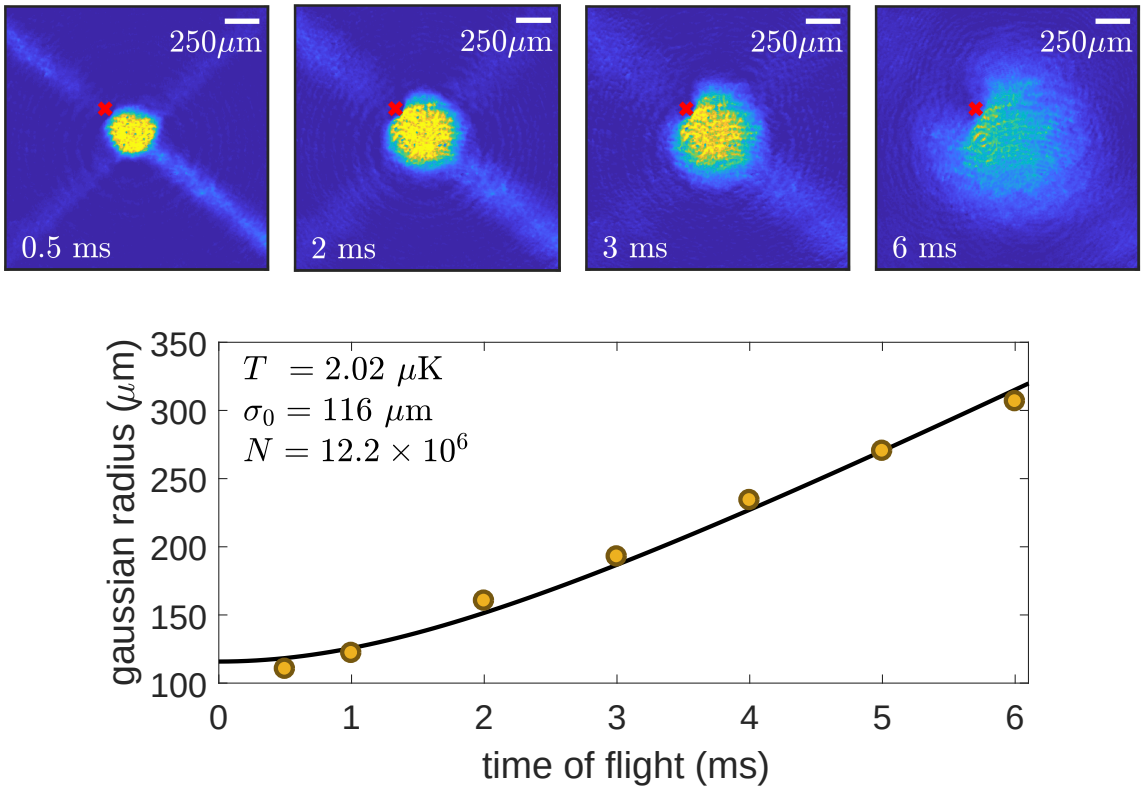

Figure 3.44: Time of flight out of the crossed optical dipole trap. **(top)** Optical densities of the images in time of flight. The effect of the plug can be observed in time of flight as decrease in local atom number density. **(bottom)** Measurement of the increase of the cloud size as function of time of flight yields a temperature of 2.02 μK. The atom number is around 12.2×10^6 with a minimal gaussian radius of 116 μm.

of the imaging lenses and should be modified with achromatic lenses.

Fine alignment is performed empirically by optimizing the number of atoms captured in the crossed optical dipole trap, and a graphical summary of the textual description here is outlined in Figure 3.45. After the coarse alignment, enough atoms are trapped to use atom number as a good optimization metric. While intersecting the beams at the true magnetic field center would load the least energetic atoms, this is technically challenging due to the presence of the plug beam. We currently turn down the optical power in the plug with a waveplate rotator which results in an extinction ratio of about 98%. However, this rotation is slow compared to the transfer time into the optical dipole trap, and we also observe that the remaining plug power perturbs the trap [6]. To circumvent this problem, we intersect the ODT beams away from the magnetic field center at an approximate distance equal to the waist of the beams.

Once one of the ODT beams is roughly set by the criterion above, the other is aligned using a picomotor mounted mirror (Newport 8821). The horizontal degree of freedom is set by choosing an appropriate location away from the plug beam, while the vertical degree of freedom (transverse to the vertical imaging axis) is set by directly optimizing the atom number after the transfer.

The transfer consists of turning down the field gradient of the magnetic trap to zero over 140 ms while simultaneously turning up the ODT power to their maximum values over 100 ms. We also find that leaving a residual bias field small enough to not affect the plug alignment during RF evaporation, but large enough to induce translation in the direction of the XODT to be beneficial as seen in Figures 3.45 and 3.46. The optical power in the ODT beams is set using a PID with a photodiode which samples the total optical power [4, 6].

[6] We haven't tried loading on center since increasing our ODT beam sizes. Perhaps we should try loading at the center again.

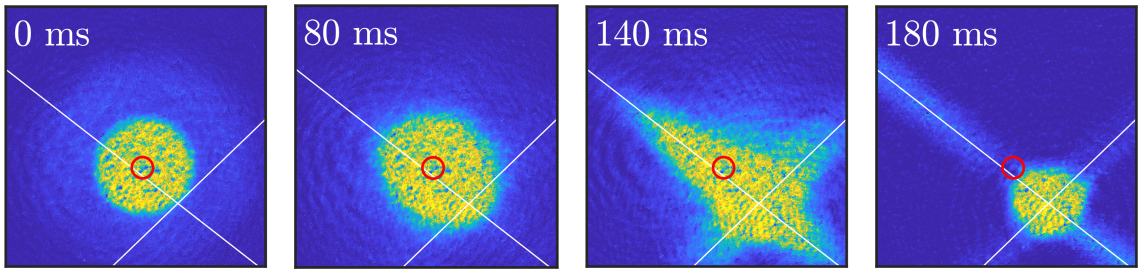

Figure 3.45: Transfer into the crossed optical dipole trap from the magnetic trap. As the field gradient decreases, the atomic cloud translates into the optical dipole trap as a consequence of the residual bias magnetic field. The laser beams of the optical dipole trap (white) intersect away from the magnetic trap center (red) to avoid the plug beam. The field gradient is ramped down to zero from 42 G/cm in 140 ms and the ODT beams are ramped up in 100 ms.

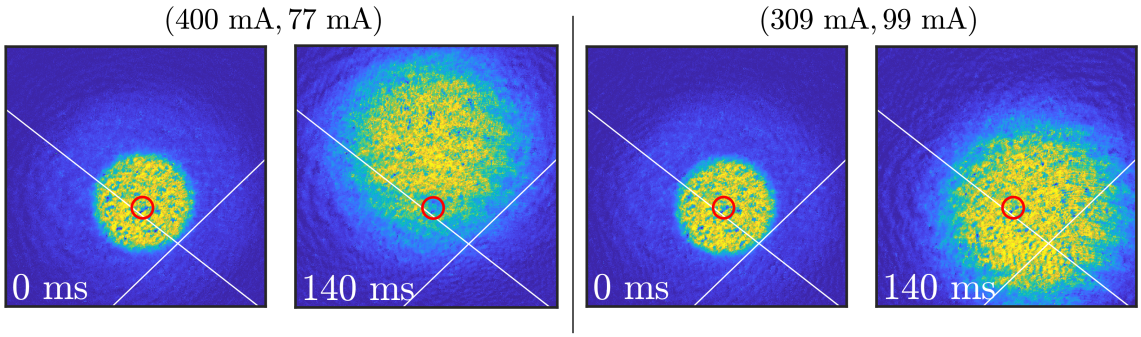

Figure 3.46: Benefit of a small residual magnetic bias field during the transfer from the magnetic trap into the crossed optical dipole trap. **(left)** At shim current values of 400 mA and 77 mA, the residual bias field causes the atomic cloud to translate away from the location of the crossed optical dipole trap (white) as the field gradient decreases. **(right)** At shim current values of 309 mA and 99 mA, the residual bias field causes the motion to be in the direction of the crossed optical dipole trap which results in more atoms trapped.

3.8 Adiabatic State Transfer

After the atoms are loaded into the optical dipole trap, the final cooling stage consists of optical evaporation in the crossed optical dipole trap with the Feshbach resonance. As discussed in the next section, the Feshbach resonance we utilize exists for the $|1,1\rangle$ state while the atoms are currently polarized in the $|2,2\rangle$ state after loading into the optical dipole trap. To achieve the desired spin polarization, we adiabatically transfer the atomic internal state from the $|2,2\rangle$ state to the $|1,1\rangle$ state via application of a RF frequency sweep across the transition energy. The RF magnetic field is polarized perpendicularly to the quantiziation axis defined by a small magnetic bias field.

As diagrammed in Figure 3.47, the small bias field splits the ground state hyperfine manifolds to resolve the different m_F states. This bias field is crucial as it energetically resolves the desired magnetic dipole transition. A transverse oscillating magnetic field is applied which couples the $|2,2\rangle$ and $|1,1\rangle$ states. The resonant coupling frequency ν_0 is given by the following

$$h\nu_0 = E_{|2,2\rangle} - E_{|1,1\rangle} \tag{3.51}$$

$$\nu_0 \approx 803.5 \text{ MHz} + (2.1 \text{ MHz/G})\, B_0 \tag{3.52}$$

where B_0 is the bias field. As the applied frequency ν is smoothly varied across the resonance at ν_0, the atomic internal state transfers from the $|2,2\rangle$ to the $|1,1\rangle$ state. Adiabatic variation of the coupling frequency continuously transforms the instantaneous Floquet eigenstate from the $|2,2\rangle$ into the $|1,1\rangle$ state. Far away from resonance, the Floquet eigenstates are the bare uncoupled states, while at resonance the eigenstates are superpositions of the two bare states. Experimentally, we run approximately 2.7 A through the slower shims to establish the bias field B_0 of approximately

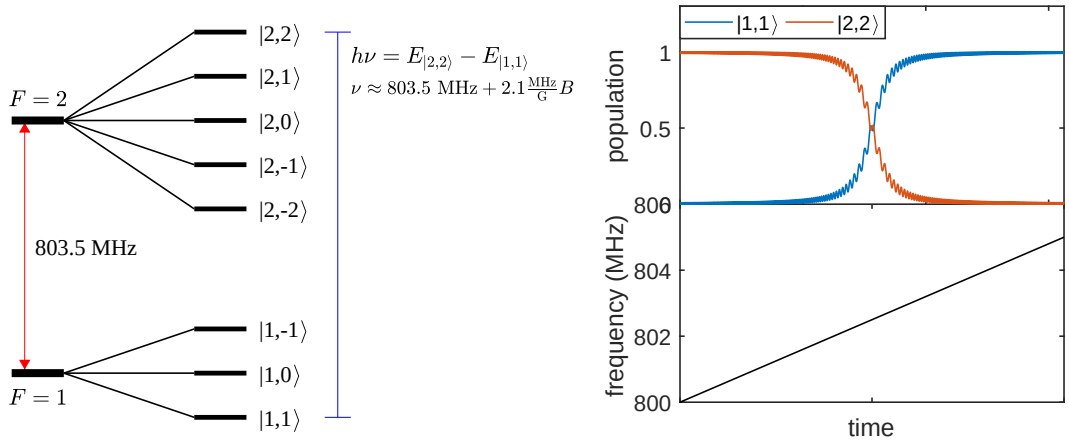

Figure 3.47: Schematic of adiabatic spin transfer. **(left)** A small magnetic field splits the states while RF radiation magnetic couples the desired states. **(right)** As the frequency of the applied RF is varied the spin population is adiabatically transfered.

$B_0 \approx (0.72\ \text{G/A}) \cdot (2.7\ \text{A}) = 2\ \text{G}$. This field places the resonant transition frequency ν_0 at roughly 807.7 MHz. The slower axis shim is chosen since we utilize the same antenna and VCO source during RF evaporation whose magnetic polarization is in the vertical direction; this choice realizes the desired perpendicular orientation of the bias and coupling field. The coupling frequency ν is linearly swept from 809.56 MHz to 807.45 MHz in 65 ms. The state transfer can be directly observed by imaging the atomic cloud in the crossed optical dipole trap on the $F = 2$ cycler transition without a repumper and measuring a characteristic drop in apparent atom number. This reduction in the measured optical density is shown in Figure 3.48 and shows that the resonance is traversed at roughly 36.5 ms into the sweep sequence which corresponds to an estimated coupling frequency at $\nu_0 \approx 809.56\ \text{MHz} - \frac{809.56\ \text{MHz} - 807.45\ \text{MHz}}{65\ \text{ms}} 36.5\ \text{ms} = 808.4\ \text{MHz}$. The discrepancy between the estimated resonance via the shim current and the measured resonance given by the data in Figure 3.48 represents a slight miscalibration. Experimentally, it is only required that the coupling frequency ν sweep *over* the resonant frequency ν_0 and that it does so reliably on a day to day basis. The measured fidelity is approximately 99% and is

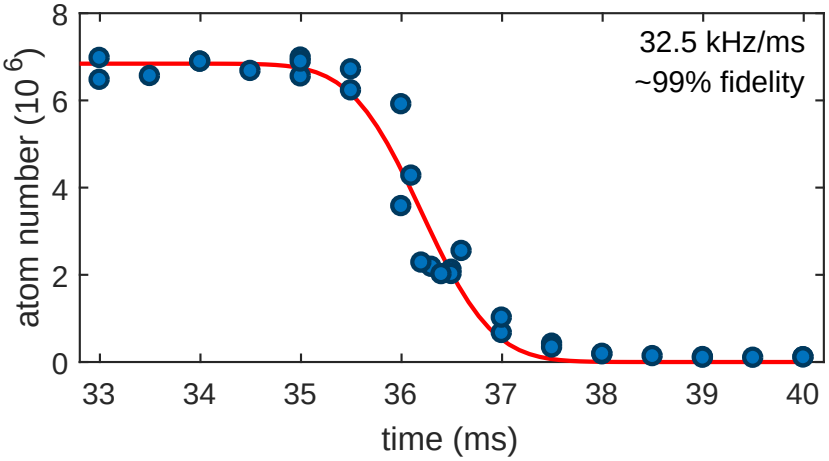

Figure 3.48: Measurement of adiabatic state transfer. As the radio freuqency is sweeped across the resonance, the number of atoms in the $F = 2$ manifold is reduced. By imaging without a repumper, the decrease in atom number only probes the remaining atoms in the $F = 2$ manifold.

limited by the dynamic range of our imaging system. While it is possible that the small number of remaining atoms in the $|2, 2\rangle$ state may be detrimental to optical evaporation because of undesired interactions, we do not empirically find this to be the case. The remaining $|2, 2\rangle$ atoms could be ejected from the trap by pulsing a beam resonant with the $F = 2$ cycler transition, but we do not do so as of the writing of this thesis.

As alluded previously, the bias field is important to maintain the spin polarization of the atomic cloud. Therefore, we ramp on the bias field as the magnetic field of the magnetic trap is ramped down during the transfer into the crossed optical dipole trap. Furthermore, since the state transfer does not require the usage of the primary magnets, we also use this period of time to switch the configuration of the coils from anti-Helmholtz to Helmholtz to prepare the Feshbach field. After the Feshbach field is ramped on, the small bias field is turned off.

Theoretically, the state transfer is well modeled via a simple two level coupled spin model. At any given time, the state vector is well described by a two component basis of the excited and ground state with time dependent amplitudes $|\psi\rangle = c_1(t)|g\rangle + c_2(t)|g\rangle$.

The problem then simplifies to two parameter space of the rabi frequency Ω and detuning δ. Visualization of the time evolution is easily done via the Bloch sphere and the density matrix formalism

$$u = \tilde{\rho}_{12} + \tilde{\rho}_{21} \tag{3.53}$$

$$v = -i\left(\tilde{\rho}_{12} - \tilde{\rho}_{21}\right) \tag{3.54}$$

$$w = \rho_{11} - \rho_{22} \tag{3.55}$$

where the elements of the density matrix ρ_{ij} relate to the amplitudes c_i via $\rho_{ij} = c_i^* c_j$ and $\tilde{\rho}_{ij} = \rho_{ij}\exp(-i\delta t)$. In this case, the time evolution reduces to the following set of equations:

$$\dot{u} = \delta v \tag{3.56}$$

$$\dot{v} = -\delta u + \Omega w \tag{3.57}$$

$$\dot{w} = -\Omega v \tag{3.58}$$

The adiabatic sweep can then modeled by a time dependent detuning $\delta(t)$ that traverses over the resonance condition at $\delta = 0$. This can also be handily visualized on the Bloch sphere by defining the the Bloch vector $\mathbf{R} = (u, v, w)$.

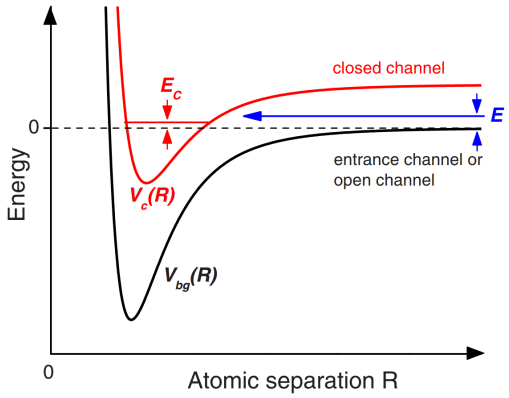

Figure 3.49: Basic model for a Fesbach resonance [18]. The scattering state (blue) is brought into resonance with a bound state in the so called closed channel (red). For low energy collisions, such as the ones in our experiment, the scattering energy $E \to 0$. The resonance condition can occur via a magnetic field if the magnetic moments of the two channels are different.

3.9 Feshbach Resonance

For optical evaporation out of the crossed optical dipole trap to proceed efficiently, a high positive scattering length is desired to promote thermalization. To achieve this, we utilize ^{7}Li's magnetic Feshbach resonance for the $|1,1\rangle$ state, which causes the scattering length to vary with applied magnetic field [17]. The fundamental mechanism is that when a scattering state is brought into resonance with a molecular bound state via an applied magnetic field, variations in the scattering phase shift causes the scattering length to diverge. The two states can be brought into resonance if they have different magnetic moments and therefore different energy dependences on magnetic field. While [18] provides an excellent discussion of the subject, this thesis shall restrict this treatment to briefly outline the key aspects needed to understand how we implement it in our experiments.

Assuming a magnetic Fesbach resonance, the scattering length assumes the form of equation 3.59 near the resonant magnetic field. As discussed in previously, the elastic scattering rate which governs the thermalization time scale is proportional to the square

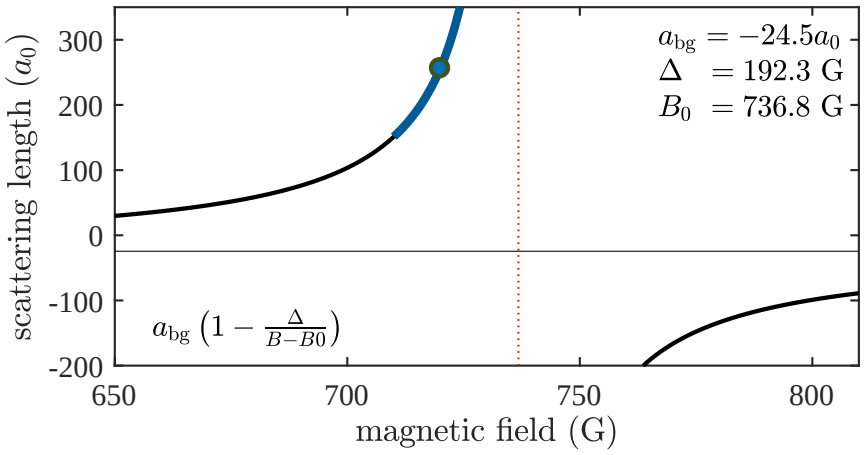

Figure 3.50: Lithium-7 Feshbach resonance. The solid black line represents the theoretically predicted ideal curve given the parameters listed. The range of magnetic fields at which we operate are indicated in blue.

of the scattering length. Therefore it is desirable to operate close to resonance to achieve a fast thermalization timescale. However, experimental uncertainty in the magnetic field make it advantageous to operate somewhat off resonance where the scattering length can be more reliably set.

$$a(B) = a_{\rm bg}\left(1 - \frac{\Delta}{B - B_0}\right) \tag{3.59}$$

For the experimentally measured Feshbach resonance of the $|1,1\rangle$ state, the parameters are $\Delta = 192.3$ G, $a_{\rm BG} = -24.5a_0$, and $B = 736.8$ G [17] which is shown in Figure 3.50. In comparison to other Feshbach resonances, this resonance is rather broad in magnetic field which makes the required experimental specificity of the magnetic field less stringent. However, this also means we have not taken care to precisely characterize the magnetic field strength as a function of current, and we only require it be reproducible. Experimentally, the operating current of our magnets is empirically set by optimizing the BEC reliability, but we estimate our operating field to be around 710 G to 720 G as indicated in Figure 3.50.

During the state transfer we switch the polarity of the primary magnets from anti-

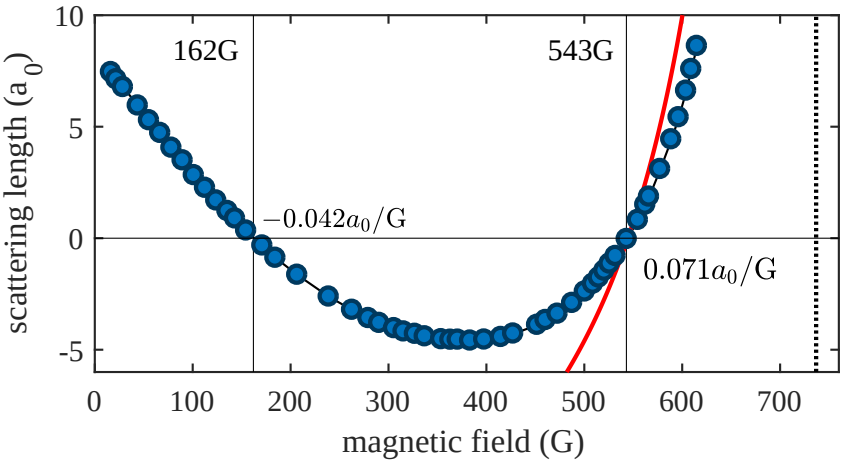

Figure 3.51: Zero scattering length crossing of the Feshbach resonance. The scattering length deviates from the simple model (red) to the experimentally measured values (blue points) [19]. There are two magnetic field values which result in $a = 0$ which correspond to 162 G and 543 G. Linear fits of the scattering length with respect to field at the zero scattering length condition are shown.

Helmholtz to Helmholtz using our high current H-bridge. After which, the magnets are ramped up to the evaporating magnetic field value in about 50 ms. We find it important to tailor the ramp up sequence to not bring the magnetic field too close to resonance.

In addition to this resonant behavior, this particular magnetic state of ^{7}Li exhibits a zero in the scattering length at approximately 543.6 G and 162 G[17]. Such a feature is advantageous as it lets us tune experiments from a highly interacting regime to a non-interacting regime. While such behavior is predicted by equation 3.59 for a negative background scattering length, it does not accurately capture the dependence across the entire range, and a comparison of experimentally measured values and the theory are shown in Figure 3.51.

3.10 Optical Evaporation and Bose Condensation

With sufficient number of atoms inside the crossed optical dipole trap with a high scattering length set by a Feshbach resonance, the final cooling stage is **optical evaporation**. As the trap depth is slowly decreased, the most energetic atoms escape the trap, and the temperature of the remaining sample decreases as diagrammed in Figure 3.52. The trap depth is decreased by lowering the optical power in the trapping beams in an exponential ramp over a few seconds. This cooling procedure brings the atoms to quantum degeneracy and forms a Bose-Einstein condensate. The resultant Heisenberg uncertainity limited object is the starting point of all experiments documented in this thesis.

The transition temperature for a harmonic trap in three dimensions is given by equation 3.60 and the fraction of atoms in the condensate by equation 3.61 [2]. Here, $\bar{f}$ represents the geometric mean of the harmonic trapping frequencies. These functions are plotted for experimentally relevant parameters in Figure 3.53

$$k_{\mathrm{B}} T_{\mathrm{C}} \approx 0.94 h \bar{f} N^{1/3} \tag{3.60}$$

$$\frac{N_{\mathrm{C}}}{N} = 1 - \left(\frac{T}{T_{\mathrm{C}}} \right)^{1/3} \tag{3.61}$$

Experimentally, the optical power is lowered from the initial 6 W power to a final value of 1.5 W in each beam over 4.5 s with an exponential time constant of 2.25 s. This corresponds to a final trap frequency $\bar{f}$ of 419 Hz and a transition temperature of 877 nK at 10^5 atoms. The day to day final optical power is empirically set by finding the value which optimizes the stability and atom number of the resultant condensate. The optical power is controlled via a PID circuit which samples the optical power in each ODT beam [4]. The author notes that the PID's regularly under perform and present

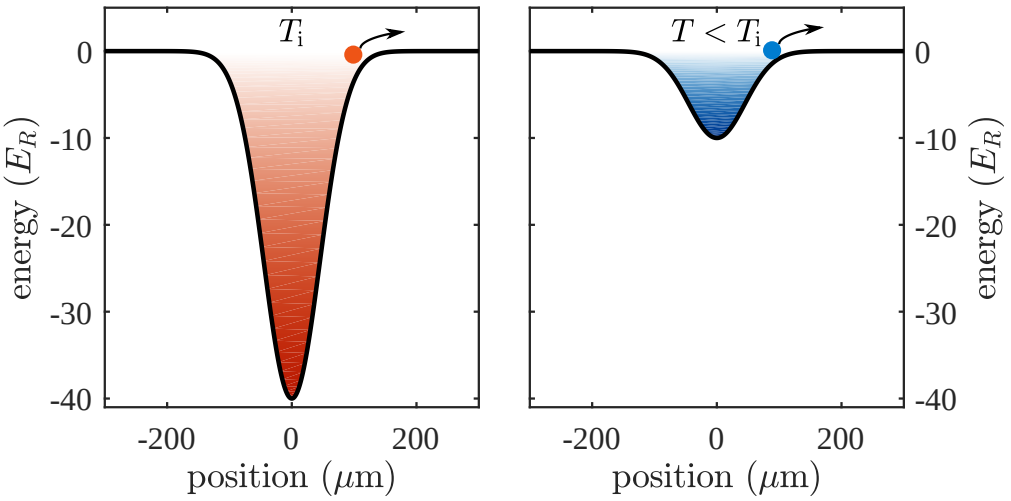

Figure 3.52: Schematic of optical evaporation. As the trap depth is lowered atoms with the highest energy escape the trap. After thermalization, the temperature of the remaining sample has decreased.

an opportunity for improvement of the stability and efficiency of optical evaporation. The specific value of the Feshbach field and exponential ramp down in optical power are empirically optimized.

Detection of the condensate is done by imaging the spatial density profile in time of flight as the trap depth is lowered. The thermal distribution expands ballistically in accordance with a Maxwell Boltzmann distribution in both the spatial and momentum degrees of freedom. In contrast, the condensate is described by the many body ground state wavefunction, which is set by the interaction strength and the confining harmonic trap. The result is that density and velocity distributions of the condensate are much narrower than those of the thermal cloud and have a different functional form [2]. In time flight this can clearly be seen as the manifestation of a bimodal distribution near the transition temperature. By independently fitting the distributions, the thermal atom number and and condensate atom number are determined. The temperature of the thermal distribution can be measured using typical time of flight thermometry which allows us to relate the condensate fraction to the cloud temperature.

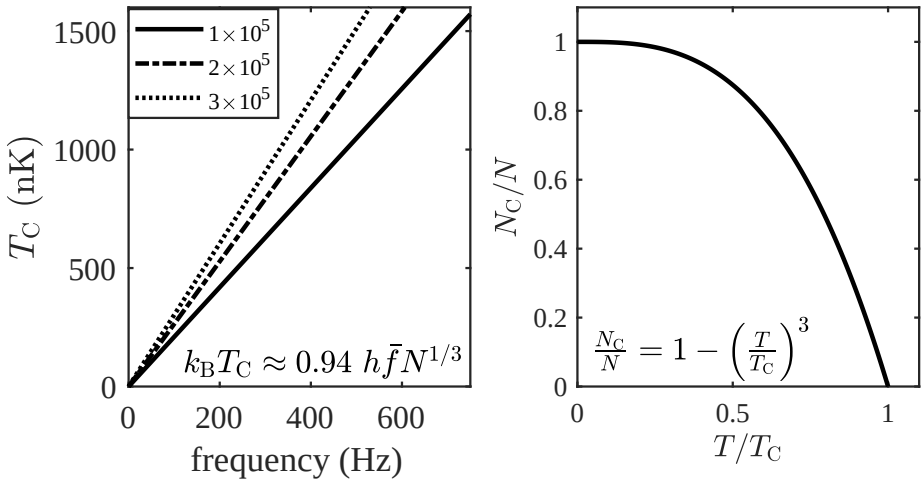

Figure 3.53: Theoretical predictions for BEC thermal phase transition **(left)** The calculated transition temperature as a function of the trap frequency $\bar{f}$ shown for experimentally relevant atom numbers. **(right)** The characteristic dependence of condensate number below the transition temperature T_C.

Example data demonstrating the detection of the condensate is shown in Figure 3.54. The bimodal distribution in time of flight (shown here for 3 ms) is clearly seen from the optical density images. Fitting the bimodal distribution is done over the entire two dimensional domain or radially. In practice we find it easiest to fit only the wings of the gaussian distribution and use the residue to calculate the condensate number. Practically speaking, we find that the human eye is generally good enough in assessing the optical density images to determine an appropriate final trap that has a large enough condensate fraction.

Quantitative analysis on the formation of the condensate is shown in Figure 3.55. Tracking the ratio of the condensate atom number to the thermal atom number, we find the condensate fraction to be greater than 95% at typical operating conditions. The atom number in the condensate ranges between one to two hundred thousand. Time of flight thermometry indicates a measured transition temperature T_C of 420 nK. Deviations between the expected and measured transition temperatures are attributed to experimental

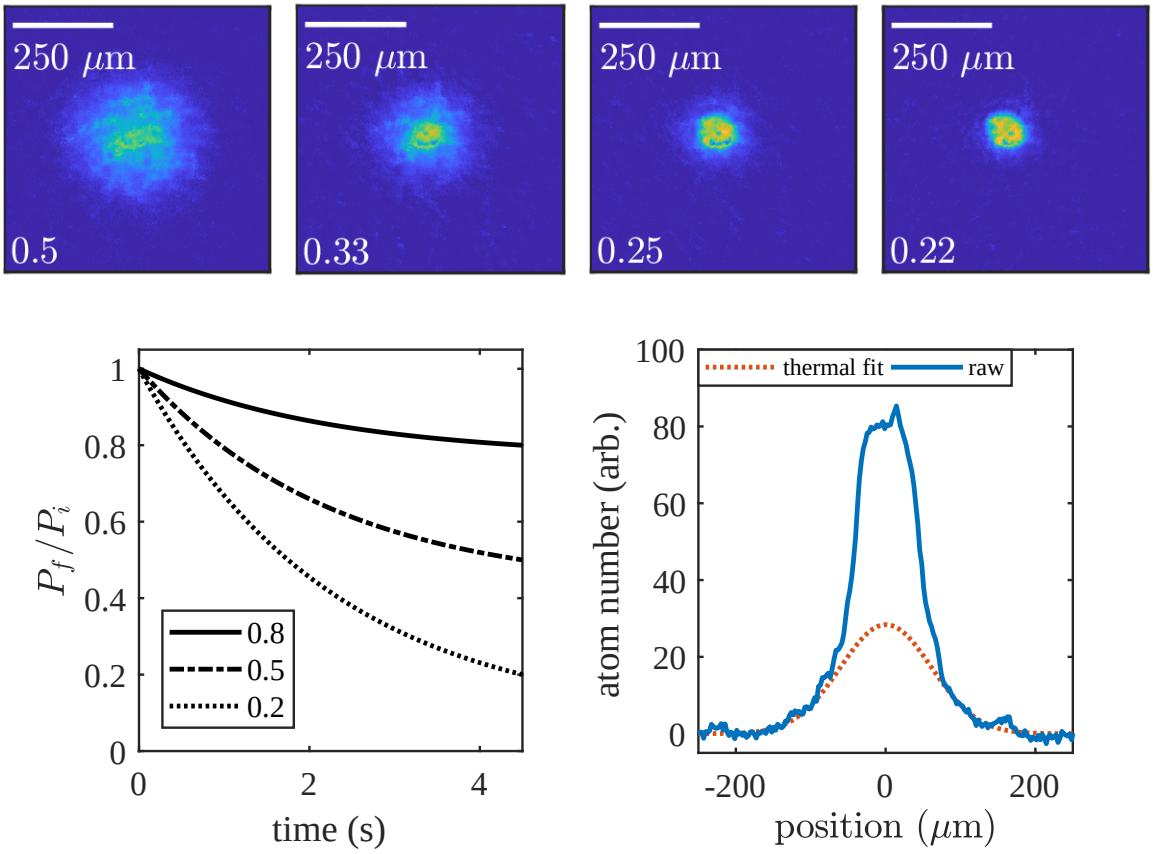

Figure 3.54: Experimental detection of the condensate. As the trap depth decreases the formation of the condensate is evidenced by the bimodal density and momentum distribution. **(top)** Images of the atomic cloud after a 3 ms time of flight. Here shown for an ending relative trap depth P_f/P_i of 0.5, 0.33, 0.25, and 0.22. The condensate appears as a dense core inside the relatively diffuse thermal atoms. **(bottom left)** Demonstration of exponential ramp down of the trap depth. The total ramp time is 4.5 s with a characteristic time of 2.25 s. **(bottom right)** Optical density profile summed over one dimension. The optical density profile (blue) is not gaussian. The thermal atom number is extracted by fitting the wings of the distribution to a gaussian (red dotted). The condensate number is obtained by measuring the residual optical density.

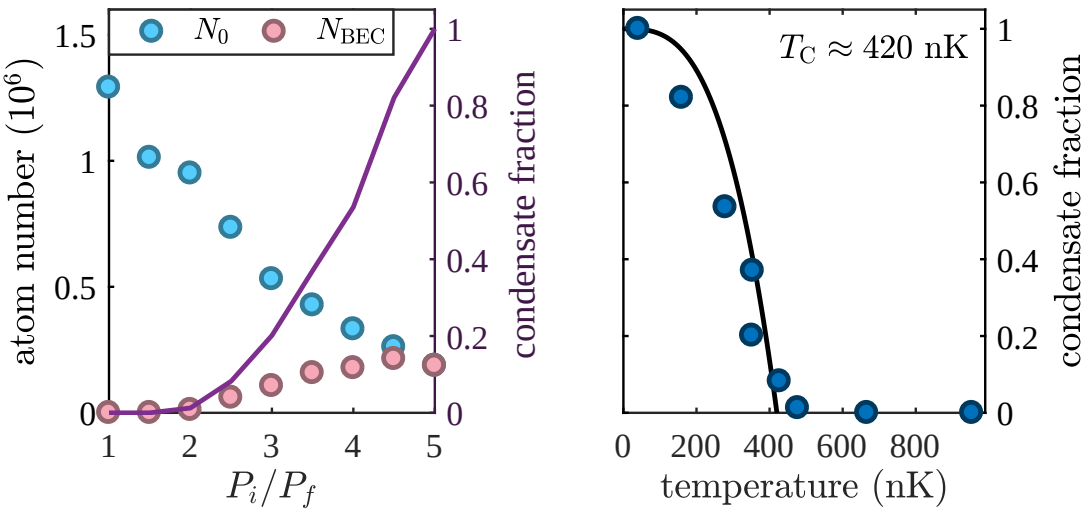

Figure 3.55: Characterization of the condensate fraction over the transition temperature. **(left)** For lower final trap depths, more atoms are evaporated resulting in a decrease in total atom number (blue), and as the temperature decreases the number of atoms in the condensate increases (pink). The measured number of atoms in the condensate is limited by the saturation of the optical density. For sufficiently deep optical evaporation, the condensate fraction (purple) reaches near unity. **(right)** Measured condensate fraction as a function of the temperature which is measured by fitting the thermal gaussian distribution. We estimate the transition temperature to be around 420 nK.

uncertainty in the trap frequency and atom number. For the experiments documented in this thesis, such differences are not of concern; we only care that the temperature is low enough to produce a reliably high condensate fraction. Depending on the experiment, we may ramp the Feshbach field to the non-interacting regime in 100 ms after the formation of the condensate.

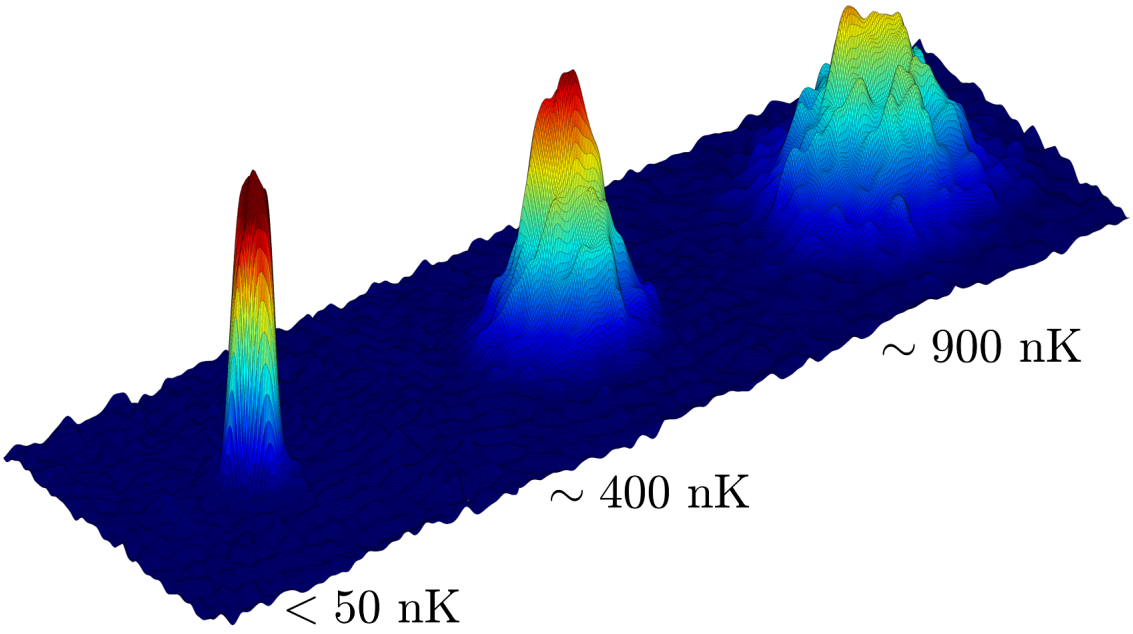

Figure 3.56: Bose-Einstein condensate of ^{7}Li.

3.11 Optical Lattices

After the generation of the condensate, the atomic cloud is loaded into a variety of one dimensional optical lattice potentials depending on the particular experiment. In this section we discuss the experimental generation of the lattice potentials and a few important technical calculations; a discussion of the theory and calibration of the lattices is found in the next chapter. The lattice potential energy is generated by the same AC stark shift mechanism as the crossed optical dipole trap given by equation 3.44. A periodic tiling in light intensity is created by retroreflecting a far detuned laser beam to make a standing wave. This modulates the local light intensity periodically, and via the AC stark shift, creates a periodic tiling in potential energy. This can be calculated directly by considering the interference pattern generated by two counter propagating gaussian beams defined by the electric field in the following equation.

$$\mathbf{E}(z,r,t) = \mathbf{E_0}\frac{w_0}{w(z)}e^{-r^2/w(z)^2}\exp\left[-i\left(kz - kr^2/2R(z) - \psi(z)\right)\right]\exp\left[i\omega t\right] \tag{3.62}$$

Here, the parameters specified are identical to those in equation 3.46 with the addition of the Gouy phse $\psi(z) := \arctan\left(z/z_R\right)$ and the radius of curvature $R(z) := z\left(1+(z/z_R)^2\right)$. The total electric field is the sum of the two counter propagating beams $\mathbf{E}_{\text{tot}} = \mathbf{E}(k) + \mathbf{E}(-k)$, and the expected intensity found by averaging over a single light period where $I = \langle \mathbf{E}_{\text{tot}}^2 \rangle$. The peak expected intensity of an individual beam is $I_0 = E_0^2/2$.

$$I(r,z) = 4I_0^2\left(\frac{w_0}{w(z)^2}\right)^2 e^{-2r^2/w(z)^2}\cos^2\left(\frac{2\pi z}{\lambda}\left[1+\frac{1}{2}\frac{r^2}{z_R^2}\frac{w_0^2}{w(z)^2}\right]\right) \tag{3.63}$$

Since $r \ll z_R$, the resultant intensity pattern has spatial periodicity of $\lambda/2$ and a peak intensity four times greater than that of a single beam in equation 3.46; a sketch of

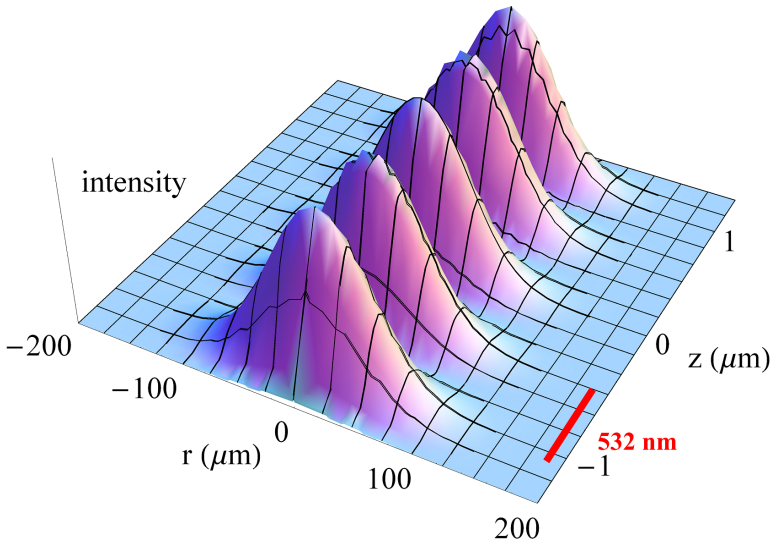

Figure 3.57: Intensity landscape of a retroreflected optical lattice. The lattice spacing 532 nm is half the lattice light wavelength. The local light intensity drops to zero at the nodes of the standing wave profile, and the radial confinement drops off with the beam waist w_0.

the potential is provided in Figure 3.57. Note that normalizing appropriately and taking $r = 0$, the potential energy produced by equation 3.63 reduces to a simple cosine lattice $U(z) = U_0 \cos(2\pi z/\lambda)^2$. Identical to the optical dipole trap, harmonic approximation yields trap frequencies in the axial and radial directions. The expression for the radial trap frequency is the same as in equation 3.49, and the axial trap frequency is set by the lattice light wavelength $\lambda = 1064$ nm. Qualitatively, the axial frequency f_z sets the size of the lowest band gap. The radial trap frequency f_r sets the energy scale of transverse dynamics and interactions.

$$f_r = \frac{1}{2\pi}\sqrt{\frac{4U_0}{mw_0^2}} \tag{3.64}$$

$$f_z = \sqrt{\frac{U_0}{m\lambda^2}} = 50.35 \text{ kHz}\sqrt{\frac{U_0}{E_R}} \tag{3.65}$$

Experimentally, the lattice light is generated from the same seed and fiber amplifier as

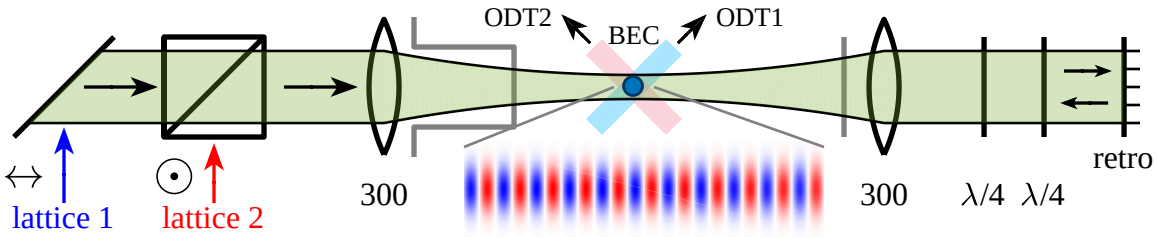

Figure 3.58: Schematic of lattice beams relative to the condensate and the optical dipole trap beams. The two lattice beams (red and blue) are focused through the side bucket window with an $f = 300$ mm lens and are retroreflected on the other side of the chamber. The two beams are orthogonally polarized as indicated by the figure. The two $\lambda/4$ waveplates induce a relative phase shift in the two beams such that their intensity maxima are phase shifted by half a lattice site as indicated by the inset image. Not shown are the dichroic and imaging optics that enable imaging along this axis for alignment of the lattice beams.

the optical dipole trap beams with beam waist $w_0 = 80$ μm and wavelength $\lambda = 1064$ nm. With a total approximate power of 10 W the peak lattice depth is 165 E_R, and these values are calibrated by both Kapitza-Dirac diffraction and amplitude modulation spectroscopy. The light is detuned many MHz away from the optical dipole trap beams to minimize interference effects. At the end of optical evaporation, a motorized waveplate rotator diverts power away from the optical dipole trap beams towards the acoustic optic modulators that control the lattice beams. A schematic of the relative orientation of the lattice beams and the optical dipole trap is provided in Figure 3.58. The condensate is adiabatically loaded into the ground band of the optical lattice potential about quasimomentum zero by simultaneously ramping down the optical dipole traps and ramping up the lattice beams over 100 ms.

The lattice beams are aligned to the image of the *insitu* condensate position along the propagation direction of the lattice beams. The retroreflection mirror is coarsely set by optimizing the rejected power in the fiber amplifier optical isolator and is finely aligned by maximizing the number of diffracted orders in Kapitza-Dirac diffraction. We find good agreement with the measured lattice depth and *ab initio* calculations.

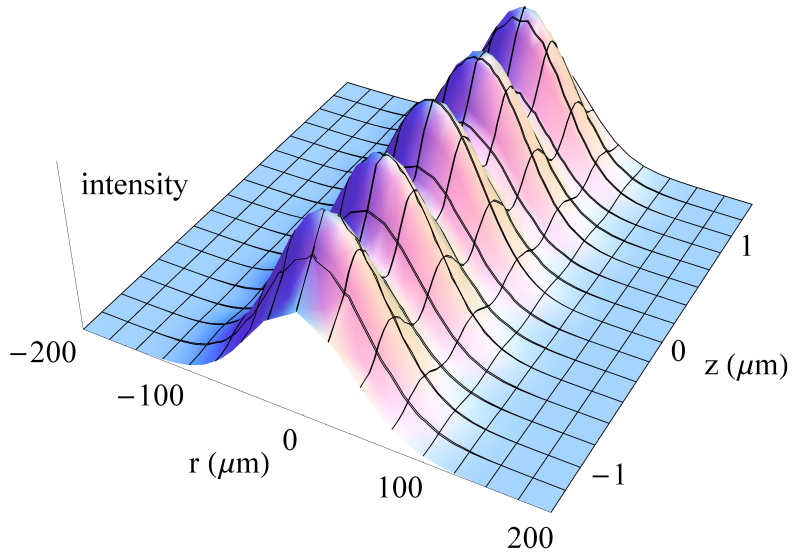

Figure 3.59: Intensity landscape for double beam optical lattice. The additional lattice beam keeps the effective lattice depth fixed but increases the overal chemical potential and increases the radial trap frequency.

3.11.1 Double Optical Lattice

As alluded to in the previous text and indicated in Figure 3.58, our one dimensional lattice potential is generated by two separately controllable co-aligned retroreflected lattices, which enable modulation of the effective lattice depth greater than 100%. For a single retroreflected lattice, changing the sign of the potential would require sweeping the detuning which is not experimentally viable. Such a technical requirement is necessary for our experiments studying strongly driven lattice systems. Our weakly modulated experiments use only a single lattice for which the previous discussion is complete. By orthogonally linearly polarizing the two beams, interference effects are eliminated, and the total potential energy is simply the sum of the individual potentials. The utility of such a configuration arises because the two lattice potentials are phase shifted by half a lattice site. By appropriately modulating the depths in time, the desired modulation scheme is realized. To see this, consider individual lattice potentials given by the following

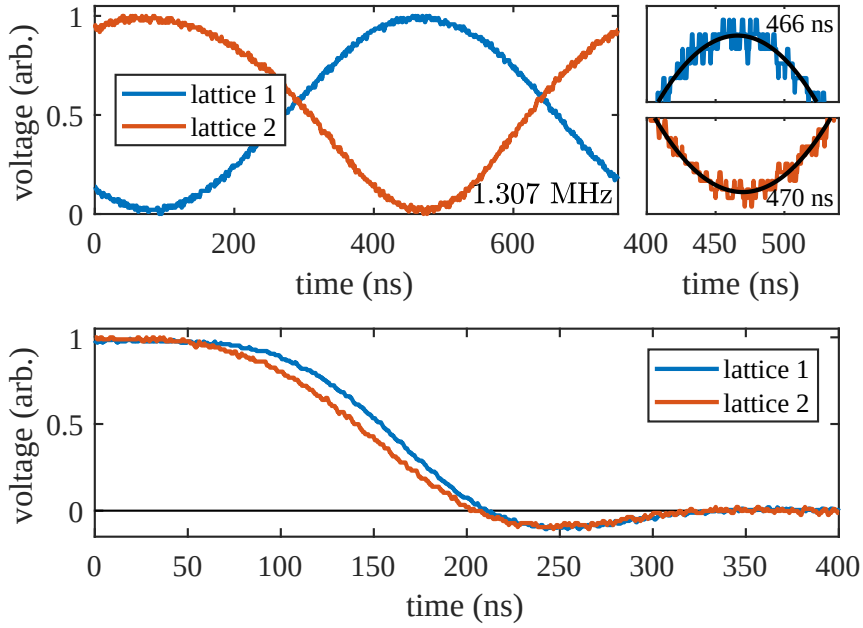

Figure 3.60: Characterization of phase differences in the time modulation between the lattice beams. **(top)** Example amplitude modulation of the lattice depth. The frequency of modulation is fitted to be 1.307 MHz. The estimated phase difference between the modulation is around 4 ns. **(bottom)** Quenching the lattice depth via the radio frequency from the direct digital synthesizer. The measured fall time of approximately 200 ns is consistent with estimations using the beam diameter of 2 mm and the speed of sound 4.25 km/s. At these timescales, the time response of the photodiode (10 MHz) limits accurate characterization of the quench which is evidenced by negative voltages.

$$U_1(z,t) = -A\alpha \sin^2\left(\frac{\omega t}{2} + \frac{\pi}{2}\right)\cos^2(kz) \tag{3.66}$$

$$U_2(z,t) = -A\,(1+\alpha)\sin^2\left(\frac{\omega t}{2}\right)\cos^2\left(kz + 2\frac{\pi}{4}\right) \tag{3.67}$$

where A is the static lattice depth, α the depth of modulation, and ω the modulation frequency. Experimentally, this equates to modulating one lattice from zero to $A\alpha$ and and the other to $A(\alpha+1)$ out of phase. Summing the two together yields a total potential of

$$U_{\text{tot}}(z,t) = -\frac{A}{2}(1+\alpha) - \frac{A}{2}\cos(2kx)\left[1+\alpha\sin(\omega t)\right] \tag{3.68}$$

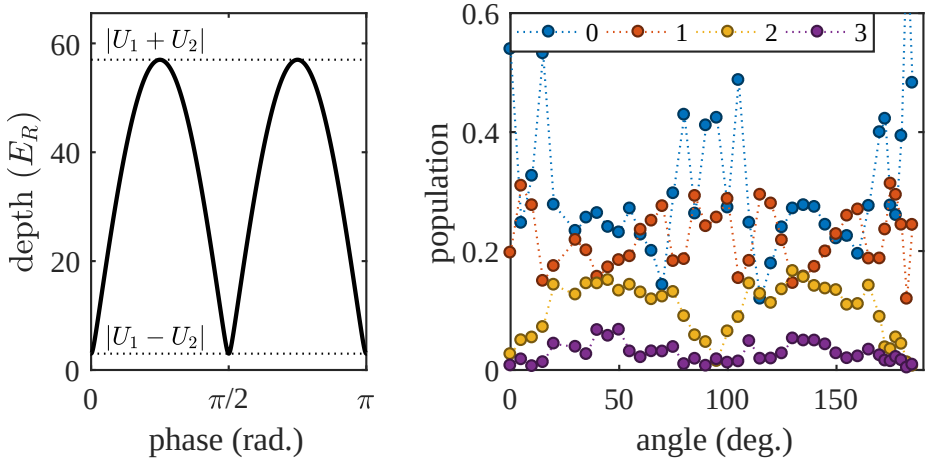

Figure 3.61: Characterization of varying the spatial phase between the two lattices. **(left)** As the phase difference between the lattices is varied the effective lattice varies between $|U_1 + U_2|$ and $|U_1 - U_2|$. **(right)** Data of the population amplitudes in each diffracted order for varying waveplate angle in Kapitza-Dirac diffraction. As the waveplate is rotated the effective lattice depth changes and the population in each diffracted mode alters.

where we have realized a 1D optical lattice whose depth can change sign. However, since the energy shift from the beams is always attractive, this results in an increase in the overall chemical potential indicated by the first term in equation 3.68. A schematic of the modulation and the total potential is provided in Figure 3.59 to elucidate this. This increases the effective radial trap frequency and the interaction energy depending on the modulation strength. Different modulation schemes can keep the total chemical potential fixed at the cost of experimental precision in the lattice depth.

To keep the modulation in phase, the radio frequency source for the lattice beam acousto-optic modulators come from the same direct digital synthesizer, and a description of this driver is found in Appendix B. We also find the use of a delay line to be experimentally helpful in eliminating phase error caused by differences in the relative position of the beams on the acousto-optic modulator crystal. A characterization of the time phase difference is provided in Figure 3.60.

The half lattice site phase offset is generated by two $\lambda/4$ waveplates such that upon

retroflection, the equivalent Jones matrix is represented by $\lambda/4$-$\lambda/2$-$\lambda/4$ waveplate chain. By setting the beginning and ending $\lambda/4$ waveplate to 45°, the $\lambda/2$ waveplate continuously tunes the relative phase offset between the lattices. Implementing modulation schemes utilizing a spatial phase offset different than half a lattice site would cause the modulation to induce a force, which would enable study of different modulation phenomena. The veracity of the lattice offset is confirmed by measuring the reduction in effective lattice depth during Kapitza-Dirac diffraction; example data is shown in Figure 3.61.

Loading into the double optical lattice potential is similar to the one beam case, except that both beams must be turned on in tandem. As described in Figure 3.62, this smoothly ramps on the effective lattice depth which minimizes heating.

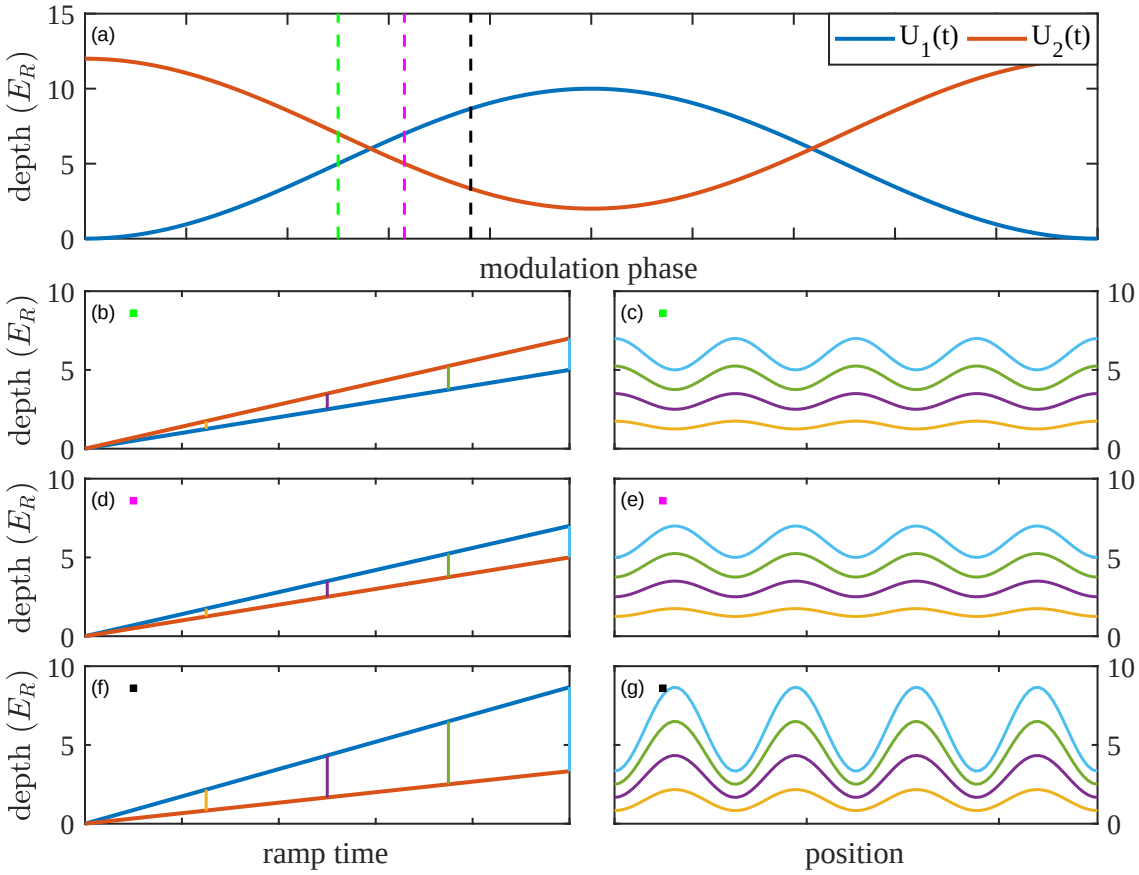

Figure 3.62: Loading into the double optical lattice. **(a)** The lattice depth of each lattice during a modulation cycle. The dashed lines refer to different moments in time during the modulation. **(b,d,f)** By fixing the initial phase and ramping up the power in each beam, the effective lattice depth can be adiabatically turned on. This allows the total lattice to have minima at either lattice 1 (pink) or lattice 2 (blue). **(c,e,g)** The resultant lattice depth in space as the power in the beams are increased for the initial phase conditions of (b,d,f).

Chapter 4

Lattice Techniques and Floquet Band Engineering

In this chapter we describe the theoretical framework for understanding our optical lattice experiment.

4.1 1D Optical Lattice

The experiments in this thesis utilize one dimensional optical lattices to study lattice physics. To serve as a fundamental bedrock for future discussion of our experiments, the author presents here a brief discussion on the case study of a simple one dimensional optical lattice. The aim of this section to provide a brief overview of some important properties and how we do numerical calculations. The single particle Hamiltonian of the one dimensional optical lattice is given by

$$\hat{H} = \frac{\hat{p}^2}{2m} - V_0 \cos^2(k_L \hat{x}) \tag{4.1}$$

where m is the particle mass, V_0 the lattice depth, and $k_L = 2\pi/\lambda$ the lattice k-vector. For all experiments in this thesis we use $m_{\mathrm{Li}} = 7$ amu and $\lambda = 1064$ nm. For theoretical simplicity we express equation 4.1 in terms of the unitless position and momentum operators $\phi := k_L x$ and $p := p_\phi \hbar k_L$ for which the commutator is now unitless as shown in equation 4.2

$$[x, p] = i\hbar \rightarrow [\phi, p_\phi] = i \tag{4.2}$$

This transforms the Hamiltonian and the time dependent Schrodinger equation into the unitless expressions of equations 4.3 and 4.4 which are scaled by the recoil energy $E_R = \hbar^2 k_L^2 / 2m = \hbar\omega_R$.

$$h = -\partial_\phi^2 + v(\phi) \tag{4.3}$$

$$h\psi = i\frac{\partial \psi}{\partial \tau} \tag{4.4}$$

where $h := H/E_R$, $v(\phi) := V(\phi)/E_R$, and $\tau := \omega_R t$ are the dimensionless Hamilto-

nian, potential, and time respectively. For reasonable values of h, it is clear from the definition of τ that time dynamics will occur on timescales with the recoil frequency $\nu_R := E_R/h$ of 25.18 kHz. The undimensionalized Hamiltonian gotten from the dimensionful Hamiltonian in equation 4.1 then becomes the expression shown in equation 4.5.

$$h = -\partial_\phi^2 - v_0 \cos^2(\phi) \tag{4.5}$$

$$= -\partial_\phi^2 - \frac{v_0}{2}\cos(2\phi) - \frac{v_0}{2} \tag{4.6}$$

We shall commonly drop the constant term for notational simplicity. The stationary solutions to the time dependent Schrodinger equation of equation 4.4 can be found by utilizing the discrete translation symmetry of equation 4.5 ($h(\phi + \pi) = h(\phi)$) using of Bloch's theorem in the typical way. The solutions will be then characterized by a band index n and quasimomentum k where k is restricted to the first Brillouin zone $-1 < k < 1$. Assuming an ansatz solution of equation 4.7

$$\psi = u_{n,k}(\phi)e^{ik\phi} \tag{4.7}$$

where $u_{n,k}$ is a π periodic function, the time dependendent Schrodinger equation $h\psi = \epsilon\psi$ reduces to the eigenvalue problem of equation 4.8 over the domain $[-\pi/2, \pi/2]$.

$$\epsilon_{n,k}u_{n,k} = \left[k^2 - 2ik\partial_\phi - \partial_\phi^2 + v(\phi)\right] u_{n,k} \tag{4.8}$$

Solving equation 4.8 is done numerically by choosing an orthogonal basis $\{w_n(\phi)\}$ shown in equation 4.9 over the domain $[-\pi/2, \pi/2]$. Practically speaking, one must choose a truncated basis to perform calculations, and thus we elect to use π periodic functions which resemble free particle states.

$$w_n(\phi) = \begin{cases} \sqrt{\frac{1}{\pi}} & n = 0 \\ \sqrt{\frac{2}{\pi}}\cos(n\phi) & n = 2, 4, 6... \\ \sqrt{\frac{2}{\pi}}\sin((n+1)\phi) & n = 1, 3, 5... \end{cases} \tag{4.9}$$

The effect of the operators of equation 4.5 on this basis are

$$\partial_\phi w_n = \begin{cases} 0 & n = 0 \\ -n w_{n-1} & n = 2, 4, 6... \\ (n+1) w_{n+1} & n = 1, 3, 5... \end{cases} \quad \partial_\phi^2 w_n = \begin{cases} 0 & n = 0 \\ -n^2 w_n & n = 2, 4, 6... \\ -(n+1)^2 w_n & n = 1, 3, 5... \end{cases}$$

which allows us to recast the problem into the matrix equation

$$\left[k^2 \mathbf{I} - ik\mathbf{M_1} - \mathbf{M_2} + \mathbf{M_3}\right] \vec{v} = \epsilon_{n,k} \vec{v}, \tag{4.10}$$

where $\{\mathbf{M_i}\}$ are given by,

$$\mathbf{M_1} := \langle w_m | \partial_\phi | w_n \rangle = \begin{pmatrix} 0 & & & & \\ & 0 & -2 & & \\ & 2 & 0 & & \\ & & & 0 & -4 \\ & & & 4 & \ddots \end{pmatrix} \tag{4.11}$$

$$\mathbf{M_2} := \langle w_m \left| \partial_\phi^2 \right| w_n \rangle = \begin{pmatrix} 0 & 0 & 0 & \cdots & & 0 \\ 0 & -2 & \ddots & & & \\ 0 & \ddots & -2 & & & \\ \vdots & & & -4 & & \\ & & & & -4 & \\ 0 & & & & & \ddots \end{pmatrix} \tag{4.12}$$

And the potential is similarly represented by:

$$\mathbf{M_3} := \langle w_m \left| v(\phi) \right| w_n \rangle = \frac{(V_0/E_R)}{4} \begin{pmatrix} 0 & 0 & \sqrt{2} & \cdots & & 0 \\ 0 & 0 & 0 & 1 & & \\ \sqrt{2} & 0 & 0 & 0 & 1 & \\ \vdots & 1 & 0 & \ddots & \ddots & \\ & & 1 & \ddots & & \\ 0 & & & & & \end{pmatrix} \tag{4.13}$$

Once equation 4.10 is defined, the eigenvalues and eigenvectors for a given quasi-momentum are found using an eigenvalue solver program. Example calculated band structures for the cosine lattice are shown in Figure 4.1, and we shall take a moment to discuss some qualitative features. The lattice provides coupling with momentum of a reciprocal vector and therefore opens up energy gaps at the zone edge and center. The curvature of the bands alternates between band indices n and becomes more flat for larger lattice depths. The band structure is also symmetric about $k \to -k$ owing to the inversion symmetry and the lack of spin-orbit coupling terms of the simple lattice of

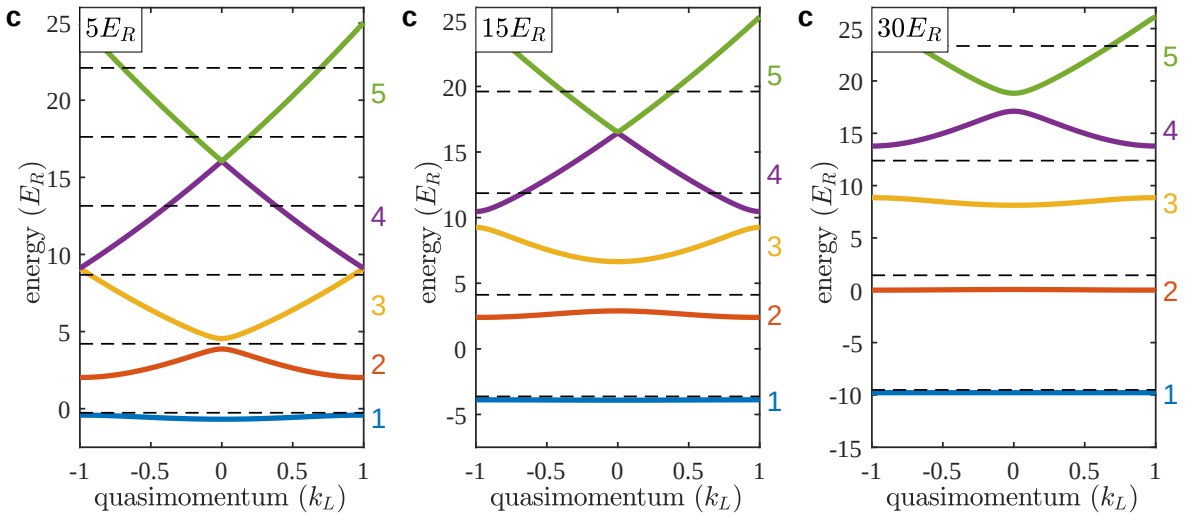

Figure 4.1: Calculated band structure $E_n(k)$ for the 1D optical lattice for lattices depths of 5, 15, and 30 E_R. Colored lines separate energies into the band indeces n, and solid dashed lines correspond to harmonic oscillator equivalent spectrum.

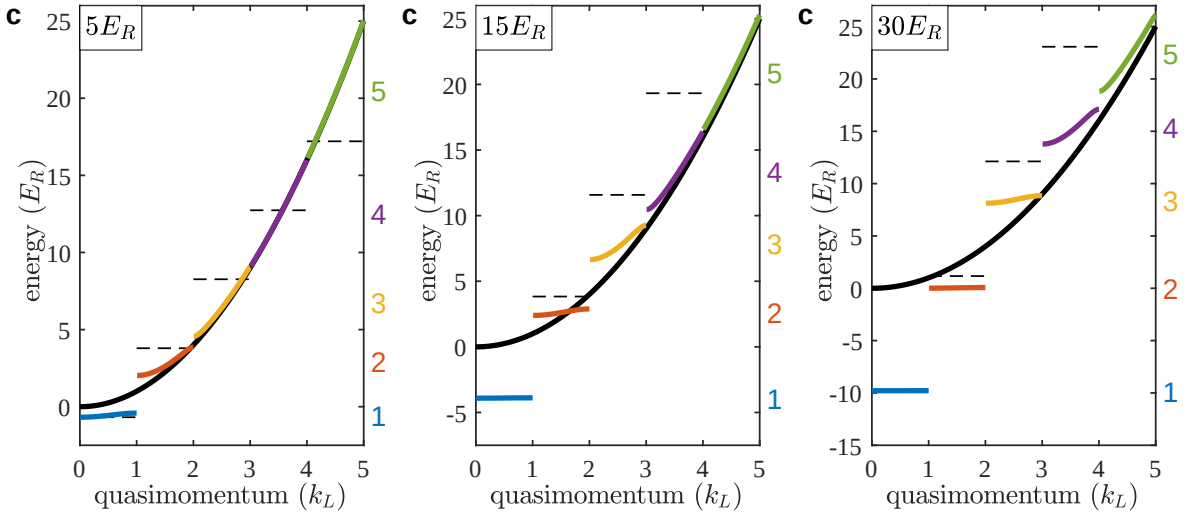

Figure 4.2: Calculated band structure $E_n(k)$ for the 1D optical lattice for lattices depths of 5, 15, and 30 E_R in the extended zone scheme. Colored lines separate energies into the band indices n, and solid dashed lines correspond to harmonic oscillator equivalent spectrum. Solid black line is the free particle dispersion.

equation 4.3.

We also consider limiting cases of the lattice depth V_0. In the limit that the lattice depth V_0 is very large, we anticipate that the behavior of the low energy solutions to 4.3 should resemble a harmonic approximation about the lattice potential energy minimum given by equation 4.14.

$$v(\phi) = -\frac{v_0}{2}\left(1 + 2\phi^2 + \dots\right) \tag{4.14}$$

The resultant Hamiltonian and eigenvalues are given by equations 4.15 and 4.16.

$$h_{\text{ho}} = -\partial_\phi^2 + v_0\phi^2 \tag{4.15}$$

$$\epsilon_{n,\text{ho}} = 2\sqrt{v_0}\left(n + \frac{1}{2}\right), \quad n \in 0, 1, 2, \dots \tag{4.16}$$

These are also plotted in Figure 4.1, and we note that consistent with our intuition, the harmonic approximation matches the numerically calculated eigenvalues for large lattice depths. This can also be seen be comparing the wavefunctions for the approximate harmonic and numerical lattice calculations as shown in Figure 4.3. Again, we can see that the lattice wavefunctions are well approximated by the harmonic ones for low energies and large lattice depths.

In the opposite limit where the lattice depth V_0 vanishes, we anticipate the solutions to match those given by a the free particle Hamiltonian

$$h_{\text{free}} = -\partial_\phi^2 \tag{4.17}$$

$$\epsilon_{k,\text{free}} = k^2, \tag{4.18}$$

and we compare all calculated energies in Figure 4.2 in the extended zone scheme

where the momentum k is unfolded by the band index n under the transformation $k \rightarrow k + n$. In this case, we note that the lattice energies match those for the free particle dispersion for low lattice depths and high energy states consistent with our intuition.

Additional examination of the extended zone scheme provides further intuition as shown in Figure 4.4. Crossings in the free particle dispersion k^2 displaced by the lattice reciprocal vector $2\hbar k_L$ are momenta at which the lattice provides coupling. Gaps in the energy spectrum then generically open at these coupling resonances. To lowest order, the size of the gaps are consistent with predictions from first order perturbation theory.

For the experiments covered in this thesis, we measure the semi-classical behavior of the condensate by a wavepacket in the band structure. In particular, a useful metric is the group velocity v_g which is expressed in equation 4.19

$$v_g = \frac{\partial \epsilon}{\partial k} \tag{4.19}$$

The group velocity will then dictate the motion of the condensate in the lattice given by the simple evolution $\dot{x} = v_g$.

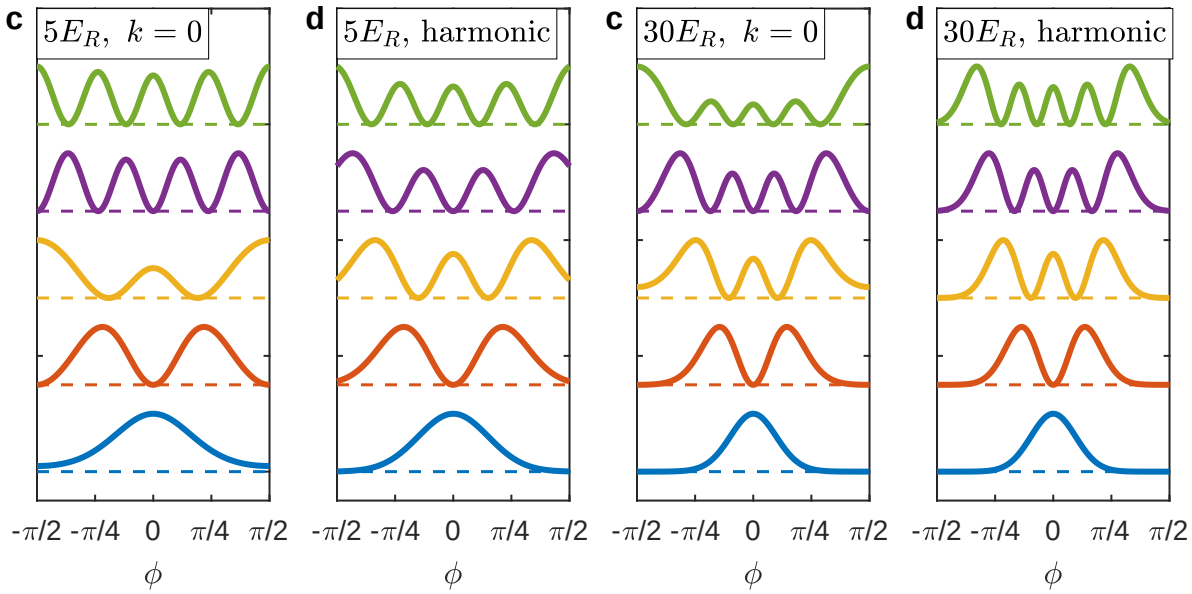

Figure 4.3: Comparison of probability density for lattice and harmonic oscillator eigenstates. Here shown for lattice depths of $5E_R$ and $30E_R$ at the center of the Brillouin zone at $k = 0$. For deeper lattice depths, the harmonic oscillator wavefunctions more accurately reflect the lattice eigenstates. For the shallow lattice the excited states resemble plane waves.

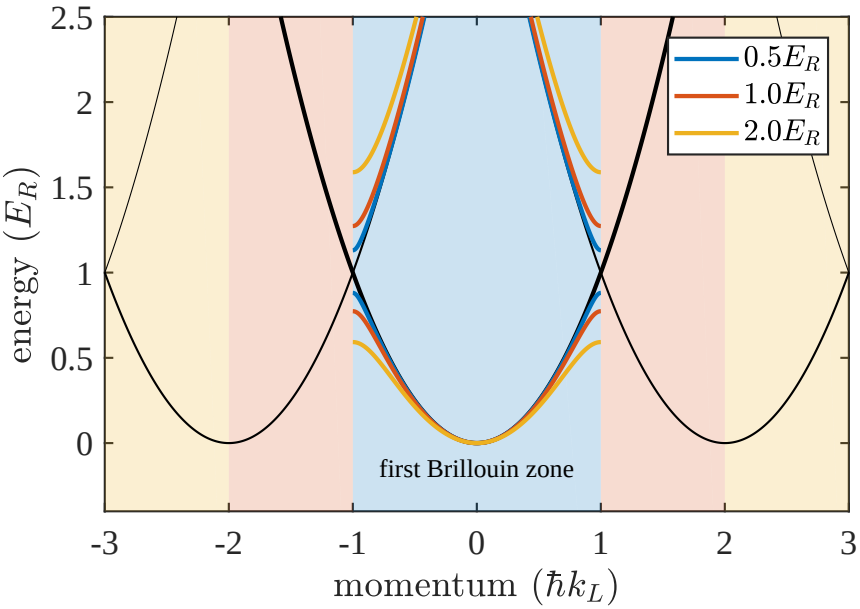

Figure 4.4: Opening of gaps in the energy spectrum from the lattice potential. The black lines are the free particle dispersion k^2 displaced by multiples of the lattice reciprocal vector $2\hbar k_L$. As the lattice depth increases gaps in the spectrum at the zone edge open from the coupling provided by the lattice.

4.2 Band Mapping

When conducting an experiment, it is useful to read out the populations of the lattice band state $|n, k\rangle$, and **band mapping** is a technique used to read out this information. The fundamental goal of band mapping is to map the eigenstate $|n, k\rangle$ inside the lattice to a free particle momentum state $|p\rangle$ which can then be identified through time of flight imaging [20, 21, 22]. Experimentally, this is achieved by ramping down the lattice potential which projects the eigenstates of the lattice Hamiltonian of equation 4.3 onto the free particle Hamiltonian of equation 4.17 which is diagrammed in Figure 4.5. The relationship between the band states $|n, k\rangle$ and the free particle state is then given by

$$p = (n + k)\hbar k_L \tag{4.20}$$

The fidelity of this mapping is preserved with a ramp that is slow compared to the band gap but faster than any dynamics that would alter the intraband momentum distribution. Instead of providing a more theoretical discussion of these requirements, we shall instead focus on numerical results to elucidate the dynamics of band mapping since the solutions to equation 4.3 are already numerically found.

For the lattice Hamiltonian of equation 4.3 we shall consider a time dependent lattice depth $v_0(t)$ given by equation 4.21, and an initial wavefunction which is the Bloch state modulated by a Gaussian envelope σ as in equation 4.22 where the radius will be many lattice sites.

$$v_0(t) = v_0 e^{-2t^2/\tau^2} \tag{4.21}$$

$$\psi(\phi) = u_{n,k}(\phi) e^{ik\phi} \left[\frac{1}{\sqrt{2\pi\sigma^2}} e^{-\phi^2/(2\sigma^2)} \right] \tag{4.22}$$

Time dependent numerical integration is then conducted in the position basis using an

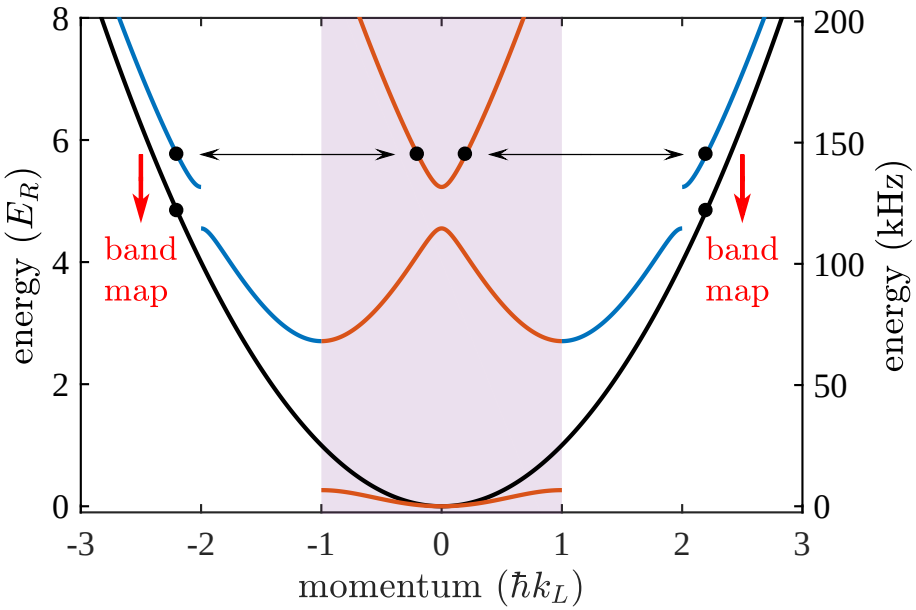

Figure 4.5: Schematic of band mapping where quasimomentum is mapped on free particle momentum states momentum states by ramping down the lattice potential. As the lattice depth decreases, the lattice eigenstates (red) transform into those of the free particle dispersion (black) as can be directly visualized by plotting the lattice band structure in the extended zone scheme (blue). The effect of bandmapping is to then transform the blue states into the black ones.

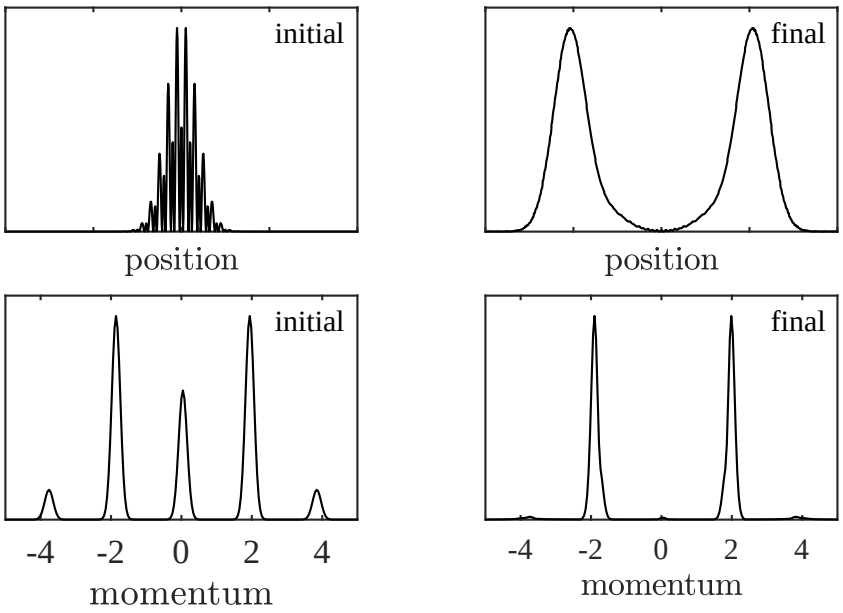

Figure 4.6: Demonstration of band mapping. For initial state $|n, k\rangle = |2, 0\rangle$, $c = 2.5$ sites, and $\tau = 10$ μs which are the approxiate conditions as diagrammed in Figure 4.5. The cloud splits in two equal components each with momentum $2\hbar k_L$ which is a consequence of that the initial wavefunction is spread evenly about $k = 0$.

midpoint Crank Nicolson time evolution operator. In particular we shall be interested in the time dependent position and momentum probabilities $|\psi(\phi, t)|^2$ and $|\psi(k, t)|^2$. An example calculation is summarized in Figure 4.6 for an initial wavepacket in the $|2, 0\rangle$ state. The band mapping is in accordance with equation 4.20. In general, such calculations are not useful on a day to day basis, but they historically provided us with intuition of the inner workings of band mapping. Experimentally, the ramp down time is set by the specific experimental conditions but typically we utilize ramp times of around a hundred microseconds. Example data for band mapping can be found in the next section on amplitude modulation spectroscopy.

4.3 Amplitude Modulation Spectroscopy

To calibrate our lattice depths for the experiments described in this thesis, we utilize **amplitude modulation spectroscopy**. Periodic modulation of the lattice depth excites atoms to higher bands based upon resonances between the bands and the population of the higher bands is measured via band mapping. By identifying the location of these resonances the lattice depth is inferred [20]. The time dependent modulation modifies the hamiltonian of equation 4.3 to that of equation 4.23 where α is the drive strength and ω the drive frequency. The number of atoms excited from the initial state $|n_g, k_g\rangle$ to the excited state $|n_e, k_e\rangle$ then depends on the resonance condition of equation 4.24 and the strength of the coupling χ in equation 4.25.

$$h = -\partial_\phi^2 - v_0(1 + \alpha \sin(\omega t)) \cos^2(\phi) \tag{4.23}$$

$$\hbar\omega = \epsilon_{n_e,k_e} - \epsilon_{n_g,k_g} \tag{4.24}$$

$$\chi = \left|\left\langle n_e, k_e \right| \cos^2(\phi) \left| n_g, k_g \right\rangle\right|^2 \tag{4.25}$$

The form of the perturbing Hamiltonian provides coupling that conserves quasimomentum such that $k_g = k_e$. While the coupling strength increases with drive strength, it is important to keep α low enough to remain in the perturbing regime to maintain the Fermi's golden rule interpretation of the modulation. We typically operate with modulation strengths of 5% to 10%. The resonance condition of equation 4.24 is mapped out by utilizing the calculated band energies which is shown in Figure 4.7 for excitations from the ground band $n_g = 0$ to the first few excited bands.

In Figure 4.8 we calculate the coupling strength χ for an example $5E_R$ and $10E_R$ lattice. Note that the coupling from the ground band to the first excited band vanishes at the zone center. This is a consequence of the even parity of the modulation, but this

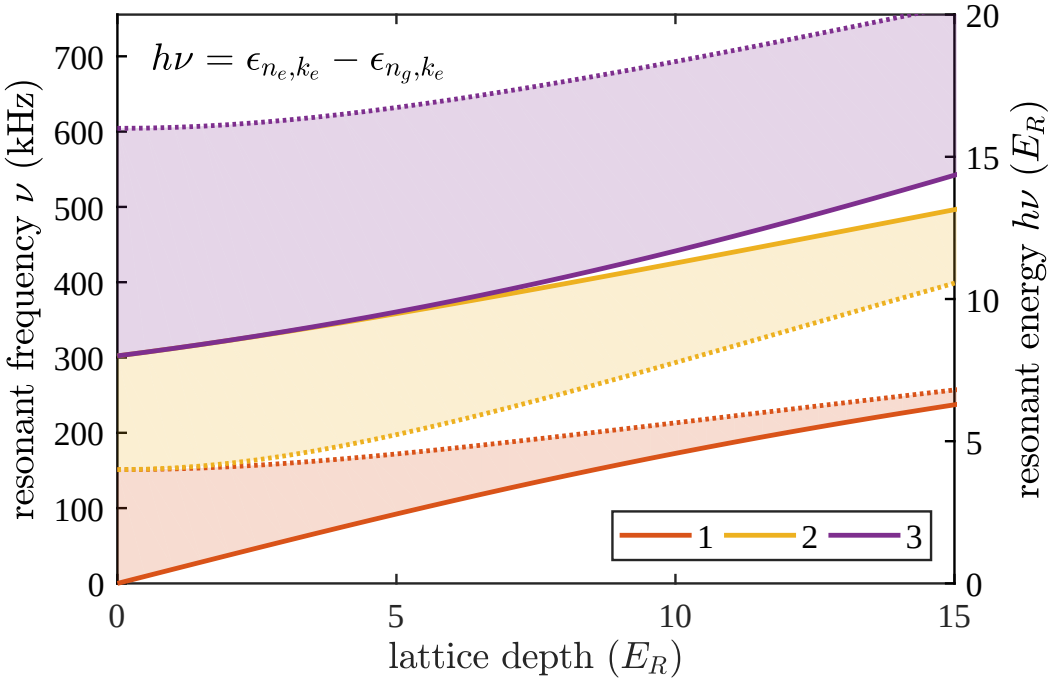

Figure 4.7: Calculated energy resonances between bands in the one dimensional optical lattice from the ground band $n_g = 0$. The solid lines are calculated at the zone edge, the dotted ones are at the zone center, and the shaded region indicates quasimomenta throughout the rest of the zone. Calculations done for $\lambda = 1064$ nm and $m = m_{\mathrm{Li}}$.

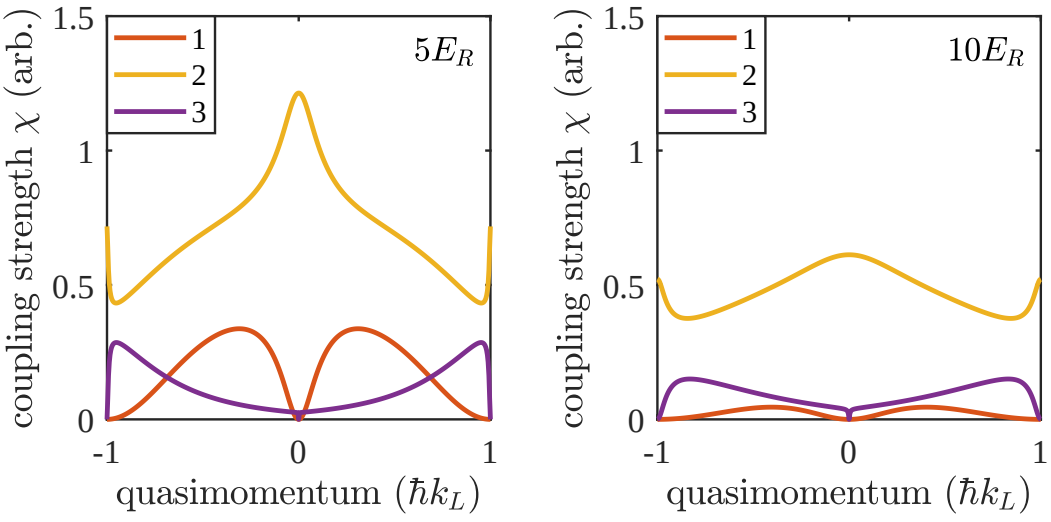

Figure 4.8: The coupling strength χ from the ground band to the first few excited bands. **(left)** For a lattice depth of $5E_R$. **(right)** For a lattice depth of $10E_R$.

parity selection rule is broken away from the zone center. Also note that the coupling strength decreases for deeper lattice. For deep lattice the wavefunctions are similar to the harmonic oscillator eigenstates of Figure 4.3 which do not resemble plane wave states with spatial periodicity of the lattice and therefore do not couple strongly to the modulation. For these reasons, we typically perform amplitude modulation on the $0 \rightarrow 3$ transition about the zone center at $k = 0$.

Example data is shown in Figure 4.9 for measuring the $0 \rightarrow 3$ resonance for an atomic cloud initially in the ground band about $k = 0$. After the modulation, a band mapping procedure is performed to map the quasimomentum onto momentum which is detected in time of flight. By fitting the relative population as a function of the modulation frequency, the resonance can be mapped out and the lattice depth inferred.

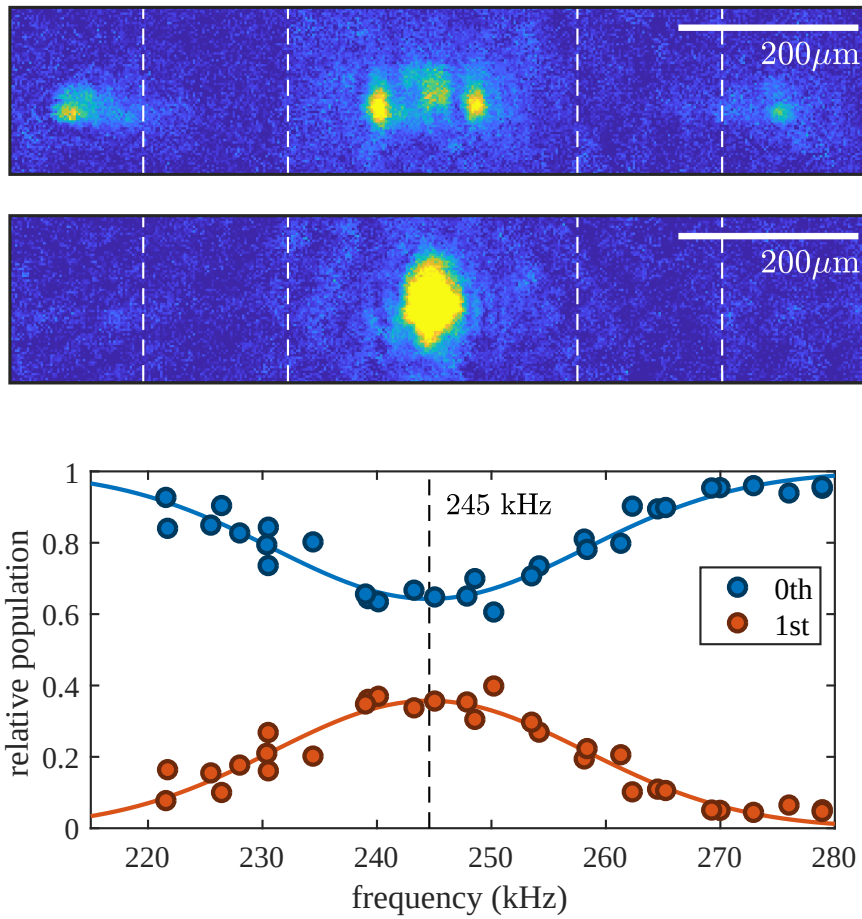

Figure 4.9: Amplitude modulation spectroscopy. Atoms in the ground band are excited by modulating the lattice depth resonantly with an interband transition Here for a transition between the ground band $n_g = 0$ and the second excited band $n_e = 2$. **(top)** After the modulation, a band mapping procedure is performed which maps quasimomentum onto momentum. The population in the higher band is detected by the atoms that are excited into the higher momentum states. For a time of flight of 3 ms, the locations of the zone edge are drawn as dashed lines. **(bottom)** Comparison of the relative number of atoms in the ground band (blue) to the excited band (red) as a function of the modulation frequency. The resonance here is measured to be at 245 kHz by fitting to the the distributions.

4.4 Kapitza-Dirac Diffraction

Kapitza-Dirac diffraction is a pulsed lattice technique which we use to measure the optical lattice depth. A diabatic pulse of the lattice onto the BEC causes the matter wave to diffract off the lattice, like a grating, into higher order plane wave momentum states. This process can also be thought of as two photon process where the BEC undergoes stimulated absorption in one lattice beam and stimulated emission into the other. These two perspectives are diagrammed in Figure 4.10. The treatment here follows that found in [23]. Experimentally speaking we compare measured relative populations in each scattering mode as a function of optical power and compare to the numerical predictions as described here. The Hamiltonian for during the pulse is the same as 4.5,

$$h = -\partial_\phi^2 + v_0 \cos^2(\phi) \tag{4.26}$$

and we shall represent the condensate wavefunction in the discrete plane wave basis as shown in equation 4.27, since we are concerned with discrete momenta scattering from the lattice. Since the spatial extent of the condensate is large compared to that of a lattice site, it is appropriate to consider the initial state to be that of a plane wave with zero momentum as shown in equation 4.28.

$$\psi(\phi, t) = \sum_{n=-\infty}^{\infty} c_n(t) e^{i2n\phi} \tag{4.27}$$

$$c_n(t = 0) = \delta_{n0} \tag{4.28}$$

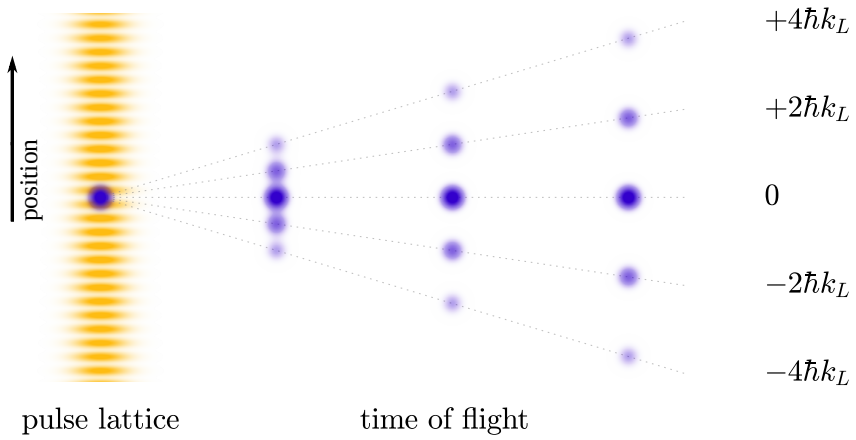

Figure 4.10: Schematic of Kapitza-Dirac diffraction. When the optical lattice potential energy (yellow) is pulsed onto the condensate the atoms absorb discrete momentum of multiples of $2\hbar k_L$ which can be seen in time of flight as a linear expansion in position. Only first few modes are shown for clarity. The population of the modes depends on the lattice depth v_0 and the pulse duraction.

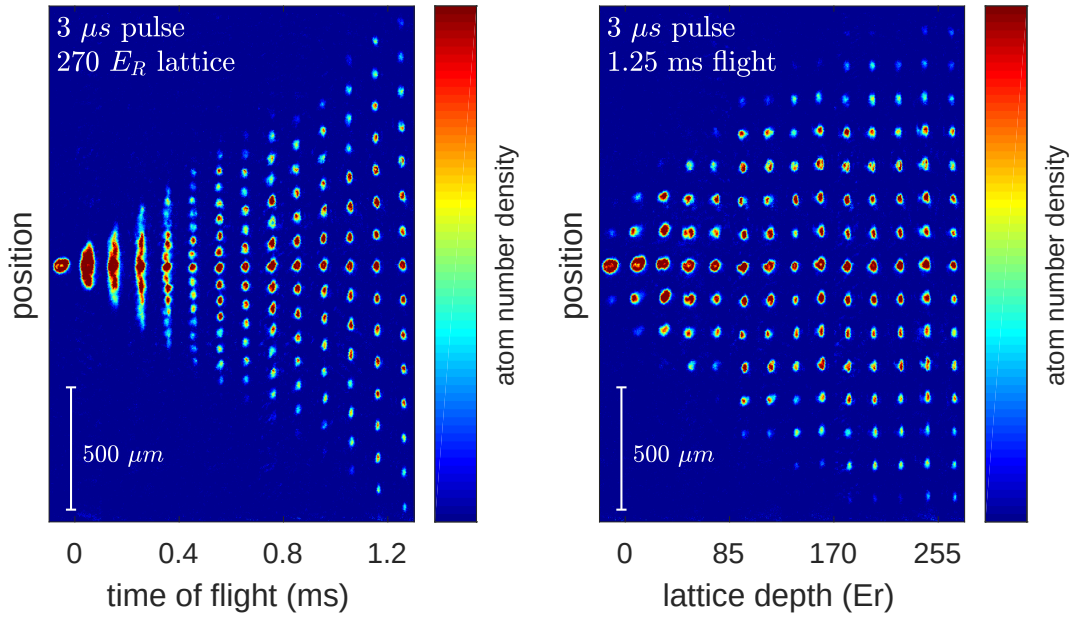

Figure 4.11: Experimentally measured Kapitza-Dirac diffraction. **(left)** The lattice beam is pulsed for 3 μs at an approximate lattice depth of $270E_R$ and the resultant atomic distribution is allowed to expand in time of flight. Discrete absorption of lattice momenta is see as the formation of discrete momentum peaks which are travel linearly away at their respective momentum. **(right)** Kaptiza-Dirac diffraction for a fixed pulse time and time of flight for varying lattice depth. As the lattice depth increases, the relative population of different momentum states changes.

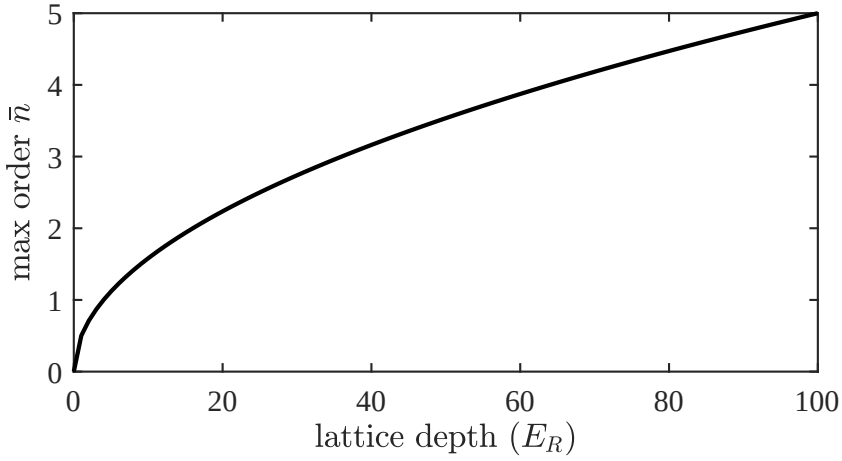

Figure 4.12: Maximum populated order $\bar{n}$ as a function of lattice depth V_0. As the lattice depth increases the number of orders that participate in the time evolution grows. The relatively slow increase is a consequence of the quadratic dependence of kinetic energy on wave number n.

In this basis the operators of equation 4.5 are expressed as

$$\partial_\phi^2 |n\rangle = -4n^2|n\rangle \tag{4.29}$$

$$\cos^2(\phi)\,|n\rangle = \frac{1}{2}|n\rangle + \frac{1}{4}|n+1\rangle + \frac{1}{4}|n-1\rangle \tag{4.30}$$

For which the time dependent Schrodinger equation says the time evolution for the coefficients $\{c_n\}$ to be given as

$$i\dot{c_n} = 4n^2 + \frac{v_0}{4}\left(c_{n+1} + 2c_n + c_{n-1}\right) \tag{4.31}$$

Before proceeding, examination of equation 4.31 reveals some qualitative behavior. First, for a given lattice depth, the highest order n that will be occupied is given by equation 4.32 which is shown in Figure 4.12.

$$\bar{n} = \sqrt{\frac{V_0}{4E_R}} \tag{4.32}$$

Furthermore, neglecting the n^2 terms in equation 4.31 which is equivalent to ignoring the kinetic energy of the atoms, yields the Raman-Nath approximation where the solutions to 4.31 are given by the J_n Bessel functions of the first kind. Such an approximation is mostly valid for small pulse amplitudes and large mass atoms, and in the case for ^{7}Li in our experiment is almost always broken. Therefore, the time dependent amplitudes are found numerically by representing the time dependent amplitudes as a the matrix equation in equation 4.33 with matrix operators $\mathbf{M_1}$ and $\mathbf{M_2}$.

$$\dot{\vec{c}} = -i\left(4\mathbf{M_1} + \frac{v_0}{4}\mathbf{M_2}\right)\vec{c}(t) \tag{4.33}$$

$$\mathbf{M_1} = \begin{pmatrix} \ddots & & & & & & \\ & 2^2 & & & & & \\ & & 1^2 & & & & \\ & & & 0 & & & \\ & & & & 1^2 & & \\ & & & & & 2^2 & \\ & & & & & & \ddots \end{pmatrix} \tag{4.34}$$

$$\mathbf{M_2} = \begin{pmatrix} 2 & 1 & & & \\ 1 & 2 & 1 & & \\ & 1 & \ddots & \ddots & \\ & & \ddots & & \end{pmatrix}.$$

Numerical integration of equation 4.33 yields time dependent probabilities as shown in Figure 4.13. The population in the modes oscillate in time with frequency that increases with lattice depth, and more modes participate in the evolution as predicted by equation 4.32. While in principle, we could calibrate our lattices by comparing the measured time

evolution to the theoretical predictions of Figure 4.13 this is not ideal. Since our timing software is not able to reliably resolve below 1 μs mapping out the time evolution for lattice depths deeper than a few recoils would be challenging. This also requires keeping the lattice depth constant from run to run, which is not easily done to within the precision necessary as alluded to by the sensitive time evolution. Instead, we experimentally fix the pulse time to 3 μs to a high degree of precision and vary the lattice depth via a VVA controlling the RF power which directs the lattice beam to the atoms. The optical power is measured using a photodiode. We then compare the photodiode pulse amplitude to the measured scattering peaks to extract the linear relationship between photodiode voltage and the lattice depth. This technique not only eliminates the timing requirements on the pulse but also allows us to calibrate the lattice photodiode using fewer runs of the machine. To this end, we perform the numerics previously outlined for a fixed final pulse time and vary the lattice depth. The results of this calculation are shown in Figure 4.14 and show an oscillatory behavior with lattice depth reminiscent of the time evolution. This evolution masks the fact that there are fast oscillations in time at every point shown.

To minimize any dephasing it is then advantageous to operate at a minimum pulse time to reduce the amount of oscillations in time, which is experimentally limited by the photodiode response time, the AOM response time, and the timing software. The AOM response time is limited by the size of the lattice beam through the AOM aperture, the speed of sound, and the RF drive. For a tellurium dioxide AOM with speed of sound 4.25 km/s and a beam diameter of 1 mm, we approximate the rise time to be approximately 235 ns. The RF switch that controls the RF drive to the AOM has a rise and fall time of 10 ns (ZASWA-2-50DR+). The photodiode has an estimated 100 ns rise time (PDA20CS, 10 MHz), and updated software can run as quickly as 20 ns. As of writing of this thesis, we have found a pulse time of 3 μs to be sufficiently long compared to these experimental considerations.

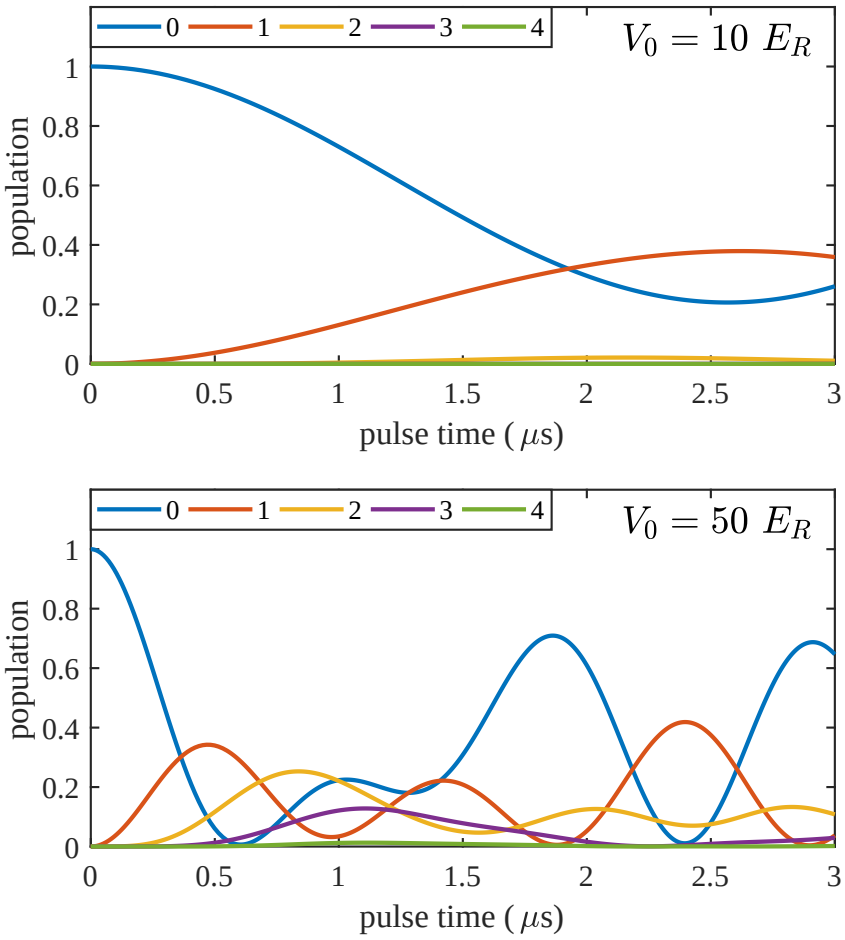

Figure 4.13: Time evolution of the scattering into higher order plane waves modes from the pulsed lattice. The negative modes are not plotted. **(top)** The time evolution for a lattice with depth 10 E_R. The evolution is slow and only a few modes participate. **(bottom)** The time evolution for a lattice with depth 50 E_R. The evolution is faster than of the 10 E_R lattice and more modes participate.

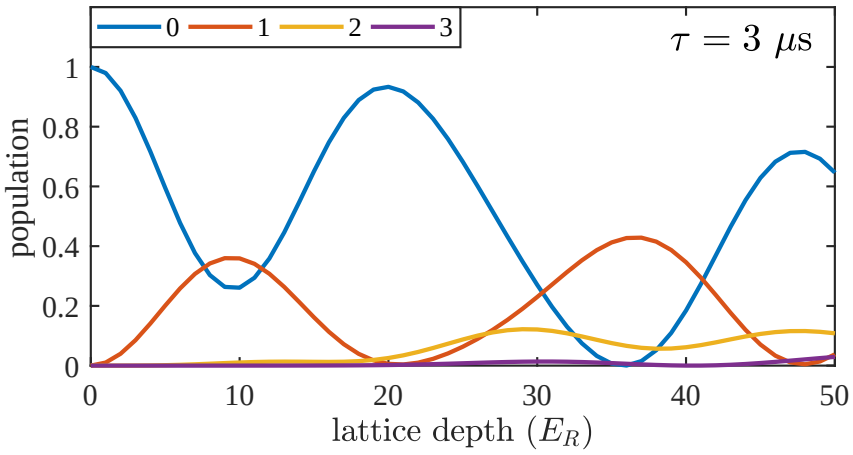

Figure 4.14: Relative momentum populations as function of lattice depth for a pulse time of 3 μs.

The dominant mechanisms leading to dephasing is the finite spatial extent of the lattice beam in comparison to the size of the BEC. Since the pulse time is much shorter than the transverse oscillation period in the ODT and lattice beam, this effectively means that atoms closer to the beam center will feel a higher effective lattice depth. Assuming that the condensate with Gaussian radius σ is centered about the lattice with waist w_0, the transverse lattice depth and radial atom number density $U(r)$ and $\rho(r)$ are given below.

$$U(r) = U_0 \exp\left(-2r^2/w_0^2\right) \tag{4.35}$$

$$\rho(r) = \frac{r}{\sigma^2} \exp\left(-r^2/2\sigma^2\right) \tag{4.36}$$

Where $\rho(r)$ satisfies the normalization constraint $\int \mathrm{d}r\rho(r) = 1$. In addition to smearing out the lattice depth across the condensate this will reduce the effective lattice depth $\langle U \rangle$ in equation 4.37 as shown in Figure 4.15 for realistic experimental parameters. The combination of these effects reduces the dynamic range of the oscillations in the relative

population of the scattering modes especially at large lattice depths and makes accurately calibrating the lattice depth via Figure 4.14 alone difficult.

$$\langle U \rangle = \int_0^\infty U(r)\rho(r) \tag{4.37}$$

To mitigate this effect, we perform a weighted average over the expected probability distribution for $\rho(r)$ and $U(r)$ as shown in Figure 4.16. At higher lattice depths only do the higher scattering modes exhibit oscillatory motion. However, we find that these theoretical predictions are good enough to accurately measure the optical lattice depth using Kapitza-Dirac diffraction.

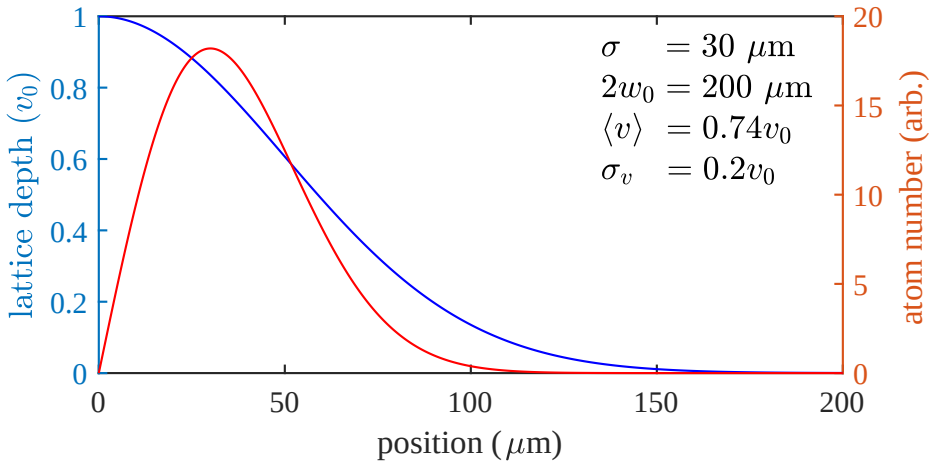

Figure 4.15: Comparing the radial distribution of condensate number and lattice depth for realstic experimental parameters. Here the lattice beam waist w_0 is 30 μm and the condesnate gaussian radius σ is 200 μm.

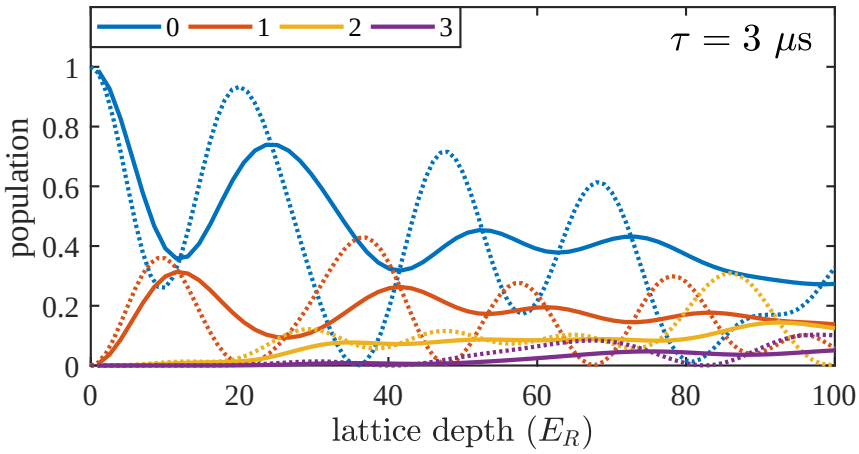

Figure 4.16: Reduction of dynamic range of the oscillations in relative momentum scattering populations due to the finite extent of the lattice beam. Negative scattering modes are no shown, and the relative size of the condensate and lattice beam are as in Figure 4.15. The dashed lines are calculated assuming only a single lattice depth while the solid lines are the expected curves taking the finite extent into account. Not only does the peak-to-peak amplitude change but also does the location of the relative minima and maxima. At large lattice depths only the higher scattering modes exhibit oscillatory dependence on lattice depth.

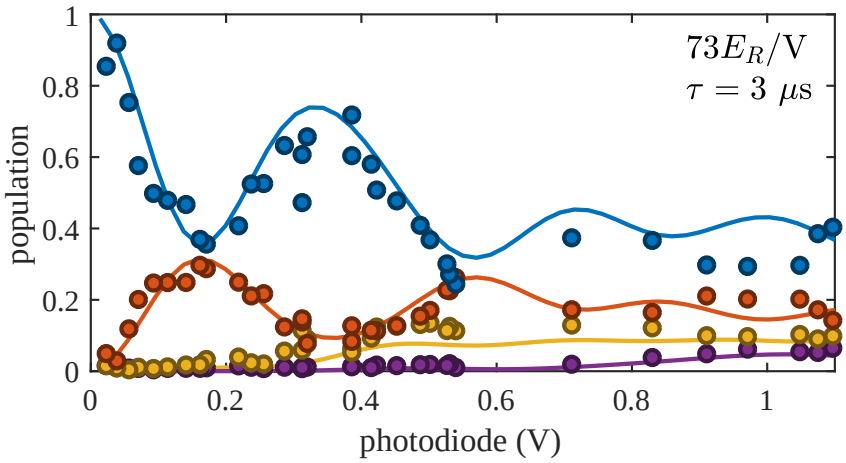

Figure 4.17: Calibrating the optical lattices via Kaptiza-Dirac diffraction. The measured relative population in the scatter modes are compared to the theoretical predictions accounting for the finite extent of the condensate and lattice beam. The pulse time is 3 μs and the fitted calibration is $73E_R$/V. The measured population in the negative and positive modes are averaged.

4.5 Floquet Theory

The experiments in this thesis examine the dynamics of **Floquet** systems which are characterized by a time periodic Hamiltonian as indicated in equation 4.38. In particular, in the case where the drive is fast compared to the dynamics characterized by the time independent part of the Hamiltonian, it is appropriate to consider some effective time independent **Floquet Hamiltonian**. This will be characterized by so called **Floquet eigenstates** with eigenvalues called the **quasienergies** which are the time periodic equivalent of the time independent case. We focus our intuition based upon the analogy between the discrete spatial translation symmetry of crytalline materials to those of the discrete time translation symmetry of Floquet systems. It is the goal of this section to briefly outline the basic theoretical framework for non-interacting Floquet systems, specifically focusing on a few numerical tools utilized to understand the experiments detailed in this thesis. This treatment follows that outlined in [3] and will frequently outsource important calculations.

Our discussion begins by considering the time periodic Hamiltonian as shown in equation 4.38. This implies that the Hamiltonian commutes with the discrete time translation operator $U(T)$.

$$H(t) = H(t+T) \tag{4.38}$$

$$0 = [U(T), H] \tag{4.39}$$

Time evolution is completely understood by knowledge of the operator $U(t)$ for times $t \in [0, T]$ which is diagrammed in Figure 4.18. Furthermore, the stroboscopic unitary time evolution operator can be written with a Hermitian generator G, the Floquet Hamiltonian, which is characterized by eigenvalues $\{\epsilon_n\}$ called the quasienergies.

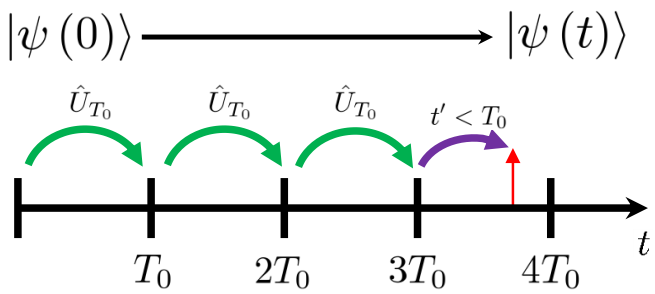

Figure 4.18: Time evolution by the stroboscopic time evolution operator. Time evolution for any time t is described by some integer number of evolution by the drive period and a part for time $t < T_0$.

$$U(T) := \exp\left(iGT/\hbar\right) \tag{4.40}$$

From this, it can be shown that time evolution can be written as

$$|\psi(t)\rangle = \sum_n a_n |u_n(t)\rangle e^{-i\epsilon_n t/\hbar} \tag{4.41}$$

where $|u_n(t)\rangle$ are the T periodic Floquet functions and a_n are time independent coefficients. This is highly reminiscent of time evolution under a static Hamiltonian except with time periodic basis states, and is why we call G and its spectrum the Floquet Hamiltonian and quasienergies. A key difference is that since G is defined by the stroboscopic time evolution operator, any eigenvalue is only defined up to $\hbar\omega$ where $\omega = 2\pi/T$.

$$\exp(i(\epsilon + n\hbar\omega)T/\hbar) = \exp(i\epsilon T/\hbar), \quad n \in \mathbb{Z} \tag{4.42}$$

It is useful then to define all the quasienergies with respect to a *first quasienergy Brillouin zone* as defined by equation 4.43.

$$\epsilon_n \in [-\hbar\omega/2, \hbar\omega/2] \tag{4.43}$$

This naming convention is draw a direct comparison to the first Brillouin zone of quasimomentum for crystalline materials. Continuous spatial translation symmetry is exchanged for a discrete one $[U(x \to x + a), H] = 0$. The eigenstates are described by spatial periodic bloch waves characterized by a quasimomentum k defined only up to a reciprocal lattice vector $2\pi/a$. From a computational standpoint, equation 4.43 raises the issue in that there is no a priori quasienergy ordering. However, an appropriate ordering typically arises from knowledge of the specifics of the driven system which we shall demonstrate later through case studies. In particular we shall focus on the case of the amplitude modulated optical lattice potential.

4.6 Floquet Band Engineering

The starting point shall be the amplitude modulated lattice Hamiltonian of equation 4.23.

$$h = -\partial_\phi^2 v_0 \left(1 + \alpha \sin(\omega t)\right) \cos^2(\phi) \tag{4.44}$$

Instead of considering the dynamics from a Fermi's golden rule perspective where atoms are transferred to the excited band, we shall consider solving for the new single particle Floquet eigenstates and their quasienergy bands. Using our intuition from the static lattice Hamiltonian and amplitude modulation spectroscopy, we anticipate the opening of gaps in the quasienergy spectrum given by the resonance condition of equation 4.24 which we reshow below. This can be visualized by "folding" the static lattice bands by integer multiples of the drive energy using equation 4.46. Wherever there are band crossings in the folded spectrum, we expect a gap to open for finite drive strength depending on the coupling strength χ of equation 4.25. Such a procedure is shown in Figure 4.19 for a static depth of $5.4E_R$ and a modulation frequency of 210 kHz.

$$n\hbar\omega = \epsilon(i,k) - \epsilon(j,k) \quad n \in \mathbb{Z} \tag{4.45}$$

$$\epsilon_{\text{fold}}(i,k) = \text{mod}(\epsilon(i,k), \hbar\omega) \tag{4.46}$$

Calculation of the quasienergy band structure is done by numerical diagonalization of the Floquet Hamiltonian derived from the stroboscopic time evolution operator $U(T)$. This done by calculating the time dependent Hamiltonian $H(\{t_i\}, k)$ over a discrete mesh $\{t_i\}$ with a time dependent amplitude of equation 4.23. Time evolution of each time step $\Delta t = t_{i+1} - t_i$ is calculated using either the Crank Nicolson method in equation 4.48 or the exponential midpoint method in equation 4.49. The stroboscopic time evolution

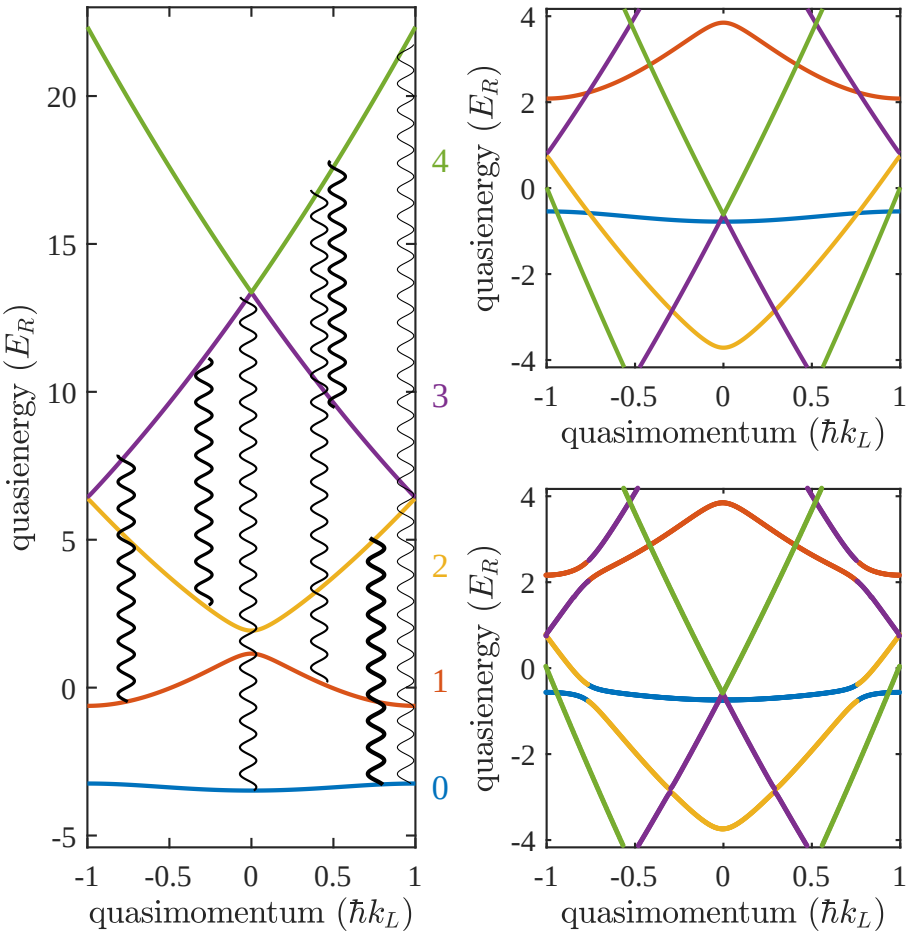

Figure 4.19: Calculating the Floquet quasienergy spectrum of an amplitude modulated optical lattice. The static lattice depth is $5.4E_R$, $\alpha = 0.4$, and the modulation frequency 210 kHz which sets the first quasienergy Brillouin zone to be $8.34E_R$. **(left)** Visualization of interband resonances induced from the amplitude modulation. The static lattice band structure is plotted as colored lines. The resonances are indicated by the squiggly lines where the linewidth indicates the photon number of the excitation. For visual simplicity each transition is only drawn on one side of the Brillouin zone. **(top right)** The folded energy band structure for the first few bands as shown on the left. **(bottom right)** The calculated quasienergy band strucutre. Gaps open at the interband structure depending on the coupling strength. The plotted bands are the ones that have the highest overlap with the static states and color coded accordingly.

operator is then calculated by the product over each discrete time evolution operator.

$$U(T) \approx U(t_1)U(t_2)....U(t_N) \tag{4.47}$$

$$U(t+\Delta t, t) = \frac{I - \frac{i\Delta t}{2}h(t+\frac{\Delta t}{2})}{I + \frac{i\Delta t}{2}h(t+\frac{\Delta t}{2})} \tag{4.48}$$

$$U(t+\Delta t, t) = e^{-i\Delta t h(t+\Delta t/2)} \tag{4.49}$$

From there, the Floquet Hamiltonian is found from matrix manipulation and the spectrum then calculated by numerical diagonalization

$$U(T) = \exp\left[-2\pi i G(\omega_R/\omega)\right] \tag{4.50}$$

$$G(k) = i\frac{1}{2\pi}\frac{\omega_R}{\omega}\log(U(T)) \tag{4.51}$$

$$\{\tilde{\epsilon}(n,k)\} = \mathrm{eig}(G(k)) \tag{4.52}$$

This then raises the issue of quasienergy ordering as in principle one must account for the entire spectrum $\{\tilde{\epsilon}(n,k)\}$ as demonstrated in Figure 4.21. In the experiments of this thesis we are typically interested in hybridization between the ground band and one of the low lying excited bands. To this end, we can select out the desired Floquet state $|\tilde{\epsilon}(n,k)\rangle$ by computing its probability overlap with the unperturbed spectrum $|\epsilon(n,k)\rangle$, and only examining those states with large overlap.

$$P = |\langle\tilde{\epsilon}(n,k)|\epsilon(n,k)\rangle|^2 \tag{4.53}$$

The end result is a Floquet band structure which demonstrates the hybridization of those specific bands as shown in Figure 4.19. The spectrum does indeed show the opening of gaps at the predicted resonances where the gap size depends on the matrix coupling χ. The discrimination process of equation 4.53 also makes it possible to isolate

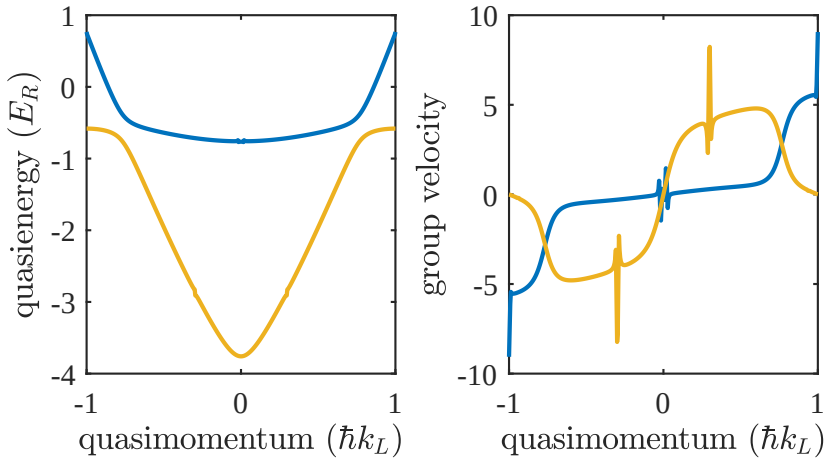

Figure 4.20: Analyzing the hybridized band, for the modulation parameters of Figure 4.19. **(left)** The hybrid bands corresponding to the static bands $n = 0$ and $n = 2$. **(right)** The numerically calculated group velocity using the calculated band structure. The discontinuities are consequences of higher order resonance and the computational uncertainty associated with 4.53

and analyze a particular hybrid band $\tilde{\epsilon}(n, k)$. Ignoring higher order resonances and interaction mediated effects, the hybrid band functions exactly like the static band under the stroboscopic assumption. Therefore by tuning the drive conditions α and ω, a wide variety of Floquet Bloch bands can be constructed which leads to the terminology **Floquet band engineering**. In context of this thesis, we are particularly interested in the semi-classical behavior of these systems for which we obtain a modified group velocity determined by the hybrid band.

$$v_g = \frac{\partial \tilde{\epsilon}(n, k)}{\partial k} \tag{4.54}$$

By utilizing the discrimination criterion of equation 4.53 we can isolate a particular hybridized band $\tilde{\epsilon}(n, k)$ and examine the group velocity as shown in Figure 4.20.

But is the post selection process of equation 4.53 physically motivated? Since we typically consider atoms initialized in the ground band, it appropriate to reduce this question to whether multi-photon coupling from the ground band is significant enough to affect the system. While in general this will depend on the particulars of the experiment,

it is a statement regarding the effect of an $\mathcal{O}(n)$ perturbation theory where n is the photon number, which in this case goes as the coupling strength χ^n. The strength of these couplings can therefore be directly observed by the size of the gaps that they open in the spectrum which is outlined in Figure 4.22. Crossing between the perturbative and strongly driven limit is directly investigated in the experiments of this thesis.

In some sense, the success of equation 4.53 in defining a hybrid band structure is a measure of the accuracy of a perturbing limit where the new eigenstates resemble those of the static Hamiltonian but slightly modified. This prompts us to consider the strongly driven limit for which we plot the quasienergy band structure in Figure 4.23. As the drive strength α increase the resultant quasienergy spectrum becomes increasingly deformed and multi photon resonances become more pronounced.

Another extension of this revolves around increasing the complexity of the drive. Instead of the single frequency modulation consider instead a polychromatic drive

$$h = -\partial_\phi^2 + v_0 \left(1 + \sum_i \alpha_i \sin(\omega_i t)\right) \tag{4.55}$$

where the relative phases have been eliminated to maintain the static lattice depth at $t = 0$. The numerical treatment is the same as before expect that the size of the first quasienergy Brillouin zone is decreased due to longer total repetition period.

$$\Omega = \frac{2\pi}{\mathrm{LCM}(\{T_i\})} \tag{4.56}$$

The result of such a calculation is presented in Figure 4.24 for a static lattice depth of $5E_R$ $\alpha_1 = \alpha_2 = 0.4$ and $f_1 = 2f_2 = 160$ kHz, where we have chosen a relatively simple modulation scheme to simplify the quasienergy band structure.

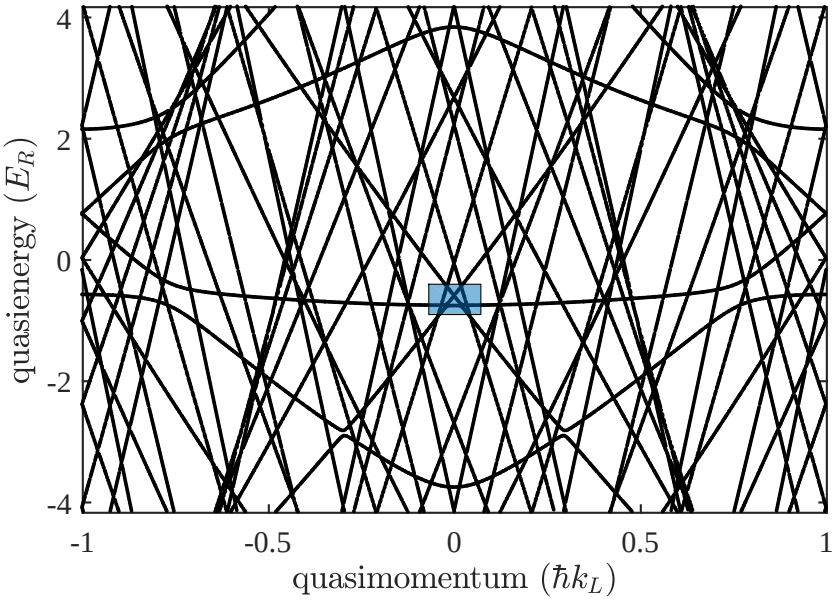

Figure 4.21: Distinguishing relevant quasienergies. For the same parameters as Figure 4.19, the quasienergy spectrum is plotted for the lowest fifteen hybrid bands chosen to elucidate the problem. Without imposing an external condition on what quasienergies to use, the spectrum becomes complicated quite quickly which in principle has the same cardinality of the static lattice system - infinite.

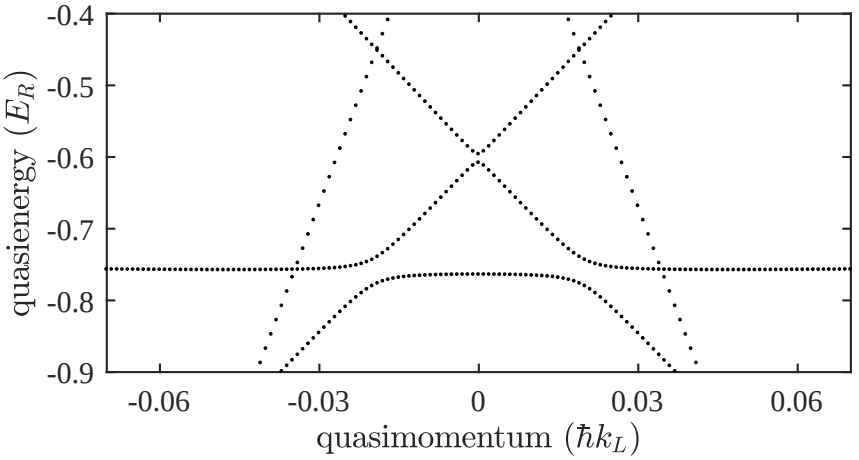

Figure 4.22: Higher order resonances. The same data as Figure 4.21 except zoomed in on the blue shaded region. The gap here represents a two photon coupling between the ground band and the third excited band.

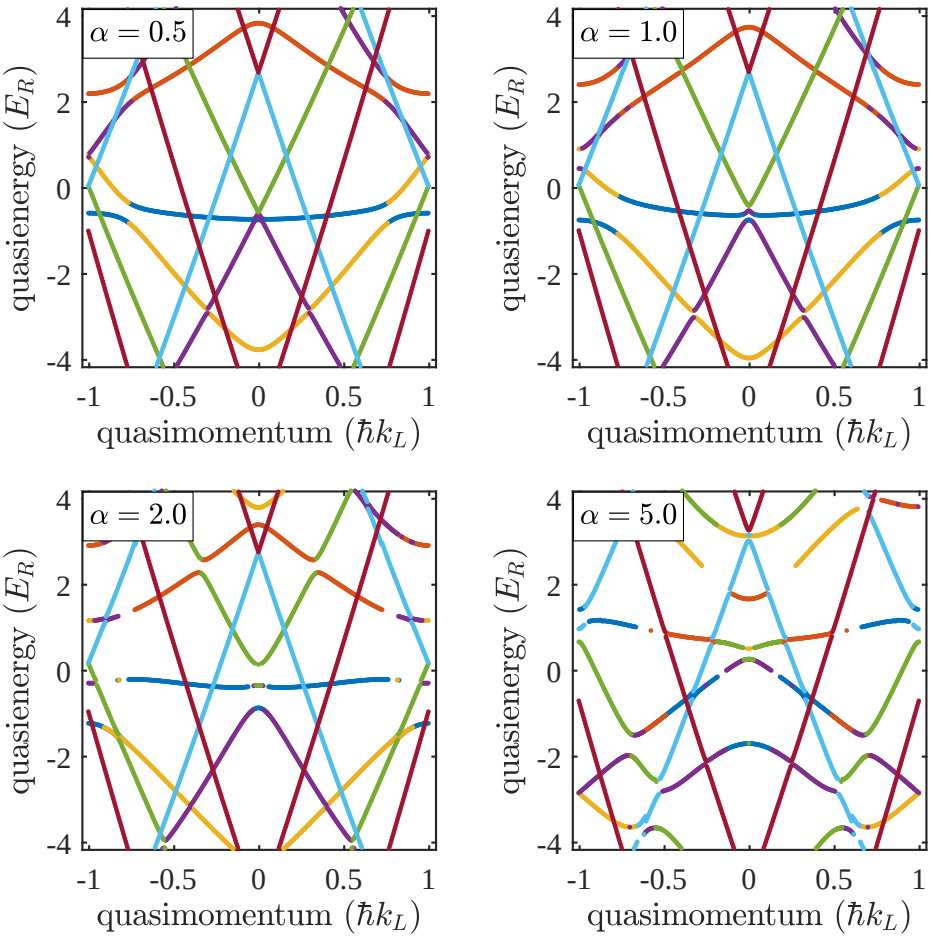

Figure 4.23: Exploring the strongly driven limit. Here the static lattice depth is $5.4E_R$, the modulation frequency is 210 kHz, and the driving strength $\alpha = 0.5, 1, 2, 5$ as is indicated in each plot. In the weakly driven limit the Floquet bands are well described by a the original static bands hybridized at the resonant condition. However, as the drive strength increases the resultant spectrum becomes almost unrecognizable as multiphoton processes become relevant and avoided crossing strongly perturb the band structure. Apparant discontinuities in the spectrum are a consequence of the finite number of bands considered in discrimination process. Note that the modulation strength of the bottom right panel is only half that explored in Chapter 8.

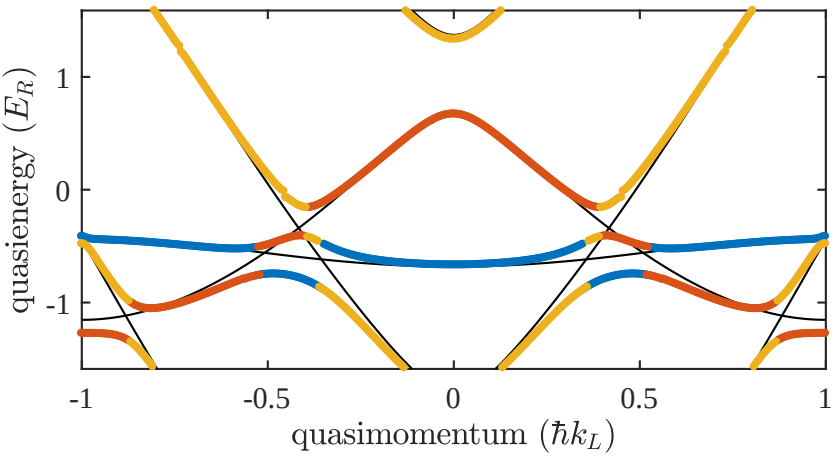

Figure 4.24: Floquet-Bloch bands for polychromatic driving. The static lattice depth is $5E_R$, $\alpha = .4$, and $f_1 = 2f_2 = 160$ kHz. Observe that all three bands mix at a point in quasimomentum.

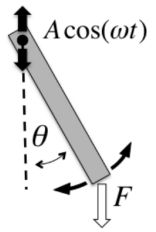

Figure 4.25: The classical Kapitza pendulum. A rigid rotor's pivot is modulated at some fixed frequency ω and amplitude A.

4.7 Optical Lattice Kapitza Pendulum

As discussed in the previous section, the limit of strong driving complicates the interpretation that amplitude modulation hybridizes the static bands into a new quasienergy spectrum. This raises the question of how to appropriately think of the strongly driven limit, and we glean intuition from the classical limit. As shall be demonstrated in this section and alluded to in Figure 4.25, the driven optical lattice has a one to one classical mapping onto the driven rotor of the Kapitza pendulum. This driven pendulum is a prototypical driven system which exhibits driving dependent stability. Using this analogy we therefore recast interpreting the strongly driven amplitude modulated lattice as an **optical lattice Kapitza pendulum**. In particular, we shall focus on the two potentially stable fixed points of motion which are the so called "normal" and "inverted" positions which correspond to stability about the time average energy minima and maxima respectively. After a discussion about the classical dynamics we shall then delve into the quantum limit.

4.7.1 Kapitza Pendulum

The classical Kapitza pendulum shown in Figure 4.25 consists of rigid rotor whose pivot position is modulated parallel to gravity. The full equation of motion is shown

below [24].

$$mr^2\frac{d^2\theta}{dt^2} + b\frac{d\theta}{dt} + mr\left[g - A\omega^2\cos(\omega t)\right]\sin(\theta) = 0 \tag{4.57}$$

where b is a damping parameter, m is the mass of the pendulum, r is the length, θ is the angular displacement measured from the vertical down position, A is the modulation amplitude, and ω is the drive frequency. If time is normalized via the transformation $\tau = \omega t$ the equation of motion becomes

$$\frac{d^2\theta}{d\tau^2} + \left(\frac{1}{\Omega Q}\right)\frac{d\theta}{d\tau} + \left[\left(\frac{1}{\Omega^2}\right) - \left(\frac{A}{r}\right)\cos(\tau)\right]\sin(\theta) = 0, \tag{4.58}$$

where the quality factor $Q = \frac{\omega_0 mr^2}{b}$ and the normalized drive frequency $\Omega = \frac{\omega}{\omega_0}$, where ω_0 is the undamped natural frequency $\omega_0 = \sqrt{\frac{g}{r}}$. Since we are interested in the localized motion which occurs when the time average force goes to zero , we shall consider small deviations about the fixed points $\theta = 0$ and $\theta = \pi$ which further simplify the equation of motion to

$$\frac{d^2\theta}{d\tau^2} + \beta\frac{d\theta}{d\tau} \pm \left[\delta + \epsilon\cos(\tau)\right]\theta = 0 \tag{4.59}$$

where $\beta = 1/\Omega Q$, $\delta = 1/\Omega^2$, and $\epsilon = A/r$. Here, $\delta > 0$ is for motion about $\theta = 0$ and $\delta < 0$ is for motion about $\theta = \pi$. In the limit of weak damping β the canonical Mathieu equation is obtained.

$$\frac{d^2\theta}{d\tau^2} \pm \left[\delta + \epsilon\cos(\tau)\right]\theta = 0 \tag{4.60}$$

The relevance of the transformation of equation 4.57 into equation 4.60 is that the stability of small oscillations for the Kapitza pendulum about the fixed points is governed by the stability of the Mathieu equation, which depends on the parameters δ and ϵ. In particular, the fixed point $\theta = \pi$ represents stability that is not present in the absence of

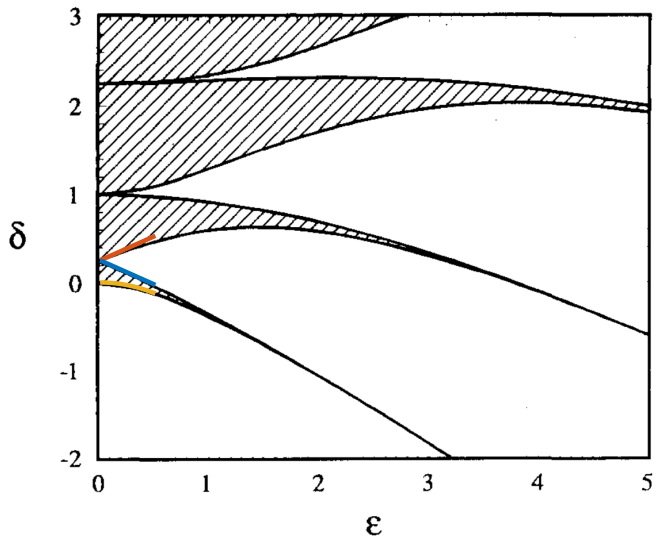

Figure 4.26: Stability of the Mathieu equation where shaded regions are stable. Negative δ corresponds to inverted stability about $\theta = \pi$ while positive δ corresponds to normal stability about $\theta = 0$. The approximate curves for the low ϵ that bound the stability are shown.

the drive. Stability over the δ-ϵ phase space is shown in Figure 4.26[24]. The observation that the region of stability for $\delta < 0$ is smaller than that for $\delta > 0$ is indicative that the inverted stability about $\theta = \pi$ has more stringent requirements than that of $\theta = 0$. For small ϵ the region of inverted stability is approximately bounded by the curves given by equations 4.61 and 4.62 while the region of normal stability is approximately bounded by equation 4.63.

$$\delta \approx -\frac{1}{2}\epsilon^2 \tag{4.61}$$

$$\delta \approx 0.556\epsilon - 1/4 \tag{4.62}$$

$$\delta \approx -0.556\epsilon + 1/4 \tag{4.63}$$

4.7.2 Mapping parameters

Mapping the driven lattice onto the the Kapitza pendulum is most easily done starting from the dimensionful Hamiltonian of equation 4.64. The Euler Lagrange equations determine the classical equation of motion of equation 4.65.

$$H = \frac{1}{2}m\dot{x}^2 + V_0(1 + \alpha\sin(\omega t))\cos^2(k_L x) \tag{4.64}$$

$$m\ddot{x} = -k\sin(2kx)V_0\left(1 + \alpha\sin(\omega t)\right) \tag{4.65}$$

Motivated by the frequency scaling of the Kapitza pendulum, we consider small oscillations about the static lattice where $\alpha = 0$ about $x = 0$

$$\ddot{x} = -\frac{k}{m}V_0\sin\left(2kx\right) \tag{4.66}$$

$$\ddot{x} \approx -\frac{2V_0k^2}{m}x \tag{4.67}$$

$$\rightarrow \omega_0 = 2\omega_R\sqrt{v_0} \tag{4.68}$$

The entire equation of motion is then undimensionalized through the parametrization of $kx = \phi$ and $\omega_0 t = \tau$

$$m\frac{\omega_0^2}{k}\frac{\partial^2\phi}{\partial\tau^2} = -2k\sin\left(2\phi\right)V_0\left(1 + \alpha\sin\left(\Omega\tau\right)\right) \tag{4.69}$$

$$\frac{\partial^2\phi}{\partial\tau^2} = -\frac{\sin(2\phi)}{2}\left(1 + \alpha\sin\left(\Omega\tau\right)\right), \tag{4.70}$$

where $\Omega = \omega/\omega_0$. Mapping onto the Mathieu equations is performed by taking the small angle limit and transforming $\Omega\tau \rightarrow \tau$ (equivalent to $\tau = \omega t$).

$$\frac{\partial^2\phi}{\partial\tau^2} + \phi\left(\Omega^2 + \Omega^2\alpha\sin\left(\tau\right)\right) = 0 \tag{4.71}$$

Parameter	Lattice Value	Kapitza Pendulum Value
$1/\delta$	Ω^2	Ω^2
ϵ	α/Ω^2	A_{mod}/r
Ω	ω/ω_0	ω/ω_0
ω_0	$2\omega_R\sqrt{v_0}$	$\sqrt{g/r}$

Figure 4.27: Mapping the parameters of the Kapitza pendulum and modulated lattice onto the Mathieu equation.

A summary of the parameter mapping is given in Figure 4.27. An interesting note is that the mapping from the optical lattice system to the pendulum system goes beyond that of the small angle approximation and is therefore valid beyond the Mathieu equation. The primary difference being the exchange of the compact parameter θ with the extended parameter x. Furthermore, we note that for the lattice case in the infinite frequency limit, the relative strength of the modulation $\epsilon \to 0$ which motivates increasing the modulation strength α with Ω^2. The approximate bounding curves of equations 4.61 to 4.63 transform to following

$$\Omega \approx \sqrt{\alpha}/2 \tag{4.72}$$

$$\Omega \approx 2\sqrt{0.556\alpha + 1} \tag{4.73}$$

$$\Omega \approx 2\sqrt{1 - 0.556\alpha} \tag{4.74}$$

4.7.3 Classical Numerics

Numerical calculations of the classical stability are conducted assuming a constant lattice depth v_0 for which the equation of motion of equation 4.70 is most applicable. Time evolution is numerically performed using MATLAB's ode45 function after converting equation 4.70 into two first order differential equations with initial angle $\phi_i = 0$ or $\phi_i = \pi$. For a given initial velocity $\dot{\phi}_i$ the stability is a binary measurement of whether

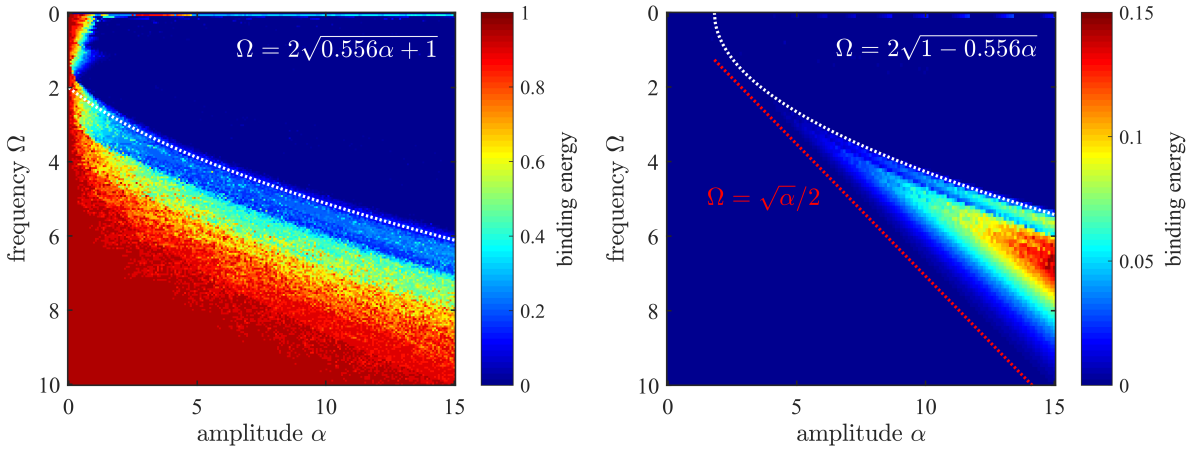

Figure 4.28: Classically predicted stabiity of the optical lattice Kapitza pendulum via the binding energy. The predicted boundaries for stability given by the Mathieu equation capture the qualitative behavior of stability. **(left)** About $\phi = 0$. **(right)** About $\phi = \pi$.

the atom's position has moved away from the initial lattice site after some long time in the modulation. The binding energy is then estimated by finding the critical speed v_c such that for $\dot{\phi}_i > v_c$ the atom is unstable about the initial position. This is averaged for velocities $\pm v_c$. No damping parameter is used.

The results of this calculation are shown in Figure 4.28 as function of drive frequency Ω and drive strength α shown for both the normal stability about $\phi = 0$ and the inverted stability $\phi = \pi$. The boundaries of the stability are well approximated by equations 4.72-4.74. Of particular note is that the binding energy of the normal case is maximized as $\Omega \to \infty$ but is not for the inverted case. Specifically, there is a finite region where the inverted position is stable, and this only occurs in the strongly driven limit.

One analytic perspective of this behavior is via an effective time independent potential

of the following form [13, 25]

$$V_{\text{eff}} = V_0(q) + \frac{\bar{F}^2(q)}{2m\omega^2} \tag{4.75}$$

$$F = -\frac{\partial V_1(q,t)}{\partial t} \tag{4.76}$$

where V_1 is the time dependent portion of the potential with frequency ω and the bar denotes time averaging over a single cycle. The validity of equation 4.75 depends on a high frequency assumption. The resultant time independent potential of the amplitude modulated lattice is the following

$$V_{1,\text{eff}} = \frac{v_0}{8}\left(\frac{\alpha}{\Omega}\right)^2 \sin^2(2\phi) \tag{4.77}$$

And the total effective potential is shown for some example parameters at a static lattice depth $V_0 = 10E_R$ in Figure 4.29. The curvature and the trap depth at the inverted stable point $\phi = \pi$ is also shown. From these plots we draw a few conclusions about the veracity of the effective potential. From the curvature at $\phi = \pi$ we note that the presence of a positive curvature coincides with the boundary for inverted stability in equation 4.74. However, the potential of equation 4.77 monotonically increases with decreasing frequency Ω which does not agree with the numerically calculated binding energy. Such a breakdown is attributed to inaccuracy of a high frequency assumption of ω [26] [1].

[1]The author thanks Shmuel Fishman for helpful discussions.

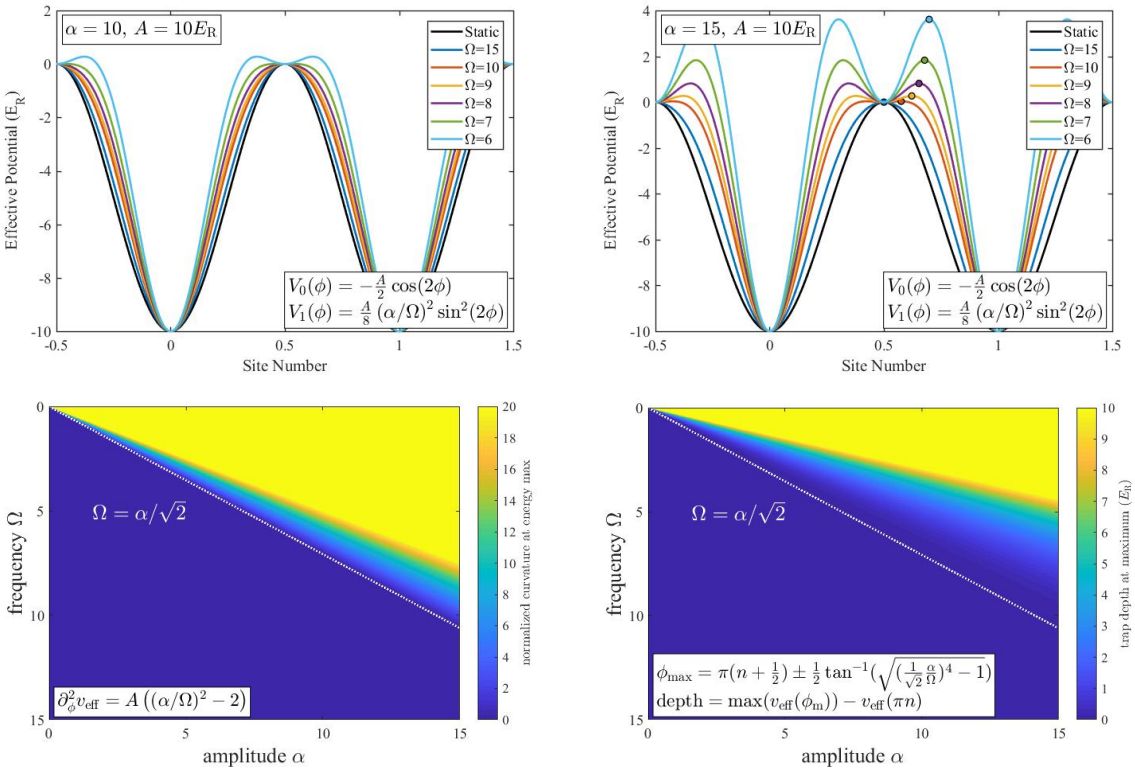

Figure 4.29: Effective time independent potential of the amplitude modulated lattice. **(top)** The effective time independent potential for varying normalized drive frequecny Ω at $\alpha = 10$ (left) and $\alpha = 15$ (right) for a static lattice depth of $10E_R$. Larger α and smaller Ω result in a potential energy landscape that results in a positive curvature at the time average energy maxima which allows for a classically bound state. **(bottom)** The value of the curvature (left) and trap depth (right) at the time average energy maxima as a function of Ω and α. Regions of positive curvature and non-zero trap depth are bounded by the estimated stabiity $\Omega = \alpha/\sqrt{2}$. Notably, the the time independent effective potential is unable to reproduce the low Ω stability boundary as numerically found in Figure 4.28.

Chapter 5

Position Space Bloch oscillations

This chapter includes the contents of our paper, "Observation and uses of position-space Bloch Oscillations".

We report the observation and characterization of position-space Bloch oscillations using cold atoms in a tilted optical lattice. While momentum-space Bloch oscillations are a common feature of optical lattice experiments, the real-space center-of-mass dynamics are typically unresolvable. In a regime of rapid tunneling and low force, we observe real-space Bloch oscillation amplitudes of hundreds of lattice sites, in both ground and excited bands. We demonstrate two unique capabilities enabled by tracking of Bloch dynamics in position space: measurement of the full position-momentum phase-space evolution during a Bloch cycle, and direct imaging of the lattice band structure. These techniques, along with the ability to exert long-distance coherent control of quantum gases without modulation, may open up new possibilities for quantum control and metrology.

Quantum particles in a periodic potential exhibit an oscillatory response to constant forces [28, 29]. During these Bloch oscillations, both the quasimomentum and the position

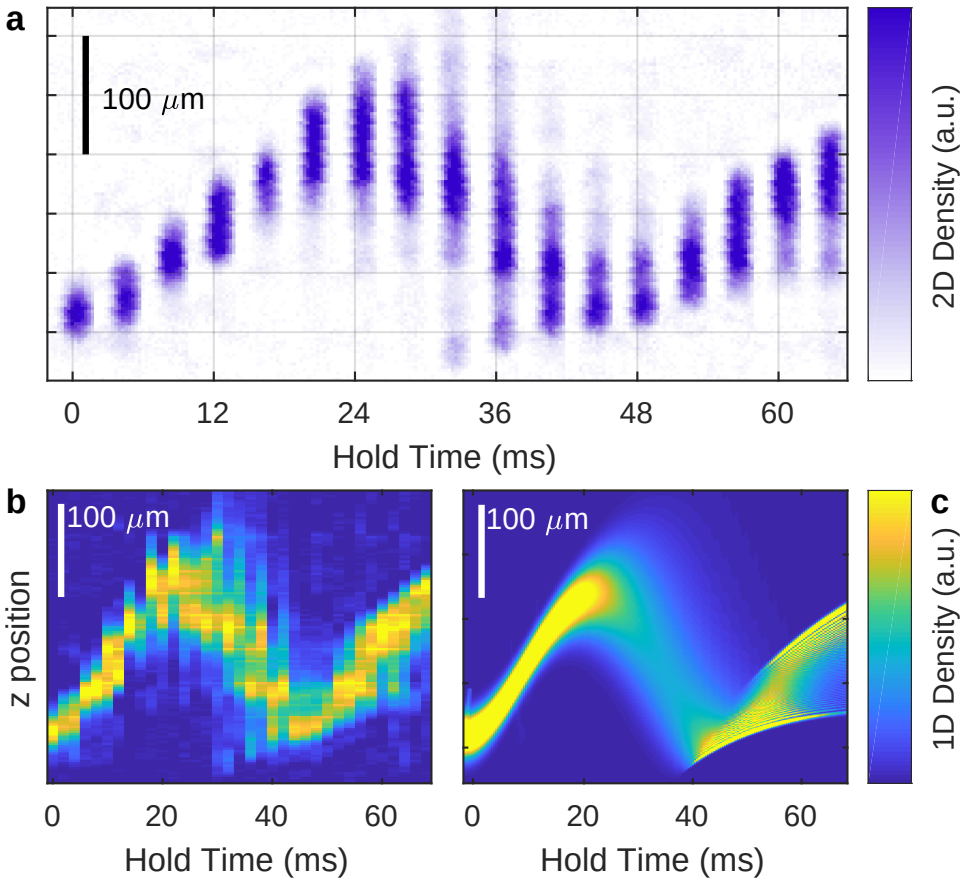

Figure 5.1: Position-space Bloch oscillations. **(a)** Time sequence of in-situ absorption images of atoms in a 5.4 E_R-deep optical lattice subjected to a force corresponding to a Bloch frequency of 21.1 Hz. Each image corresponds to an individual experimental run with the indicated hold time. **(b)** Measured evolution of integrated density distribution as a function of axial position during a Bloch oscillation. **(c)** Numerical GPE prediction for (b), using the split-step Fourier method [27]. Asymmetrical width variation is due to force inhomogeneity.

of the particles evolve periodically, as a direct consequence of the periodicity of the band structure. The resultant localization is a fundamental feature of coherent transport in a lattice. In conventional electronic systems rapid decoherence complicates the observation of Bloch oscillations, though their realization is possible using superlattices [30] and photonic waveguide arrays [31]. Ultracold atomic gases in optical lattices, however, provide a nearly ideal platform for the observation of momentum-space Bloch oscillations [32, 33] and related phenomena, including interaction-dependent effects [34, 35, 36, 37, 38], spatial

breathing modes [39], and control of Bloch dynamics using applied modulations [40, 41]. However, even in cold atom experiments, direct observation of position-space Bloch oscillations of the center of mass has remained elusive. Position-space center-of-mass Bloch oscillations have generally either been inferred through observations of the quasimomentum evolution [32], or artificially magnified using dynamical perturbations for rectification of Bloch dynamics [40]. Thus, in a sense, Zener's original conception of Bloch oscillations has yet to be directly observed with cold atoms.

In this letter, we report the observation and characterization of position space-Bloch oscillations using ultracold ^{7}Li in a tilted optical lattice. Lithium's low mass facilitates the simultaneous realization of fast tunneling and weak tilt which are required for observation of real-space Bloch oscillations, and the shallow zero crossing of lithium's Feshbach resonance allows elimination of interactions. Our experiments begin with a Bose condensate of lithium in an optical lattice. The mean-field behavior can be described by the Gross-Pitaevskii equation (GPE)

$$i\hbar\frac{\partial\Psi}{\partial t} = -\frac{\hbar^2}{2m}\nabla^2\Psi + V(r,z)\Psi + \mathcal{F}z\Psi + g\left|\Psi\right|^2\Psi. \tag{5.1}$$

The potential due to the lattice beams with wavelength $\lambda = 2d = 1064$ nm and an axial parabolic trap of frequency $\omega_0 \simeq 2\pi \times 15.6$ Hz is (in cylindrical coordinates)

$$V = -V_L\cos^2\left(\pi z/d\right)\exp\left(-r^2/2\sigma^2\right) + m\omega_0^2 z^2/2. \tag{5.2}$$

Here $\sigma \simeq 42.5$ μm is the transverse trap width, $\mathcal{F}$ is the applied force, m is the atomic mass, and g is the interaction amplitude which we make negligible by Feshbach tuning. This 3D potential is non-separable, but as transverse dynamics do not play a significant

role a 1D Bose-Hubbard Hamiltonian,

$$\hat{H} = -J \sum_i \hat{a}_{i+1}^\dagger \hat{a}_i + \sum_i \frac{U}{2} \hat{n}_i(\hat{n}_i - 1) + F \sum_i i\hat{n}_i, \tag{5.3}$$

provides an alternative tight-binding single-band description capturing the main features of Bloch oscillations. In Eq. (A.1) $\hat{a}_i^\dagger$ and $\hat{a}_i$ are bosonic creation and annhilation operators at lattice site i, J is the tunneling energy, $\hat{n}_i = \hat{a}_i^\dagger \hat{a}_i$, U is the onsite interaction energy, and $F = \mathcal{F}d$ the energy offset per lattice site due to the force $\mathcal{F}$. Below we quote values for F and J in Hz; multiplication by Planck's constant h yields an energy in Joules. By Feshbach tuning to the scattering length zero-crossing we are able to operate in the $J \gg F \gg U$ regime for the entirety of the experiment, avoiding interaction-induced dephasing and instabilities [42, 43, 44, 45]. When an atomic ensemble is subjected to this Hamiltonian in this regime, the center of mass position oscillates at the Bloch frequency $f_B = F/h$ with oscillation amplitude given by the Wannier-Stark localization length $l_{WS} = 2J/F$ [29, 32].

The experiments begin with creation of a Bose condensate of approximately 10^5 ^{7}Li atoms in the $|F = 1, m_F = 1\rangle$ hyperfine state in a crossed optical dipole trap. After evaporation, the magnetic field is ramped to the scattering length zero crossing near 543.6 G in 100 ms [17]. The condensate is then loaded into the optical lattice in 100 ms, initializing the atomic ensemble into the ground band around zero quasimomentum. By varying the lattice laser power the depth V_L is adjusted between 4 and 15 E_R (calibrated with amplitude modulation spectroscopy), where $E_R = \hbar^2 k_L^2/2m$ is the recoil energy and $k_L = 2\pi/\lambda$ is the lattice wavevector. For a given V_L, band structure calculations determine J [46]. A magnetic field gradient along the lattice direction creates a tunable applied force giving rise to a Bloch frequency f_B between 20 and 50 Hz. The optical dipole trap is suddenly switched off to initiate Bloch oscillations at a constant force. For

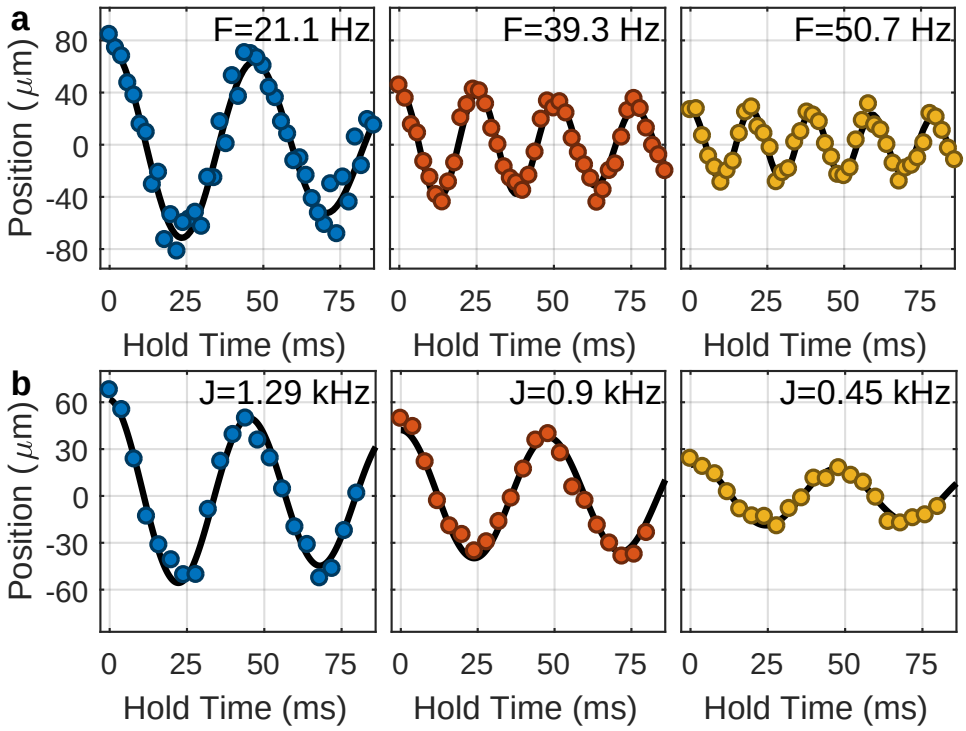

Figure 5.2: Characterization of position-space Bloch oscillations. **(a)** Ensemble position versus time during Bloch oscillations at different forces with a constant tunneling rate $J = 1.55$ kHz. **(b)** Position versus time during Bloch oscillations with different tunneling rates at a constant force of $F = 23$ Hz. Solid black lines in (a) and (b) are fits to damped sinusoids; thicker solid red lines in (a) are the result of numerical GPE calculations.

an atomic ensemble in a band with a dispersion relation $E(k)$, the mean position $x(t)$ evolves in time according to the group velocity:

$$\frac{dx(t)}{dt} = \frac{1}{\hbar}\frac{\partial E(t)}{\partial k}. \tag{5.4}$$

After a variable hold time during which Bloch oscillations occur, the in-situ spatial distribution of the atomic ensemble is measured using absorption imaging.

Fig. 5.1 presents a typical measurement of position-space Bloch oscillations. As the quasimomentum linearly increases, the center of mass position evolves according to Eq. (5.4), changing direction after a Bragg scattering event at the edge of the Bril-

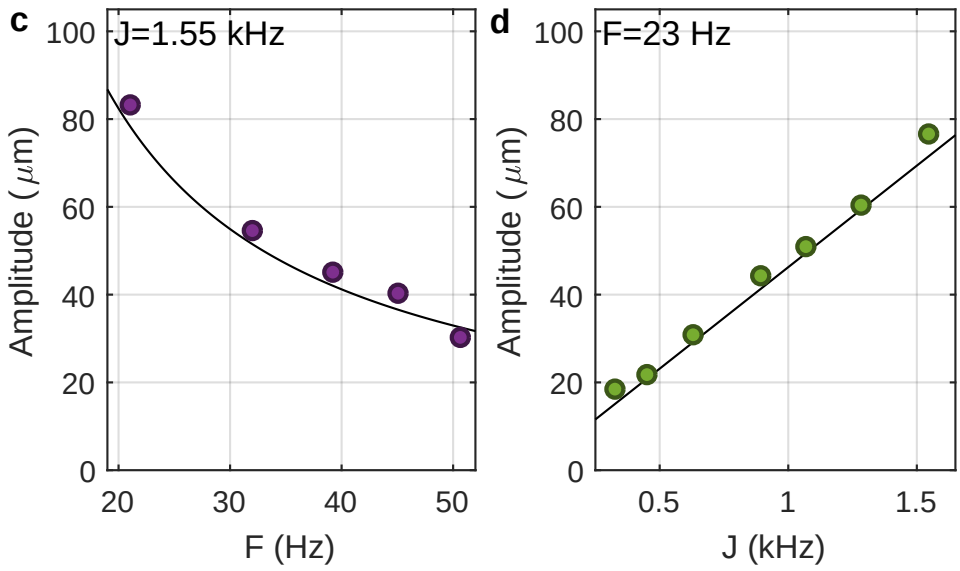

Figure 5.3: Characterization of position-space Bloch oscillations. **(c)** Bloch oscillation amplitude as a function of force at $J = 1.55$ kHz. **(d)** Bloch oscillation amplitude as a function of tunneling rate at $F = 23$ Hz. Solid lines in (c) and (d) represent the predicted $l_{WS} = 2J/F$ with no fit parameters.

louin zone and oscillating with an amplitude of over 150 μm ($\simeq$300 lattice sites). The measured oscillation amplitude and frequency are consistent with theoretical predictions for l_{WS} and f_B, and the detailed dynamics are in agreement with the results of numerical GPE calculations shown in Fig. 5.1c. The direct measurement of position-space atomic Bloch oscillations of the center of mass in the absence of any external modulation is the first main result of this paper.

To characterize the position-space Bloch dynamics, we directly probe the dependence of the Wannier-Stark localization length l_{WS} on tunable system parameters by repeating the measurement of Fig. 5.1 at varying values of J and F. Fig. 5.3a shows position-space Bloch oscillations for different applied forces at a constant tunneling rate $J = 1.55$ kHz. The measured initial oscillation amplitude depends inversely on the force (Fig. 5.3c), and agrees quantitatively with the expected localization length l_{WS}. The observed decrease of the oscillation amplitude with increasing hold time is consistent with expectations due

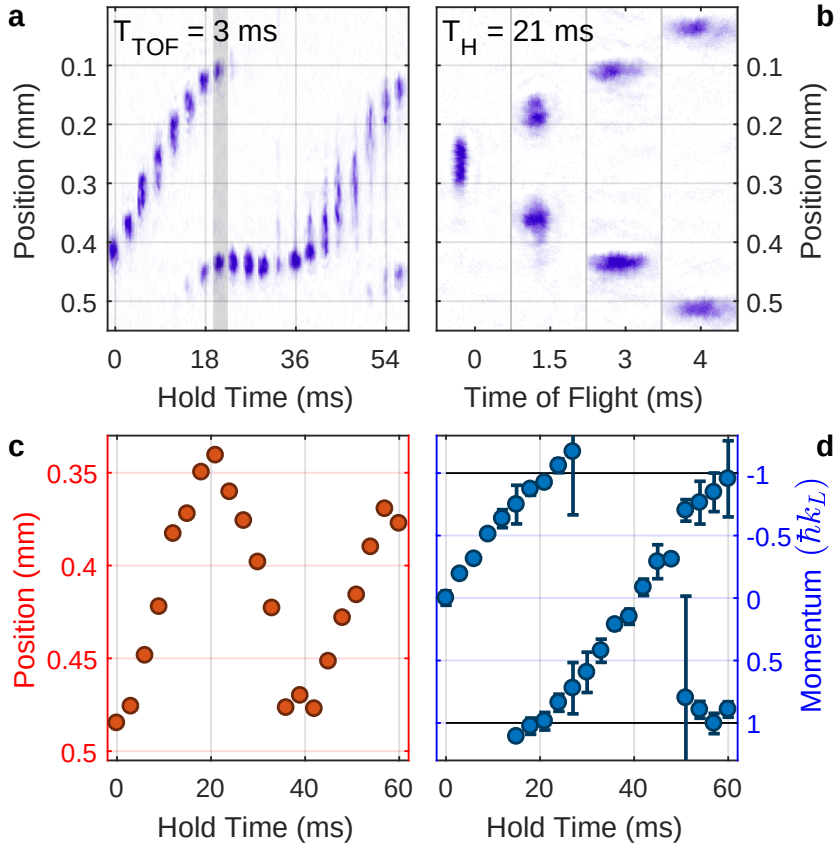

Figure 5.4: Phase-space evolution during a Bloch oscillation. Here $J = 1.55$ kHz and $F = 23$ Hz. **(a)** Absorption images of the atomic distribution after a 3 ms time of flight. The distribution at each hold time is a convolution of initial quasimomentum and position. **(b)** Absorption images after varying times of flight, for a hold time of 21 ms. The initial quasimomentum can be extracted via a linear fit. **(c,d)** Ensemble position and momentum versus time during a Bloch oscillation. Where multiple momentum peaks can be distinguished, both are plotted.

to the axial harmonic confinement [47], and with numerical GPE calculations. Fig. 5.3b and Fig. 5.3d present a complementary measurement, in which tunneling rates were varied at a constant force. The measured oscillation amplitude increases linearly with the tunneling rate J and is again in agreement with the theoretically expected value of l_{WS}, with no adjustable fit parameters.

To elucidate the connection between real-space Bloch oscillations and previously-studied momentum-space Bloch oscillations, we measure the quasimomentum evolution.

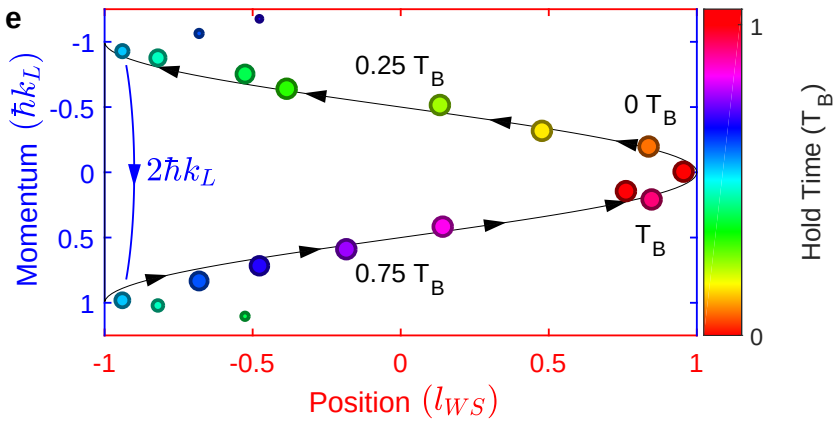

Figure 5.5: Phase-space evolution during a Bloch oscillation. Here $J = 1.55$ kHz and $F = 23$ Hz. **(e)** Combining (c) and (d) yields the phase space evolution of the ensemble during the first Bloch period $T_B = 1/f_B$. Color map corresponds to the hold time in units of T_B. Where multiple momentum peaks can be distinguished, both are plotted with symbol size indicating relative atom number. At $0.5T_B$, Bragg scattering is observed as a discontinuity of $2\hbar k_L$ in the measured momentum distribution.

In these experiments, instead of imaging the in-situ distribution, we ramp down the lattice depth over 100 μs to map the quasimomentum onto momentum, turn off all traps, and perform absorption imaging of the spatial distribution after some time of flight. For finite time of flight, this image represents a convolution of the quasimomentum distribution and the initial spatial distribution. By performing this measurement at multiple different times of flight we can deconvolve these distributions to measure the evolution of both quasimomentum and position. Fig. 5.5a shows the image of the atomic ensemble after variable hold times and a constant time of flight of 3 ms. The asymmetrical evolution is a result of the position-momentum convolution. At each hold time we repeat the measurement for various times of flight (Fig. 5.5b) and fit the linear translation of the ensemble to extract the quasimomentum. This procedure allows direct comparison of the time evolution of position (Fig. 5.5c) and quasimomentum (Fig. 5.5d). The measured quasimomentum evolves linearly until it Bragg scatters at the edge of the first Brillouin zone. The turning points of the position-space Bloch oscillations are coincident with the

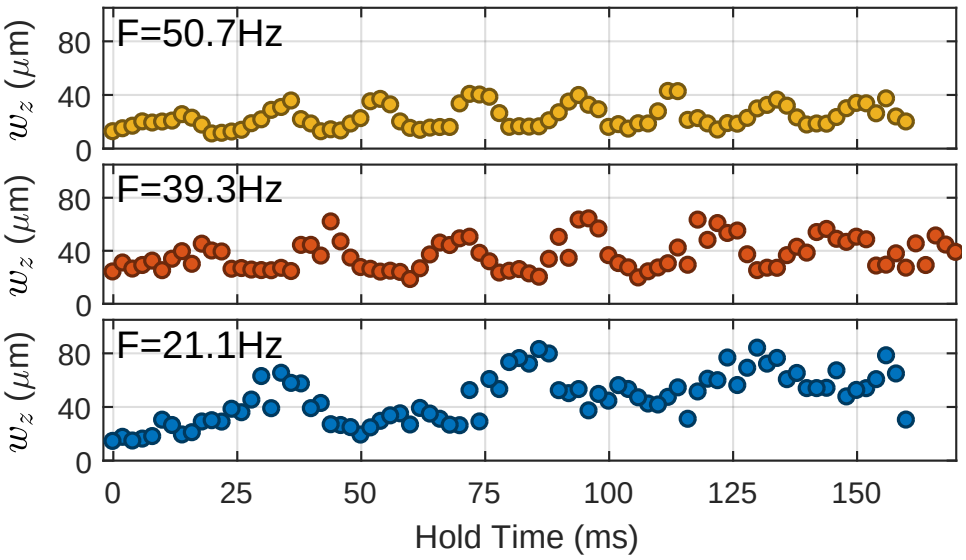

Figure 5.6: Ensemble width evolution during Bloch oscillations. Measured time evolution of the second moment of the atomic distribution w_z for different forces with $J = 1.55$ kHz. Black lines correspond to semi-classical evolution, using the calculated band dispersion, of an ensemble with the measured initial width, and red lines to numerical GPE results. At lower values of F (higher values of l_{WS}), the effects of force inhomogeneity are more pronounced.

measured Bragg scattering events. As a demonstration of the unique scientific utility of accessing both real- and momentum-space Bloch dynamics in the same experiment, we plot in Fig. 5.5e the position-momentum phase space evolution over a single Bloch cycle with period T_B. This directly-measured phase-space image of a Bloch oscillation is the second main result we report.

In addition to center-of-mass oscillations, we also observe oscillations in the width of the atomic cloud. In contrast to previous experiments initialized at a single lattice site [39] and previous theoretical predictions for an ensemble [48, 49], here the width oscillations are dominated by the inhomogeneity in applied force across the large transport distance. We confirm this by measuring the width oscillations for different forces at a constant tunneling rate and comparing them to semi-classical predictions and numerical GPE calculations which include the independently-measured harmonic axial potential

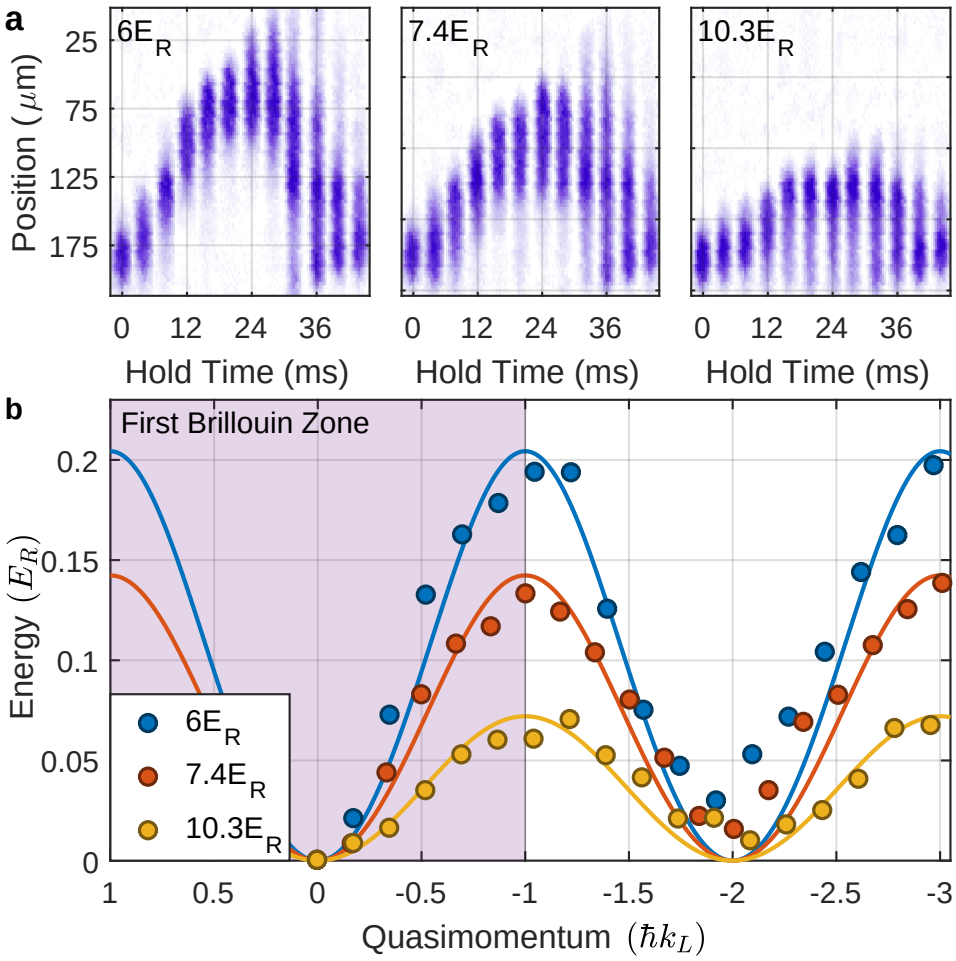

Figure 5.7: Band imaging with position-space Bloch oscillations. **(a)** Time-series images of atomic ensembles undergoing Bloch oscillations in lattice depths of 6 E_R, 7.4 E_R, and 10.3 E_R. **(b)** Measured band structure $E(k)$ for the three lattice depths (circles), determined by scaling the measured center positions from (a) according to Eq. (7.2). Lines show independently-calculated band structures with no adjustable parameters.

(see Fig. 5.6). The good agreement with the two theoretical calculations indicates that the width evolution is a well-understood consequence of force inhomogeneity.

Strikingly, macroscopic position-space Bloch oscillations can also be used to directly image the lattice band structure. Eq. (5.4) indicates that for constant force the band dispersion $E(k)$ is simply the center-of-mass time evolution $x(t)$ during a Bloch cycle

with position and time scaled as

$$E = \frac{hf_B}{d}x, \qquad k = \frac{k_L}{2T_B}t. \tag{5.5}$$

CCD images of real-space Bloch oscillations like those shown in Fig. 5.1a can thus be interpreted as direct images of the lattice band dispersion $E(k)$, in a manner reminiscent of the interpretation of angle-resolved photoemission maps in condensed matter experiments [50, 51]. The Bloch frequency f_B sets the spatial magnification of the band imaging, which can be varied. For a Bloch frequency of 22 Hz, the calculated energy-position conversion factor is 41.6 Hz/μm. In Fig. 5.7 we demonstrate this band imaging technique by comparing the measured position-space Bloch oscillations to the theoretically calculated band structure for a variety of lattice depths. We find good agreement with the expected band structure at each lattice depth without the use of any fit parameters. Asymmetries in the measured band structure are consistent with expectations from the measured force inhomogeneity, and represent the current technical limit on this new band imaging technique. The demonstration of direct band imaging with position-space Bloch oscillations is the third main result we report.

Real-space Bloch oscillations are not limited to the ground band of the lattice. In excited bands of a sinusoidal lattice, much larger-amplitude position-space Bloch oscillations should be possible due to the increased bandwidth. To explore excited-band real-space Bloch dynamics, we transfer population to the first excited band by applying a resonant amplitude modulation pulse after the atoms have Bloch oscillated to $k = 0.5k_L$ in the ground band. The resulting excited-band dynamics are compared to ground-band dynamics in Fig. 5.8. Measured Bloch oscillations in the excited band are, as predicted, characterized by a larger amplitude than ground-band oscillations. The amplitude ratio is consistent with theoretical expectations from band structure calculations.

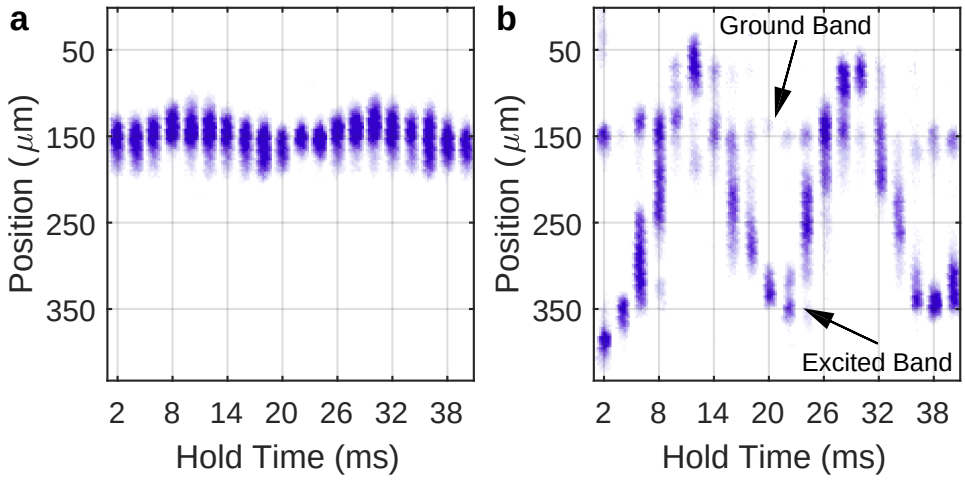

Figure 5.8: Position-space Bloch oscillations in an excited band. The lattice depth is set to $9.5E_R$ and the Bloch frequency to 50.7 Hz. **(a)** Time-series absorption image of ground-band Bloch oscillations. **(b)** Time-series image of Bloch oscillations in the first excited band, which are characterized by the same frequency as ground-band oscillations, but exhibit a significantly larger amplitude due to the larger bandwidth. Also visible is a remnant fraction of atoms in the ground band, due to imperfect excitation. These Bloch-oscillate independently.

In addition to their fundamental interest, real-space Bloch oscillations may serve as a useful tool for quantum metrology and spatiotemporal control. The fine control over transport enabled by the techniques demonstrated here may be of use for atom-interferometric force sensing and gradiometry [52, 53, 54, 55]. New dispersion-control schemes may be enabled by spatially addressing different phases of a Bloch oscillation. Interferometric probes similar to those reported in [56] but in real space are another possible avenue of exploration. Finally, the simplicity of the full phase-space evolution and band dispersion probing techniques we demonstrate opens up the possibility of imaging dynamics and band structures in more complex systems; particularly interesting possibilities include the study of higher-dimensional lattices, Floquet-hybridized bands, and topologically nontrivial bands [57, 58, 59].

In conclusion, we report the experimental observation of position-space Bloch oscillations in an ultracold gas, in both ground and excited bands. The dependence of oscillation

amplitude on applied force and lattice depth are in good agreement with theory. We have used these real-space Bloch oscillations to directly image the full phase-space evolution during a Bloch oscillation, and to perform direct imaging of the structure of a Bloch band.

Chapter 6

Experimental Realization of a Relativistic Harmonic Oscillator

The contents of this chapter include our paper "Experimental Realization of a Relativistic Harmonic Oscillator".

We report the experimental study of a harmonic oscillator in the relativistic regime. The oscillator is composed of Bose-condensed lithium atoms in the third band of an optical lattice, which have an energy-momentum relation nearly identical to that of a massive relativistic particle, with a reduced effective mass and speed of light. Imaging the shape of oscillator trajectories at velocities up to 98% of the effective speed of light reveals a crossover from sinusoidal to nearly photon-like propagation. The existence of a maximum velocity causes the measured period of oscillations to increase with energy; our measurements reveal beyond-leading-order contributions to this relativistic anharmonicity. We observe an intrinsic relativistic dephasing of oscillator ensembles, and a monopole oscillation with exactly the opposite phase of that predicted for non-relativistic harmonic motion. All observed dynamics are in quantitative agreement with longstanding but

hitherto-untested relativistic predictions.

The harmonic oscillator has been a concept of central significance in physics and technology since Galileo's observations of constant-period pendulum motion. The advent of special relativity suggested a simple question: what happens to this archetypal physical system when the maximum oscillator velocity approaches the speed of light? While theories of the relativistic harmonic oscillator have been discussed for decades [60, 61, 62, 63, 64], the combination of special relativity and harmonic motion has proven resistant to physical realization. The infeasibility of realizing harmonic traps with depths on the order of a particle's rest mass energy (Boltzmann's constant times nearly six billion degrees Kelvin for an electron) has motivated work studying relativistic phenomena in disparate physical contexts, including a measurement of the Dirac oscillator spectrum in an array of microwave resonators [65] and proposals and realizations of effective relativistic effects in trapped atoms [66, 67, 68, 69, 70, 71, 72], trapped ions [73, 74, 75], photonic waveguides [76], and graphene [77].

Here we report the experimental realization of a harmonic oscillator in the relativistic regime, using ultracold atoms moving in the third band of an optical lattice. Optical lattices are an ideal context in which to study dynamics in excited bands: previous experiments in higher bands have, for example, observed Bloch oscillations [78], demonstrated coherent matter-wave behavior in higher-bands [79, 80], studied issues relevant to quantum transport [81], measured band nonlinearities and momentum-space Fermi-gas dynamics [82] and demonstrated precise wavepacket manipulation [83, 84]. The results reported here depend crucially upon the ability to image the time evolution of the position of atomic wavepackets in higher bands.

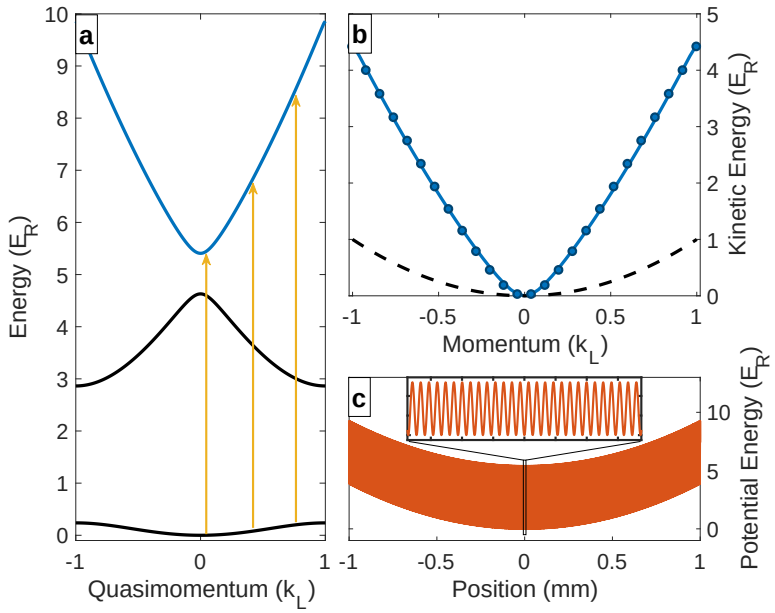

Figure 6.1: Realizing a relativistic harmonic oscillator. **a:** Calculated band structure of 5.4-E_{R}-deep optical lattice. Here $E_{\mathrm{R}} = \hbar^2 k_{\mathrm{L}}^2 / 2m_{\mathrm{Li}}$ is the recoil energy, $k_{\mathrm{L}} = 2\pi/\lambda$ is the lattice wavevector, and $\lambda = 1064$ nm is the wavelength of the lattice laser. Arrows indicate the 137, 170, and 210 kHz excitations used to prepare the three oscillators shown in figure 6.2. **b:** Calculated dispersion relation for the third band (solid line), compared to the relativistic kinetic energy fit (circles). Note the close agreement throughout the Brillouin zone. The free particle dispersion (dashed line) is also shown. **c:** Position-dependent potential energy due to the combination of the lattice and the harmonic confinement. Inset shows a horizontally magnified view of the central 15 μm of the trap.

Einstein's relativistic dispersion relation

$$\mathcal{E}_{\mathrm{rel}} = \sqrt{p^2c^2 + m^2c^4} = \mathcal{E}_{\mathrm{kin}} + mc^2, \tag{6.1}$$

where $\mathcal{E}_{\mathrm{rel}}$ is the energy, $\mathcal{E}_{\mathrm{kin}}$ the kinetic energy, p the momentum, m the effective rest mass, and c the effective speed of light, is achieved in our experiments by placing non-interacting Bose-condensed lithium atoms into the third band of a 1D optical lattice. While it is common to speak informally of any approximately linear higher-band dispersion relation as having "relativistic" character, here we demonstrate a near-exact

quantitative correspondence, which holds throughout the Brillouin zone, between the third-band dispersion and the relativistic kinetic energy of a massive particle (see figure 6.1b). Motion of atoms in the third band will thus have relativistic character to an excellent approximation: atomic trajectories will trace out the worldlines of relativistic particles with effective rest mass m and an effective speed of light c. The addition of a harmonic potential allows the direct experimental study of the worldlines and dynamics of a relativistic harmonic oscillator, with total energy given by $\mathcal{E} = mc^2 + \mathcal{E}_{\text{kin}} + m\omega^2 x^2/2$, where ω is the harmonic oscillator frequency in the non-relativistic limit and x is displacement.

Figure 6.1b compares the third-band dispersion relation to a relativistic fit of the form of equation 6.1, with an effective mass m and effective speed of light c treated as fit parameters. Here, and throughout this article, $c = 143$ mm/s and $m = 0.07\ m_{\text{Li}}$ (roughly half a proton mass). m_{Li} represents the bare atomic mass of lithium in the absence of the lattice. Crucially, the relativistic fit shows excellent agreement throughout the Brillouin zone. The origin of this striking correspondence is the zero-quasimomentum avoided crossing between the second and third bands, which on general grounds is expected to have the same mathematical form as equation 6.1. For momenta much smaller or larger than a lattice recoil, modifications to the relativistic dispersion are anticipated; these momenta are outside the range experimentally probed in this work. It is important to note that the results we report explore the relativistic physics of normal matter, not antimatter, as our band structure does not model the negative-energy branch of the relativistic dispersion. In particular, our relativistic fit involves only the third band, and the gap between the second and third bands is not equal to twice the rest mass energy.

Before describing the experiments it is useful to briefly outline existing predictions for the behavior of a relativistic harmonic oscillator [60, 61, 62, 63, 64]. As the maximum velocity v_{max} approaches c, relativistic effects are expected to modify the character of

harmonic motion in several ways. The shape of the oscillator's trajectory changes from the familiar sinusoidal form in the non-relativistic limit to an increasingly triangular shape indicative of nearly photon-like propagation, with worldline curvature more and more concentrated at the turning points. Physically, this is because the force due to the harmonic confinement is less and less effective at changing the particles' velocity as it approaches the effective speed of light c. For the same reason, the oscillation amplitude diverges as $\beta_{\max} \equiv v_{\max}/c$ approaches 1. Relativistic anharmonicity is manifested by an increase in period with energy and a characteristic monopole oscillation and dephasing of oscillator ensembles initialized with a range of energies. All these behaviors can be quantitatively captured by an exact theoretical model [61]. The relation between coordinate displacement x and coordinate time t that constitutes the theoretically predicted trajectory or worldline of a relativistic oscillator in the lab frame is given by the equations

$$\omega t = \sqrt{2\,(\gamma_0+1)}E\,(\phi,\kappa) - \sqrt{\frac{2}{\gamma_0+1}}F\,(\phi,\kappa) \tag{6.2}$$

$$\omega x/c = \sqrt{2(\gamma_0-1)}\sin\phi \tag{6.3}$$

where $\gamma_0 \equiv \mathcal{E}/mc^2$, the maximum Lorentz factor, is the total energy in units of the rest energy, $\kappa = \sqrt{(\gamma_0-1)/(\gamma_0+1)}$, and F and E are the incomplete elliptic integrals of the first and second kind respectively [61]. Setting $\phi = 2\pi$ in equation 6.2 gives an exact expression for the period T of the motion, which can be Taylor expanded to lowest order in $(\gamma_0 - 1)$ as [60]

$$\frac{T}{T_0} \simeq 1 + \frac{3}{8}(\gamma_0 - 1) = 1 + \frac{3}{16}\frac{\omega^2}{c^2}A^2, \tag{6.4}$$

where T_0 is the oscillator period in the nonrelativistic limit, and the oscillation amplitude

A is related to the total energy as $A = c\sqrt{2(\gamma_0 - 1)}/\omega$. At sufficiently high energies, the trajectories described by equations 6.2 and 6.3 exhibit all the relativistic effects on harmonic motion which are qualitatively described above. Experimental observation and measurement of such trajectories is the main subject of this work.

Here we briefly describe our procedure for Bose-condensing lithium and loading atoms into the third band with tunable energy. The low mass, which gives rise to rapid dynamics, and the shallow scattering length zero-crossing of the low-field Feshbach resonance [17] make Lithium particularly suitable for excited-band experiments. The experiments are initiated by creating a Bose condensate of approximately 10^5 ^{7}Li atoms in the $|F = 1, m_F = 1\rangle$ state at a temperature of 20 nK, produced by evaporation in an optical dipole trap after loading a magneto-optical trap from a collimated atomic beam [11] and precooling with gray molasses [12, 86] and RF evaporation. Atom-atom interactions are set to zero after evaporation by ramping an applied magnetic field to the s-wave scattering length zero-crossing of a Feshbach resonance, at approximately 543.6 G [17]. Atoms are then loaded into the ground band of a 1D optical lattice of depth 5.4 E_{R}, produced by a retroreflected laser of wavelength $\lambda = 1064$ nm focused to a 150 μm beam waist. Lattice beam power is ramped to the final depth in 100 ms, keeping the optical trap power constant. Lattice depth is measured by a combination of matter-wave diffraction from pulsed lattices [87] and amplitude-modulation spectroscopy [88]. The lattice depth, laser wavelength, and bare mass of ^{7}Li determine the effective mass m and effective speed of light c in equation 6.1. Magnetic field curvature from external coils generate the overall harmonic confinement with frequency $\nu = 16.6$ Hz, centered approximately 0.3 mm from the original BEC position along the lattice direction. Note that this frequency is measured for bare ^{7}Li atoms, so differs from the frequency $\omega/2\pi$ by the square root of the ratio between the bare and effective masses. When the optical trap beams are suddenly switched off, the atoms evolve in the combined potential of this harmonic trap and the

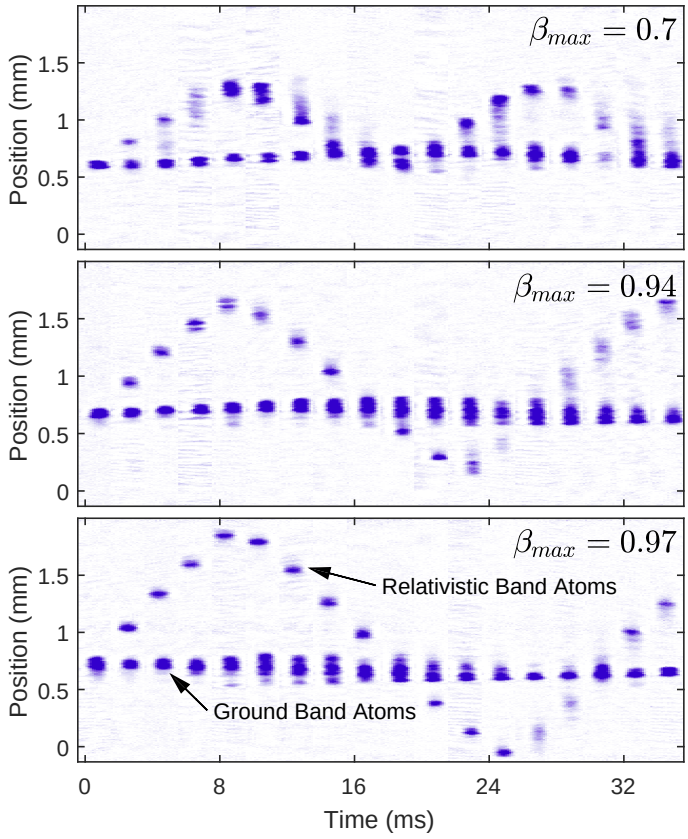

Figure 6.2: Measured trajectories of relativistic harmonic oscillators. Each panel shows a time sequence of in-situ absorption images of a non-interacting atomic cloud with population in the first and third bands of an optical lattice. Third-band atoms trace out relativistic harmonic oscillator worldlines of increasing amplitude and period. Ground-band atoms Bloch oscillate [85] around their original position, and are irrelevant to the relativistic dynamics. The maximum value of $\beta = v/c$ indicated in each panel was attained by loading the third band at varying quasimomenta, using excitation frequencies of (from top to bottom) 137, 170, and 210 kHz and corresponding hold times before excitation of 0 ms, 8 ms, and 16 ms.

optical lattice. For atoms in the ground band of the lattice, the evolution in the combined potential takes the form of Bloch oscillations [28, 29, 32, 36, 85]. Relativistic dynamics are initiated after a variable hold time by amplitude modulation of the lattice beam intensity which resonantly excites a fraction of the atoms to the third band. Because the quasimomentum depends on the phase of the Bloch oscillation and the excitation conserves quasimomentum, appropriately timed resonant modulation pulses can initialize the atomic ensemble with tunable initial kinetic energy as diagrammed in figure 6.1. For the experiments reported here the pulse duration and depth are 500 μs and 20% respectively. This method is used to prepare relativistic-band harmonic oscillators with varying values of the total energy.

We investigate the dynamics of this relativistic harmonic oscillator by measuring the atomic spatial distribution using absorption imaging after variable hold time in the third band. Figure 6.2 shows a sequence of such images which map out the evolution for three different values of $\beta_{\max}$. The relativistic anharmonicity is clearly evident: as the energy increases, the period and amplitude of the oscillation increase, and the trajectories become less sinusoidal. For velocities comparable to the effective speed of light, atomic trajectories are straight for the majority of the period, with curvature concentrated near the turning points, in agreement with expectations for a highly relativistic oscillator. The atoms which remain in the ground band are also visible in the images; they continue to Bloch oscillate near their original position during this time [85]. Due to the absence of interactions, ground-band atoms do not affect higher-band relativistic dynamics, though on a practical level spatial overlap with ground-band atoms can impede imaging of very low-energy (non-relativistic) higher-band oscillations.

Beyond simply reproducing qualitative features of relativistic dynamics, this system allows a direct quantitative experimental test of the theory of the relativistic harmonic oscillator. Figure 6.3a shows the measured trajectories for oscillators at three maximum

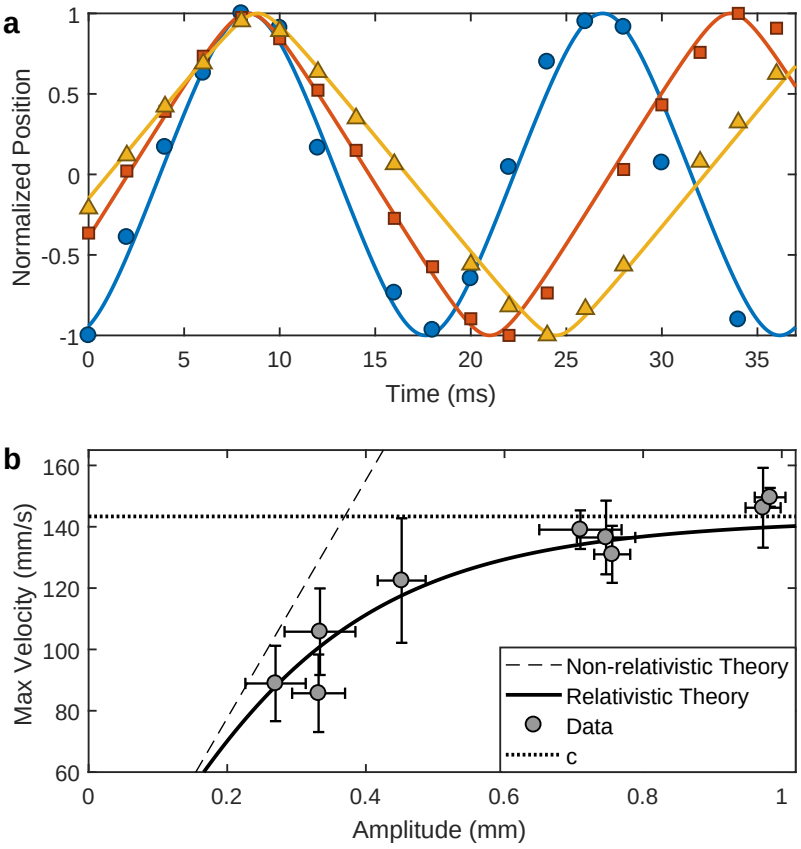

Figure 6.3: Measuring relativistic harmonic oscillator dynamics. **a:** Comparison of measured and theoretical trajectories. Measured normalized mean atomic position versus time for $\beta_{\max} = 0.7$ (blue circles), 0.94 (red squares), and 0.97 (yellow triangles). Solid lines show theoretically predicted evolution according to Eqs. 6.2 and 6.3, with no adjustable fit parameters. **b:** Amplitude-velocity relation of the relativistic harmonic oscillator. Points show measured peak velocity versus measured amplitude. Amplitude error bars indicate the $1/e$ ensemble radius and velocity error bars indicate estimated uncertainty of numerical differentiation. Lines show the non-relativistic expectation (dashed), the exact relativistic prediction (solid), and the effective speed of light (dotted).

velocities corresponding to $\beta_{\max} = 0.7$, 0.94, and 0.97. Predicted trajectories from equation 6.2 are plotted as solid lines, without the use of any fitting parameter. The observed evolution of trajectory shape, from a sinusoidal and approximately harmonic form at low energies to an increasingly triangular form with a growing period, is in good quantitative agreement with the predictions of the relativistic theory.

A fundamental feature of the relativistic harmonic oscillator is that the maximum velocity saturates at the effective speed of light, with the amplitude diverging at finite maximum velocity rather than increasing linearly with maximum velocity as in the non-relativistic case. Figure 6.3b presents an experimental measurement of this phenomenon, showing the velocity asymptotically approaching c as the amplitude increases. Results are consistent with the relativistic theory to within the estimated measurement error. Here, velocity and amplitude were derived directly from measured position-versus-time datasets like those plotted in figure 6.3a; this procedure avoids the use of fits or theoretical assumptions, though it does give rise to sizable velocity error bars due to the noise-intolerance typically associated with numerical differentiation.

Relativistic anharmonicity can also be quantitatively measured and compared to theory; we find that the experiment is a sufficiently accurate realization of a relativistic oscillator to distinguish beyond-leading-order corrections at high energy. Figure 6.4a shows the measured oscillation period T as a function of measured oscillation amplitude A. The leading-order prediction of reference [60] and equation 6.4, plotted as a dashed line, matches the data at low values of A and γ_0 but predicts too high a period for the highest-energy oscillators. As the maximum Lorentz factor γ_0 increases, higher-order corrections become important. The exact prediction, calculated by setting $\phi = 2\pi$ in equation 6.2 and evaluating the elliptic integrals, is plotted as a solid line. Measured periods are in close agreement with the exact theoretical predictions for relativistic anharmonicity.

We observe that relativistic effects modify the dynamics of oscillator ensembles initialized with a spread of energies: the ensembles dephase due to relativistic anharmonicity, and exhibit a monopole oscillation with phase opposite to that of a non-relativistic oscillator ensemble. The initial atomic spatial distribution inherited from the Bose-Einstein condensate gives rise to a distribution of frequencies with a width that depends

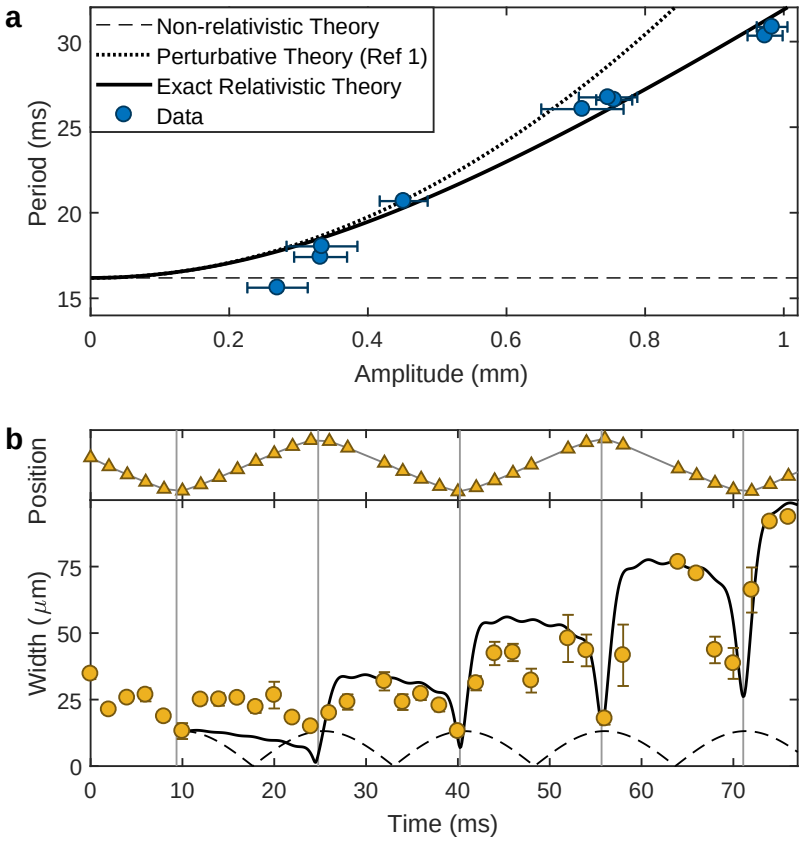

Figure 6.4: Measuring the effects of relativistic anharmonicity. **a:** Measured oscillation period versus amplitude (circles). Amplitude error bars indicate the $1/e$ cloud radius. The non-relativistic harmonic theory (dashed), the leading-order theoretical prediction of reference [1] and equation 6.4 (dotted) and the exact theoretical prediction derived from equation 6.2 (solid) are plotted, without adjustable fit parameters. **b:** Relativistic monopole oscillation and dephasing of an oscillator ensemble. Top panel: center-of-mass dipole oscillations of an oscillator ensemble with average $\beta_{\max} = 0.98$. Bottom panel: measured $1/e$ width versus time of the ensemble (circles). Error bars indicate estimated 95% confidence interval. The non-relativistic (dashed) and relativistic (solid) predictions for ensemble width evolution are plotted from the first turning point without adjustable fit parameters.

on the relativistic anharmonicity at the average amplitude. As the members of the oscillator ensemble acquire varying amounts of phase, the dephasing manifests first as an exponentially-enveloped increase in the width of the spatial distribution. A quantitative theoretical prediction for the time-dependent spatial width can be derived numerically

by applying Eqs. 6.2 and 6.3 to an appropriate initial ensemble, starting from the first turning point. Figure 6.4b shows a comparison between such a prediction and the measured time-dependent width for an oscillator ensemble with average energy deeply in the relativistic regime. The observed increase in width is quantitatively well-matched by the theory without any adjustable fit parameters, indicating that the dephasing of the oscillator ensemble is dominated by relativistic effects. In addition to the overall increase in width, both theory and experiment show oscillations of the width at twice the average oscillator frequency. These monopole oscillations are also a consequence of relativistic anharmonicity; intriguingly, they have the opposite phase from non-relativistic monopole oscillations. The trajectories of two non-relativistic harmonic oscillators initialized at the same phase but slightly different energies will cross at the origin, leading to minimum ensemble width at the minimum of the potential. In contrast, the trajectories of two similarly initialized highly relativistic oscillators will cross near the turning points, leading to minimum ensemble width there. As figure 6.4 demonstrates, the observed minimum ensemble width of the relativistic monopole oscillations indeed occurs at the turning points; this is exactly the opposite of the expected behavior for a non-relativistic oscillator.

In conclusion, we have experimentally realized and quantitatively studied a harmonic oscillator in the relativistic regime using ultracold lithium atoms in the third band of an optical lattice. Though relativistic harmonic motion has been studied theoretically for decades, to the best of our knowledge this represents the first experimental observation of relativistic harmonic oscillator worldlines and dynamics. The measured worldline shapes, relativistic anharmonicity, monopole oscillations, and relativistic dephasing of oscillator ensembles are in good quantitative agreement with relativistic predictions.

Chapter 7

Transport in Floquet-Bloch Bands

The contents of this chapter include our paper "Transport in Floquet-Bloch Bands".

We report Floquet band engineering of long-range transport and direct imaging of Floquet-Bloch bands in an amplitude-modulated optical lattice. In one variety of Floquet-Bloch band we observe tunable rapid long-range high-fidelity transport of a Bose condensate across thousands of lattice sites. Quenching into an opposite-parity Floquet-hybridized band allows Wannier-Stark localization to be controllably turned on and off using modulation. A central result of this work is the use of transport dynamics to demonstrate direct imaging of a Floquet-Bloch band structure. These results demonstrate that transport in dynamical Floquet-Bloch bands can be mapped to transport in quasi-static effective bands, opening a path to cold atom quantum emulation of ultrafast multi-band electronic dynamics.

Quantum control of transport in driven lattices may hold the key to new device types, unexplored techniques for ultrafast transport of energy and information in solids, and dynamical tools for controlling and probing condensed matter [89, 3, 90, 91, 92, 93,

94, 95, 96, 97, 98]. Ultracold atomic gases have enabled investigation of a wide variety of transport-related phenomena, including Bloch oscillations [32, 40, 85], Anderson localization [99, 100, 101], photoconductivity [82], superfluid critical velocity [102, 103, 104], spin-orbit coupling [105], and pulsed modulation techniques for wavepacket manipulation [106, 107]. The application of Floquet techniques in optical lattices [3, 90] has expanded the control over these systems and enabled study of phenomena including topological dynamics [108], renormalization of tunneling [109], correlated tunneling [110], tunable mobility [111], and synthetic ferromagnets [112]. While modulation techniques have been used to modify the spatial width of wavepackets [41], real-space control of center-of-mass transport in Floquet-Bloch bands remains largely unexplored.

Amplitude modulation of an optical lattice creates quasimomentum-selective band crossings which can be used to stitch together hybridized Floquet-Bloch bands in a variety of ways, allowing robust tunable modification of transport phenomena. We report a series of experiments probing and controlling transport of ultracold bosonic lithium atoms in Floquet-Bloch bands and demonstrating that transport in these dynamical bands can be understood in the context of a quasi-static effective band structure. Floquet hybridization in the presence of an applied force can be used to generate coherent transport over thousands of lattice sites, switch on and off Bloch oscillations, and tune the band dispersion by manipulating drive parameters. As we demonstrate, experimental measurements of dynamical evolution enable direct imaging of Floquet-Bloch band structure.

Our experimental platform for Floquet band engineering is a degenerate quantum gas of ^{7}Li in an amplitude-modulated optical lattice and an applied harmonic magnetic potential (see Fig. 7.1f). Each experiment begins by producing a Bose condensate of approximately 10^5 ^{7}Li atoms in the $|F = 1, m_F = 1\rangle$ hyperfine state in a crossed optical dipole trap centered at $x = 0$. After the final stage of cooling, a Feshbach magnetic field is tuned to the shallow scattering length zero-crossing near 543.6 G [17] to eliminate

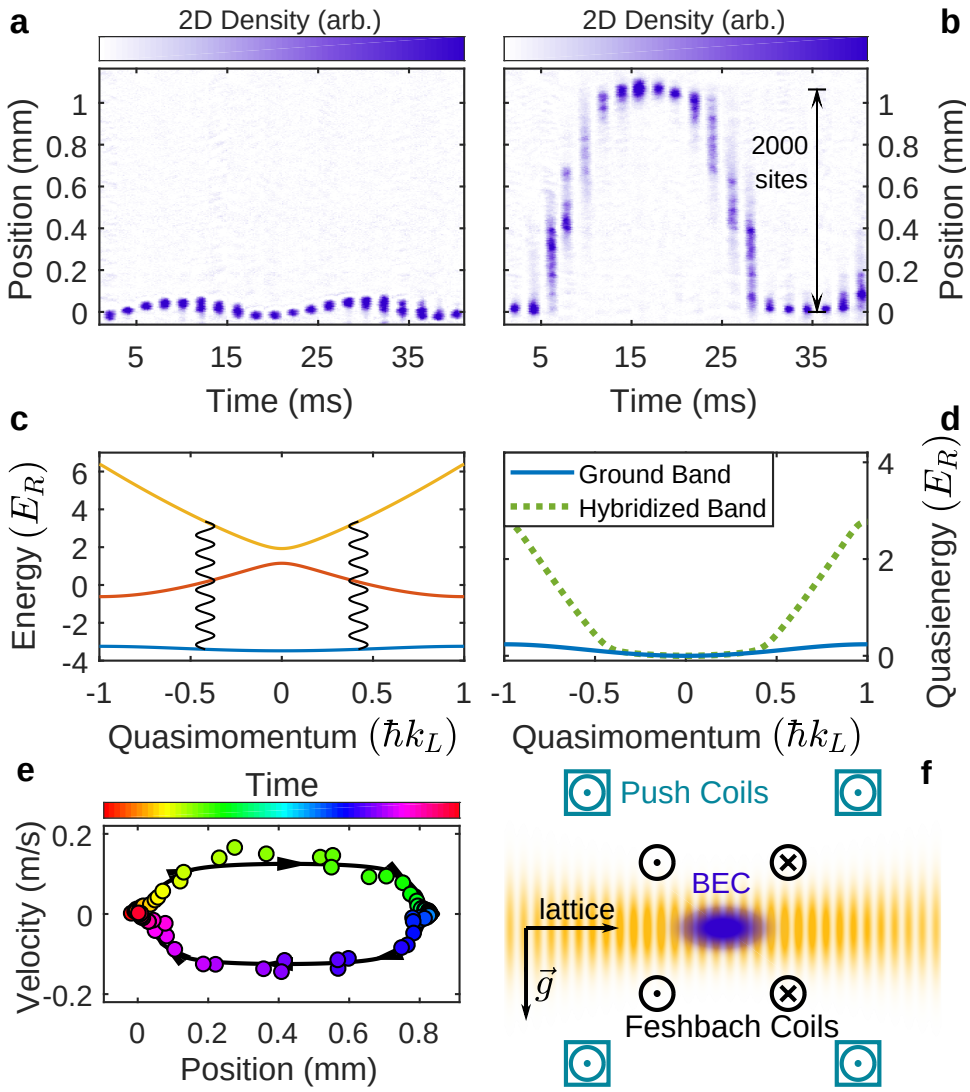

Figure 7.1: Rapid long-range transport in a Floquet-Bloch band. **(a)** Time sequence of images of a condensate in the ground band of a 5.4 E_R-deep lattice undergoing 48 Hz Bloch oscillations [85]. **(b)** Time sequence of images of a condensate in a $(0, 2)$ hybridized Floquet-Bloch band created via amplitude modulation with $\nu = 170$ kHz and $\alpha = 0.2$, with the same initial force as in (a). Note the rapid cyclic high-fidelity transport across the trap. **(c)** Unmodified band structure. Vertical rippled lines indicate band coupling at the hybridizing quasimomentum for this modulation frequency. **(d)** Calculated dispersion of the unmodified ground band (solid) and hybridized Floquet-Bloch band (dashed). **(e)** Position-velocity evolution in the same hybrid band as (b) with an initial force corresponding to a Bloch frequency of 38 Hz. Solid line is theory; points are data at equally-spaced times. Error bars are smaller than plotted points. **(f)** Experimental schematic.

interatomic interactions, and the condensate is adiabatically loaded into a Heisenberg-limited quasimomentum distribution in the ground band of a retro-reflected optical lattice with an 85 μm beam waist. The static lattice depth V_0 is 5.4 E_R unless otherwise specified, where $E_R = \hbar^2 k_L^2/2m$ is the recoil energy, $k_L = 2\pi/\lambda$ is the lattice wavevector, $\lambda =$ 1064 nm is the lattice wavelength, and m is the atomic mass. The curvature of the Feshbach field generates harmonic confinement with trap frequency $\omega = 2\pi \times 15.5$ Hz. A field gradient from push coils translates the trap center x_0 such that resulting force $F(x) = -m\omega^2 (x - x_0)$ drives transport in the lattice direction once the much-tighter optical dipole trap which pins the atoms to $x = 0$ is removed. Dynamics are initiated by switching off the optical dipole trap and simultaneously turning on the lattice modulation using an acousto-optic modulator; this quenches the atomic ensemble into the hybridized Floquet-Bloch band. If the hybridizing quasimomentum q^* is sufficiently different from the initial quasimomentum we do not observe heating from the quench, although in some cases projection of a small fraction of the atoms to higher bands can occur via multiphoton transitions. After variable hold time in the modulated lattice, the atomic position distribution is measured by *in-situ* absorption imaging.

Floquet-Bloch band properties and dynamics are calculated numerically by computing the eigenvalues and eigenstates of the hermitian generator of the single-period time evolution operator [3]. The system can be described by the 1D time-dependent Hamiltonian

$$\begin{aligned} H = &- \frac{\hbar^2}{2m}\partial_x^2 - V_0 \left(1 + \alpha \sin(2\pi\nu t)\right) \cos^2\left(\frac{\pi x}{d}\right) \\ &+ \frac{1}{2} m\omega^2 \left(x - x_0\right)^2 , \end{aligned} \tag{7.1}$$

where x is position along the lattice, d is the lattice spacing, m is the atomic mass of ^{7}Li, V_0 is the static lattice depth, α is the modulation strength, and ν is the modulation

frequency. Transverse degrees of freedom play no role in the dynamics we report. In the absence of the modulation and for weak force, the spectrum of equation (7.1) consists of Bloch bands with energy $\{E_j(q)\}$, where j is the band index and q the quasimomentum. Amplitude modulation satisfying an interband resonance of the ith and jth band $nh\nu = (E_i(\pm q^*) - E_j(\pm q^*))$, where q^* is the resonant quasimomentum and n the photon number, hybridizes the static spectrum into quasienergy bands $\{\widetilde{E}_i(q)\}$. The wavepacket center-of-mass dynamics are dictated by the local force and the group velocity of the hybridized band: $dq/dt = F$ and $dx/dt = d\widetilde{E}/dq$. While the drive can in principle hybridize any set of bands with arbitrary order n, this work focuses on the case of single-photon resonant hybridization of the ground band with the jth excited band, which we denote as $(0, j)$ hybridization.

Fig. 7.1 demonstrates the dramatic difference between transport in the static ground band and transport in a $(0, 2)$ Floquet-Bloch band. In the absence of modulation, the local force F induces Bloch oscillations (Fig. 7.1a) whose amplitude in position space is proportional to the static bandwidth [85]. Amplitude modulation at frequency $\nu =$ 170 kHz and amplitude $\alpha = 0.2$ hybridizes the ground and second excited band at quasimomentum $q^* \approx 0.4\ \hbar k_L$ as diagrammed in Fig. 7.1c. In the Floquet-Bloch band, instead of exhibiting Wannier-Stark localization, the atomic ensemble undergoes rapid coherent oscillatory transport across approximately 2000 lattice sites (Fig. 7.1b).

This striking transport behavior is a direct consequence of the hybridized structure of the Floquet-Bloch band. As the quasimomentum evolves, the group velocity sharply increases at the high-curvature point of the Floquet-Bloch band where $|q(t)| = q^*$. The resulting rapid transport carries the ensemble thousands of lattice sites in real space. On such large length scales, the force due to the harmonic confinement is no longer approximately constant; the ensemble moves across the entire applied potential, gaining and then losing quasimomentum without reaching the edge of the Brillouin zone. At the position

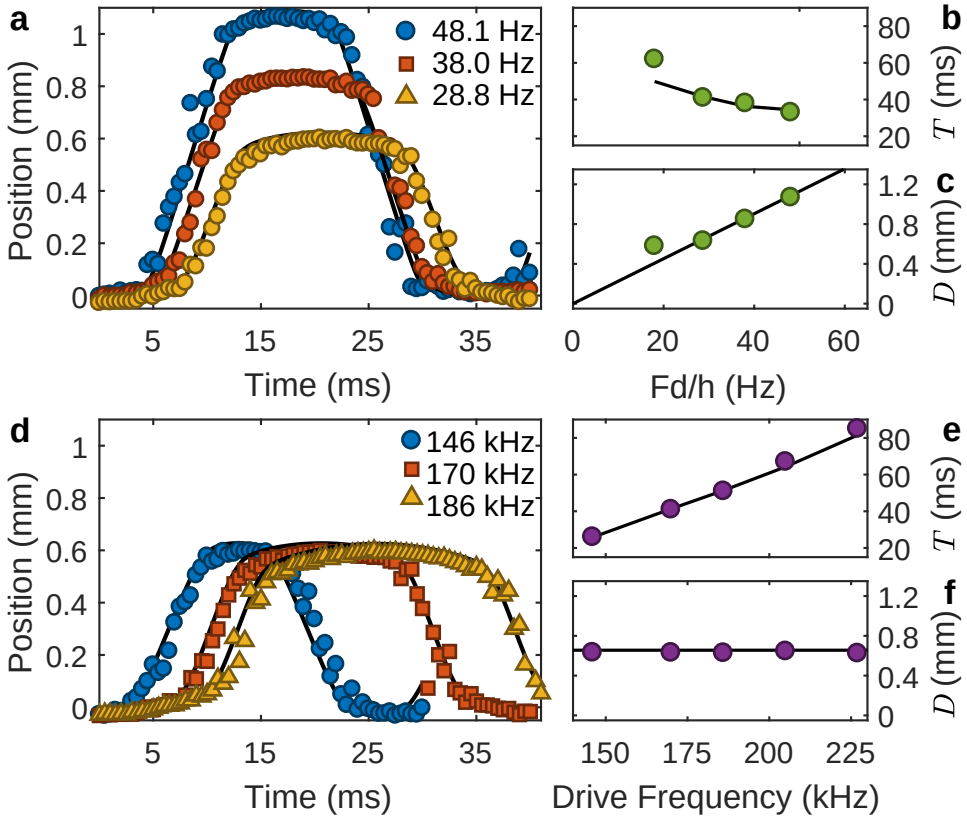

Figure 7.2: Tunable transport in Floquet-Bloch bands. Panels a-g show measurements in a $(0, 2)$ hybrid band with $\alpha = 0.2$. **(a)** Atomic center-of-mass position versus time for constant drive frequency $\nu = 170$ kHz and varying initial force, corresponding to the Bloch frequencies indicated in the legend. In panels a-f, theoretical expectations from the calculated Floquet-Bloch band structure are plotted as solid lines, with no fit parameters, and calculated uncertainty intervals are smaller than plotted points. **(b,c)** Transport period and total transport distance as a function of initial force. **(d)** Atomic position versus time for three modulation frequencies as indicated in the legend, at a constant initial force corresponding to a 26.5 Hz Bloch frequency. **(e,f)** Transport period and total transport distance as a function of drive frequency ν.

where the potential energy is the same as it was at the first point of high band curvature, energy conservation requires that the ensemble again has quasimomentum q^*, and the group velocity sharply decreases. The microscopic dynamics at the high-curvature point involve exchange of photons with the lattice, as occurs for example in pulsed Bragg acceleration techniques used in atom interferometry to increase free-space momentum [113]. Both direct measurement and Landau-Zener calculations indicate that deviations from

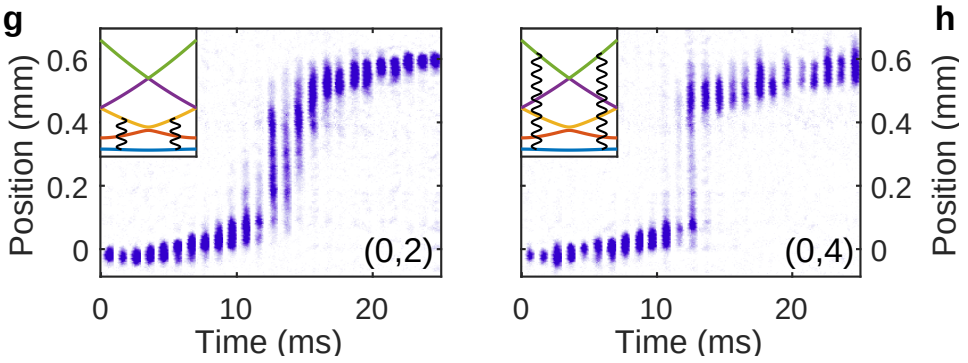

Figure 7.3: Comparison of transport in a $(0, 2)$ versus $(0, 4)$ hybridization scheme.**(g)** Time sequence of position-space distribution in a $(0, 2)$ Floquet-Bloch band with $\nu = 186$ kHz and $\alpha = 0.2$. **(h)** Time sequence of position-space distribution in a $(0, 4)$ Floquet-Bloch band with $\nu = 530$ kHz and $\alpha = 1$. Insets in (g) and (h) indicate hybridization in the static band structure.

perfect fidelity of transfer between static bands at the Floquet-induced avoided crossings are below one part in 10^4 for all data we report. Transport in the hybridized band is characterized by periods of rapid transfer across the entire trapping region connected by relatively slow Bloch-oscillation-like motion at the turning points. Variations in ensemble width during transport can arise from both force inhomogeneity [85] and from the modified dispersion [114]. The full position-velocity evolution is shown in Fig. 7.1e. Notable features of the observed dynamics include high-fidelity long-range transport of nearly all atoms in the condensate, coherent Bloch oscillation dynamics at opposite ends of the trap, maximum transport velocities far in excess of those characterizing the bare harmonic potential, and a high degree of control attainable by varying drive properties.

To further probe the dynamics we study the dependence of long-range transport on initial applied force, drive frequency, and hybridized band indices. As shown in Fig. 7.3a and b, the total transport distance D increases with increasing force while the oscillation period T decreases. The observed behavior agrees quantitatively with fit-parameter-free numerical calculations for the Floquet-Bloch band shown as solid black lines in Figs. 7.3a, b, and c. Larger total transport distances can be achieved by reducing the harmonic trap

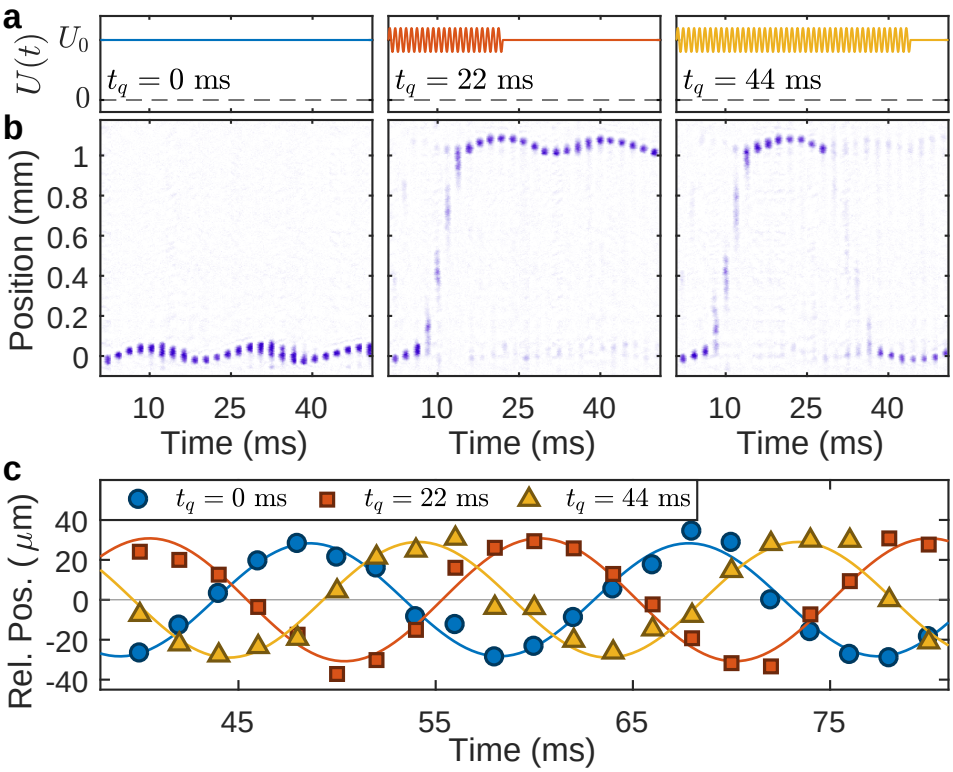

Figure 7.4: Transport control via Floquet quenches with $\nu = 170$ kHz and $\alpha = 0.4$. **(a)** Quench protocol for modulation times of 0, 22, and 44 ms. **(b)** Time sequence of images of atomic ensemble for the three quench protocols. **(c)** Relative position evolution of the atomic ensemble after all quenches. Solid lines are sinusoidal fits, and estimated uncertainty in measured data is smaller than plotted points.

frequency or increasing the applied force, although the latter method will eventually be limited by Bragg scattering. Figs. 7.3d, e, and f show the results of varying the hybridizing frequency ν at constant force. Increasing ν hybridizes the bands closer to the edge of the Brillouin zone, which increases the time to reach q^* so that the oscillation period increases while the transport distance remains fixed. Again, the observed wavepacket evolution agrees quantitatively with fit-parameter-free numerical predictions, demonstrating the effectiveness of the Floquet-Bloch formalism for describing this controllable long-distance transport.

Floquet hybridization of different pairs of static bands gives rise to distinct transport properties. Fig. 7.3g and 7.3h compare transport dynamics in $(0, 2)$ and $(0, 4)$ hybrid

bands. Evolution in the $(0, 4)$ band leads to dramatically faster long-range transport, due to the increased group velocity and band curvature. During this evolution, the ensemble stretches across the entire extent of the trapping potential, but still returns to the static ground band at the far edge of the trap.

Diabatic quenches between static bands and hybridized Floquet bands provide a powerful experimental tool for dynamical control of transport properties. Quenching back to the static lattice after a total modulation time t_q projects the Floquet-Bloch state back onto the original static spectrum. Fig. 7.4 shows the results of such quenched modulation experiments in which the modulation depth α is set suddenly to zero after some variable evolution time in the Floquet-Bloch band. Quenching near the turning points of the position-space oscillation projects the atomic ensemble back onto the Wannier-Stark localized ground band, at a position which can vary by thousands of lattice sites depending on t_q. Quenching into an excited static band is also possible; a recent study demonstrated that a related technique can be used to experimentally realize a relativistic harmonic oscillator [114]. The small fraction of atomic population away from the main ensemble visible in Fig. 7.4b arises from multiphoton projection to higher bands during the initial quench. The identical amplitude and frequency of position-space Bloch oscillations after the three distinct quench protocols in Fig. 7.4c indicates the non-dissipative nature of quenched Floquet-Bloch transport.

Hybridizing bands of opposite parity gives rise to qualitatively different phenomena. While opposite-parity coupling is forbidden at $q^* = 0$ due to the even-parity nature of amplitude modulation, hybridization at finite quasimomentum is both allowed and observed. Fig. 7.5 shows the result of $(0, 1)$ coupling at $q^* \approx 0.66\ \hbar k_L$, using amplitude modulation with $\nu = 56$ kHz, $\alpha = 0.25$, and $V_0 = 3.6\ E_R$. At this reduced lattice depth, atoms in the unmodified ground band do not Bloch oscillate but undergo ballistic transport in the trapping potential, never reaching the Brillouin zone edge (Fig. 7.5a).

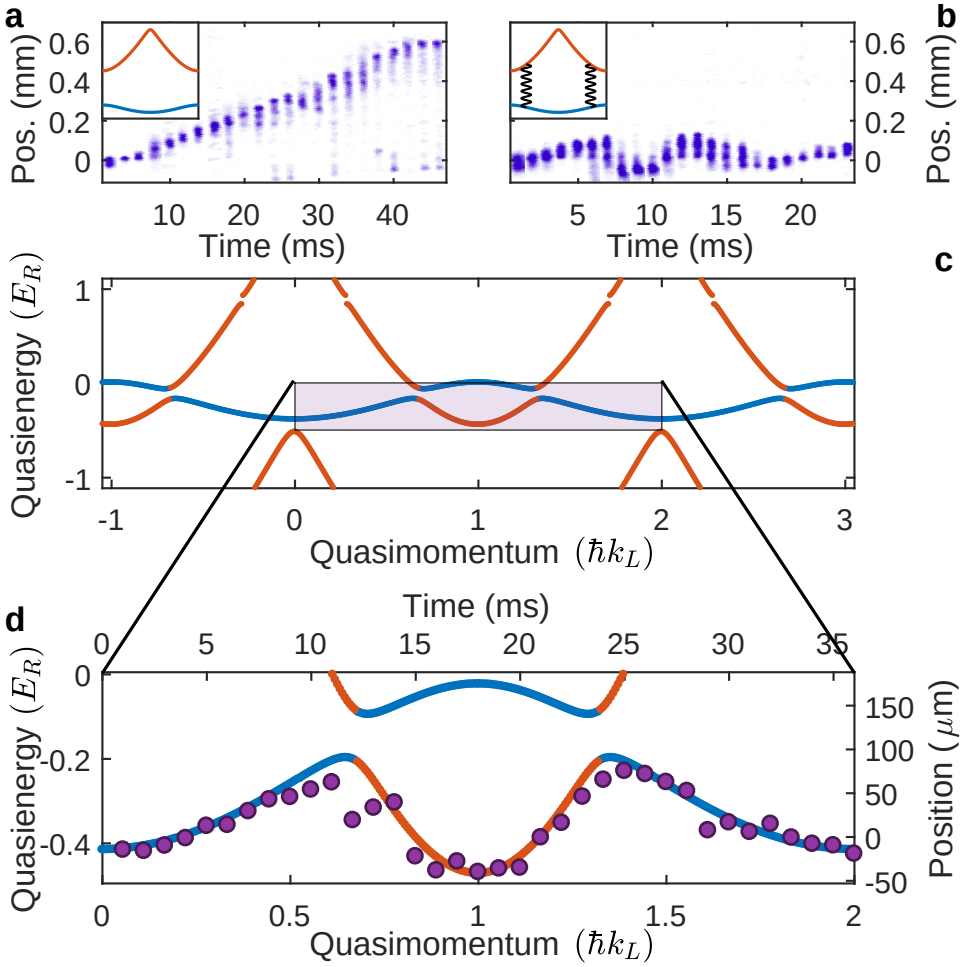

Figure 7.5: Imaging a Floquet-Bloch band. **(a)** Time sequence of images of atoms in a static band with reduced lattice depth $V_0 = 3.6\ E_R$, subjected to an initial force per atom corresponding to a Bloch oscillation frequency of 28.9 Hz. Inset is the calculated band structure. **(b)** Evolution in a $(0, 1)$ hybrid Floquet-Bloch band with $\nu = 56$ kHz, $\alpha = 0.25$, and the same lattice depth as (a). Inset is the static band structure with rippled lines indicating the resonant coupling. **(c)** Calculated quasienergy spectrum in the extended zone scheme for the $(0, 1)$ hybrid band of (b). Color corresponds to the static band with maximal probability overlap with the Floquet state according to the band colors in (a). Shaded region corresponds to the mapped part of the Floquet band in (d). **(d)** Comparison of the real-space evolution in (b) to the Floquet spectrum in (c) according to the mapping of equation (7.2) with no fit parameters. Measurement uncertainty is smaller than plotted points. The atomic motion images the Floquet-Bloch band dispersion.

Quenching into the $(0, 1)$ hybrid band causes Wannier-Stark localization due to Bloch oscillations in the Floquet-hybridized band (Fig. 7.5b). Here the opposite curvature of

the two static bands results in a flatter hybrid band with smaller bandwidth and local extrema in the dispersion, as shown in Fig. 7.5c. Deviations from unit Landau-Zener fidelity for Bloch oscillations near the avoided crossings are calculated to be below a part per million for this drive amplitude and Bloch frequency, and are not observed.

Strikingly, these oscillations enable direct imaging of the Floquet-Bloch band structure. A recent experiment [85] demonstrated that for a constant force, the position evolution of an atomic ensemble undergoing Bloch oscillations in a *static* band constitutes a direct image of the energy-momentum dispersion relation according to the mapping:

$$E = Fx, \qquad q = Ft. \tag{7.2}$$

This can be intuitively understood by considering that the group velocity is equal to both dE/dq and dx/dt. Fig. 7.5d experimentally demonstrates that this mapping can be generalized to Floquet-Bloch bands by comparing the center-of-mass motion in a $(0, 1)$ hybrid band to the calculated band dispersion of Fig. 7.5c, scaled according to equation (7.2). There are no fit parameters in this plot, as the force is measured independently. The close agreement between the measured atomic position and the band dispersion demonstrates direct imaging of a hybridized Floquet-Bloch band.

This Floquet-Bloch band image is reminiscent of time- and angle-resolved photoemission maps of Floquet bands in laser-driven topological insulators [91]. This analogy suggests potentially fruitful connections between the results we present and topics of current interest in condensed matter, including the effect of Bloch oscillations and interband transitions on high-harmonic generation in crystals and prospects for all-optical band structure reconstruction in solids [92, 93, 94, 95, 96, 97, 98]. Using techniques like those we present, cold atom quantum simulation experiments could serve as a complementary tool for exploration of band dynamics, probing and realizing phenomena at the

edge of current ultrafast experimental capabilities.

The controlled Floquet-Bloch transport dynamics presented here also open the path to the realization and study of more complex phenomena, including polychromatic driving for hybridization of multiple bands at multiple quasimomenta, Floquet-based creation of topologically nontrivial bands [115, 116], and the controlled introduction of disorder. The enhanced control of band structure and transport demonstrated here may also be useful for lattice-based metrology. One possibility along these lines would be continuously-trapped atom interferometry using wavepackets split by a large distance in a $(0, 2n)$ hybrid band for some n. While this study has focused on coherent dynamics in the absence of interaction-induced dephasing, the introduction of tunable interatomic interactions would open up a broader array of possibilities in many-body Floquet engineering; some of these are explored in recent work using the same apparatus [117].

In summary, we have demonstrated tunable coherent control of long-range quantum transport in hybridized Floquet-Bloch bands. We have used hybridization of various pairs of four separate static bands at varying quasimomenta to realize rapid long-distance transport of a Bose condensate, switchable Wannier-Stark localization, and direct imaging of a hybrid Floquet-Bloch band.

Chapter 8

Quantifying and controlling prethermal nonergodicity in interacting Floquet matter

The contents of this chapter include our paper "Quantifying and controlling prethermal nonergodicity in interacting Floquet matter".

The use of periodic driving for synthesizing many-body quantum states depends crucially on the existence of a prethermal regime, which exhibits drive-tunable properties while forestalling the effects of heating. The underlying localized nonergodic nature of the wave function in this metastable regime is largely unexplored experimentally. We report experiments on a many-body Floquet system consisting of atoms in an optical lattice subjected to ultrastrong sign-changing amplitude modulation. Using a double-quench protocol we measure an inverse participation ratio quantifying the degree of prethermal localization as a function of tunable drive parameters and interactions. We obtain a complete prethermal map of the drive-dependent properties of Floquet matter spanning four

square decades of parameter space. Following the full time evolution, we observe sequential formation of two prethermal plateaux, interaction-driven ergodicity, and strongly frequency-dependent dynamics of long-time thermalization. The complete experimental control and quantitative characterization of prethermal Floquet matter demonstrated here opens a new frontier for probing far-from-equilibrium quantum statistical mechanics and new possibilities for dynamical quantum engineering.

Time-periodic driving is a powerful technique for synthesizing tailored quantum matter with drive-dependent properties and phase structures beyond the constraints imposed by thermodynamic equilibrium [118, 119, 120, 57, 121, 112, 122, 123, 124, 125, 126, 127, 128], and therefore beyond a description in terms of thermal Gibbs ensembles. In many cases of interest, approximate integrals of motion can localize driven systems in metastable prethermal states [129, 130, 131, 132, 133] that admit a statistical description in terms of a periodic Gibbs ensemble (PGE) [134, 135, 136, 137, 130, 138, 139]. While pioneering experiments have explored the uses and properties of metastable driven quantum systems [140, 141, 142, 143, 144, 145, 146], directly probing the localized nature of the prethermal many-body quantum state has remained an outstanding challenge. In this work, we experimentally probe a universal quantitative measure for non-ergodic localization of a driven quantum system based on a stroboscopically time-averaged return probability to an initial energy-localized state. This quantity directly corresponds to an inverse participation ratio quantifying localization in the eigenbasis of the approximate Floquet Hamiltonian, and can be experimentally measured using a double-quench protocol starting from an almost fully Bose-condensed undriven ground state.

The experiments we report use tunably-interacting ^{7}Li atoms in an amplitude-modulated optical lattice to create and probe prethermal Floquet matter. Uniquely, our experiment

enables the use of amplitude modulation extending from 10 to 1000 percent of the static lattice depth and drive frequencies extending from 0.1 to 10 times the lattice band gap. This regime of ultrastrong drive amplitudes is previously unrealized experimentally, and this range of drive frequencies extends through and well beyond typical regimes of Floquet engineering. Realization of these extreme parameter values allows us to map out a sharp threshold between differently-localized regimes of prethermal ergodicity breaking. Observed characteristics of the prethermal state are in quantitative agreement with theoretical calculations based on a periodic Gibbs ensemble. Tracking the time evolution of the driven system we observe and quantify not only the formation of a prethermal non-ergodic plateau, but also the long-time departure from it, either by a transition to a second prethermal plateau or, for stronger interactions, by the onset of ergodicity.

The initial condition for all experiments discussed here is a Bose-condensed gas of lithium loaded into the ground band of a static 1D optical lattice of depth V_0 and wavelength $\lambda = 1064$ nm at zero quasimomentum. Interatomic interactions are set to the desired value using a magnetic Feshbach resonance. The system is quenched into the Floquet Hamiltonian by applying lattice amplitude modulation at some frequency ω and relative amplitude α, keeping the cycle-averaged lattice depth fixed at V_0. After some modulation time, the atoms are quenched back to the original optical lattice, bandmapped, and imaged in order to measure the resulting distribution in the eigenbasis of the undriven lattice. This double-quench protocol provides a direct probe of the evolution of system properties under the Floquet Hamiltonian, and of localization in the Floquet state basis. More details on the experimental protocol appear in the appendices.

If interactions are tuned to zero, the Hamiltonian of this driven system is

$$H(t) = -(\hbar^2/2m)\partial_x^2 + V_0[1 + \alpha \sin(\omega t)] \cos^2(k_L x), \tag{8.1}$$

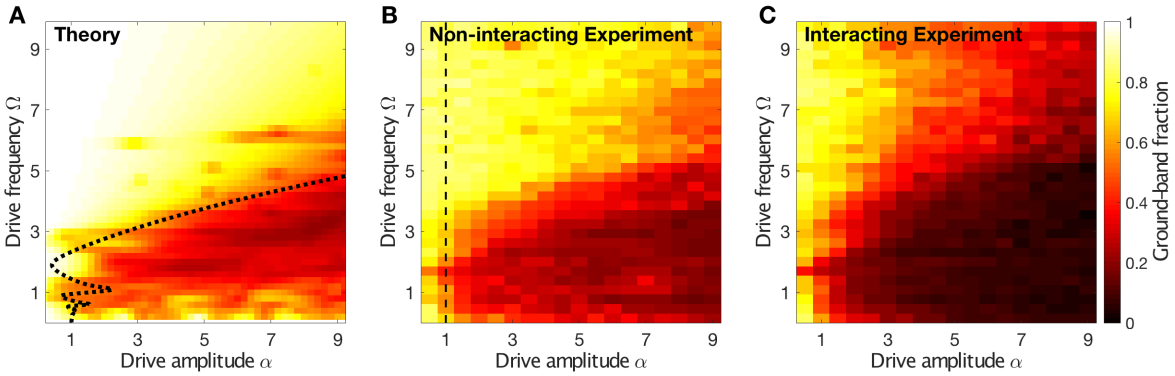

Figure 8.1: Mapping the prethermal state in the space of drive parameters. **A:** Theoretical map of the projected static ground band occupation fraction for a periodic Gibbs ensemble, as a function of normalized drive frequency Ω and normalized drive amplitude α. Dotted line shows classical stability boundary of the equivalent driven pendulum. **B:** Experimental measurement of normalized population in the center of the lowest band after a 500 μs hold of a non-interacting quantum gas in a modulated optical lattice, as a function of the same parameters. The $\alpha > 1$ region to the right of the vertical dashed line is inaccessible without the sign-changing amplitude modulation introduced in this work. **C:** Same measurement as B, but in the presence of interatomic interactions (s-wave scattering length 30 nm). Colorbar and axes are the same for all three panels.

where x is position along the lattice, m is the atomic mass, $k_L = 2\pi/\lambda$ is the wavenumber of the lattice laser, and $V_0 = 10E_R$ is the static lattice depth, with recoil energy $E_R = \hbar^2 k_L^2/2m$. It is intuitively useful to note that this is a quantum mechanical version of the Hamiltonian for a rigid pendulum with a vertically modulated pivot point, with the compact phase variable of the pendulum replaced by the position x. The role of classical rigid pendula as archetypes for the study of stability and instability in driven systems provides natural motivation for the quantum mechanical experiments reported here.

The drive frequency can be expressed dimensionlessly as $\Omega = \omega/\omega_0$ where $\omega_0 = 2\sqrt{V_0 E_R}/\hbar$ is the frequency of harmonic motion in a single lattice site, which approximates the lowest band gap of the static lattice. The experiments reported here explore four square decades of drive parameter space, with a dimensionless frequency from $\Omega = 0.1$ to $\Omega = 10$ and a dimensionless amplitude from $\alpha = 0.1$ to $\alpha = 10$. This wide

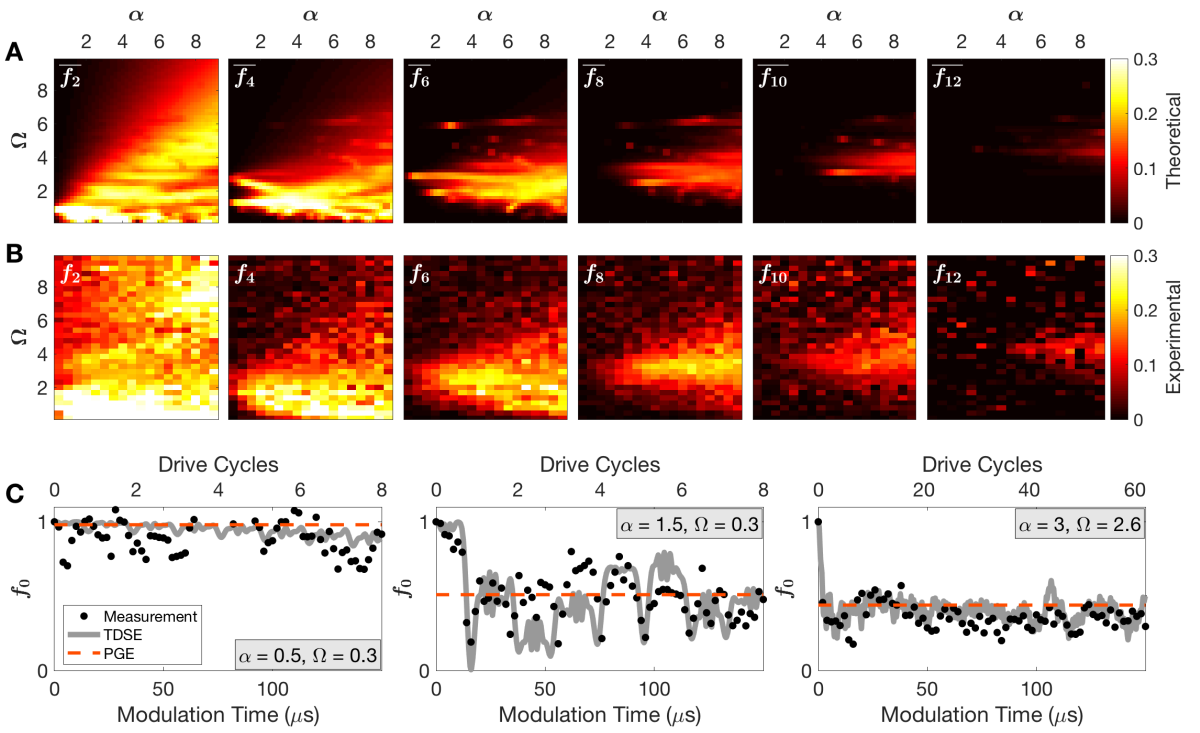

Figure 8.2: Characterizing the prethermal periodic Gibbs ensemble. **A:** PGE prediction for occupation of excited even bands as a function of drive parameters α and Ω. **B:** Measured atom number fraction in the central 40% of the same bands. All axes and colorbars are the same as for the theory panels. **C:** Measured f_0 versus modulation time for the first 150 μs of the drive, for three different values of (α, Ω) all for vanishing interactions. Dashed line shows PGE prediction corresponding to the time average of the calculated evolution of the non-interacting system (solid line). For these data, the optical lattice is immediately quenched back to the initial 10 E_R static lattice at the indicated modulation time and then band-mapped.

range represents a challenge both for theory, due to the absence of any reliably small scale in the problem, and for experiment, due to the difficulty of attaining modulation amplitudes greater than 100%. We realize the strongly-driven regime $\alpha > 1$ by simultaneously modulating two orthogonally-polarized co-axial 1D optical lattices with a relative spatial phase shift of $\lambda/4$. Extending exploration into this regime of ultrastrong driving is a key experimental novelty of the work we report, and it is required for access to the majority of the parameter space we explore in maps of prethermal Floquet matter properties like those shown in Fig. 8.1.

We characterize and quantify prethermalization in our Floquet system via the fraction f_0 of atoms which occupy the single-particle ground state after the modulation is quenched off. This quantity naturally contains information about heating in the Floquet system since those atoms which are excited out of the initial ground state automatically lead to a reduced f_0. Beyond this intuitive argument, we find that f_0 in fact represents a powerful quantitative measure for localization and therefore for prethermalization and the absence of heating: specifically, f_0 can be directly related to an inverse participation ratio (IPR) in our experimental context. An IPR, defined as IPR $= \sum_n |\langle\psi_0|n\rangle|^4$, quantifies how strongly the state $|\psi_0\rangle$, here representing the initial condition, is localized in the basis $|n\rangle$, which in our case is the eigenbasis of the Floquet time-evolution operator. The participation ratio 1/IPR measures the number of Floquet states $|n\rangle$ required to represent the initial state. In a localized prethermal state the IPR takes on a nonzero value whereas in the delocalized ergodic regime the IPR becomes vanishingly small. We find, crucially, that if interactions are neglected the long-time average of f_0 is exactly equivalent to the IPR; this is demonstrated in detail in appendix 8.4. While the IPR is a standard diagnostic of localization, the experimental measurement of such a quantity is, in general, very challenging for a many-body system. For an interacting system in the prethermal regime described by the PGE, the exact identification of f_0 as an IPR does not hold, since for example the condensate fraction will be depleted slightly already in the ground state by quantum fluctuations, but f_0 remains a useful and experimentally accessible metric for characterizing the properties of the interacting driven system. In particular, a non-zero f_0 still indicates a non-ergodic interacting prethermal state.

The dependence of Floquet matter attributes on drive properties can be directly calculated in the non-interacting case. We calculate $f_0(\alpha, \Omega)$ from the periodic Gibbs ensemble $\rho \propto \exp(-\sum_i \eta_i \hat{n}_i(t))$ characterized by integrals of motion given by the occupations $\hat{n}_i(t)$ of the single-particle Floquet modes $|i(t)\rangle$ of the multi-band Hamiltonian.

Here, the coefficients are $\eta_i = \log\left(1 + \langle\psi_0|\hat{n}_i(0)|\psi_0\rangle^{-1}\right)$, where the mean-occupations $\langle\psi_0|\hat{n}_i(0)|\psi_0\rangle = N|\langle 0|i(0)\rangle|^2$ are directly given by single-particle overlaps with the undriven (single-particle) ground state $|0\rangle$. The predicted dependence $f_0(\alpha, \Omega)$ is shown in Fig. 8.1A as a function of dimensionless driving amplitude α and frequency Ω. The theory predicts that $f_0 \simeq 1$ for a large region in (α, Ω) space, but as Ω decreases from large values for any given drive amplitude, there is always some α-dependent drive frequency below which f_0 sharply decreases to a lower but still non-ergodic value between 0 and 1. Intriguingly, this sharp crossover corresponds approximately to the stable-unstable crossover of the corresponding classical system: a rigid pendulum with a vertically modulated pivot point. The dashed line in Fig. 8.1A shows the classical boundary of stability for the downward-pointing pendulum; exploration of a possible quantum analogue of the upward-pointing Kapitza state [147, 148] is an interesting potential direction for future work.

The wide tunability afforded by our flexible experimental platform enables measurement of the full prethermal map of Floquet material properties predicted in Fig. 8.1A, and direct observation of the Floquet delocalization crossover. Figures 8.1B and 8.1C show experimentally measured maps of $f_0(\alpha, \Omega)$, for non-interacting and interacting samples respectively. Because experimental quasimomentum resolution is limited by the finite initial spatial size of the condensate and a finite time-of-flight, the experimental maps are based on integrals over the central 40% of the Brillouin zone. The non-interacting measurement of Fig. 8.1B shows good agreement with the PGE-based theoretical prediction of Fig. 8.1A. The interacting data in Fig. 8.1C display a qualitatively similar but not quantitatively identical behavior; the crucial effects of interactions are explored further in the time-evolution measurements discussed below. Both measurements clearly show the predicted amplitude-dependent Floquet delocalization crossover.

Measuring higher-band observables in addition to f_0 allows a fuller comparison be-

tween experimental and theoretical descriptions of the prethermal state. Over the timescales shown in Fig. 8.2 the dynamics of the noninteracting driven system mainly redistribute population among the lowest few even Bloch bands, as expected from parity conservation at $k = 0$. Fig. 8.2A shows the results of a PGE-based calculation of fractional projected occupations $f_{2\nu}, \nu \in (1, \ldots 6)$ of the first six even excited bands, as a function of drive parameters α and Ω. The theory predicts a rich dependence of Floquet material properties on drive parameters, with a distinct map for each projected band population. Our experiment can quantitatively test these predictions by directly imaging such maps. Fig. 8.2B shows the experimentally measured fractional population of the first six even-parity excited bands at each (α, Ω) point, using the same double-quench protocol used to produce Fig. 8.1. The observed close match between theory and experiment lends further support to the PGE-based theoretical description of the prethermal state. We do not observe significant occupation above the twelfth band, in agreement with the PGE model. These detailed experimental maps of the properties of prethermal Floquet matter throughout a wide range of drive parameter space reveal the intricate structure of the amplitude-dependent Floquet delocalization crossover in the strong-driving regime and constitute the first main result of this report.

Moving beyond such fixed-time maps, it is possible to experimentally explore the full time evolution of f_0 and higher-band observables at any point in drive parameter space. This allows direct measurement of the temporal emergence of the prethermal state, as well as investigation of its long-term fate. As shown in Fig. 8.2C, the measured time evolution of f_0 for various drive parameters shows remarkably rapid attainment of an average value in close agreement with the PGE theoretical prediction, on timescales near a single drive period [134]. The rapid but not instantaneous nature of the dephasing responsible for the emergence of the prethermal plateau can be revealed by measuring a different observable: the interference patterns after the system is quenched back to

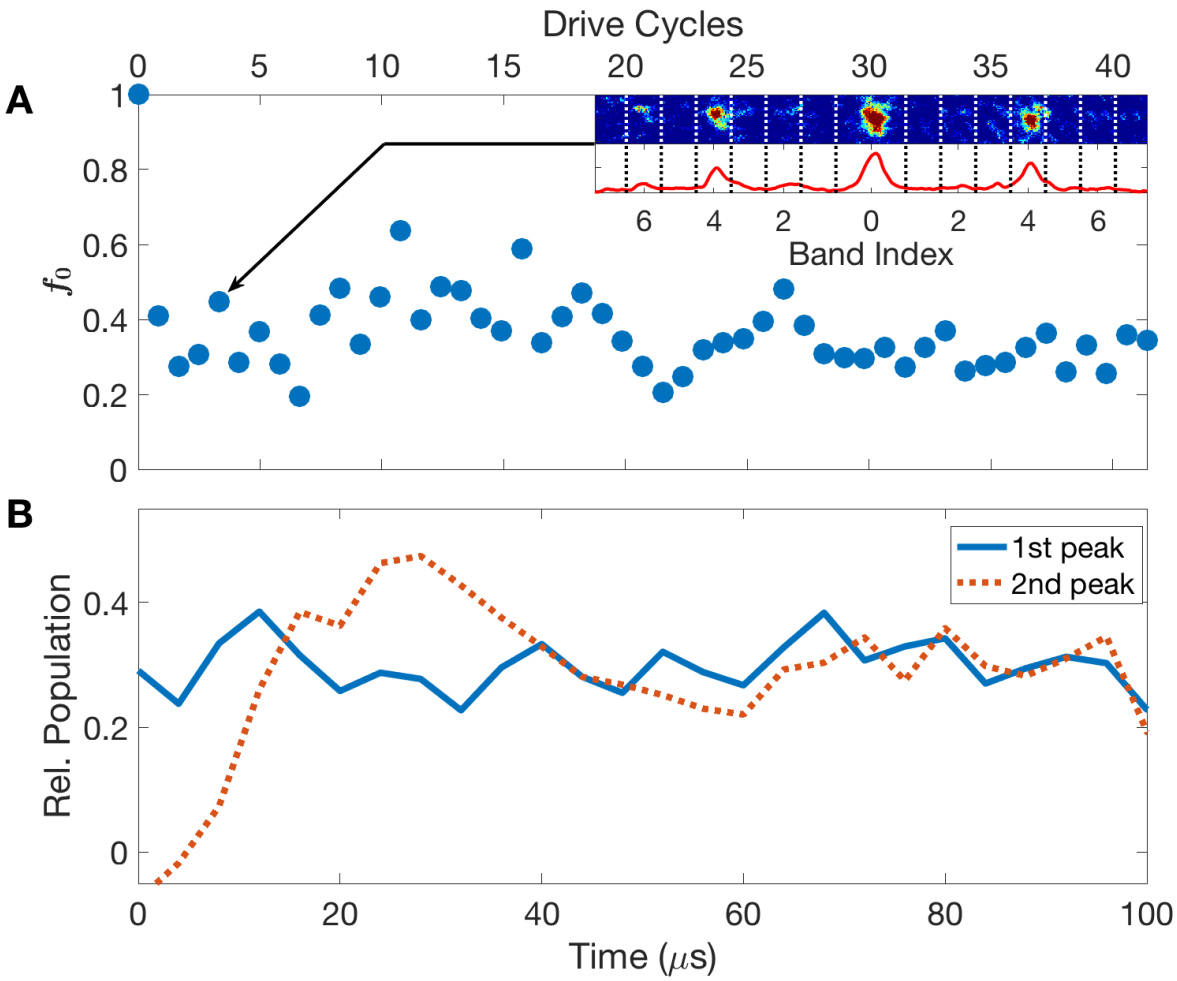

Figure 8.3: Entering the prethermal state. **A:** Normalized ground band occupation f_0 as a function of time during modulation with $\alpha = 3$, $\Omega = 2.6$, $a = 0$. The system attains the prethermal value of f_0 on time scales comparable to a single drive cycle. Inset shows a sample bandmapped image and its column integration for the indicated data point, with Brillouin zone boundaries and band indices labeled; most population here is in bands 0 and 4. **B:** Population fraction in diffracted peaks after diabatic lattice snapoff, as a function of time during the same drive. x axes are the same for the two plots. Gradual attainment of the prethermal steady-state is apparent in the increase and settling of the second-peak population.

a static lattice which is snapped off immediately rather than band-mapped. Fig. 8.3 shows that over the course of a few dozen drive cycles, the occupations of the first two interference peaks approach their quasi-steady-state values.

For a drive with $\Omega = 0.3$ and $\alpha = 0.5$, f_0 remains close to 1, while for higher drive

amplitudes and frequencies it fluctuates around a lower average value which agrees well with the PGE prediction. Since the inverse of the IPR provides a measure for the number of eigenstates of the time-evolution operator the system can access, it might appear surprising that even at large driving strengths the predicted and measured f_0 remains so high throughout the dynamics; as discussed in appendix 8.5 this can be understood as a consequence of the eventual dominance of higher-band kinetic energy splittings over any fixed coupling matrix element. Moreover, return probabilities such as f_0 yield on general grounds fluctuations of the same order as the mean for unitary dynamics; thus, the fact that we not only measure the expected temporal mean but also observe large temporal fluctuations can be interpreted as a signature of the unitary quantum character of the real-time dynamics of the experiment. In principle, such fluctuations also contain information on the spectrum of the Floquet Hamiltonian.

To probe the effects of varying interparticle interactions, we measure the evolution of strongly-driven Floquet matter over much longer timescales than those shown in Figs. 2 and 3. The long-time evolution of interacting driven systems is both especially relevant for the realization of useful many-body Floquet engineering, and especially challenging to address theoretically. Fig. 8.4A compares the initial evolution of samples with different Feshbach-tuned interaction strengths under the same drive parameters ($\Omega = 2.6$, $\alpha = 3$). For all three values of the interaction strength, the early-time dynamics are in agreement with the PGE description. As the system continues to evolve to large times over thousands of drive cycles, the PGE plateau decays. Strikingly, for a wide range of parameters we observe, as shown in Fig. 8.4B, that the system enters a second plateau in which f_0 is non-zero but smaller than in the first plateau. Non-interacting and weakly-interacting samples remain in this second plateau for at least twenty thousand drive cycles at $\Omega = 2.6$. We hypothesize that this second plateau can be understood as a consequence of a slow spreading in both position and quasimomentum: in particular,

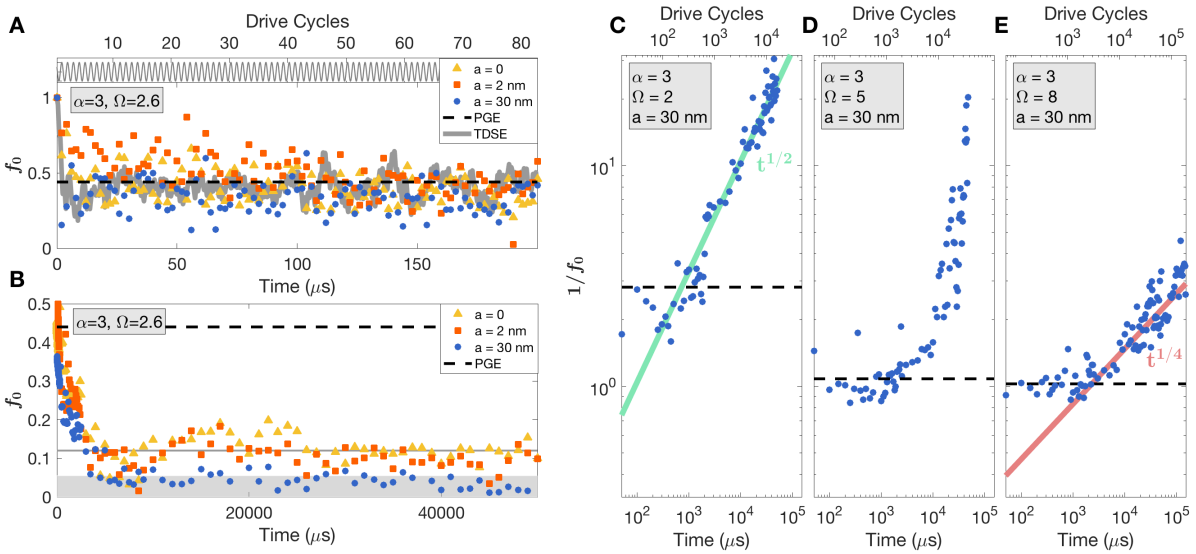

Figure 8.4: Effects of interaction and drive frequency on the long-time evolution of Floquet matter. **A:** Short-time evolution of f_0 for a drive with $\Omega = 2.6$ and $\alpha = 3$, at three different values of the s-wave scattering length a. Regardless of interaction strength, f_0 fluctuates near the PGE value (dashed line). Solid gray line shows the solution to the time-dependent Schrödinger equation for the non-interacting case. Top panel shows the driving waveform. **B:** f_0 as a function of time for much longer times, for the same drive and interaction parameters. Data are boxcar-averaged into 200 μs bins. The non-interacting and weakly-interacting samples attain a second plateau (solid line) well below the PGE value (dashed line), while the strongest-interacting sample decays to a high-temperature state consistent with ergodicity. Shaded area indicates the estimated noise floor: at long times we measure no significant ground-band occupation only for the strongest-interacting sample. **C-E:** Evolution of the participation ratio $1/f_0$ for $a = 30$ nm, $\alpha = 3$, and varying drive frequency as indicated in the inset. Dashed line indicates the PGE prediction for the constant-f_0 plateau which extends as the frequency increases. The time-dependence of heating away from the prethermal plateau is observed to be strongly Ω-dependent: at low frequency the participation ratio grows approximately as the square root of time (green solid line), while at the highest frequency the heating is consistent with a $t^{1/4}$ dependence (red solid line).

increasing quasimomentum extent will break the selection rules that prohibit odd band occupation at $k = 0$. To account in part for this spreading, all measurements of f_0 in Fig. 8.4 integrate over the entirety of the first Brillouin zone. The strongest-interacting samples, subjected to the same drive, behave in a fundamentally different way: they do not exhibit this second plateau but instead are observed to attain ergodicity, heating up

indefinitely with no detectable atoms in the ground band after modulation. The second main result of this report, after the maps of the IPR and drive-dependent material properties, comprises these measurements of the detailed time evolution of Floquet matter: at short time scales, we observe a rapid emergence of a PGE prethermal state exhibiting large fluctuations, and at long time scales, we observe a second prethermal plateau and interaction-dependent ergodicity.

These results raise a crucial question: is the rapid onset of ergodicity for the strongest-interacting system inevitable? To quantitatively explore the possibility of delaying the onset of ergodicity in driven interacting systems, we measured the long-time evolution of the participation ratio $1/f_0$ for the strongest-interacting samples at increasing values of Ω. The results are shown in Figs. 4C-E. At $\Omega = 2, \alpha = 3$, the observed long-time evolution of $1/f_0$ is consistent with the $\sqrt{t}$ dependence naively expected from Joule heating, and no significant plateau is observed. As the drive frequency is increased holding α constant, we observe the emergence of a quasi-static prethermal plateau lasting thousands of drive cycles, at a value of f_0 consistent with the PGE prediction. This plateau too eventually decays. We note that this high-frequency stabilization of the prethermal plateau cannot be simply explained by the exponential suppression of Floquet heating, predicted for single-band and spin models [129, 130, 131, 132], though it may be related; neither is the prethermal state characterized by simple high-frequency Floquet-Magnus-type expansions. Intriguingly, for the highest-frequency drives like the $\Omega = 8$ drive of Fig. 8.4E, the long-time departure from this plateau is consistent with a $t^{1/4}$ time dependence, and is clearly slower than for the lower drive frequencies. This unusual behavior, while still poorly understood, is consistent with the sub-Joule heating predicted by recent theoretical analyses of a driven $O(N)$ model [136, 137]. The recovery of the prethermal plateau by increasing the drive frequency in the presence of interactions, and the observation of anomalously slow heating dynamics away from the recovered plateau, together constitute

the third and final main result of this report.

In conclusion, we have used a flexible platform for studying strongly driven interacting quantum systems to acquire a complete prethermal map of the drive-dependent properties of tunable Floquet matter, revealing a Floquet delocalization crossover which is in quantitative agreement with predictions of a theory based on the periodic Gibbs ensemble. The measurement of an IPR via a double quench protocol represents a powerful quantitative tool for characterizing strongly-driven quantum systems in a variety of experimental contexts. Measuring the evolution of driven ensembles at both short and long times, we have observed two prethermal plateaux and a long-time transition to ergodicity at a rate and onset time which depend critically on drive frequency and interaction strength.

8.1 Sample preparation and loading

The experiments begin with evaporation of bosonic ^{7}Li atoms in a crossed optical dipole trap (λ=1064 nm, 7 W per beam, 100 μm beam waist, 1 kHz transverse trap frequencies) to generate a Bose-Einstein Condensate (BEC) with approximately 100,000 atoms at a temperature of 20 nK. During and after evaporation, the interatomic interaction strength is controlled by Feshbach tuning using a homogeneous magnetic field. We hold the BEC in the optical trap while ramping the field from the value used for evaporation (729 G, $a\approx$30 nm) to the desired final value in 100 ms. We then adiabatically load the atoms into the ground state of a combined 1D optical lattice with an initial static lattice depth of $V_0 = 10E_R$, where $E_R = \frac{\hbar^2 k_L^2}{2m}$ is the lattice recoil energy. In the static lattice, the tunneling rate between lattice sites is 483 Hz and the lattice site trap frequency is $\omega_0 = 159$ kHz. The transverse confinement is provided by the Gaussian lattice beams, resulting in a transverse trapping frequency of 449 Hz$\times\sqrt{1+\alpha/2}$. We observe

no significant excitation of transverse oscillator modes in the experiments reported here. Any additional forces along the lattice direction arising from magnetic field curvature or lattice beam intensity gradients are nulled out using magnetic shim coils to increase the period of Bloch oscillations to time scales significantly longer than our longest experiments [85]. The interacting experiments are performed at Feshbach-induced s-wave scattering lengths of 2 nm and 30 nm, resulting in Thomas-Fermi interaction energies of 1.3 kHz and 3.8 kHz, respectively, for $\alpha = 0$. Because the Thomas-Fermi interaction energies grow weakly with the modulation depth due to increased transverse confinement, we characterize interactions by the scattering length, which does not depend on the drive parameters.

8.2 Optical lattice for sign-changing modulation

To enable realization of the $\alpha > 1$ regime of ultrastrong lattice modulation, a combined lattice is formed by overlapping two 1D optical lattices with a relative spatial phase shift of half a period. We use up to 7 W of 1064 nm light per beam and an 88 μm beam waist. The two lattices are separated in frequency by 160 MHz and have orthogonal linear polarizations. The beams are retroreflected by the same mirror to form two independent lattices. The relative phase is controlled by means of a waveplate stack, arranged so that the one of the lattices receives a $\lambda/4$ phase shift as it is retroreflected. This causes the two lattices to cancel each other when both beams have the same power, resulting in a featureless optical dipole trap; intentionally imbalancing the power results in a lattice of controllable sign. The depth of the combined lattice and the relative spatial phase between the two lattices are calibrated using matter-wave diffraction. After ramp-up of the combined lattice to an initial depth of 10 E_R, the system is quenched into the Floquet Hamiltonian by applying lattice amplitude modulation with some Ω and α. The ampli-

tude of the combined lattice is modulated at up to 2 MHz by simultaneously varying the power of RF signals sent to two acousto-optical modulators from an AD9854 DDS board. Crucially for the results we present, this double lattice modulation allows us to create a combined optical lattice that can change sign, where maxima (minima) become minima (maxima) during a drive cycle.

8.3 Measurement protocol

After the system is allowed to evolve for some time in the modulated lattice, the modulation is quenched off and the combined lattice can either be snapped off or ramped off adiabatically with respect to the bandgaps to perform band-mapping [149]. When measuring a prethermal map of Floquet material properties at a fixed total drive time like those shown in Figs. 1B and 1C, the drive is allowed to fully complete the final modulation cycle before band-mapping, but for following the full time-dependent evolution as is done in Figs. 2C and 3A the quench can be performed at any point in the drive cycle. After band-mapping, resonant absorption imaging measures the atom number in the ground and excited bands. All band-mapping measurements are performed at a time of flight of 1.25 ms. At this time of flight, convolution of the initial Heisenberg-limited spatial distribution of the condensate with the momentum distribution limits our quasimomentum resolution to $\sim 0.2k_L$.

8.4 Identification of f_0 as an IPR for quantifying ergodicity

Here we show explicitly that for a non-interacting driven system the ground-band occupation f_0 is equal to the inverse participation ratio in the Floquet state basis. Fur-

thermore we argue that for interacting systems in the prethermal regime, where the PGE can be applied, f_0 provides a straightforward and experimentally accessible metric for localization and ergodicity.

The time-dependent Schrödinger equation of a driven system possesses quasi-stationary solutions called Floquet states, which are of the form $|n(t)\rangle e^{it\varepsilon_n/\hbar}$, with real quasienergy ε_n and time-periodic Floquet mode $|n(t)\rangle = |n(t+T)\rangle$, where $T = 2\pi/\omega$ denotes the driving period. For each time t they form an orthogonal basis, so that for a given pure initial state $|\psi(0)\rangle$ the evolved state can be expressed as $|\psi(t)\rangle = \sum_n c_n |n(t)\rangle e^{-i\varepsilon_n t/\hbar}$, with time-independent coefficients $c_n = \langle n(0)|\psi(0)\rangle$. Accordingly, the expectation value of an observable $\hat{O}$ evolves as $\langle\hat{O}\rangle(t) = \sum_{nn'} c_n^* c_{n'} \langle n(t)|\hat{O}|n'(t)\rangle e^{it(\varepsilon_n - \varepsilon'_n)/\hbar}$. The relaxation to a quasi-steady state (i.e. a time-periodic state) in the long-time limit can be associated with the dephasing and averaging out of the off-diagonal terms, so that asymptotically $\langle\hat{O}\rangle(t) \simeq \sum_n |c_n|^2 \langle n(t)|\hat{O}|n(t)\rangle$, corresponding to a Floquet diagonal ensemble described by a periodic density operator $\hat{\rho}_{\mathrm{dia}}(t) = \sum_n |c_n|^2 |n(t)\rangle\langle n(t)|$ [150]. For a non-interacting driven gas, there are an extensive number of integrals of motion given by the number operators $\hat{n}_j(t)$ of the single-particle Floquet modes $|j(t)\rangle = |j(t+T)\rangle$. The expectation values of these operators determine the PGE. To quantify the degree of localization (non-ergodicity), we initially prepare the system in the undriven ground-state $|\psi_0\rangle$, so that $c_n = \langle n(0)|\psi_0\rangle$, and consider the expectation value of the projector $\hat{O} = |\psi_0\rangle\langle\psi_0|$ at stroboscopic times $t_\nu = \nu T$ with integer ν, which is equal to the squared overlap $|\langle\psi_0|\psi(t_\nu)\rangle|^2$ with the evolved state $|\psi(t_\nu)\rangle$. According to the diagonal ensemble and employing $|n(t_\nu)\rangle = |n(0)\rangle$, the long-time average (indicated by an overbar) over the stroboscopic dynamics of this quantity gives

$$\overline{|\langle\psi_0|\psi(t_\nu)\rangle|^2} = \sum_n |\langle\psi_0|n(0)\rangle|^4 \equiv \mathrm{IPR}. \tag{8.2}$$

This quantity is directly identifiable as the inverse participation ratio that quantifies the localization of the ground state $|\psi_0\rangle$ in the basis of the Floquet states. Its inverse, 1/IPR, measures the number of Floquet states required to represent $|\psi_0\rangle$. For the non-interacting gas, we find that the desired overlap is given by the fraction of atoms populating the single-particle ground state (i.e. the quasimomentum $k = 0$ mode in the lowest Bloch band), $|\langle\psi_0|\psi(t_\nu)\rangle|^2 = f_0(t_\nu)$, which we have measured for example in Fig. 8.1B. Thus, having relaxed to a quasi-steady state, we have

$$\mathrm{IPR} = \overline{f_0(t_\nu)}, \tag{8.3}$$

so that the measured observable directly quantifies non-ergodicity.

In an interacting many-body system, the diagonal ensemble is still formally characterized by an exponentially large number of probabilities $|c_n|^2$. However, it is believed that the quasi-steady state is characterized by a periodic Gibbs ensemble (PGE), $\rho_{PGE}(t) = Z^{-1}\exp[-\sum_j \lambda_j \hat{I}_j(t)]$, with $\hat{I}_j(t) = \hat{I}_j(t+T)$ denoting the integrals of motion of the system [134]. It is important to note that while a generic interacting Floquet system should at sufficiently long times approach a fully ergodic high-temperature state $\rho_{\mathrm{ergodic}} \propto 1$ [135, 151], even the interacting system can approach a prethermal state that is accurately described by the PGE on intermediate, and potentially exponentially long, time scales. This motivates the use of f_0 as a prethermal diagnostic of Floquet localization even in the interacting regime.

8.5 Calculating expected number of occupied bands

Here we briefly discuss the reason that only a finite number of bands are expected to be significantly occupied even in the presence of a strong drive. Since quasimomentum is

conserved in the absence of interactions, the single-particle Hamiltonian H of the system can be expressed in terms of states $|m\rangle$ having momentum wave numbers $K_m = (4\pi/\lambda)m$ for integer m. In units of the recoil energy E_R,

$$H = 4\sum_m \left[m^2 |m\rangle\langle m| + \frac{V(t)}{16}\Big(|m+1\rangle\langle m| + |m-1\rangle\langle m| \Big) \right] \tag{8.4}$$

with $V(t) = (V_0/E_R)[1 + \alpha\cos(\omega t)]$. Thus, already for $|m| \simeq 1$, the energy separation $(m+1)^2 - m^2 = 2m + 1$ to higher-lying states becomes larger than the time-dependent coupling matrix elements $V(t)/16$ and the driving frequency. This suggests that the drive will cause substantial redistribution among small m, while for large m the Floquet states will not significantly differ from the undriven eigenstates of the system that correspond to the scattering continuum. In other words, the ground state of the non-interacting system will mainly overlap with a few Floquet states. The Hamiltonian of Eq. 8.4 explains also the origin of the crossover to a highly localized regime with f_0 close to one for large frequencies, as we observe in Fig. 8.1. The fact that it couples only neighboring momenta m and $m \pm 1$ shows that (except for narrow resonances) the ground state is predominantly coupled to low energy states, transitions to which become off-resonant for large drive frequencies.

Appendix A

Non-Exponential Decay

The contents of this appendix include a series of notes on our proposed experiment investigating non-exponential decay of quantum systems.

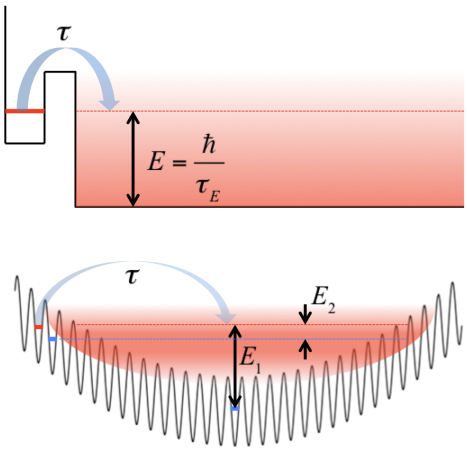

Figure A.1: **Top:** Simple potential $V(x)$ in which non-exponential decay is expected on general grounds. τ is the decay time of the exponential part of the tunneling process, and $\tau_E = \hbar/E$ is the timescale associated with the energy of the decay product. **Bottom:** Schematic of proposed optical lattice experiment probing non-exponential decay. E_1 and E_2 are different characterizations of the decay product energy, as discussed in the text.

Background

Despite the apparent ubiquity of exponential decay, quantum mechanics requires that decay processes to a continuum with a lowest-energy state have non-exponential time dependence at both very short and very long times. The underlying physics is discussed in Sakurai's *Modern Quantum Mechanics*,[1] and in a 1988 *Nature* news & views piece by Greenland [152]. Short-time non-exponential decay was detected in 1997 in an experiment using cold sodium atoms in optical lattices [153]; Greenland's discussion of this result [154] coined the appealing term "quantum procrastination." Eva Lindroth and collaborators recently pointed out [155] that the predicted long-time deviations from the exponential decay law have not yet been directly experimentally observed, and furthermore that attosecond chronoscopy of a resonance in the H^- ion might reveal such deviations.

Here are a few other relevant references: a very nice review of the treatment of quantum decay [156], a general theoretical discussion of long-time quantum decay prop-

[1]The relevant portion of the text is appended to this document.

erties [157], a discussion of the role of fluctiations by Greenland [158], a paper presenting some calculations on non-exponential decay of a specific excited state of a negative helium ion [159], a 1982 theory paper discussing nonexponential decay in laser-induced negative ion photodetachment, a 2015 paper discussing the theory of non-exponential tunneling ionization of an atom in an intense laser field [160], a *Phys. Rev. C* article from 2004 claiming indirect evidence for non-exponential decay from an analysis of experimental data on scattering phase shifts in ^{8}Be [161], and a 1988 *PRL* presenting negative results of a careful experimental search for non-exponential nuclear decay [162].

Predicted regime of detectable non-exponential decay

According to the arguments presented by Sakurai, quantum mechanical decay processes can *never* be perfectly exponential, yet of course they are generally observed to be exponential to an excellent approximation. Why is this? According to Greenland's 1988 article, the expected timescale τ_L for long-time deviations from the exponential decay law is of order

$$\tau_L \simeq 3\tau \log\left(E\tau/\hbar\right) = 3\tau \log\left(\tau/\tau_E\right), \tag{A.1}$$

where τ is the decay time (of the exponential part of the decay), and $E = \hbar/\tau_E$ is the energy released in the decay. For the deviations from exponential decay to be experimentally detectable, τ_L/τ should not be too large, so that a measurable fraction of the systems under consideration will remain undecayed to exhibit the nonexponential behavior. Eq. A.1 thus suggests the study of decaying states where τ/τ_E is not much greater than 3, so that the desired effect can be seen in a few e-foldings of the decay. This, and the absence of long-range interaction between decay products, motivates the study of non-exponential decay in anions [152, 155]. In particular, τ/τ_E is around 1 for the H^- resonance proposed in [155]. This also helps explain the negative result of

attempts to directly observe non-exponential nuclear decay: for the ^{56}Mn experiments reported in [162], τ/τ_E was around 10^{25}, and the indirect approach to measurement of the ^{8}Be decay discussed in [161] suggests that τ_L/τ is around 30, making direct-detection experiments infeasible.

In designing an experiment to test this, it is useful to see how Greenland's prediction for the onset of non-exponential behavior compares to calculated time evolution. To this end, Eva set up some Mathematica calculations to calculate the time dynamics of a metastable state by taking the Fourier transform of a truncated Breit-Wigner energy distribution. David ported these to MATLAB and ran the calculation for various values of the product of the decay energy and the lifetime; the results appear in Fig. A.2.

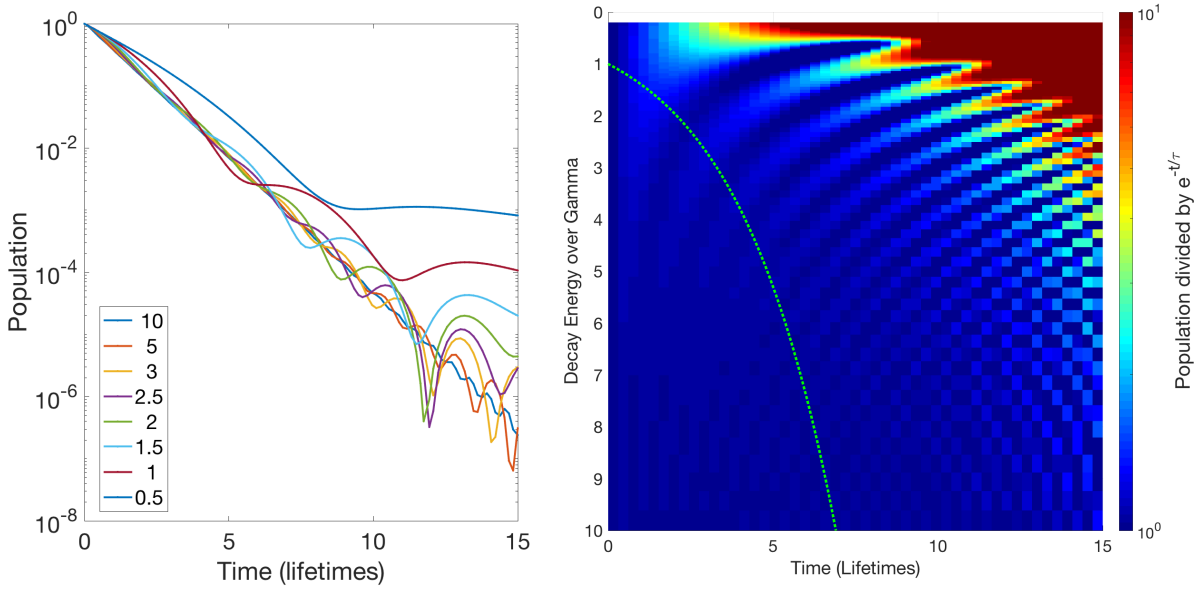

Figure A.2: Calculated deviations from exponential behavior for various values of E/Γ. Green dashed line in the right-hand panel is the Greenland limit of Eq. 1.

Measuring long-time non-exponential decay with cold atoms in optical lattices

Ultracold atoms in optical lattices offer wide tunability of a variety of parameters: interatomic interactions can be controlled or switched off using Feshbach resonances, the potential landscape can be finely tuned by applying magnetic field gradients and non-resonant light fields, and hundreds of thousands of atoms can be placed in an identical initial quantum state by Bose condensation. Here we explore the possibility of applying this tunability to the experimental study of long-time non-exponential decay.

A schematic of the proposed experiment appears in Fig. A.1. The top panel shows a conceptual position-dependent potential in which non-exponential decay could be cleanly studied, and the bottom panel presents a not-to-scale sketch of the actual position-dependent potential used in current experiments on our group's ^{7}Li BEC machine. This potential, consisting of an overall harmonic confinement combined with a sinusoidal 1D optical lattice, is exactly what we used in recent experiments investigating position-space Bloch oscillations [85], relativistic harmonic motion [114], synthetic Floquet-Bloch bands [128], and Floquet prethermalization [117]. In the diagram, the red and blue solid lines indicate the ground state of the relevant lattice well, τ is the decay lifetime of the initial state indicated by the red solid line, and E_1 and E_2 are two possible characterizations of the decay product energy for use in Eq. A.1.

The **overall idea of the proposed experiment** would be to study the decay of the unstable state indicated by the solid red line in the bottom panel of Fig. A.1. This state decays via tunneling through one or more lattice barriers into a continuum of unbound states (indicated as a red gradient in the figure) with energies larger than the lattice depth. Tuning the depth of the optical lattice exponentially affects tunneling lifetimes, and tuning the curvature and offset of the harmonic confinement controls the

decay product energy. The combination of these two experimental knobs should let us tune τ/τ_E from a regime where the decay is dominantly exponential into a regime where deviations from exponential decay are readily detectable.

Various complications to this simple idea require discussion. The most important complication is that atoms in a lattice actually occupy delocalized energy bands (assuming interactions are turned off), so Fig. A.1's picture of a single initial occupied well is not really appropriate. This was also the case in the short-time decay experiments of [153]. A more physically realistic picture of the decay process we propose to study is based on the concept of Wannier-stark ladders. A nice overview of this topic appears in [163]. For the connection to our picture of exponential decay, see the discussion surrounding Eq. 1.17 in that reference; basically, non-avoided Landau-Zener crossings drive population to higher (incompletely bound) bands once per Bloch cycle, so the effective decay rate is proportional to the Landau-Zener probability times the Bloch frequency. Note that both of these parameters can be controlled with the same two experimental knobs discussed above.

The second complication in mapping non-exponential decay as discussed by Sakurai and Greenland onto a lattice experiment is that in a true Wannier-Stark ladder there is no ground state, since energy decreases forever in the positive x direction. This is analogous to the slightly pedantic statement that no true bound states exist in an atom in any finite electric field. What happens to Sakurai's argument here? Well, we can note a few things. One is that of course there *is* an overall ground state in our experiment and any real experiment; no electric field goes on forever. More quantitatively one can ask what the relevant value is to use for the energy of the decay products which enters Eq. A.1. I currently think it's E_2 (the energy offset between adjacent sites) rather than E_1 (the energy with respect to the global minimum of the harmonic confinement), but it's a question which could use some more thought.

Finally, it is worth considering orthogonalization to a few other relevant experiments. For a beautiful but different example of using tunable cold atom systems to study spontaneous decay processes, see [164], in which multicomponent lattice-trapped cold atoms decaying via matter-wave emission are used to study the way in which decay into a structured vacuum gives rise to non-Markovian behavior. David has spoken to Dominik about this several times recently; their group also has a PRA with some more detailed calculations (INSERT REFERENCE). Their focus so far is less on fundamental quantum corrections to exponential decay and more on a generalization of Purcell enhancement, which has also been studied in photonic crystals [165]. These results are certainly related to the proposed decay experiments with both anions and neutral atoms, but perhaps the corrections to exponential decay we propose to study are in a sense more fundamental since they do not rely on any structuring of the vacuum beyond the existence of a ground state. Additionally, our experiments focus on the physics of a single emitter, rather than an optically-dense assembly of emitters as is the case in the Stonybrook experiment. Sebastian Blatt at the Max Planck in Munich is also developing a strontium experiment which will have capabilities along these lines. My (David's) overall impression is that probes of open quantum systems like this are a pretty hot topic right now, so if we can get a result soon it will fit in well to the discussion; in other words, orthogonalization is not a huge concern but timeliness may be.

A few open questions

1. What is the correct value to use in Eq. A.1 for the energy of the decay products? E_1? E_2?

2. Do we all agree on the Wannier-Stark version of decay?

3. What is the relation to cavity QED phenomena like Purcell enhancement or sup-

pression of spontaneous processes? Is this topic in a sense more fundamental, since it does not involve structuring the vacuum? Are coherent vacuum Rabi oscillations the extreme non-exponential case? (Yes to both, David thinks).

4. What quantitative experimental parameters would we need? First approximation: plug E_2 into Eq. A.1, assume the decay rate is the Bloch frequency times the Landau-Zener probability, and calculate τ_L/τ as a function of harmonic trap offset and lattice depth. (See Cora calculations below).

Further thoughts and notes on experimental feasibility (mainly by Cora)

Exponential Decay

Prof. Lindroth's writeup (and this one) refer to a derivation of an exponential decay rate as given in Sakurai. I (Cora) shall redo it here, since it took me a while to interpret. We are interested in the time evolution of a decaying state $|q_i, t_0\rangle \rightarrow |q_i, t\rangle$, where q is some arbitrary index. The survival probability $P(t)$ is then just given by the overlap of the initial state and the time evolved state:

$$a(t) = \langle q_i, t_0 | q_i, t \rangle \tag{A.2}$$

$$P(t) = |a(t)|^2 \tag{A.3}$$

Since the discrete eigenstates are stationary and therefore do not decay, we don't anticipate the decaying states to be associated with them at all. Therefore, we assume that our state can be written as integration over all continuum states $|\epsilon\rangle$. The time

evolution of $|q_i, t\rangle$ can be then written as.

$$|q_i, t\rangle = \int_{-\infty}^{\infty} \mathrm{d}\epsilon \langle \epsilon | q_i, t_0 \rangle \exp\left[-i\epsilon t/\hbar\right] |\epsilon\rangle \tag{A.4}$$

and it easily follows that the survival amplitude is

$$a(t) = \int_{-\infty}^{\infty} \mathrm{d}\epsilon \exp\left[-i\epsilon t/\hbar\right] \rho(\epsilon) \tag{A.5}$$

$$\rho(\epsilon) = \left|\langle \epsilon | q_i, t_0 \rangle\right|^2 \tag{A.6}$$

where the information about the state is all contained now in the probability density $\rho(\epsilon)$. We assume that $\rho(\epsilon)$ has the Breit-Wigner form,

$$\rho_{\mathrm{BW}}(\epsilon) = \frac{\Gamma}{2\pi} \frac{1}{\left(\epsilon - \epsilon_0\right)^2 + \Gamma^2/4} \tag{A.7}$$

which is a Lorentzian probability distribution centered about energy ϵ_0 with some width Γ. This makes intuitive sense to me from a classical damped oscillator model. (DMW note: reference [156] discusses why this assumption is OK. Basically other peaked distributions which look kind of like this will give similar results.)

The survival probability for this distribution can be calculated readily by using Mathematica and we find that

$$P_{\mathrm{BW}} = \exp\left[-\Gamma t/\hbar\right] \tag{A.8}$$

which is the expected exponential decay. From a quick look through, it seems the main assumptions about this form are:

- The decay state is written as a superposition of continuum states

- This applies to continuum states of all energies
- We assume the Breit-Wigner distribution.

Non Exponential Decay

According to the Sakurai document, this reasoning breaks down because of the presence of a ground state $|\epsilon\rangle$ which makes a cutoff in the integration of eq. A.5. This means that $\rho(\epsilon) = 0$ for any $\epsilon < \epsilon_0$. (I'm confused why they use the same character ϵ_0, I feel like the center point of the state should not necessarily be related to the ground state.) As a consequence, the result can never be an exponential (with some more math discussion and theorems).
Some points:

- Sakurai says that this is true even without using Breit-Wigner (This is discussed further in Ref. [156])
- He says "[this] does not shed any light on when the non-exponential behavior sets in or on how much the surival probability deviates from the exponential form"
- The second part of the Sakurai section seems to be discussing short time deviations and we haven't gone through it carefully.

Landau-Zener Probabilities

In our proposed experiment and in Raizen's experiment the decay process is modeled as tunneling from a ground band to an excited band which can be roughly thought of as continuum states. From a band structure perspective, we can model the tunneling to higher bands as a Landau-Zener transition over an avoided crossing. We have already

calculated LZ probabilities in Floquet bands for our transport PRL [128], and we are including a discussion here for clarity. We should add a link to the code.

The simplest Landau-Zener calculation comes from the simple two-level system outlined in Fig. A.3.

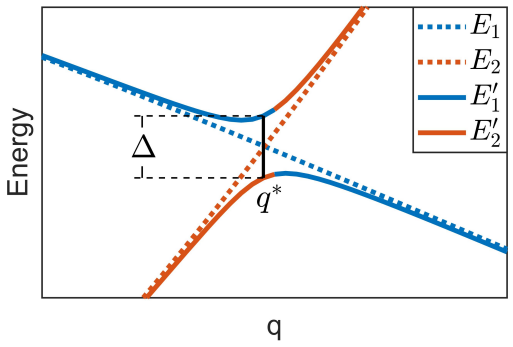

Figure A.3: General schematic for a Landau-Zener transition. The unperturbed energies E_1 and E_2 normally cross energies, but the presence of a perturbation couples them to new energies E_1' and $E_2\prime$. The new states have an avoided crossing with gap Δ at the coupling parameter q^*.

Here q can be any parameter which controls the energy levels, which for us will usually be quasimomentum. Supposing the initial wavefunction is localized in state E_2' at $q_i \ll q^*$, as $q(t)$ traverses the crossing at q^*, the state can non-adiabatically transition to the upper branch of E_2' depending on $\dot{q}$ and Δ. The key figure of merit is the Landau-Zener velocity

$$v_{\mathrm{LZ}} = \frac{\frac{\partial}{\partial q}|E_2 - E_1|}{\frac{\partial}{\partial t}|E_2 - E_1|} \approx \frac{\partial q}{\partial t} \tag{A.9}$$

The Landau Zener probability of a diabatic transition P_D is then

$$P_D = e^{-2\pi\Gamma} \tag{A.10}$$

$$\Gamma = \frac{1}{4}\frac{\Delta^2/\hbar}{\frac{\partial q}{\partial t}\frac{\partial}{\partial q}|E_2 - E_1|} \tag{A.11}$$

Intuitively, we see that the transition probability decreases for larger gaps Δ, increases for faster ramps $\dot{q}$, and increases for larger unperturbed energy slopes. It is important to note that this Landau Zener calculation is an approximation and can break down (I forget the exact requirements).

At this point it is useful to consider two cases of a Landau Zener transition which apply to this experiment in the context of Bloch oscillations.

- Bloch oscillations in static bands - the periodic potential opens gaps between free particle states.
- Bloch oscillations in floquet bands - the periodic drive opens gaps in the quasienergy spectrum between hybrid Floquet-Bloch bands.

In each case, it should be clear what the unperturbed and perturbed states should be. In either case, the parameter q is the momentum of the ensemble. We un-dimensionalize q in terms in terms of the lattice k-vector such that the size of the first Brillouin zone is $q \in [-1, 1]$, and we express the energy in units of the recoil energy E_R. In the context of Bloch oscillations, this makes $\dot{q} = 2f_B$ where f_B is the Bloch oscillation frequency. This simplifies eq. A.11 to the suggestive form

$$\Gamma = \frac{1}{4\pi}\left(\frac{\Delta}{hf_B}\right)\left(\frac{\Delta}{\frac{\partial}{\partial q}|E_2 - E_1|}\right) \tag{A.12}$$

which just says that the gap Δ needs to be compared to the Bloch oscillation frequency and the rate of change of the unperturbed states. In the case of the static band picture, the slope of the unperturbed energies $\partial E/\partial q = 2q$ is easily computed from the free particle dispersion $E = q^2$. An example showing the static case is given in Fig. A.4.

For Landau-Zener transitions between Floquet-Bloch bands, the analysis is summarized in Fig. A.5.

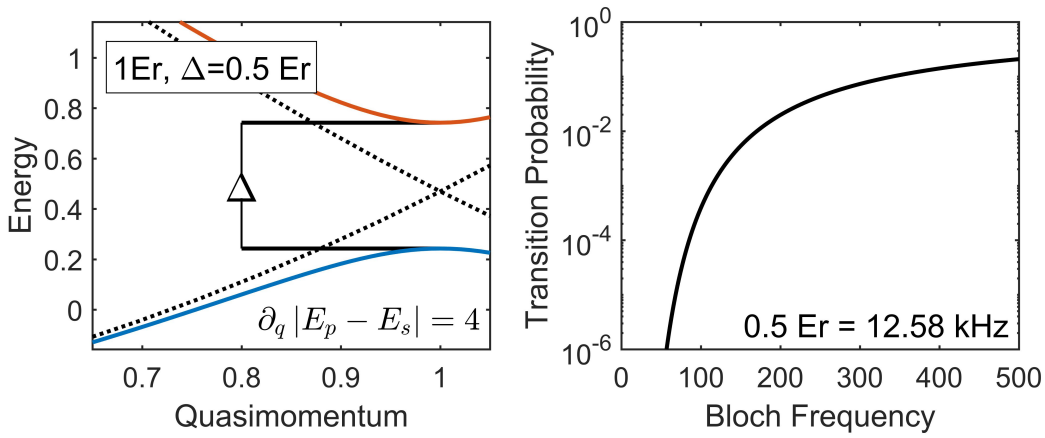

Figure A.4: Landau Zener transition analysis between static Bloch bands. Here the unperturbed states are the free particle states (dotted) and the perturbed states are the bloch bands (solid colored). Here the group velocity at the edge of the zone $\partial_q E$ is simple. For Bloch frequencies less than gap energy, the transition probability is very small. This presents an experimental challenge for us; given the forces we can easily apply with our current apparatus, the Bloch frequencies can't get too much larger than 50 Hz.

We think that in terms of the Bloch frequency and Landau-Zener probabilities discussed above, the decay rate should be

$$R = P_D f_B, \tag{A.13}$$

which is to say that the ensemble attempts a tunnel decay every Bloch period at the avoided crossing. See also Ref. [163]. DMW feels like there might be a factor of 2 here– doesn't it attempt to tunnel twice per Bloch period?

In any case, the upshot of these calculations so far is that we probably cannot study non-exponential decay with ordinary Bloch oscillations, but we probably can do so with Floquet-Bloch oscillations due to the highly tunable nature of the avoided crossing between Floquet-Bloch bands. We do not currently anticipate that this will require any experimental upgrades, although we will need to think carefully about atom number measurement techniques since the signals are not expected to be gigantic (see Fig. A.2).

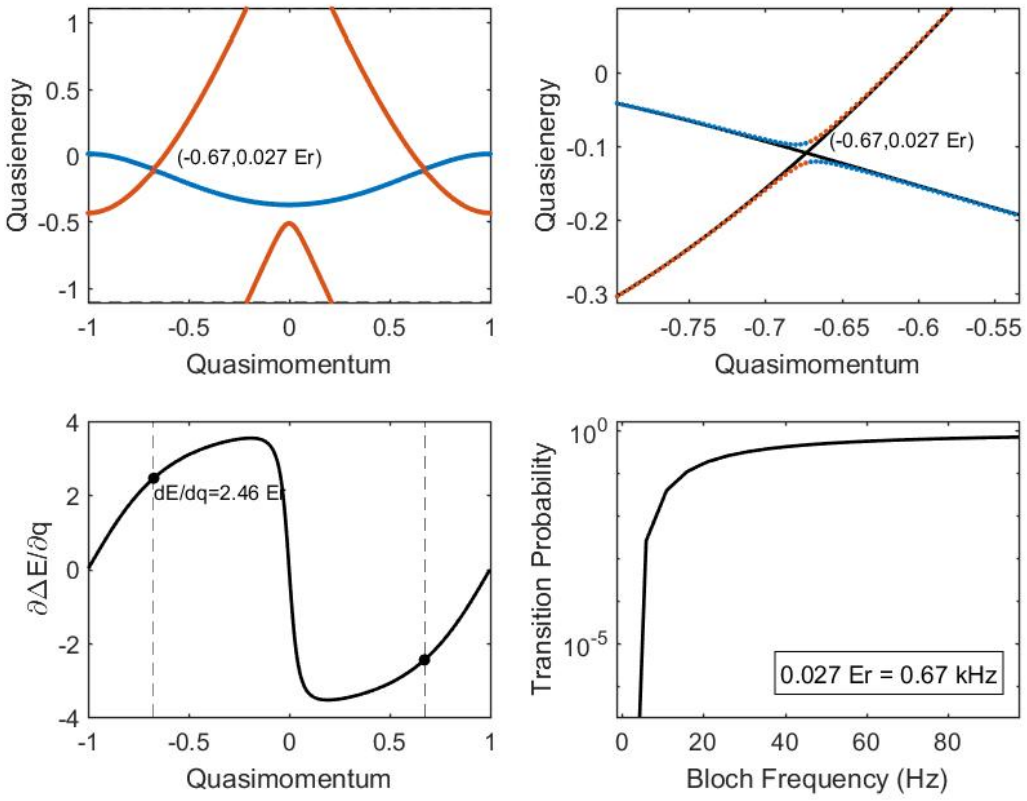

Figure A.5: Landau-Zener analysis for Floquet-Bloch bands. Here the static lattice depth 3.6 E_R, the modulation depth is 5.5%, and the modulation frequency is 56 kHz. Note that since the drive amplitude can tune the gap, we can easily access a wide range of Landau-Zener probabilities even at accessible Bloch frequencies (below 50 Hz).

Appendix B

Direct Digital Synthesis for Fast Modulation

In this section we shall discuss the workhorse radio-frequency (RF) source for driving the acoustic-optic modulators controlling the lattice laser beams in our modulated lattice experiments. The system which we've designed utilizes an AD9854 direct digital synthesizer (DDS) from Analog Devices in tandem with the commercially available single-board computer BeagleBone Black (BBB). The necessity of such a system stems from the high frequency requirements of the RF power modulation required to amplitude modulate the lattice beams. While the precise requirements are specified by the exact experimental sequence, the amplitude modulation frequencies for the experiments discussed in this thesis need to exceed 1 MHz at a wide range of modulation depths. Our group historically has used a combination of voltage controlled oscillators (VCO) and voltage variable attenuators (VVA) to generate the RF to drive our AOMs, but this solution in untenable for this application as such devices are typically limited to modulation speeds in the few tens of kilohertz.

The basic architecture is outlined in Figure B.1 with the primary two components of

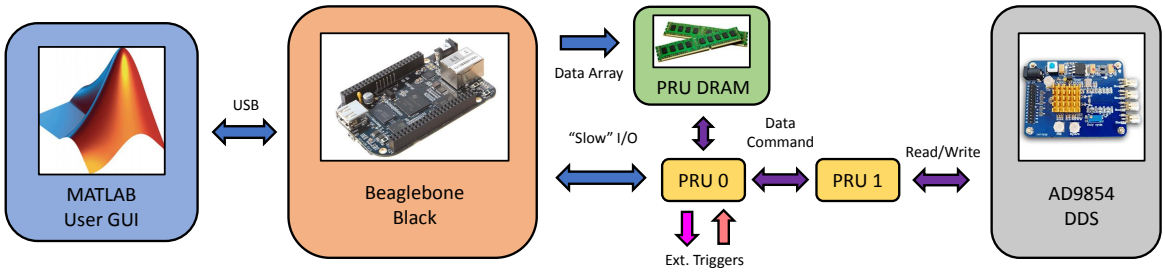

Figure B.1: Schematic of the different working components of the DDS. The user interacts with the BBB

concern being the BBB and the actual DDS the AD9854. We take advantage of the the fast physical real time unit (PRU) on the beaglebone black which can write to its digital output pins with a 5 ns update time. When combined with the parallel programming port of the DDS which operates on a 300 MHz clock, we can alter the RF from the DDS with an update write time of around 20 ns which corresponds to a overall update speed of 50 MHz. This fastest update speed sets the maximum bandwidth on how quickly the lattice amplitudes can be rewritten. We run both the PRU's on the BBB (PRU0 and PRU1) in parallel that run in tandem. PRU0 reads from the PRU DRAM and then feeds the relevant parameters to be run into PRU1 which actually writes the IO pins to the DDS. PRU0 also handles the job of monitoring and controlling the triggers to and from the rest of the experiment. Writing to the DRAM is limited by the operating system on the BBB and is therefore fixed for an experimental sequence. Since this architecture writes to the DDS in the time domain, we are fundamentally limited by the size of the local DRAM on the PRU to 28 KB.

Appendix C

Primer on Numerical Techniques

This appendix briefly discusses a basic overview of numerical techniques for evolving the time dependent Schrödinger equation.

Quite often it is of practical importance to numerically time evolve quantum systems, and while this problem is incredibly rich, some basic numerical tools are useful in providing qualitative understanding. In this appendix, we discuss some straightforward techniques to solving the single particle time dependent Schrödinger equation given below

$$\hat{\mathbf{H}}(\tau)\psi(\tau) = i\frac{\partial\psi(\tau)}{\partial\tau} \tag{C.1}$$

$$\hat{\mathbf{H}}(\tau)\hat{\mathbf{U}}(\tau) = i\frac{\partial\hat{\mathbf{U}}(\tau)}{\partial\tau}, \tag{C.2}$$

where have also assumed unitary time evolution such that $\hat{\mathbf{U}}^\dagger\hat{\mathbf{U}} = \mathbf{I}$. Solving this first order differential equation for $\psi(\tau)$ or $\hat{\mathbf{U}}(\tau)$ depends on the time dependence of the Hermititan generator - the Hamiltonian.

In the case that the Hamiltonian is time independent, the solution is found by

$$\hat{\mathbf{H}}\hat{\mathbf{U}} = i\frac{\partial\hat{\mathbf{U}}}{\partial\tau} \tag{C.3}$$

$$\hat{\mathbf{U}}(\tau) = e^{-i\hat{\mathbf{H}}\tau}, \tag{C.4}$$

in the usual way. Therefore, knowledge of the Hamiltonian leads immediately to time evolution as defined by equation C.4, and time evolved states can then be computed numerically via matrix exponentiation.

If the Hamiltonian is time dependent, such a simplification is not permitted. One solution is to time evolve the system over small discrete time steps over which the Hamiltonian is approximately constant. The accuracy of this trotterization is expressed by the Baker-Campbell-Hausdorff formula

$$e^{\mathbf{A}}e^{\mathbf{B}} = e^{\mathbf{A}+\mathbf{B}+\frac{1}{2}[\mathbf{A},\mathbf{B}]+\cdots}. \tag{C.5}$$

Qualitatively, the time steps $\Delta\tau$ should be chosen smaller than any relevant time scale of the time dependent system. But what is the appropriate and efficient way to discretize time? The rest of this section discusses some approximate ways of evolving in time.

The most basic numerical approximation of equation C.1 utilizes the **forward Euler method**, which implements a first order approximation of time differentiation

$$\hat{\mathbf{H}}(\tau)\hat{\mathbf{U}}(\tau) = i\frac{\partial\hat{\mathbf{U}}(\tau)}{\partial\tau} \tag{C.6}$$

$$\hat{\mathbf{H}}(\tau)\hat{\mathbf{U}}(\tau) \approx i\frac{\hat{\mathbf{U}}(\tau+\Delta\tau)-\hat{\mathbf{U}}(\tau)}{\Delta\tau} \tag{C.7}$$

$$\hat{\mathbf{U}}(\tau+\Delta\tau) = \left(1 - i\hat{\mathbf{H}}(\tau)\Delta\tau\right)\hat{\mathbf{U}}(\tau) \tag{C.8}$$

$$\hat{\mathbf{U}}_{j+1} = \left(1 - i\hat{\mathbf{H}}_j\Delta\tau\right)\hat{\mathbf{U}}_j, \tag{C.9}$$

where we have utilized the index j to indicate the discretization of time. Alternatively, by taking $\Delta\tau \to -\Delta\tau$ the **backwards Euler method** is obtained which evolves backwards in time. In addition to being correct to only first order, the Euler method is not unitary ($\hat{\mathbf{U}}\hat{\mathbf{U}}^\dagger \neq 1$) and is therefore numerically unstable.

An alternative and better solution is the **Crank-Nicolson method** which is numerically stable and is frequently used to solve diffusion based partial differential equations. It averages the forward and backward Euler methods describes previously.

$$\frac{\partial u}{\partial t} = F(u) \tag{C.10}$$

$$\frac{u_{j+1}-u_j}{\Delta\tau} = \frac{1}{2}\left(F_{j+1}+F_j\right) \tag{C.11}$$

In the context of the time dependent Schrödinger equation, the evolution is expressed by

$$\frac{\psi_{j+1}-\psi_j}{\Delta\tau} = -i\frac{1}{2}\left[\hat{\mathbf{H}}_j\psi_j + \hat{\mathbf{H}}_{j+1}\psi_{j+1}\right] \tag{C.12}$$

$$\left(\hat{\mathbf{I}} + \frac{i\Delta\tau}{2}\hat{\mathbf{H}}_{j+1}\right)\psi_{j+1} = \left(\hat{\mathbf{I}} - \frac{i\Delta\tau}{2}\hat{\mathbf{H}}_j\right)\psi_j \tag{C.13}$$

$$\psi_{j+1} = \frac{\hat{\mathbf{I}} - \frac{i\Delta\tau}{2}\hat{\mathbf{H}}_j}{\hat{\mathbf{I}} + \frac{i\Delta\tau}{2}\hat{\mathbf{H}}_{j+1}}\psi_j, \tag{C.14}$$

where the divided by symbol implies matrix inversion. While inversion operations are computationally expensive, we shall primarily consider tridiagonal matrices for which the computation time is reduced.

In the case that $\hat{\mathbf{H}}(t) = \hat{\mathbf{H}}_0$, then we see that this technique is indeed unitary. Inversion operations can be costly, but we frequently can produce Hamiltonians which are tridiagonal. In this case, there are quick matrix solvers for finding the inverse of a tridiagonal matrix. In the case that the Hamiltonian is time dependent, the Crank Nicholson time evolution operator as given above is not unitary. However, unitarity can be restored by making a midpoint approximation.

$$\hat{\mathbf{U}}(\tau+\Delta\tau,\tau) = \frac{\hat{\mathbf{I}} - \frac{i\Delta\tau}{2}\hat{\mathbf{H}}(\tau+\frac{\Delta\tau}{2})}{\hat{\mathbf{I}} + \frac{i\Delta\tau}{2}\hat{\mathbf{H}}(\tau+\frac{\Delta\tau}{2})} \tag{C.15}$$

As another alternative, one may use an **exponential midpoint** to time evolve. This is will be unitary by construction, but in general will have a longer computation time.

$$\hat{\mathbf{U}}(\tau+\Delta\tau,\tau) = \exp\left[-i\Delta\tau\hat{\mathbf{H}}(\tau+\Delta\tau/2)\right] \tag{C.16}$$

For one dimensional systems, the Hamiltonians commonly take the following form

$$H\psi = i\frac{\partial\psi}{\partial\tau} \tag{C.17}$$

$$H = p_\phi^2 + v(\phi,\tau) \tag{C.18}$$

$$i = [\phi, p_\phi], \tag{C.19}$$

where it can be seen that p_ϕ and $v(\phi,\tau)$ are diagonal in the momentum and position basis respectively. In the position basis, $p_\phi^2 \to -\partial_\phi^2$, and it is common to implement a finite difference method such that the kinetic energy operator is tridiagonal.

$$\partial_\phi^2\psi\big|_n = \frac{\psi_{n+1} - 2\psi_n + \psi_{n-1}}{\Delta\phi^2} \tag{C.20}$$

$$-\partial_\phi^2 = \frac{1}{\Delta\phi^2}\begin{bmatrix} 2 & -1 & & 0 \\ -1 & \ddots & \ddots & \\ & \ddots & \ddots & -1 \\ 0 & & -1 & 2 \end{bmatrix} \tag{C.21}$$

$$v(\phi,\tau) = v\left(\phi,\tau\right)\hat{\mathbf{I}} \tag{C.22}$$

Combining equation C.21 with C.15 or C.16, we note the discretization step $\Delta\tau/\Delta\phi^2$. Decreasing $\Delta\phi$ increases the accuracy in H at any time, but numerical stability in time evolution mandates an even smaller $\Delta\tau$. While this specific quantity arises in the position basis, such a balancing of discretization will manifest generically.

Appendix D

Basics Scattering Theory

This appendix contains some notes on scattering theory.

The theory of elastic collisions is well documented in many quantum mechanics textbooks. According to scattering theory, the cross section σ encapsulates all the necessary information about scattering events. In our case, we shall consider the low energy scattering events by indistinguishable bosons. The lowest energy scattering events are s-wave scattering, which can be treated analytically.

A general Hamiltonian for two interacting particles with a central potential $V(r)$ is written below.

$$\hat{\mathbf{H}} = \frac{p_1^2}{2m_1} + \frac{p_2^2}{2m_2} + V(|\vec{r_1} - \vec{r_2}|) \tag{D.1}$$

$$= \frac{P^2}{2M} + \frac{p^2}{2\mu} + V(r) \tag{D.2}$$

$$\tag{D.3}$$

where the reduced mass $\mu = \frac{m_1 m_2}{m_1 + m_2}$. As illustrated in the rewritten Hamiltonian, we can consider addressing the problem in the center of mass reference frame which considerably simplfies the calculation. In the context of collisional theory, we are interested in solutions that close to non interacting free particle one. In a cartersian sense, first consider the plane wave solution to the non-interacting Hamiltonian which can be interpretted physically as the two particles undergoing a head on collision. Such a solution can be recast in terms of incoming and outgoing spherical waves.

$$\psi(\vec{r}) = e^{i\vec{k}\cdot\vec{r}} \tag{D.4}$$

$$= \frac{i}{2k} \sum_{l=0}^{\infty} i^l (2l+1) \left[\frac{e^{-i(kr - \frac{l\pi}{2})}}{r} - \frac{e^{i(kr - \frac{l\pi}{2})}}{r} \right] P_l(\cos\theta) \tag{D.5}$$

Far away from the scatterer, for any reasonable interaction, the interaction potential must drop off and the actual solution must approach that given in equation (D.5). Imposing a strict time ordering of an initial incoming wave,we reason that the only possible net effect is an overall phase shift on each out going spherical plane wave.

$$\psi(\vec{r}) \approx \frac{i}{2k}\sum_{l=0}^{\infty} i^l(2l+1)\left[\frac{e^{-i(kr-\frac{l\pi}{2})}}{r} - S_l(k)\frac{e^{i(kr-\frac{l\pi}{2})}}{r}\right]P_l(\cos\theta) \tag{D.6}$$

$$S_l(k) := e^{2i\delta_l(k)} \tag{D.7}$$

To separate the incoming state from the ougoing one, subtract off the incoming plane wave solution from this total, time independent one.

$$\psi(\vec{r}) - e^{i\vec{k}\cdot\vec{r}} = \frac{1}{2ik}\sum_{l=0}^{\infty} i^l(2l+1)\left[(S_l(k)-1)\frac{e^{i(kr-\frac{l\pi}{2})}}{r}P_l(\cos\theta)\right] \tag{D.8}$$

$$\psi(\vec{r}) = e^{i\vec{k}\cdot r} + \left(\sum_{l=0}^{\infty} i^l(2l+1)\frac{(S_l(k)-1)}{2ik}e^{-i\frac{l\pi}{2}}P_l(\cos\theta)\right)\frac{e^{i\vec{k}\cdot\vec{r}}}{r} \tag{D.9}$$

$$= \psi(\vec{r}) \approx e^{i\vec{k}\vec{r}} + f(\theta)\frac{e^{ikr}}{r} \tag{D.10}$$

where the i^l cancelled with the $e^{-i\frac{l\pi}{2}}$. As we shall verify later, $f(\theta)$ is the differential cross section, which can be expressed in terms of the partial wave scattring ampltidues $f_l(k)$:

$$f(\theta) = \sum_{l=0}^{\infty}(2l+1)f_l(k)P_l(\cos\theta) \tag{D.11}$$

$$f_l(k) = \frac{(S_l(k)-1)}{2ik} \tag{D.12}$$

$$= \frac{1}{k}e^{i\delta_l(k)}\sin\delta_l(k) \tag{D.13}$$

$$= \frac{1}{k\left(\cot\delta_l(k) - i\right)} \tag{D.14}$$

The expression in eq. (D.10) has the convenient physical interpretation that the scattered state is a sphereical wave function modulation by some function.

Probability Flux and Cross Section

Given the expansion as outlined above, it is important to understand the qualitative aspects of the potential. Consider the particle flux operator:

$$\hat{\mathbf{j}} = -i\frac{\hbar}{m}\left(\psi^*\nabla\psi + \psi\nabla\psi^*\right) \tag{D.15}$$

$$= \frac{\hbar\vec{k}}{m} + \frac{\hbar\vec{k}}{m}\hat{\mathbf{r}}\frac{|f(\theta)|^2}{r^2} + O(\frac{1}{r^3}) \tag{D.16}$$

$$\approx \hat{\mathbf{j}}_{\text{in}} + j_{\text{in}}\frac{|f(\theta)|^2}{r^2} \tag{D.17}$$

And we see that we can interpret $|f(\theta)|^2$ as the fraction of atoms that exit through a differential solid angle for an incoming particle flux. This allows us to define the differntial and total cross section:

$$\frac{d\sigma}{d\Omega} := |f(\theta)|^2 \tag{D.18}$$

$$\sigma_{\text{tot}} = \int \mathrm{d}\Omega \; |f(\theta)|^2 \tag{D.19}$$

$$= \frac{4\pi}{k^2} \sum_{l=0}^{\infty} (2l+1) \sin^2 \delta_l(k) \tag{D.20}$$

And we demonstrate that all the relevant scattering information can be encompassed in terms of the phase shifts $\delta_l(k)$.

Interpretation of Expansion

Remembering that we imposed an initial condition of an incoming cartersian plane wave $e^{i\vec{k}\cdot\vec{r}}$, we have generated an expression that predicts the scattered waves in terms of a series expansion of angular momentum. The reason for such an expansion is that we have transformed the problem into a cartersian one, where the natural expression is in the angular momentum basis since our potential is central.

If instead we had chosen an initial incoming state to be a spherical wave of angular momentum l, that scattered state would have been the spherical wave corresponding to no change in angular momentum. Ie. we woud have picked out a single term in the expansion. Since the potential is central, angular momentum has to be consereved the spherical plane waves could not couple to different angular momentum states.

D.0.1 S-wave Scattering Theory

Practically speaking, the lowest order scattering event is the $l = 0$ s-wave scattering. At higher angular mometum, a centrifugal barrier ($\propto r^2$) which weakens the effect of the interaction potential. For short range interactions, the centrifugal barrier can completely

"wash" out effects of the interaction by preventing scattering events at the relevant energies from accessing the inside of the centrifugal barrier.

In the presence of long range interactions the centrifugal barrier still weakens the effect of higher angular momentum collisions, but since we are intersted in the effect of the presence of the interaction, something more complicated must be done.

Let us for now, only consider the s-wave scattering which does not have a centrifugal barrier, and we may apply our intuition about 1D quantum mechanics for the radial schrodinger equation. In this case the cross section reduces to

$$\sigma_s = \frac{8\pi}{k^2}\frac{1}{\cot^2\delta_l + 1} \tag{D.21}$$

where a factor of two has been introduced because of the indishtinguisability for indentical bosons. In the case of sufficiently small energies, this can be expanded in powers of k.

$$\cot(\delta_l(k)) = \frac{1}{ka} + \frac{1}{2}r_s k + ... \tag{D.22}$$

Then consider the limiting case where $k \to 0$

$$\lim_{k\to 0}\sigma_s = \frac{8\pi a^2}{1 + k^2a^2} \tag{D.23}$$

$$\sigma_s(0) = 8\pi a^2 \tag{D.24}$$

Thus we may consider the parameter a as the zero energy scattering length leading to a classical surface area (modulo a factor of two from indistinguishableness).

Let us now examine two simple examples to demonstrate the existence of such an

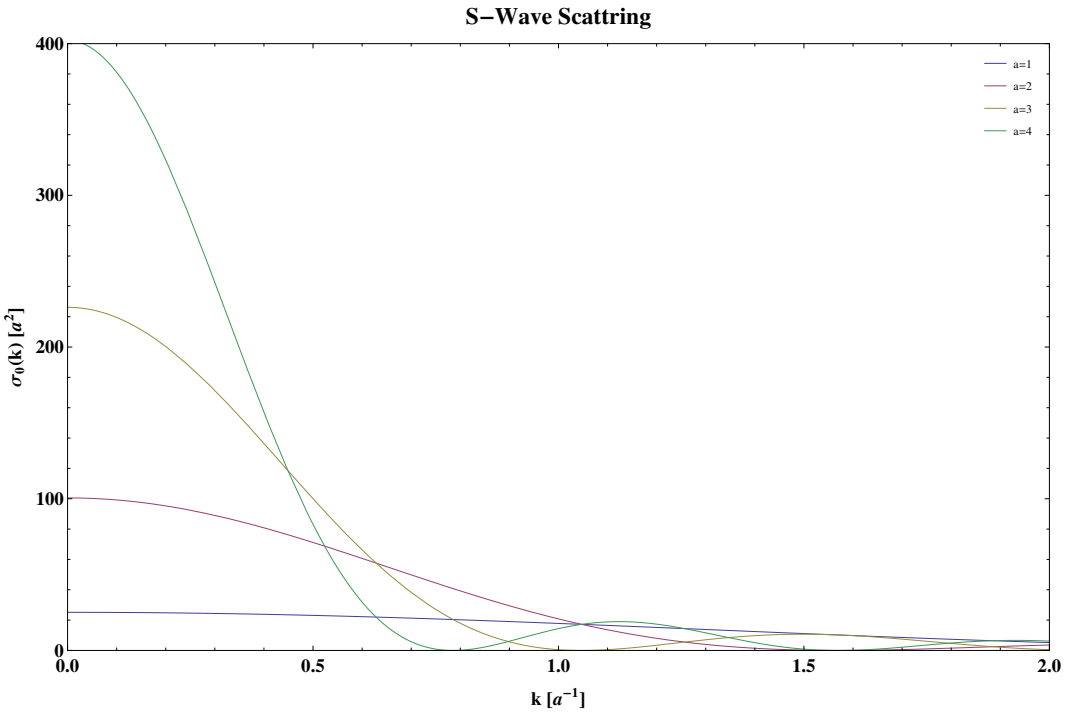

Figure D.1: $\sigma_l(k)$ for different scattering lengths ($r_s = 0$).r For larger scattering lengths the absolute cross section is generally higher, but reaches zero more quickly than lower ones.

expansion and motivate some intuition about r_s and a. ift for two very simple cases

D.0.2 Example: Hard Core Shell

In this case, the potential is given by:

$$V(r) = \begin{cases} +\infty & r < a \\ 0 & r \geq a \end{cases}$$

The wavefunction goes to zero inside a and outside the solution is the familar plane wave. Thus the phase shift is simply

$$\delta_l(k) = ka \tag{D.25}$$

and the cross section is

$$\sigma(k) = \frac{8\pi a^2}{1 + k^2 a^2} \tag{D.26}$$

D.0.3 Example: Finite Square Well

Consider intead, the finite square well, which demonstrates some key interesting features of scattering with attractive interactions.

$$V(r) = \begin{cases} -V_0 & r < r_0 \\ 0 & r \geq r_0 \end{cases}$$

$$\left[-\frac{\hbar^2}{2\mu} \partial_r^2 + V(r) \right] U(r) = E(r) \tag{D.27}$$

$$r\psi(r) = U(r) \tag{D.28}$$

The solutions in the two regions are just plane waves.

$$\psi(r) = \begin{cases} Be^{-i\kappa r} + Ae^{i\kappa r} + & r < r_0 \\ e^{-ikr} - Ce^{ikr} & r \geq r_0 \end{cases}$$

$$\kappa = \sqrt{\frac{2\mu\left(E + V_0\right)}{\hbar^2}} \tag{D.29}$$

$$E = \frac{\hbar^2 k^2}{2\mu} \tag{D.30}$$

where we have chosen to normalize the incoming wave to 1, and have sent the coefficient of the outgoing wave to be negative which is in accordnace with our setup of he definition of $S_l(k)$. The boundary conditions are

$$U(r_0 - \epsilon) = U(r_0 + \epsilon) \tag{D.31}$$

$$U'(r_0 - \epsilon) = U'(r_0 + \epsilon) \tag{D.32}$$

$$U(0) = 0 \tag{D.33}$$

Though the full phase shift can be computed analytically, consider for now the small momentum expansion:

$$k\cot(\delta_l(k)) = \frac{1}{a} + \frac{1}{2}r_s k^2 \tag{D.34}$$

$$a = -r_0\left[1 - \frac{\tan(r_0\kappa_0)}{r_0\kappa_0}\right] \tag{D.35}$$

$$r_s = r_0\left[1 - \frac{r_0^2}{3a^2} + \frac{1}{\kappa_0^2 a r_0}\right] \tag{D.36}$$

$$\kappa_0 = \frac{2mV_0}{\hbar^2} \tag{D.37}$$

Notice that the scattering length a is negative for $r_0\kappa < 4.5$. This is a general feature that attractive potential have negative scattering lengths. In terms of phase shfits, this corresponds to attractive potential ‘’sucking in” wavefucntion. Also observe that for reasonable scattering length the effective range r_0 is positive.

Bound Energy States

What is happening though when the scattering length crosses zero or diverges? Consider the bound states of energy $-E$ for the finite square well $-V_0$ of size $2r_0$. The radial equation is the same as looking for the antisymmetric solutions. This leads to a implicit equation for bound state energies $\{E_i\}$.

$$\tan\left[-\sqrt{(\kappa_0 r_0)^2 - (\kappa r_0)^2}\right] = \sqrt{\left(\frac{\kappa_0 r_0}{\kappa r_0}\right)^2 - 1} \tag{D.38}$$

$$\kappa = \sqrt{\frac{2mE}{\hbar^2}} \tag{D.39}$$

$$\kappa_0 = \sqrt{\frac{2mV_0}{\hbar^2}} \tag{D.40}$$

This can be undimensionaized in terms of the unitless parameter $x = \kappa_0 r_0$ and the

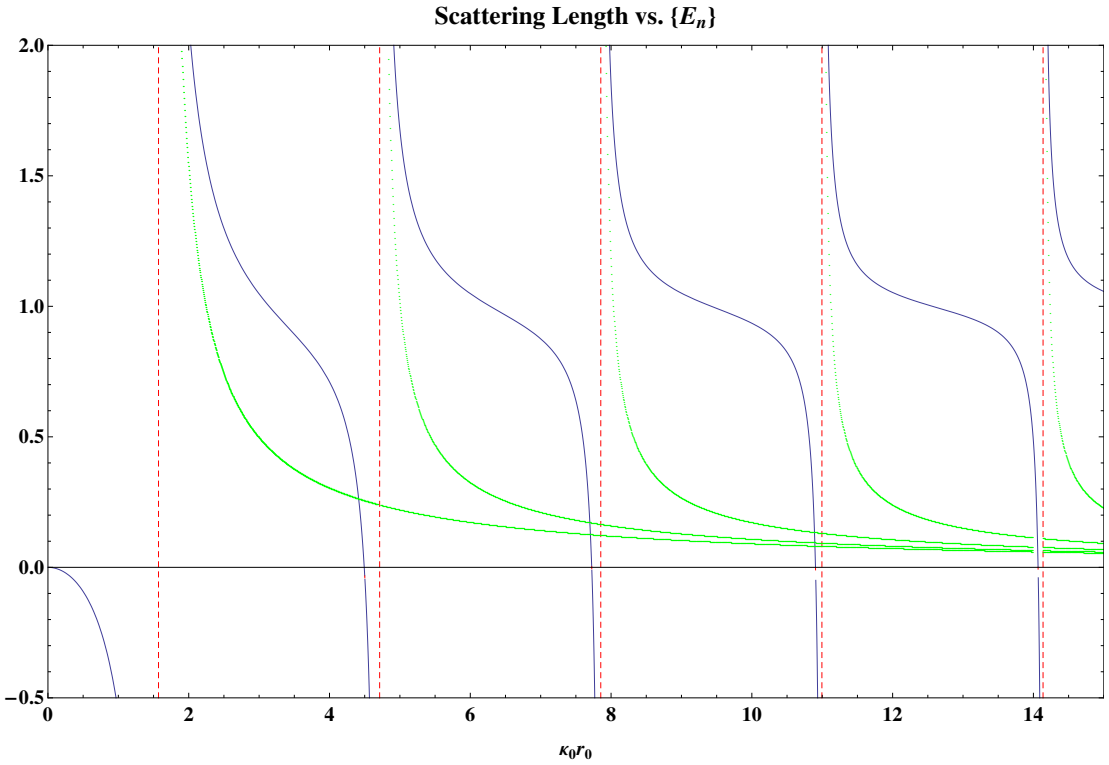

Figure D.2: Resonances in the scattering length $\frac{a}{r_0}$ (blue) are observed to be coincidence with the generation of a new bound state with inverse normalized wave number $l = \frac{1}{\kappa r_0}$ (green). The parameter $\kappa_0 = \sqrt{\frac{2\mu V_0}{\hbar^2}}$ describes the strength of the attractive interaction.

unitless inverse wave number of the bound state $l = \frac{1}{\kappa r_0}$

$$\tan\left[-\sqrt{x^2 - \frac{1}{l^2}}\right] = \sqrt{x^2 l^2 - 1} \tag{D.41}$$

The plot given in figure (D.0.3) illuminates the qualitative origin of the resonant phenomenom. As the interaction paramter $\kappa_0 r_0$ is tuned, bound states are generated. When the most energetic bound state is very weakly bounded, it becomes close to resonance with the scattering state. The phase shift between the two varies rapidly which causes the scattering length to diverge.

Although ths toy model does not acurately represent actual attractive interatomic interactions it does demonstrate some key qualitative aspects of attractive scattering:

(a) A "weak" attractive potential is characterized by a negative scattering length.

(b) Resonances between weakly bounded and scattering states causes wild fluctuations in the scattering length.

D.0.4 General Method for Finding a and r_e

The finite square well is one of the simplest attractive potentials, but is not quite realistic. Generally speaking, solving the entire Hamiltonian is not possible, and not even necessary as we mostly care about the lowest order expansion. In this section I shall consider a general method for determing the coeffcients from an s-wave potential.

The time independent 1D radial schrodinger equation is:

$$\left[\frac{\partial^2}{\partial r^2} + k^2 - \frac{2\mu}{\hbar^2}V(r)\right]U(r) = 0 \tag{D.42}$$

$$\tag{D.43}$$

The expansion goes as:

$$k\cot(\delta_0(k)) = -\frac{1}{a} + \frac{1}{2}r_e k^2 \tag{D.44}$$

$$r_e = 2\int_0^\infty \left[v_0^2 - u_0^2\right]\mathrm{d}r \tag{D.45}$$

Where the functions $v_0(r)$ and $u_0(r)$ are the solutions to the no potential and no kinetic energy case respectively. To lowest order we make take the approximate solutions

when $k \to 0$.

$$\frac{\partial^2}{\partial r^2} u_0(r) = \frac{2\mu}{\hbar^2} V(r) u_0(r) \tag{D.46}$$

$$\lim_{r\to\infty} u_0(r) = 1 - \frac{r}{a} \tag{D.47}$$

$$\frac{\partial^2}{\partial r^2} v(r) = -k^2 v_k(r) \tag{D.48}$$

$$\lim_{k\to 0} v_k(r) = 1 - \frac{r}{a} \tag{D.49}$$

$$:= v_0(r) \tag{D.50}$$

In the large distane limit then both $u_0(r)$ and $v_0(r)$ become the same function which expresses the fact that far away fromthe pontetial the solution is the same. The effective range is given as an expression as the difference of those solutions.

D.0.5 Example: Van Der Waals with Hard Shell

. In this example we shall demonstrate a method to compute the effective range from approxiate solutions to the time independent schrodinger equation. Consider the Van Der Waals potential with a hard core shell.

$$V(r) = \begin{cases} +\infty & r < r_c \\ -\frac{C_6}{r^6} & r \geq r_c \end{cases}$$

The parameters C_6 and r_c define the interaction potential. From our persepctive, we desire instead the scattering length a and effective range r_e. The functions given above are:

$$a_c := \left(\frac{2C_6\mu}{\hbar^2}\right)^{\frac{1}{4}} \tag{D.51}$$

$$u_0(r) =; mess \tag{D.52}$$

$$v_0(r) = 1 - \frac{r}{a} \tag{D.53}$$

Evidently, in the case that $a > 0$ the hard shell approimation is quite good, but in the case $a < 0$ the hard core approximation breaks down. For the interaction mentioned above there is a zero point crossing at:

D.0.6 Ramsauer-Townsend Effect for $a < 0$

For small energies, the cot expansion can be recast in the following way:

$$k \cot \delta = \frac{1}{a} + \frac{1}{2} r_s k^2 + O(k^4) \tag{D.54}$$

$$\tan \delta = -ka - \frac{1}{2} a^2 r_s k^3 + O(k^5) \tag{D.55}$$

For negative scattering lengths a zero crossing in the phase shift and consequently the scattering cross section occurs. Assuming thermal equilibrium a temperature can be set

$$k_{\text{zero}}^2 = \frac{|a|}{\frac{1}{2}a^2 r_s} \tag{D.56}$$

$$\frac{3}{2}k_B T = \frac{\hbar^2 k^2}{2m} \tag{D.57}$$

$$k_B T_{\text{zero}} = \frac{2\hbar^2}{3|a|r_s \mu} \tag{D.58}$$

This effect is of particular importance for $|2,2\rangle$ atoms in the magnetic trap which have a negative scattering length. Using the known scattering length ($a = -27.6a_0$) and effectives range ($r_s = 116a_0$), the equivalent temperature can be computed.

$$\boxed{T_{\text{zero}} = 5.15mK,\ |2,2\rangle \text{ scattering}} \tag{D.59}$$

Bibliography

[1] Christopher Foot. *Atomic Physics*. Oxford University Press, New York, first edition, 2005.

[2] H. Smith C. J.Pethick. *Bose-Einstein Condensation in Dilute Gases*. Cambridge University Press, New York, second edition, 2008.

[3] Martin Holthaus. Floquet engineering with quasienergy bands of periodically driven optical lattices. *Journal of Physics B: Atomic, Molecular and Optical Physics*, 49(1):013001, Nov 2015.

[4] Zachary Geiger. *An Apparatus for Dynamical Quantum Emulation Using Ultracold Lithium*. PhD thesis, University of California, Santa Barbara, 2017.

[5] Ruwan Senaratne. *Quantum Simulation of Strongly-Driven Systems Using Ultracold Lithium and Strontium*. PhD thesis, University of California, Santa Barbara, 2018.

[6] Kevin Singh. *Floquet Engineering with Ultracold Lithium in Optical Lattices*. PhD thesis, University of California, Santa Barbara, 2019.

[7] Shankari Vani Rajagopal. *Realizing and probing driven quantum systems with ultracold gases*. PhD thesis, University of California, Santa Barbara, 2019.

[8] Florian Schreck. *Mixtures of Ultracold Gases: Fermi Sea and Bose-Einstein Condensate of Lithium Isotopes*. PhD thesis, University of Paris, 2002.

[9] Eric Wille. *Preparation of an Optically Trapped Fermi-Fermi Mixture of 6Li and 40K Atoms and Characterization of the Interspecies Interactions by Feshbach Spectroscopy*. PhD thesis, Universitat Innsbruck, 2009.

[10] W. Ketterle, D.S. Durfee, and D.M. Stamper-Kurn. Making, probing and understanding bose-einstein condensates. *IOS Press*, pages 67–176, 1999.

[11] Ruwan Senaratne, Shankari V. Rajagopal, Zachary A. Geiger, Kurt M. Fujiwara, Vyacheslav Lebedev, and David M. Weld. Effusive atomic oven nozzle design using

an aligned microcapillary array. *Review of Scientific Instruments*, 86(2):023105, 2015.

[12] Andrew T. Grier, Igor Ferrier-Barbut, Benno S. Rem, Marion Delehaye, Lev Khaykovich, Frédéric Chevy, and Christophe Salomon. Λ-enhanced sub-doppler cooling of lithium atoms in D_1 gray molasses. *Physical Review A*, 87:063411, Jun 2013.

[13] L.D. Landau and E.M. Lifshitz. *Mechanics*. Number 1 in Course of Theoretical Physics. Elsevier Science, 1982.

[14] J. M. Gerton, C. A. Sackett, B. J. Frew, and R. G. Hulet. Dipolar relaxation collisions in magnetically trapped ^{7}Li. *Physical Review A*, 59:1514–1516, Feb 1999.

[15] C. A. Sackett, C. C. Bradley, and R. G. Hulet. Optimization of evaporative cooling. *Physical Review A*, 55:3797–3801, May 1997.

[16] R. Grimm, M. Weidemueller, and Y. Ovchinnikov. Optical dipole traps for neutral atoms. *ArXiv e-prints*, Feb 1999.

[17] S. E. Pollack, D. Dries, M. Junker, Y. P. Chen, T. A. Corcovilos, and R. G. Hulet. Extreme tunability of interactions in a ^{7}Li bose-einstein condensate. *Physical Review Letters*, 102:090402, Mar 2009.

[18] Cheng Chin, Rudolf Grimm, Paul Julienne, and Eite Tiesinga. Feshbach resonances in ultracold gases. *Rev. Mod. Phys.*, 82:1225–1286, Apr 2010.

[19] Hulet group. private communication, 2018.

[20] Bastian Hunt. *Momentum-Resolved Optical Lattice Modulation Spectroscopy on Bose-Fermi Mixtures*. PhD thesis, Universitt Hamburg, 2011.

[21] D. McKay, M. White, and B. DeMarco. Lattice thermodynamics for ultracold atoms. *Physical Review A*, 79:063605, Jun 2009.

[22] Markus Greiner, Immanuel Bloch, Olaf Mandel, Theodor W. Hänsch, and Tilman Esslinger. Exploring phase coherence in a 2d lattice of bose-einstein condensates. *Physical Review Letters*, 87:160405, Oct 2001.

[23] Bryce R.Gadway. *Bose Gases in Tailored Optical and Atomic Lattices*. PhD thesis, Stony Brook University, 2012.

[24] James A. Blackburn, H. J. T. Smith, and Niels Grnbech-Jensen. Stability and hopf bifurcations in an inverted pendulum. *American Journal of Physics*, 60(10):903–908, 1992.

[25] Ido Gilary, Nimrod Moiseyev, Saar Rahav, and Shmuel Fishman. Trapping of particles by lasers: the quantum kapitza pendulum. *Journal of Physics A: Mathematical and General*, 36(25):L409–L415, jun 2003.

[26] Saar Rahav, Ido Gilary, and Shmuel Fishman. Effective hamiltonians for periodically driven systems. *Physical Review A*, 68:013820, Jul 2003.

[27] R. H. Hardin and F. D. Tappert. R. h. hardin and f. d. tappert, siam rev. chronicle 15, 423 (1973). *SIAM Rev. Chronicle*, 15:423, 1973.

[28] Felix Bloch. Über die quantenmechanik der elektronen in kristallgittern. *Zeitschrift für Physik*, 52(7):555–600, Jul 1929.

[29] C. Zener. A theory of the electrical breakdown of solid dielectrics. *Proc. R. Soc. A*, 145(855):523–529, 1934.

[30] J. Feldmann, K. Leo, J. Shah, D. A. B. Miller, J. E. Cunningham, T. Meier, G. von Plessen, A. Schulze, P. Thomas, and S. Schmitt-Rink. Optical investigation of bloch oscillations in a semiconductor superlattice. *Physical Review B*, 46:7252–7255, Sep 1992.

[31] R. Morandotti, U. Peschel, J. S. Aitchison, H. S. Eisenberg, and Y. Silberberg. Experimental observation of linear and nonlinear optical bloch oscillations. *Physical Review Letters*, 83:4756–4759, Dec 1999.

[32] Maxime Ben Dahan, Ekkehard Peik, Jakob Reichel, Yvan Castin, and Christophe Salomon. Bloch oscillations of atoms in an optical potential. *Physical Review Letters*, 76:4508–4511, Jun 1996.

[33] B. P. Anderson and M. A. Kasevich. Macroscopic quantum interference from atomic tunnel arrays. *Science*, 282(5394):1686–1689, 1998.

[34] O. Morsch, J. H. Müller, M. Cristiani, D. Ciampini, and E. Arimondo. Bloch oscillations and mean-field effects of bose-einstein condensates in 1d optical lattices. *Physical Review Letters*, 87:140402, Sep 2001.

[35] M. Fattori, C. D'Errico, G. Roati, M. Zaccanti, M. Jona-Lasinio, M. Modugno, M. Inguscio, and G. Modugno. Atom interferometry with a weakly interacting bose-einstein condensate. *Physical Review Letters*, 100:080405, Feb 2008.

[36] M. Gustavsson, E. Haller, M. J. Mark, J. G. Danzl, G. Rojas-Kopeinig, and H.-C. Nägerl. Control of interaction-induced dephasing of bloch oscillations. *Physical Review Letters*, 100:080404, Feb 2008.

[37] Christopher Gaul, Elena Díaz, Rodrigo P. A. Lima, Francisco Domínguez-Adame, and Cord A. Müller. Stability and decay of bloch oscillations in the presence of time-dependent nonlinearity. *Physical Review A*, 84:053627, Nov 2011.

[38] F. Meinert, M. J. Mark, E. Kirilov, K. Lauber, P. Weinmann, M. Gröbner, and H.-C. Nägerl. Interaction-Induced Quantum Phase Revivals and Evidence for the Transition to the Quantum Chaotic Regime in 1D Atomic Bloch Oscillations. *Physical Review Letters*, 112(19):193003, 5 2014.

[39] Philipp M. Preiss, Ruichao Ma, M. Eric Tai, Alexander Lukin, Matthew Rispoli, Philip Zupancic, Yoav Lahini, Rajibul Islam, and Markus Greiner. Strongly correlated quantum walks in optical lattices. *Science*, 347(6227):1229–1233, 2015.

[40] Elmar Haller, Russell Hart, Manfred J. Mark, Johann G. Danzl, Lukas Reichsöllner, and Hanns-Christoph Nägerl. Inducing transport in a dissipation-free lattice with super bloch oscillations. *Physical Review Letters*, 104:200403, May 2010.

[41] A. Alberti, V. V. Ivanov, G. M. Tino, and G. Ferrari. Engineering the quantum transport of atomic wavefunctions over macroscopic distances. *Nature Physics*, 5(8):547–550, Aug 2009.

[42] Andreas Buchleitner and Andrey R. Kolovsky. Interaction-induced decoherence of atomic bloch oscillations. *Physical Review Letters*, 91:253002, Dec 2003.

[43] Yu. V. Bludov, V. V. Konotop, and M. Salerno. Dynamical localization of gap-solitons by time periodic forces. *EPL (Europhysics Letters)*, 87(2):20004, 2009.

[44] M. Salerno, V. V. Konotop, and Yu. V. Bludov. Long-living bloch oscillations of matter waves in periodic potentials. *Physical Review Letters*, 101:030405, Jul 2008.

[45] R. Driben, V. V. Konotop, T. Meier, and A. V. Yulin. Bloch oscillations sustained by nonlinearity. *Scientific Reports*, 7(1):3194, 2017.

[46] D. Jaksch, C. Bruder, J. I. Cirac, C. W. Gardiner, and P. Zoller. Cold bosonic atoms in optical lattices. *Physical Review Letters*, 81(15):3108, 1998.

[47] K. W. Mahmud, L. Jiang, E. Tiesinga, and P. R. Johnson. Bloch oscillations and quench dynamics of interacting bosons in an optical lattice. *Physical Review A*, 89:023606, Feb 2014.

[48] Christopher Gaul, Elena Díaz, Rodrigo P A Lima, Francisco Domínguez-Adame, and Cord A. Müller. Stability and decay of Bloch oscillations in the presence of time-dependent nonlinearity. *Physical Review A - Atomic, Molecular, and Optical Physics*, 84(5):1–13, 2011.

[49] F Domínguez-Adame. Beyond the semiclassical description of Bloch oscillations. *European Journal of Physics*, 31(3):639–644, 2010.

[50] L. Duca, T. Li, M. Reitter, I. Bloch, M. Schleier-Smith, and U. Schneider. An aharonov-bohm interferometer for determining bloch band topology. *Science*, 347(6219):288–292, 2015.

[51] Andrea Damascelli, Zahid Hussain, and Zhi-Xun Shen. Angle-resolved photoemission studies of the cuprate superconductors. *Rev. Mod. Phys.*, 75:473–541, Apr 2003.

[52] I. Carusotto, L. Pitaevskii, S. Stringari, G. Modugno, and M. Inguscio. Sensitive measurement of forces at the micron scale using Bloch oscillations of ultracold atoms. *Physical Review Letters*, 95(9):093202, Aug 2005.

[53] G. Ferrari, N. Poli, F. Sorrentino, and G. M. Tino. Long-lived bloch oscillations with bosonic sr atoms and application to gravity measurement at the micrometer scale. *Physical Review Letters*, 97:060402, Aug 2006.

[54] Pierre Cladé, Estefania de Mirandes, Malo Cadoret, Saïda Guellati-Khélifa, Catherine Schwob, Fran çois Nez, Lucile Julien, and Fran çois Biraben. Determination of the fine structure constant based on bloch oscillations of ultracold atoms in a vertical optical lattice. *Physical Review Letters*, 96:033001, Jan 2006.

[55] Brian Estey, Chenghui Yu, Holger Müller, Pei-Chen Kuan, and Shau-Yu Lan. High-resolution atom interferometers with suppressed diffraction phases. *Physical Review Letters*, 115:083002, Aug 2015.

[56] Sebastian Kling, Tobias Salger, Christopher Grossert, and Martin Weitz. Atomic bloch-zener oscillations and stückelberg interferometry in optical lattices. *Physical Review Letters*, 105:215301, Nov 2010.

[57] M. Aidelsburger, M. Lohse, C. Schweizer, M. Atala, J. T. Barreiro, S. Nascimbène, N. R. Cooper, I. Bloch, and N. Goldman. Measuring the chern number of hofstadter bands with ultracold bosonic atoms. *Nature Physics*, 11:162–166, Dec 2014.

[58] Tracy Li, Lucia Duca, Martin Reitter, Fabian Grusdt, Eugene Demler, Manuel Endres, Monika Schleier-Smith, Immanuel Bloch, and Ulrich Schneider. Bloch state tomography using wilson lines. *Science*, 352(6289):1094–1097, 2016.

[59] N. Fläschner, D. Vogel, M. Tarnowski, B. S. Rem, D.-S. Lühmann, M. Heyl, J. C. Budich, L. Mathey, K. Sengstock, and C. Weitenberg. Observation of dynamical vortices after quenches in a system with topology. *Nature Physics*, 14(3):265–268, 2018.

[60] E. H. Hutten. Relativistic (non-linear) oscillator. *Nature*, 205:892, 02 1965.

[61] William Moreau, Richard Easther, and Richard Neutze. Relativistic (an)harmonic oscillator. *American Journal of Physics*, 62(6):531–535, 1994.

[62] Zhi-Feng Li, Jin-Jin Liu, Wolfgang Lucha, Wen-Gan Ma, and Franz F. Schberl. Relativistic harmonic oscillator. *Journal of Mathematical Physics*, 46(10):103514, 2005.

[63] D. Babusci, G. Dattoli, M. Quattromini, and E. Sabia. Relativistic harmonic oscillator, the associated equations of motion, and algebraic integration methods. *Phys. Rev. E*, 87:033202, Mar 2013.

[64] Edward Parker. A relativistic gravity train. *General Relativity and Gravitation*, 49(8):106, Jul 2017.

[65] J. A. Franco-Villafañe, E. Sadurní, S. Barkhofen, U. Kuhl, F. Mortessagne, and T. H. Seligman. First experimental realization of the Dirac oscillator. *Physical Review Letters*, 111:170405, Oct 2013.

[66] Gediminas Juzeliūnas, Julius Ruseckas, Markus Lindberg, Luis Santos, and Patrik Öhberg. Quasirelativistic behavior of cold atoms in light fields. *Physical Review A*, 77:011802, Jan 2008.

[67] Tobias Salger, Christopher Grossert, Sebastian Kling, and Martin Weitz. Klein tunneling of a quasirelativistic Bose-Einstein condensate in an optical lattice. *Physical Review Letters*, 107:240401, Dec 2011.

[68] L J LeBlanc, M C Beeler, K Jimenez-Garcia, A R Perry, S Sugawa, R A Williams, and I B Spielman. Direct observation of zitterbewegung in a Bose-Einstein condensate. *New Journal of Physics*, 15(7):073011, 2013.

[69] Chunlei Qu, Chris Hamner, Ming Gong, Chuanwei Zhang, and Peter Engels. Observation of zitterbewegung in a spin-orbit-coupled Bose-Einstein condensate. *Physical Review A*, 88:021604, Aug 2013.

[70] Martin Leder, Christopher Grossert, and Martin Weitz. Veselago lensing with ultracold atoms in an optical lattice. *Nature Communications*, 5:3327, 02 2014.

[71] Christopher Grossert, Martin Leder, and Martin Weitz. Phase dependent loading of Bloch bands and quantum simulation of relativistic wave equation predictions with ultracold atoms in variably shaped optical lattice potentials. *Journal of Modern Optics*, 63(18):1805–1813, 2016.

[72] Javier Rodríguez-Laguna, Leticia Tarruell, Maciej Lewenstein, and Alessio Celi. Synthetic unruh effect in cold atoms. *Physical Review A*, 95:013627, Jan 2017.

[73] A. Bermudez, M. A. Martin-Delgado, and E. Solano. Exact mapping of the $2 + 1$ dirac oscillator onto the jaynes-cummings model: Ion-trap experimental proposal. *Physical Review A*, 76:041801, Oct 2007.

[74] R. Gerritsma, G. Kirchmair, F. Zähringer, E. Solano, R. Blatt, and C. F. Roos. Quantum simulation of the Dirac equation. *Nature*, 463:68, 01 2010.

[75] R. Gerritsma, B. P. Lanyon, G. Kirchmair, F. Zähringer, C. Hempel, J. Casanova, J. J. García-Ripoll, E. Solano, R. Blatt, and C. F. Roos. Quantum simulation of the Klein paradox with trapped ions. *Physical Review Letters*, 106:060503, Feb 2011.

[76] S. Longhi. Photonic realization of the relativistic Dirac oscillator. *Opt. Lett.*, 35(8):1302–1304, Apr 2010.

[77] C. W. J. Beenakker. Colloquium: Andreev reflection and Klein tunneling in graphene. *Rev. Mod. Phys.*, 80:1337–1354, Oct 2008.

[78] Ekkehard Peik, Maxime Ben Dahan, Isabelle Bouchoule, Yvan Castin, and Christophe Salomon. Bloch oscillations of atoms, adiabatic rapid passage, and monokinetic atomic beams. *Physical Review A*, 55:2989–3001, Apr 1997.

[79] Georg Wirth, Matthias Ölschläger, and Andreas Hemmerich. Evidence for orbital superfluidity in the p-band of a bipartite optical square lattice. *Nature Physics*, 7:147 EP –, 12 2010.

[80] T Kock, C Hippler, A Ewerbeck, and A Hemmerich. Orbital optical lattices with bosons. *Journal of Physics B: Atomic, Molecular and Optical Physics*, 49(4):042001, 2016.

[81] A. Browaeys, H. Häffner, C. McKenzie, S. L. Rolston, K. Helmerson, and W. D. Phillips. Transport of atoms in a quantum conveyor belt. *Physical Review A*, 72:053605, Nov 2005.

[82] J. Heinze, J. S. Krauser, N. Fläschner, B. Hundt, S. Götze, A. P. Itin, L. Mathey, K. Sengstock, and C. Becker. Intrinsic photoconductivity of ultracold fermions in optical lattices. *Physical Review Letters*, 110:085302, Feb 2013.

[83] Jacob F Sherson, Sung Jong Park, Poul L Pedersen, Nils Winter, Miroslav Gajdacz, Sune Mai, and Jan Arlt. The pump-probe coupling of matter wave packets to remote lattice states. *New Journal of Physics*, 14(8):083013, 2012.

[84] Poul L. Pedersen, Miroslav Gajdacz, Nils Winter, Andrew J. Hilliard, Jacob F. Sherson, and Jan Arlt. Production and manipulation of wave packets from ultracold atoms in an optical lattice. *Physical Review A*, 88:023620, Aug 2013.

[85] Zachary A. Geiger, Kurt M. Fujiwara, Kevin Singh, Ruwan Senaratne, Shankari V. Rajagopal, Mikhail Lipatov, Toshihiko Shimasaki, Rodislav Driben, Vladimir V. Konotop, Torsten Meier, and David M. Weld. Observation and uses of position-space bloch oscillations in an ultracold gas. *Physical Review Letters*, 120:213201, May 2018.

[86] Paul Hamilton, Geena Kim, Trinity Joshi, Biswaroop Mukherjee, Daniel Tiarks, and Holger Müller. Sisyphus cooling of lithium. *Physical Review A*, 89:023409, Feb 2014.

[87] Phillip L. Gould, George A. Ruff, and David E. Pritchard. Diffraction of atoms by light: The near-resonant kapitza-dirac effect. *Physical Review Letters*, 56:827–830, Feb 1986.

[88] J Hecker Denschlag, J E Simsarian, H Häffner, C McKenzie, A Browaeys, D Cho, K Helmerson, S L Rolston, and W D Phillips. A bose-einstein condensate in an optical lattice. *Journal of Physics B*, 35(14):3095, 2002.

[89] R. Moessner and S. L. Sondhi. Equilibration and order in quantum floquet matter. *Nat Phys*, 13(5):424–428, 05 2017.

[90] André Eckardt. Colloquium: Atomic quantum gases in periodically driven optical lattices. *Rev. Mod. Phys.*, 89:011004, Mar 2017.

[91] Y. H. Wang, H. Steinberg, P. Jarillo-Herrero, and N. Gedik. Observation of Floquet-Bloch states on the surface of a topological insulator. *Science*, 342(6157):453–457, 2013.

[92] Shambhu Ghimire, Anthony D. DiChiara, Emily Sistrunk, Pierre Agostini, Louis F. DiMauro, and David A. Reis. Observation of high-order harmonic generation in a bulk crystal. *Nat Phys*, 7(2):138–141, 02 2011.

[93] B. Zaks, R. B. Liu, and M. S. Sherwin. Experimental observation of electron-hole recollisions. *Nature*, 483(7391):580–583, 03 2012.

[94] Peter G. Hawkins, Misha Yu. Ivanov, and Vladislav S. Yakovlev. Effect of multiple conduction bands on high-harmonic emission from dielectrics. *Physical Review A*, 91:013405, Jan 2015.

[95] O. Schubert, M. Hohenleutner, F. Langer, B. Urbanek, C. Lange, U. Huttner, D. Golde, T. Meier, M. Kira, S. W. Koch, and R. Huber. Sub-cycle control of terahertz high-harmonic generation by dynamical bloch oscillations. *Nature Photonics*, 8:119 EP –, 01 2014.

[96] M. Hohenleutner, F. Langer, O. Schubert, M. Knorr, U. Huttner, S. W. Koch, M. Kira, and R. Huber. Real-time observation of interfering crystal electrons in high-harmonic generation. *Nature*, 523:572 EP –, 07 2015.

[97] Georges Ndabashimiye, Shambhu Ghimire, Mengxi Wu, Dana A. Browne, Kenneth J. Schafer, Mette B. Gaarde, and David A. Reis. Solid-state harmonics beyond the atomic limit. *Nature*, 534:520 EP –, 06 2016.

[98] G. Vampa, T. J. Hammond, N. Thiré, B. E. Schmidt, F. Légaré, C. R. McDonald, T. Brabec, D. D. Klug, and P. B. Corkum. All-optical reconstruction of crystal band structure. *Physical Review Letters*, 115:193603, Nov 2015.

[99] Giacomo Roati, Chiara D'Errico, Leonardo Fallani, Marco Fattori, Chiara Fort, Matteo Zaccanti, Giovanni Modugno, Michele Modugno, and Massimo Inguscio. Anderson localization of a non-interacting bose-einstein condensate. *Nature*, 453:895 EP –, Jun 2008.

[100] Juliette Billy, Vincent Josse, Zhanchun Zuo, Alain Bernard, Ben Hambrecht, Pierre Lugan, David Clément, Laurent Sanchez-Palencia, Philippe Bouyer, and Alain Aspect. Direct observation of anderson localization of matter waves in a controlled disorder. *Nature*, 453:891 EP –, Jun 2008.

[101] S. S. Kondov, W. R. McGehee, J. J. Zirbel, and B. DeMarco. Three-dimensional anderson localization of ultracold matter. *Science*, 334(6052):66–68, 2011.

[102] D. E. Miller, J. K. Chin, C. A. Stan, Y. Liu, W. Setiawan, C. Sanner, and W. Ketterle. Critical velocity for superfluid flow across the bec-bcs crossover. *Physical Review Letters*, 99:070402, Aug 2007.

[103] Rémi Desbuquois, Lauriane Chomaz, Tarik Yefsah, Julian Léonard, Jérôme Beugnon, Christof Weitenberg, and Jean Dalibard. Superfluid behaviour of a two-dimensional bose gas. *Nature Physics*, 8:645 EP –, Jul 2012.

[104] David Stadler, Sebastian Krinner, Jakob Meineke, Jean-Philippe Brantut, and Tilman Esslinger. Observing the drop of resistance in the flow of a superfluid fermi gas. *Nature*, 491:736 EP –, Nov 2012.

[105] Y.-J. Lin, K. Jiménez-García, and I. B. Spielman. Spin-orbit-coupled bose-einstein condensates. *Nature*, 471:83 EP –, Mar 2011.

[106] Poul L. Pedersen, Miroslav Gajdacz, Nils Winter, Andrew J. Hilliard, Jacob F. Sherson, and Jan Arlt. Production and manipulation of wave packets from ultracold atoms in an optical lattice. *Physical Review A*, 88:023620, Aug 2013.

[107] P. Cheiney, C. M. Fabre, F. Vermersch, G. L. Gattobigio, R. Mathevet, T. Lahaye, and D. Guéry-Odelin. Matter-wave scattering on an amplitude-modulated optical lattice. *Physical Review A*, 87:013623, Jan 2013.

[108] N. Fläschner, D. Vogel, M. Tarnowski, B. S. Rem, D.-S. Lühmann, M. Heyl, J. C. Budich, L. Mathey, K. Sengstock, and C. Weitenberg. Observation of dynamical vortices after quenches in a system with topology. *Nature Physics*, 14(3):265–268, 2018.

[109] H. Lignier, C. Sias, D. Ciampini, Y. Singh, A. Zenesini, O. Morsch, and E. Arimondo. Dynamical control of matter-wave tunneling in periodic potentials. *Physical Review Letters*, 99:220403, Nov 2007.

[110] F. Meinert, M. J. Mark, K. Lauber, A. J. Daley, and H.-C. Nägerl. Floquet engineering of correlated tunneling in the Bose-Hubbard model with ultracold atoms. *Physical Review Letters*, 116:205301, May 2016.

[111] Tobias Salger, Sebastian Kling, Sergey Denisov, Alexey V. Ponomarev, Peter Hänggi, and Martin Weitz. Tuning the mobility of a driven bose-einstein condensate via diabatic floquet bands. *Physical Review Letters*, 110:135302, Mar 2013.

[112] Colin V. Parker, Li-Chung Ha, and Cheng Chin. Direct observation of effective ferromagnetic domains of cold atoms in a shaken optical lattice. *Nature Physics*, 9:769 EP –, Oct 2013.

[113] Pierre Cladé, Saïda Guellati-Khélifa, Fran çois Nez, and Fran çois Biraben. Large momentum beam splitter using bloch oscillations. *Physical Review Letters*, 102:240402, Jun 2009.

[114] C.J. Fujiwara, Zachary A Geiger, Kevin Singh, Ruwan Senaratne, Shankari V Rajagopal, Mikhail Lipatov, Toshihiko Shimasaki, and David M Weld. Experimental realization of a relativistic harmonic oscillator. *New Journal of Physics*, 20(6):063027, 2018.

[115] Netanel H. Lindner, Gil Refael, and Victor Galitski. Floquet topological insulator in semiconductor quantum wells. *Nat Phys*, 7(6):490–495, 06 2011.

[116] V. Dal Lago, M. Atala, and L. E. F. Foa Torres. Floquet topological transitions in a driven one-dimensional topological insulator. *Physical Review A*, 92:023624, Aug 2015.

[117] K Singh, C.J. Fujiwara, Z. A. Geiger, E. Q. Simmons, M. Lipatov, A. Cao, P. Dotti, S. V. Rajagopal, R. Senaratne, T. Shimasaki, M. Heyl, A. Eckardt, and D. M. Weld. Quantifying and controlling prethermal nonergodicity in interacting floquet matter. *arXiv:1809.05554*, 2018.

[118] André Eckardt. Colloquium: Atomic quantum gases in periodically driven optical lattices. *Review of Modern Physics*, 89(1):011004, 03 2017.

[119] Martin Holthaus. Floquet engineering with quasienergy bands of periodically driven optical lattices. *Journal of Physics B*, 49(1):013001, 2016.

[120] Gregor Jotzu, Michael Messer, Rémi Desbuquois, Martin Lebrat, Thomas Uehlinger, Daniel Greif, and Tilman Esslinger. Experimental realization of the topological Haldane model with ultracold fermions. *Nature*, 515:237, 11 2014.

[121] Mikael C. Rechtsman, Julia M. Zeuner, Yonatan Plotnik, Yaakov Lumer, Daniel Podolsky, Felix Dreisow, Stefan Nolte, Mordechai Segev, and Alexander Szameit. Photonic Floquet topological insulators. *Nature*, 496:196, 04 2013.

[122] J Zhang, P W Hess, A Kyprianidis, P Becker, A Lee, J Smith, G Pagano, I-D Potirniche, A C Potter, A Vishwanath, N Y Yao, and C Monroe. Observation of a discrete time crystal. *Nature*, 543(7644):217–220, 03 2017.

[123] Soonwon Choi, Joonhee Choi, Renate Landig, Georg Kucsko, Hengyun Zhou, Junichi Isoya, Fedor Jelezko, Shinobu Onoda, Hitoshi Sumiya, Vedika Khemani, Curt von Keyserlingk, Norman Y Yao, Eugene Demler, and Mikhail D Lukin. Observation of discrete time-crystalline order in a disordered dipolar many-body system. *Nature*, 543(7644):221–225, 03 2017.

[124] R. Moessner and S. L. Sondhi. Equilibration and order in quantum Floquet matter. *Nature Physics*, 13:424, 04 2017.

[125] P. Roushan, C. Neill, A. Megrant, Y. Chen, R. Babbush, R. Barends, B. Campbell, Z. Chen, B. Chiaro, A. Dunsworth, A. Fowler, E. Jeffrey, J. Kelly, E. Lucero, J. Mutus, P. J. J. O'Malley, M. Neeley, C. Quintana, D. Sank, A. Vainsencher, J. Wenner, T. White, E. Kapit, H. Neven, and J. Martinis. Chiral ground-state currents of interacting photons in a synthetic magnetic field. *Nature Physics*, 13:146, 10 2016.

[126] N. Fläschner, B. S. Rem, M. Tarnowski, D. Vogel, D. S. Lühmann, K. Sengstock, and C. Weitenberg. Experimental reconstruction of the Berry curvature in a Floquet Bloch band. *Science*, 352(6289):1091, 05 2016.

[127] Hirokazu Miyake, Georgios A. Siviloglou, Colin J. Kennedy, William Cody Burton, and Wolfgang Ketterle. Realizing the Harper Hamiltonian with laser-assisted tunneling in optical lattices. *Physical Review Letters*, 111:185302, Oct 2013.

[128] C. J. Fujiwara, Kevin Singh, Zachary A. Geiger, Ruwan Senaratne, Shankari V. Rajagopal, Mikhail Lipatov, and David M. Weld. Transport in Floquet-Bloch bands. *Physical Review Letters*, 122:010402, Jan 2019.

[129] Dmitry A. Abanin, Wojciech De Roeck, and François Huveneers. Exponentially slow heating in periodically driven many-body systems. *Physical Review Letters*, 115(25):256803, 12 2015.

[130] Tomotaka Kuwahara, Takashi Mori, and Keiji Saito. Floquet–magnus theory and generic transient dynamics in periodically driven many-body quantum systems. *Annals of Physics*, 367:96 – 124, 2016.

[131] Dmitry A. Abanin, Wojciech De Roeck, Wen Wei Ho, and François Huveneers. Effective hamiltonians, prethermalization, and slow energy absorption in periodically driven many-body systems. *Physical Review B*, 95(1):014112, 01 2017.

[132] Francisco Machado, Gregory D. Meyer, Dominic V. Else, Chetan Nayak, and Norman Y. Yao. Exponentially slow heating in short and long-range interacting floquet systems. *arXiv*, 2017.

[133] Takashi Mori, Tatsuhiko N Ikeda, Eriko Kaminishi, and Masahito Ueda. Thermalization and prethermalization in isolated quantum systems: a theoretical overview. *Journal of Physics B*, 51(11):112001, 2018.

[134] Achilleas Lazarides, Arnab Das, and Roderich Moessner. Periodic thermodynamics of isolated quantum systems. *Physical Review Letters*, 112(15):150401, Apr 2014.

[135] Achilleas Lazarides, Arnab Das, and Roderich Moessner. Equilibrium states of generic quantum systems subject to periodic driving. *Phys. Rev. E*, 90(1):012110, Jul 2014.

[136] Anushya Chandran and S. L. Sondhi. Interaction-stabilized steady states in the driven $O(N)$ model. *Physical Review B*, 93:174305, May 2016.

[137] Simon A Weidinger and Michael Knap. Floquet prethermalization and regimes of heating in a periodically driven, interacting quantum system. *Sci. Rep.*, 7:45382, Apr 2017.

[138] Elena Canovi, Marcus Kollar, and Martin Eckstein. Stroboscopic prethermalization in weakly interacting periodically driven systems. *Physical Review E*, 93:012130, Jan 2016.

[139] Marin Bukov, Sarang Gopalakrishnan, Michael Knap, and Eugene Demler. Prethermal Floquet steady states and instabilities in the periodically driven, weakly interacting Bose-Hubbard model. *Physical Review Letters*, 115(20):205301, 11 2015.

[140] Martin Reitter, Jakob Näger, Karen Wintersperger, Christoph Sträter, Immanuel Bloch, André Eckardt, and Ulrich Schneider. Interaction dependent heating and atom loss in a periodically driven optical lattice. *Physical Review Letters*, 119(20):200402, 11 2017.

[141] Michael Messer, Kilian Sandholzer, Frederik Görg, Joaquín Minguzzi, Rémi Desbuquois, and Tilman Esslinger. Floquet dynamics in driven Fermi-Hubbard systems. *Physical Review Letters*, 121:233603, Dec 2018.

[142] J. Nager, K. Wintersperger, M. Bukov, S. Lellouch, E. Demler, U. Schneider, I. Bloch, N. Goldman, and M. Aidelsburger. Parametric instabilities of interacting bosons in periodically-driven 1D optical lattices. *arXiv*, 2018.

[143] M. Weinberg, C. Ölschläger, C. Sträter, S. Prelle, A. Eckardt, K. Sengstock, and J. Simonet. Multiphoton interband excitations of quantum gases in driven optical lattices. *Physical Review A*, 92:043621, Oct 2015.

[144] T. Boulier, J. Maslek, M. Bukov, C. Bracamontes, E. Magnan, S. Lellouch, E. Demler, N. Goldman, and J. V. Porto. Parametric heating in a 2D periodically driven bosonic system: Beyond the weakly interacting regime. *Physical Review X*, 9:011047, Mar 2019.

[145] N. Fläschner, D. Vogel, M. Tarnowski, B. S. Rem, D. S. Lühmann, M. Heyl, J. C. Budich, L. Mathey, K. Sengstock, and C. Weitenberg. Observation of dynamical vortices after quenches in a system with topology. *Nature Physics*, 14(3):265–268, 2018.

[146] Pranjal Bordia, Henrik Lüschen, Ulrich Schneider, Michael Knap, and Immanuel Bloch. Periodically driving a many-body localized quantum system. *Nature Physics*, 13:460, 01 2017.

[147] P. L. Kapitza. Dynamic stability of a pendulum with an oscillating point of suspension. *J. Exp. Theor. Phys.*, 21:588, 1951.

[148] Ido Gilary, Nimrod Moiseyev, Saar Rahav, and Shmuel Fishman. Trapping of particles by lasers: the quantum kapitza pendulum. *Journal of Physics A: Mathematical and General*, 36(25):L409–L415, jun 2003.

[149] D. McKay, M. White, and B. DeMarco. Lattice thermodynamics for ultracold atoms. *Physical Review A*, 79(6):063605, 06 2009.

[150] Angelo Russomanno, Alessandro Silva, and Giuseppe E. Santoro. Periodic steady regime and interference in a periodically driven quantum system. *Physical Review Letters*, 109(25):257201, 12 2012.

[151] Luca D'Alessio and Marcos Rigol. Long-time behavior of isolated periodically driven interacting lattice systems. *Physical Review X*, 4(4):041048, 12 2014.

[152] P. T. Greenland. Seeking non-exponential decay. *Nature*, 335:298 EP –, 09 1988.

[153] Steven R. Wilkinson, Cyrus F. Bharucha, Martin C. Fischer, Kirk W. Madison, Patrick R. Morrow, Qian Niu, Bala Sundaram, and Mark G. Raizen. Experimental evidence for non-exponential decay in quantum tunnelling. *Nature*, 387(6633):575–577, 06 1997.

[154] P. T. Greenland. Quantum procrastination. *Nature*, 387:548 EP –, 06 1997.

[155] R Feifel, A L'Huillier, E Lindroth, V Zhaunerchyk, M Gisselbrecht, and M Dahlström. Attosecond chronoscopy of electron wave-packets probing entanglement and time-ordering of quantum processes. Wallenberg foundation proposal (unpublished), 2018.

[156] L Fonda, G C Ghirardi, and A Rimini. Decay theory of unstable quantum systems. *Reports on Progress in Physics*, 41(4):587–631, apr 1978.

[157] K. Urbanowski. General properties of the evolution of unstable states at long times. *The European Physical Journal D*, 54(1):25–29, Jul 2009.

[158] P. T. Greenland and A. M. Lane. Exposure of decay at non-constant rate by rapid fluctuations. *Physics Letters A*, 117(4):181–184, 1986.

[159] Cleanthes A Nicolaides and Theodoros Mercouris. On the violation of the exponential decay law in atomic physics:ab initio calculation of the time-dependence of the non-stationary state. *Journal of Physics B: Atomic, Molecular and Optical Physics*, 29(6):1151–1167, mar 1996.

[160] A M Ishkhanyan and V P Krainov. Non-exponential tunneling ionization of atoms by an intense laser field. *Laser Physics Letters*, 12(4):046002, 2015.

[161] N. G. Kelkar, M. Nowakowski, and K. P. Khemchandani. Hidden evidence of nonexponential nuclear decay. *Phys. Rev. C*, 70:024601, Aug 2004.

[162] Eric B. Norman, Stuart B. Gazes, Stephanie G. Crane, and Dianne A. Bennett. Tests of the exponential decay law at short and long times. *Physical Review Letters*, 60:2246–2249, May 1988.

[163] Markus Glück, Andrey R. Kolovsky, and Hans Jürgen Korsch. Wannier–stark resonances in optical and semiconductor superlattices. *Physics Reports*, 366(3):103 – 182, 2002.

[164] Ludwig Krinner, Michael Stewart, Arturo Pazmiño, Joonhyuk Kwon, and Dominik Schneble. Spontaneous emission of matter waves from a tunable open quantum system. *Nature*, 559(7715):589–592, 2018.

[165] Ulrich Hoeppe, Christian Wolff, Jens Küchenmeister, Jens Niegemann, Malte Drescher, Hartmut Benner, and Kurt Busch. Direct observation of non-markovian radiation dynamics in 3d bulk photonic crystals. *Physical Review Letters*, 108:043603, Jan 2012.